al-Farabi Kazakh National University

UDC: 542.943 **On manuscript rights**

Anas Houbi

Creating and Studying New Composite Materials for Microwave Absorption in the Range of 8.8-12 GHz

8D07104 Chemical technology of inorganic substances

Dissertation submitted in partial fulfillment of the requirements for the degree of Doctor of Philosophy (Ph.D.)

Scientific supervisors:
Doctor of Technical Sciences, Professor,
A.A. Zharmenov

Doctor of Physical Chemistry, Professor,
Yomen Atassi

Republic of Kazakhstan
Almaty, 2022

Contents

List of Abbreviations 4
INTRODUCTION 5
1 Chapter 1: Literature review 10
1.1 Significance of microwave absorbent materials 10
1.2 Microwaves 11
1.3 Mechanisms of EM wave absorption 11
1.4 Microwave absorption materials 12
1.4.1 Magnetic loss materials 13
1.4.2 Ferrites 13
1.4.3 Carbonyl iron powder (CIP) 16
1.4.4 Dielectric loss materials 17
1.4.5 Conductive polymers (CPs) 17
1.4.6 Carbonaceous substances 18
1.4.7 Hybrid materials 19
1.5 Composite absorbent materials with graded impedance 19
1.6 Characteristics of an ideal microwave absorption material. 19
1.7 Absorbent ferrites nanoparticles for microwave 19
1.8 Incorporation of CPs with ferrite nanoparticles to absorb microwaves 21
1.9 MA behavior of carbon-based nanomaterials 23
2 Chapter 2: Practical part 26
2.1 Chemicals, raw and commercial materials 26
2.2 Tools and equipment used for sample preparation 27
2.3 Characterization devices 28
2.4 Sample preparation 30
2.4.1 Preparation of ferrite powders 30
2.4.2 Preparation of microwave nanocomposites 36
2.4.3 Preparation of hybrid nanocomposites 39
3 Chapter 3: Results and discussion 43

3.1 XRD patterns 43
3.1.1 X-ray diffraction of undoped ferrites 43
3.1.2 X-ray diffraction of doped ferrites samples prepared by the ceramic sintering technique 43
3.2 FTIR spectra 55
3.2.1 FTIR spectra of ferrites prepared by the ceramic sintering technique 55
3.2.2 FTIR spectra of ferrite samples prepared by citrate precursor and self-combustion technique 55
3.2.3 FTIR spectra of carbon black, activated carbon, graphite and carbonyl iron 58
3.2.4 FTIR spectra of PANI-based nanocomposites 58
3.3 Energy-dispersive X-ray spectroscopy (EDX) analysis 59
3.3.1 EDX analysis for some spinel ferrites and hexagonal ferrite 59
3.3.2 EDX analysis of PANI-based nanocomposites 61
3.4 Morphology investigations 65
3.4.1 Morphology investigations for some spinel ferrites and hexagonal ferrite .. 65
3.4.2 Morphology investigations of PANI-based nanocomposites 66
3.5 TGA analysis 68
3.5.1 TGA analysis of PANI-based nanocomposites 68
3.6 Microwave absorption properties of prepared samples 70
3.6.1 Microwave absorption properties of ferrite samples prepared by the ceramic sintering technique 70
3.6.2 Microwave absorption properties of ferrite samples prepared by citrate precursor technique 80
3.6.3 Microwave absorption properties of ferrite samples prepared by the self-combustion technique 82
3.6.4 Microwave absorption properties of ferrite nanocomposites 86
3.6.5 Microwave absorption properties of PANI-based nanocomposites 98
Conclusion 108
References 111

List of Abbreviations

SE_A	Absorption shielding
Z_0	Air impedance
AC	Activated carbon
BW	Bandwidth
CB	Carbon black
CF	Carbon fibre
CNTs	Carbon nanotubes
ε_r	Complex relative permittivity
μ_r	Complex relative permeability
EDX	Energy-dispersive X-ray spectroscopy
EMI	Electromagnetic interference
ER	Epoxy resin
F	Ferrite
FTIR	Fourier Transform IR
f_m	Matching frequency
ε"	Imaginary part of permittivity
μ"	Imaginary part of permeability
p_{in}	Incident electromagnetic waves
Z	Matching impedance characteristic
Z_1	Material impedance
MA	Microwave absorption
RL_{min}	Minimal reflection loss
SE_{max}	Maximum shielding efficiency
MAMs	Microwave absorption materials
NC	Nanocomposite
NSFs	Nano spinel ferrites
NHFs	Nano hexagonal ferrites
PANI	Polyaniline
PVA	Polyvinyl alcohol
RAMs	Radar absorbing materials
SE_R	Reflection shielding
p_{ref}	Reflected power
ε'	Real part of permittivity
μ'	Real part of permeability
SEM	Scanning electron microscope
SD	Surface density
TGA	Thermogravimetric analysis
p_T	Transmitted power
XRD	X-ray diffractometer

INTRODUCTION

General description of the work

This work focuses on preparing microwave absorbent materials (MAMs) characterized by lightweight, strong absorption, and wide absorption bandwidth under -10 dB $(BW)_{-10\ dB}$ in the range of 8.8-12 GHz. Spinel ferrites and hexagonal ferrites were prepared by the ceramic sintering method. The effect of ferrite type, substitution with several metal ions, the concentration of metal ions, and loading percentage of ferrite in the host matrix on electromagnetic interference (EMI) and microwave absorption (MA) properties were studied. The best result obtained at this stage was by using $Ni^{3+}_{0.25}Ni^{2+}_{0.375}Zn^{2+}_{0.25}Fe_2O_4$. A minimal reflection loss (RL_{min}) indicated -13.3 dB at 9.8 GHz and absorption $BW_{-10\ dB}$ was 1.3 GHz for a thickness of 3 mm. Also, the maximum shielding efficiency (SE_{max}) attained 15.9 dB at 10.2 GHz. In the second stage of this research, the effect of the preparation method, calcination temperature, molar ratio of metal ions to citrate acid, and solution of polyvinyl alcohol (PVA) on EMI and MA properties were investigated. The best result was obtained by using the $Ni_{0.5}Zn_{0.5}Fe_2O_4$ nanoparticles with a loading percentage of 60% at a constant calcination temperature of 650° C prepared by the citrate precursor method. It was figured out from the above-mentioned studies that the defects of these prepared absorbers are that they have a limited absorption $BW_{-10\ dB}$ and high loading percentage. This necessitated working to decrease the loading percentage and increase the absorption $BW_{-10\ dB}$ of the absorbers to cover most of the frequency band of 8.8–12.0 GHz by incorporating magnetic loss and dielectric loss materials. As a result, MA nanocomposites were prepared. The effect of nanocomposite type, weight ratios of nanocomposites, spinel ferrite type used within the nanocomposite, and absorbent layer thickness on EMI and MA properties were investigated. The results showed that the absorption $BW_{-10\ dB}$ increased from 1.1 GHz to 3.2 GHz and the loading percentage decreased from 65% to 45% compared with the aforementioned studies. To enhance the RL value and obtain 99.9% absorption (attenuation) to the microwave with improving SE and SD. This required working on using conductive polymers such as polyaniline (PANI). According to that, hybrid nanocomposites were prepared. The effect of hybrid nanocomposite type, loading percentage, and weight ratios of PANI/F nanocomposite on EMI and MA properties were investigated. The results showed at this stage of the research that the RL and SE improved by obtaining 99.9% absorption to the microwave and decreasing the loading percentage from 45% to 25% which means obtaining lightweight absorbers with distinguished properties.

Actuality of the theme

EMI is a well-known critical problem in radar and antenna systems and electronic devices [1,2]. EMI is an unwanted Electromagnetic (EM) wave that works as a noise that disturbs the natural operation of electronic devices. This noise arises from electronic devices that release EM waves, such as mobile phones, wireless devices, television/computer screens and cordless microphones in halls. Generally, EMI would be regarded as an unwanted result of modern technology that has dangerous effects on human health, intelligent devices, telecommunication devices, and military industries. Consequently, the effective disposal of EM waves from EMI is so important for public protection security and electronic safety [3–8]. The development of radar or microwave absorbing materials technology has had a great impact on the military field. Radar absorbing materials (RAMs) are significant tools in electronic warfare, as they can be used to hide targets and protect them from radar detection [9,10]. EM shielding materials and RAMs have been produced by international companies at high prices. In this regard, the relevance of the research topic of the doctoral dissertation is paving the way for putting the methodology and scientific bases for the manufacture of MAMs in the laboratory with the required international quality. As well as competing with commercial absorbers mentioned in the literature in terms of weight, reflection loss, absorption bandwidth, and shielding efficiency.

Purpose of the work: to find optimum parameters for producing new RAMs characterized by strong Rl_{min}, high SE_{max}, broad absorption $BW_{-10\ dB}$ and low SD in the range of 8.8–12.0 GHz.

Tasks of the work:

1) Detecting the effect of molar ratios of metal ions to citrate acid (1:1, 2:1, and 3:1), and aqueous solutions of PVA (1%, 4%, and 6%) on the RL_{min}, f_m, and SE_{max}.
2) Figuring out the effect of adding the dielectric loss and magnetic loss materials on the nano ferrite properties and determining the weight ratios of nanocomposites, which has the greatest positive impact on the RL_{min}, f_m, $BW_{-10\ dB}$, SD and SE_{max}.
3) Revealing the effect of the loading percentage of hybrid nanocomposite in the host matrix, and weight ratios of PANI/$Ni^{3+}_{0.25}Ni^{2+}_{0.375}Zn^{2+}_{0.25}Fe_2O_4$, and PANI/$BaNiZnFe_{16}O_{27}$ on the EMI shielding and MA properties.
4) Detecting the effect of adding carbon black (CB) and carbonyl iron (CI) to hybrid nanocomposites on the RL_{min}, $BW_{-10\ dB}$, SD and SE_{max}.

The main provisions for the defense of the thesis:

1) Increasing the metal ions to citrate acid and PVA concentration in the ferrite leads the RL attenuation peaks of samples to shift to lower frequencies. This allows the position of the f_m to be controlled.
2) The synergistic incorporation of magnetic loss and dielectric loss materials leads to decreasing the loading percentage of the absorber in the host matrix, increasing the absorption $BW_{-10\ dB}$, and enhancing the SE_{max} of the absorbers to cover most of the frequency band of 8.8–12.0 GHz.
3) The reflection loss peaks of nanocomposites lead to moving to higher frequencies by increasing the PANI in the nanocomposites. This allows for controlling the absorption bandwidth, reflection loss, and matching the frequency of the absorbers.
4) Adding CB and CI to the hybrid nanocomposites leads to improving SE and SD. This allows for obtaining 99.9% absorption to the microwave.

The object of the research is microwave absorbers incorporated from magnetic loss and dielectric loss materials.

The subject of research is obtaining microwave absorbers prepared by different physical and chemical methods. Evaluating the characteristics of the absorbers by measuring RL, SE, absorption $BW_{-10\ dB}$ and SD.

The scientific novelty of the research results obtained is ascertained by the fact that for the first time:

- Creating new absorbents by incorporating magnetic loss and dielectric loss materials that can decrease the loading percentage, increase the absorption $BW_{-10\ dB}$, and enhance the SE_{max} of the absorbents to cover most of the frequency band of 8.8–12.0 GHz.
- A low loading percentage of PANI/$Ni^{3+}_{0.25}Ni^{2+}_{0.375}Zn^{2+}_{0.25}Fe_2O_4$ nanocomposite in the host matrix of 25% was reached, which is one of the lowest published loading percentages globally.
- New absorbers have been revealed that can exceed the -10 dB threshold and cover the entire frequency band of 8.8–12.0 GHz by adding CB and CI to the hybrid nanocomposites. These absorbers are competitive with commercial absorbers.

Research methods

The prepared samples were structurally characterized using XRD, FTIR, TGA, and EDX. SEM was utilized to define the morphology of the powders. Finally, the prepared samples were functionally characterized utilizing the horn antenna connected to an oscilloscope.

Theoretical significance: The results of the dissertation research expanded the known knowledge in the field of producing EMI shielding materials and MAMs to suppress EMI and improve the effectiveness of electronic devices.

The practical significance.

1) This project (the first of its kind in the Republic of Kazakhstan as an academic attempt to prepare radar absorption materials) constitutes a nucleus for subsequent research at the Al-Farabi Kazakh National University and the other universities in Kazakhstan in the preparation field of radar absorption materials.
2) The optimal parameters for the fabrication of microwave absorber nanocomposites at the whole frequency band of 8.8–12.0 GHz with low SD obtained from magnetic loss and dielectric loss materials were determined.
3) It was revealed that PANI/spinel ferrite (SF)/hexagonal ferrite (HF) and PANI/SF/HF/CB nanocomposites obtained from in-situ polymerization had the best results to absorb microwaves. The absorption percentage of microwaves reached about 99.9% with a loading percentage of 30%.

Relation to the plan of state research programs

This dissertational work was carried out without any framework.

The personal contribution of the author of the work consists of the collection, processing and analysis of literature data on the topic of the thesis, direct planning and implementation of the experimental part. The applicant took part in the analysis, interpretation and presentation of the obtained research results and their discussion, as well as in the preparation of scientific articles.

Approbation of thesis

The materials of the thesis were reported and discussed at various international conferences:

- International Scientific Conference of Students and Young Scientists "CHEMICAL PHYSICS AND PHYSICAL CHEMISTRY" (Al-Farabi Kazakh National University, Almaty, Kazakhstan, 6-8 April 2021).
- 11th INTERNATIONAL BEREMZHANOV CONGRESS ON CHEMISTRY AND CHEMICAL TECHNOLOGY "FUNDAMENTAL AND APPLIED MATERIALS SCIENCE", Almaty, Kazakhstan, 19-20 November 2021.

- YOUTH CHEMISTRY CONFERENCE (Nazarbayev University, Astana, Kazakhstan, November 20, 2021).
- International Scientific Conference of Students and Young Scientists"CHEMICAL PHYSICS AND PHYSICAL CHEMISTRY" (Al-Farabi Kazakh National University, Almaty, Kazakhstan, 6-8 April 2022).

Publications

The main research results on the topic of the dissertation are presented in 10 published works, including:

- One scientific article, published in a journal has an impact factor according to the Scopus database.
- Two scientific articles, published in a journal indexing to the Web of Science database.
- One scientific article, published in a journal recommended by the Committee for Control in the Sphere of Education and Science of the Ministry of Education and Science of the Republic of Kazakhstan.
- Four abstracts at international conferences.
- Two scientific articles at international journals.

Volume and structure of the thesis. The thesis consists of an introduction, five chapters, and a list of references. The work is presented on 122 pages, contains 83 figures, 40 tables, and 137 bibliographical references.

1 Chapter 1: Literature review

1.1 Significance of microwave absorbent materials

Lately, the accelerated progress of the smart age is connected with the backing of intelligent devices. Particularly, with the coming of the 5G age or future 6G or 7G age, intelligent EM devices in high-frequency are getting growing consideration because of the absolute supremacy in long-range, wireless, and great-speed response, etc. They allow connecting the countries with each other with stunning unusual convenience (Figure 1.1) [11–14]. In general, EMI would be considered an undesirable result of current technology that has hazardous impacts on us. These problems have received serious consideration from researchers various EM shielding materials and RAMs have been produced to absorb EM waves with high efficiency over a wide range of frequencies. Furthermore, RAMs have been used extensively to cover the walls of anechoic halls and to prevent or reduce electromagnetic reflections from large bodies [15]. RAMs can be produced in different forms, such as paints, thin films, sheets, and sponges [16]. These products are obtained by dispersing one or more types of absorbent materials in a polymeric matrix and applying them to a substrate or surface. Understanding the techniques for producing microwave absorbent composites by incorporating components, additives, and a matrix type is crucial to the final usage of the resulting absorbent material [15].

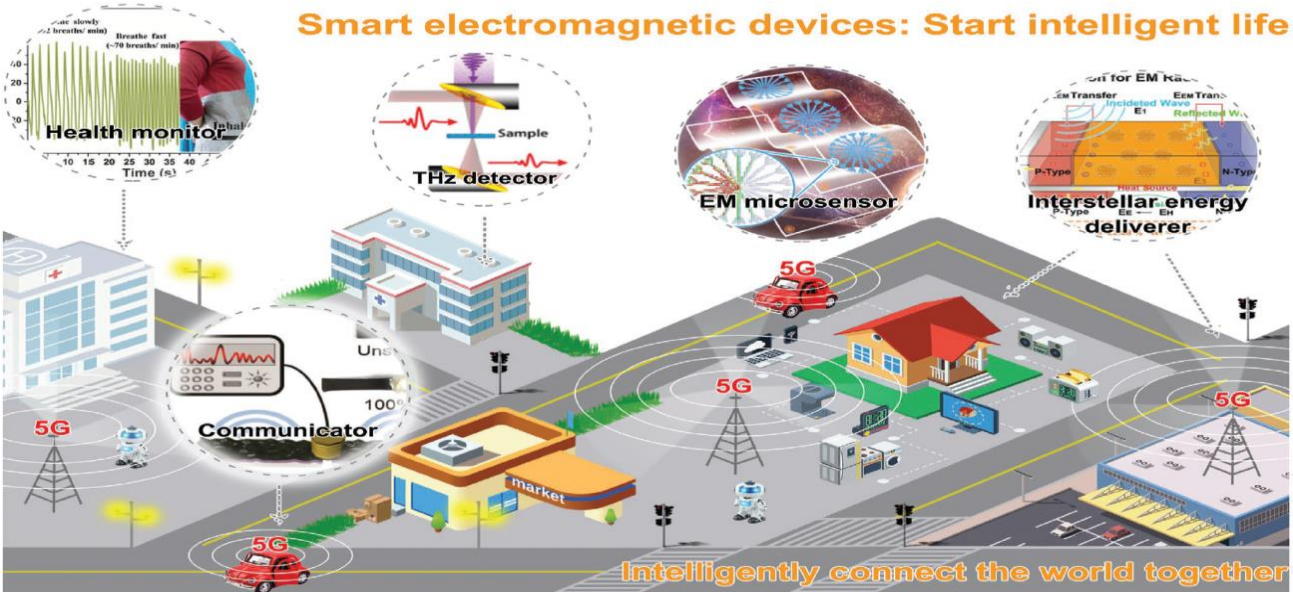

Figure 1.1 – Schematic design for smart living, involving intelligent house, intelligent clinic, intelligent market, intelligent plant, etc., illustrating that in the future, we enable to use intelligent electromagnetic apparatus (for example, electromagnetic screen (up 1), detector (up 2), microsensor (MS) (up 3), communicator (down) and power connector (up

4)) to collect the whole sides of our livelihoods together and design more intelligent models with stunning unusual comfortable

1.2 Microwaves

Microwaves are EM waves ranging from about 0.3 GHz to 300 GHz with corresponding wavelengths ranging from 1 m to 1 mm [17]. EM waves have two perpendicular components, the electric and the magnetic field. Microwaves are used in the following applications:

1) Antennas.
2) Radars.
3) Telecommunications.
4) Satellites.
5) Industrial applications.

The frequency bands of microwaves are shown in Table 1.1.

Table 1.1 – Frequency bands of microwaves [18]

Frequency bands	f (GHz)	λ (cm)
L-band	1.0-2.0	15.0-30.0
S-band	2.0-4.0	7.5-15.0
C-band	4.0-8.0	3.75-7.5
X-band	8.0-12.0	2.5-3.75
Ku-band	12.0-18.0	1.67-2.5

1.3 Mechanisms of EM wave absorption

Microwave absorption and electromagnetic interference shielding are two general approaches to resisting the interference of incident electromagnetic waves. They are usually estimated via various analysis models due to their distinct interests. For a EMI shielding model, the significant point is to attenuate the transmitted power of the EM waves.

The incident wave undergoes reflection, transmission, and absorption. The reaction of the EM power with the substance's electronic and molecular structure generates heat inside the substance because of power squandering, which turns the incident EM wave into heat or other shapes of power [19]. The electromagnetic shielding efficiency (SE) is measured in terms of a reduction in the income power/field size upon transition across the shield. SE can be expressed in the following equation:

$$\boldsymbol{SE = R + T + M} \quad (1.1)$$

Where R, T, and M are the reflection loss, the absorption loss, and the multiple reflection loss, respectively [20].

In this state, elevated reflectivity is so convenient to the shielding efficiency, and almost all incoming waves have reflected on the surface of shielding substances. The physical importance of RL in electromagnetic interference shielding is the variation between the primary incoming waves and those waves entering the shielding substances (Figure 1.2a). For the model of microwave absorption (MA) (Figure 1.2b), though, a mineral substance is put to reflect the transmission waves. As a consequence, the transmission waves are constantly negligible in MA. Here, RL indicates the variation between the primary incident and the final reflected waves.

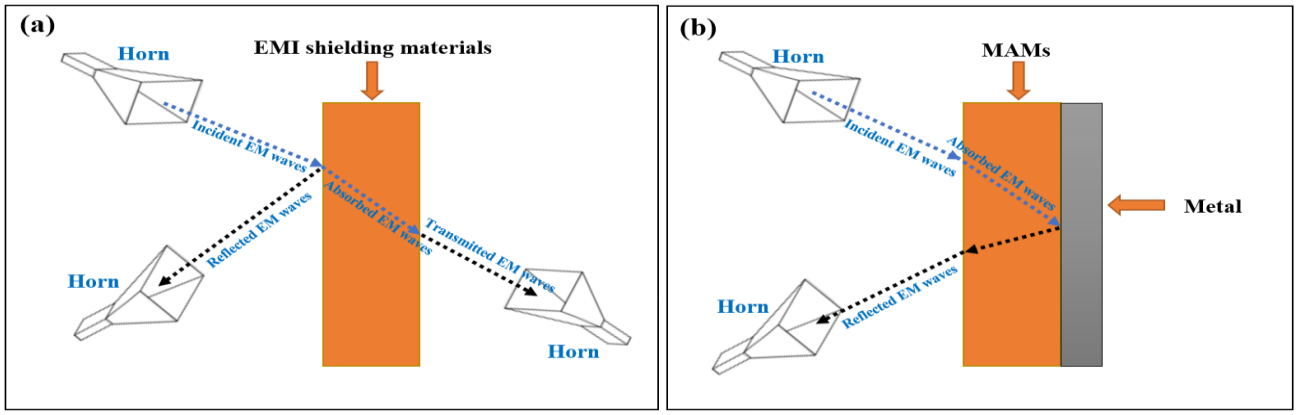

Figure 1.2 – Diagram of the estimated models of (a) electromagnetic interference shielding and (b) microwave absorption [21]

In order to get effective electromagnetic wave absorption, there should be material impedance (Z_1) close/equal to air impedance (Z_0), and the electromagnetic wave should be quickly attenuated inside the substance [22]. The model's impedance matching characteristic (Z) can be determined as shown in equation (1.2).

$$\boldsymbol{z} = \frac{\boldsymbol{z_1}}{\boldsymbol{z_0}} \qquad 1.2)$$

The EM characteristics of a substance, i.e., the complex relative permittivity (ε_r) and permeability (μ_r) are defined by equations (1.3 and 1.4) [17,23–25].

$$\boldsymbol{\varepsilon_r} = \boldsymbol{\varepsilon}' - \boldsymbol{i\varepsilon}'' \qquad 1.3)$$

$$\mu_r = \mu' - \boldsymbol{i}\mu'' \qquad (1.4)$$

The real part of permittivity and permeability (ε' and μ') describes the ability to store the energy in the pattern. In contrast, the imaginary parts (ε" and μ") describe the energy loss of the electric and magnetic [26–28].

1.4 Microwave absorption materials

Many materials can be used to absorb microwaves, and they are generally divided into three main types:

1. Magnetic loss materials.
2. Dielectric loss materials.

3. Hybrid materials.

1.4.1 Magnetic loss materials

These materials have high complex relative permeability. Many magnetic materials can absorb microwaves. The most important of these are ferrites and carbonyl iron.

1.4.2 Ferrites

Ferrites are magnetic ceramic materials, the main component of which is iron (III) oxide, in addition to other metallic elements (Ba, Mn, Co, Cu, Ni) [29].

1.4.2.1 Classification of ferrites according to their crystal structure

According to the crystal structure, ferrites can be divided mainly into three main sections:

(a) Spinel ferrites

The metal cations in this type of ferrite are located in a cubic structure. The spinel lattice comprises an arrangement of close-packed oxygen ions, where 32 oxygen ions shape the unit cell. These ions are located in a face-centered cubic arrangement (FCC), leaving two types of spaces between the ions through which metal cations can be located, which are as follows:

1. Tetrahedral sites: These sites are surrounded by 4 oxygen ions.
2. Octahedral sites: These sites are surrounded by 6 oxygen ions.

In the unit cell, there are 64 tetrahedral sites and 32 octahedral sites, but metal cations can occupy 8 tetrahedral sites and 16 octahedral sites [30].

(b) Hexagonal ferrites

They are ferrites consisting of magnetic iron oxides with a hexagonal structure. This type of ferrite has several general formulas indicated by letters such as (M, U, Y, etc.), the most important of which is $MFe_{12}O_{19}$, where M is elements such as barium, lead, or cobalt. Table 1.2 shows the most important structures of ferrites with a hexagonal structure. This type of ferrite is used as a permanent magnet, which is used at very high frequencies. The lattice of these ferrites is similar to spinel ferrite, with oxygen ions distributed according to the specific patterns.

Table 1.2 – Types of hexaferrite

Hexaferrite type	Chemical formula
M	$MFe_{12}O_{19}$
Y	$M_2Me_2Fe_{12}O_{22}$
W	$MMe_2Fe_{16}O_{27}$
Z	$M_3Me_2Fe_{24}O_{41}$
X	$M_2Me_2Fe_{28}O_{46}$
U	$M_4Me_2Fe_{36}O_{60}$

(c) Garnet ferrites

This ferrite type has the general formula $3M_2O_3.5Fe_2O_3$, where M is a trivalent metal ion (Yttrium, Gadolinium, Samarium, etc.). These ferrites have a cubic crystal structure where the divalent cations are located in the tetrahedral sites and the trivalent cations in the octahedral and hexahedral sites [30].

1.4.2.2 Classification of ferrites according to magnetic properties

According to their magnetic properties, ferrites can be classified into soft and hard.

a) Soft ferrites

Ferrites with spinel and garnet crystal structures are soft magnetic materials characterized by a low coercivity field, such as NiZn ferrite and MnZn ferrite.

b) Hard ferrites

This ferrite type is characterized by high coercivity and remanent magnetization, such as hexagonal ferrites [31].

1.4.2.3 Applications of ferrites

Magnetic materials are characterized by their high resistance, low cost, easy manufacturing methods, and super magnetic properties. Ferrites are widely used in many applications such as radar, magnetic shielding, microwave absorption, audio, telecommunications, power transformer cores, amplifiers, small motor cores, magnetic sensors, automobiles, etc.

1.4.2.4 Methods of preparing ferrites

The preparation method is considerably significant to acquiring the desired outcome where properties of different types of nano ferrites change, particularly with varying ways of preparation. For instance, the size and form of particles determine the properties of nano ferrites, which are managed by the preparation method. Nano ferrites can be fabricated via different methods as follows:

1. Ceramic sintering method.
2. Co-Precipitation method.
3. Hydrothermal method.
4. Sol-gel method.
5. Microemulsions method.

1.4.2.4.1 Ceramic sintering method

This method involves mixing the raw materials (metallic oxides or carbonates) using a ball mill. The prepared ferrites are sintered in the temperature range (900–1250 $^{\circ}$C). Table 1.3 shows a summary of the features and limitations of the ceramic sintering technique.

1.4.2.4.2 Co-Precipitation method

This method is considered one of the most essential for preparing ferrite nanomaterials. It especially depends on preparing an aqueous solution based on suitable initial materials to form the ferrite, adding a convenient sedimentation factor until a convenient pH is reached, and a precipitate is obtained, followed by a filtration and drying process, and heat treatment to obtain the nano ferrite powder. Among the most significant initial materials used in this method: are metal chlorides, metal nitrate, metal sulfate as sources of mineral cations, ammonium hydroxide, and sodium hydroxide as sedimentation agents [32–35]. Table 1.3 summarises the features and limitations of the co-precipitation technique.

1.4.2.4.3 Hydrothermal method

An ideal thermal technique includes various steps for getting nano ferrites and their composites. These synthesis methodologies involve hydrothermal, microwave-aided hydrothermal (MAH), colloid mill or mechano-hydrothermal, combustion, and thermal decomposition techniques. Nano-particles acquired from the thermal process on the decay of organometallic precursors usually submit symmetric shape and size dispensation. Chemical reactions occur in the hydrothermal method of initial materials (mineral salts) within an aqueous medium under certain conditions of temperature and pressure. The preparation process occurs in special reactors through which the interaction conditions can be controlled to crystallize the ferrite material directly from the solution [36–39]. Table 1.3 shows the features and limitations of the thermal technique.

1.4.2.4.4 Sol-Gel method

The sol-gel technique can be defined as forming a relatively stable solid phase at a specific temperature starting from the liquid phase. The main reactions in this method are the hydrolysis phase, where the acids and bases are used as catalysts, and the condensation phase. In this phase, the molecules resulting from hydrolysis are linked together to form a three-dimensional structure. The essential primary materials used in this technique are chlorides and nitrates of metals [40–42]. On the other hand, it is necessary to carefully control the variables of the sol-gel method to obtain a homogeneous final product and good magnetic and radar absorption properties, the most important of which are: purity, quality of raw materials, reaction temperature, stirring quality (mechanical, ultrasound, and magnetism), and finally the pH value. Table 1.3 shows the advantages and disadvantages of the sol-gel technique.

1.4.2.4.5 Microemulsion method

The microemulsion technique is used for attaining more concern in essential as well as manufacturing research due to its unique characteristics. We mention some of them,

like thermodynamic stability, sizeable interfacial area, and capability to get dissolvable in immiscible liquids. The microemulsion technique includes three segments, water, oil, and surfactant. During blending organometal antecedents, a precipitate is formed. This technique controls particle characteristics like homogeneity, geometry, morphology, and particle size. These particles are used in magnetic recording and microelectronic devices [43]. Table 1.3 shows the advantages and disadvantages of the microemulsion technique.

1.4.2.5 Factors impacting characteristics of nano ferrites

The difference in nano ferrites properties can be adjusted by dominating the various preparation factors, such as the components, annealing temperature, and pH value.

1.4.3 Carbonyl iron powder (CIP)

CIP is a type of magnetic loss material of EM waves. CIP has a low electrical conductivity, high saturation magnetization, and Curie temperature. However, the increased density and insufficient stability restrain their practical uses.

1.4.3.1 Applications of carbonyl iron powder

CIP is widely used in many applications such as radar, magnetic shielding, radar absorption, stealth jets, drones, vehicles, telecommunications, power transformer cores, amplifiers, small motor cores, magnetic sensors, vehicles, etc.

Table 1.3 – Summary of the features and limitations of the main synthesis techniques

Technique	Nanomaterial	Calcination temperature (°F)	Size (nm)	Features	Limitations	Ref.
Ceramic sintering	$Ni_{0.5}Zn_{0.5}Fe_2O_4$	2282	$74*10^3$	Simple method. Used raw materials are cheap.	Not obtaining a high-purity product. Consumption of grinding equipment.	[44]
Hydrothermal	$Mn_{1-x}Zn_xFe_2O_4$	338	15	Controlled size. High yield. Scalable.	Previous information on solubility is wanted. High pressure.	[45]
Mechano–Thermal	$ZnFe_2O_4$	248	9–20	Fine particle size. Accumulation of ferric oxide.	Time-consuming. Existence of impurities. Poor yield.	[46]
	$MgFe_2O_4$	752–1292	5–8			[47]
	$ZnFe_2O_4$	752–1022	3–20			[48]
Microwave – Thermal	$BiFeO_3$	356	130	Rapid operation. Cost-effective.	Exaggerated growth existence of impurities.	[49]
	$BiFeO_3$	752–1112	20–160			[50]
	$CoFe_2O_4$	1112–1472	11–12			[51]

				They obtained a crystalline structure.		
Combustion	$Zn_{1-x}Co_xFe_2O_4$	1742	30–40	Cost-effective process. Low-temperature wanted. Potentially of multi-component. Nanoparticle forming.	Opportunity for impurity forming. High temperature is wanted.	[52]
	$CdFe_2O_4$	1742	12–27			[53]
	$MgFe_2O_4$	932	12–25			[54]
	$BaNi_2Fe_{16}O_{27}$	1292–1832	10–70			[55]
Sol-Gel	$Sm_{1-x}Ca_xFeO_{3-y}$	1292–1832	100	Controlled size and form. Better homogeneity. Low cost.	Expensive process. Requests complete monitoring.	[56]
	$Sr_{0.7}Nd_{0.3}Fe_xCo_{0.3}O_{19}$	2012	40-50			[57]
	$Mn_{1-x}Zn_xFe_2O_4$	1292–2012	500			[58]
	$NiFe_2O_4$	842	11–16			[59]
Co-precipitation	$NiFe_2O_4$	*	>50	Decrease in the reaction temperature. Aqueous media. Symmetric sized. Nanoparticle forming.	The solubility of interactivity materials impacts the precipitation ratio. Poor crystallinity. Time-consuming.	[32]
	$Mg_{0.5}Ni_{0.5}Fe_2O_4$		290–340			[33]
	$CoCr_xFe_{2-x}O_4$		15–23			[34]
	$NiFe_2O_4$		8–20			[35]
Micro Emulsion	$CoFe_2O_4$	1112	28	Single-phase nano-particles. Regular crystalline structure. Cost-effective.	Temperature-dependent. Existence of impurities. Less yield.	[43]
	$SrFe_{12}O_{19}$	752–1832	60			[60]
	$Ni_{0.5}Zn_{0.5}Fe_2O_4$	1112	50			[61]

1.4.4 Dielectric loss materials

These materials have high complex relative permittivity. Many dielectric materials can absorb microwaves, such as conductive polymers (e.g., polyaniline, polypyrrole) and carbonaceous materials (e.g., carbon black, activated carbon, carbon fibers, graphene), which have played a significant role in high-frequency EM wave absorption.

1.4.5 Conductive polymers (CPs)

CPs are organic polymers that conduct electricity, usually indicated as “synthetic metals” because of their capability to integrate polymers' chemical and mechanical characteristics with the electrical characteristics of metals and semiconductors. CPs combine moderate conductivity, ease of fabrication, low cost, corrosion resistance, low density compared to metals, and the ability to absorb electromagnetic waves [15,62].

1.4.5.1 Polyaniline

PANI is one of the most studied conductive polymers due to its ease of fabrication and good electrical conductivity. PANI consists of monomer units built from reduced (y) and oxidized (1-y) blocks: where $0 \leq y \leq 1$. The redox state of the polymer is defined by the value of y, which may vary continuously from zero to unity. Figure 1.3 shows the general chemical formula of polyaniline [63].

1.4.5.2 Applications of conductive polymers

CPs seem to be one of the few substances qualified to show dynamic MA conduct, called “smart stealth substances”, because of the reversible electrical characteristics of CPs. Their benefit can also be expanded to high-tech fields such as space, military defense, navigation/communication control, or as a RAM in solar cells, computers, biosensors, etc.

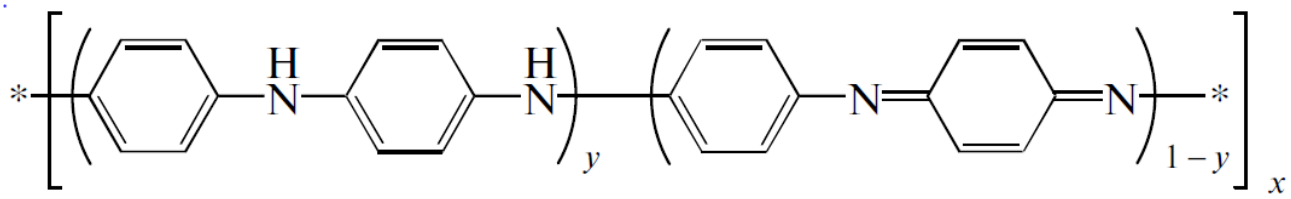

Figure 1.3 – General chemical formula of polyaniline

1.4.6 Carbonaceous substances

Carbon is considered the 4th most existing chemical element in the world by mass. It is the element that earth selected as a base for the environment under the circumstances conformable to Earth's. Pure carbon has many forms involving diamond, graphite, graphene, buckminsterfullerene, nanotube, etc.

1.4.6.1 Carbon black

CB is a shape of paracrystalline carbon that has a high surface area to volume ratio, albeit lower than that of activated carbon. CB has been used for electronics, RAMs, photocopiers, laser printer toners, and paints.

1.4.6.2 Activated carbon

AC has small, low-volume pores that increase the surface area for adsorption or chemical reactions. AC has been used for air purification, water purification, medicine, sewage treatment, and RAMs.

1.4.6.3 Graphite

C is a crystalline form of the element carbon. It consists of weakly bound layers of graphene stacked into a hexagonal structure. C occurs naturally and is the most stable form of carbon under standard conditions. Graphite has been used in batteries, solar panels, electrodes, and RAMs.

1.4.7 Hybrid materials

Hybrid materials are composites made via the incorporation of organic and inorganic components, such as composite materials with a nano ferrite core and a conducting polymer shell.

1.5 Composite absorbent materials with graded impedance

Absorption is achieved by gradually decreasing the impedance starting from the dielectric layer, whose impedance is close to the impedance value of air, to secure the entry of most of the incident waves into the material and reduce reflection. Then the absorbent layers are graded with increasing impedance.

1.6 Characteristics of an ideal microwave absorption material.

MAMs should be lightweight, prepared in various shapes, waterproof, chemically resistant, have good mechanical and physical properties, be easy to prepare, low cost, have a wide absorption field, and are strong absorption [64].

1.7 Absorbent ferrites nanoparticles for microwave

The researchers designed the absorbent ferrites of the EM waves to use them in civilian and military applications. According to this, the $Ni_{0.7}Zn_{0.3}Y_xFe_{2-x}O_4$ was successfully prepared by Chen et al. The sol-gel technique synthesized the absorbents. The results displayed that the RL_{min} peaks of absorbents shifted to lower frequencies (f_m) with the increasing absorbent thickness (t_m), as shown in Figure 1.4 [65]. This case may be determined by the λ/4 cancellation model, as indicated in formula (1.5) [66–68].

$$t_m = \frac{nc}{4f_m\sqrt{|\mu_r||\varepsilon_r|}} \ (n = 1, 3, 5, \dots) \qquad 1.5)$$

Where c is the velocity of light.

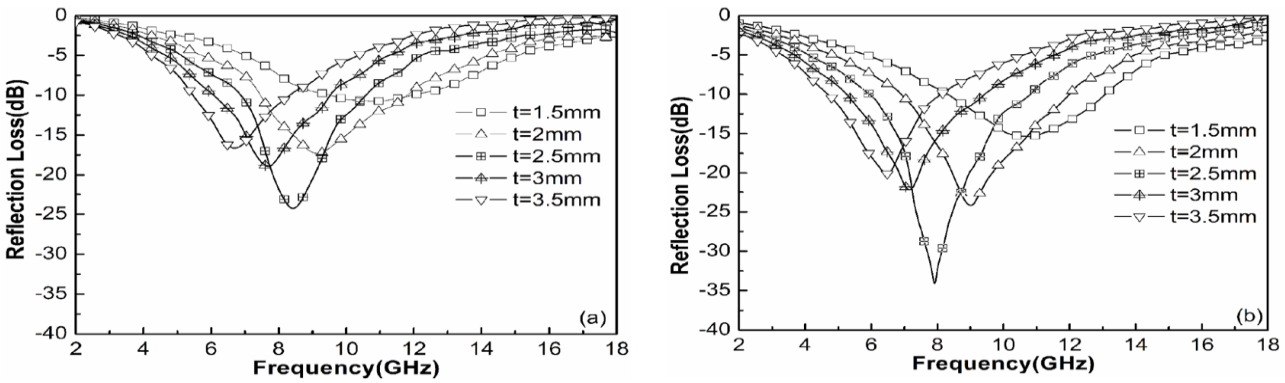

Figure 1.4 – RL curves of $Ni_{0.7}Zn_{0.3}Y_xFe_{2-x}O_4$ ferrite (x = 0, (a); x = 0.2, (b)) at different thicknesses

The $Cu_{0.2}Ni_{0.4}Zn_{0.4}Fe_2O_4$ was studied by Gregori et al. The absorbents were prepared by the citrate precursor. The absorbents were synthesized by dispersing $Cu_{0.2}Ni_{0.4}Zn_{0.4}Fe_2O_4$ powder within the wax matrix of 80 % w/w. The results displayed that $BW_{-10\ dB}$ for the absorbent reached 2.4 GHz [69]. Malas et al. prepared the

$Cu_{0.2}Ni_{0.4}Zn_{0.4}Fe_2O_4$, too but with a different technique, which was the co-sedimentation technique. The absorbents were synthesized by dispersing ferrite nanoparticles within the ER matrix of 30 % w/w. The results displayed that $BW_{-10\ dB}$ for the absorbent reached 4.1 GHz [70]. The changes in MA characteristics were observed with the variation of the synthesis method. Zhang et al. designed the $Ni_xCo_{1-x}Fe_2O_4$ (x =0.5, 0.8) by ball milling. The RL_{min} of -35.5 dB at 11.5 GHz and the absorption $BW_{-10\ dB}$ of 3.2 GHz for 2.5 mm thickness were noticed for $Ni_{0.8}Co_{0.2}Fe_2O_4$. On the other hand, the RL of -30.6 dB at 11.9 GHz and the absorption $BW_{-10\ dB}$ of 3.4 GHz for 2.5 mm thickness were noticed for $Ni_{0.5}Co_{0.5}Fe_2O_4$ [71], where the changes in MA characteristics were noticed with the variation of the compound composition, as cited above.

However, other scholars have investigated the impact of substitution operation with a number of cations and substitution rates on ferrite. According to this, the $[Ni_{0.4}Cu_{0.2}Zn_{0.4}](Nd_xY_xFe_{2-2x})O_4$ ($0.0 \leq x \leq 0.05$) was designed by Chen et al. The absorbents were synthesized by the citrate sol-gel technique [72]. The results displayed that the RL_{min} peaks of absorbents shifted to higher frequencies by increasing the substitution with several cations on ferrite. Zubar et al. designed the $Ni_{0.4}Cu_{0.2}Zn_{0.4}Tb_xFe_{2-x}O_4$ ($0.0 \leq x \leq 0.10$) by sonochemical method. The outcomes exhibited that the substitutions rate significantly influences MA properties, as shown in Figure 1.5 [73]. Kostishyn et al. designed the $Ni_{0.4}Cu_{0.2}Zn_{0.4}Eu_xFe_{2-x}O_4$ ($0.0 \leq x \leq 0.10$) by sol-gel method. The effect of Eu^{3+} ion substitution on the MA properties was studied [74]. The results displayed that the RL_{min} peaks of absorbents shifted to higher frequencies with increasing the Eu^{3+} contents. Trukhanov et al. designed the $[Ni_{0.5}Co_{0.5}](Dy_xFe_{2-x})O_4$ ($x \leq 0.08$) by citrate gel technique. The effect of Dy^{3+} ion substitution on the MA properties was studied [75]. The results displayed that the RL_{min} peaks of absorbents shifted to higher frequencies with increasing the Dy^{3+} contents. From these researches, it was noted that the unsubstituted ferrites were known for their poor capability to absorb EM waves, which required the study of the impact of the cations substituted and cations content in ferrite through which the MA properties were enhanced. On the other hand, other researchers have investigated the impact of doped on MA properties. Garg et al. studied the impact of Nd^{3+} doping on the MA properties of barium hexaferrite. The results displayed that RL_{min} was −33.17 dB at 9.5 GHz for a thickness of 2.2 mm and the absorbing $BW_{-10\ dB}$ was 2.94 GHz for $BaNd_{0.04}Fe_{11.96}O_{19}$ [76]. Ghasemi et al. studied the Mn–Co–Sn doped on barium ferrite. The barium ferrite was synthesized by the sol-gel method. The results displayed that by changing the substituted elements in barium ferrite, the absorbing $BW_{-10\ dB}$ reached 8 GHz with unique RL_{min} [77]. These investigations illustrated the substantial impact of the synthesis

technique, the kind of ferrite, the influence of the cations substituted and cations content in absorbent ferrite, the absorbent ferrite thickness, and the impact of elements doping on MA properties of absorbent ferrite.

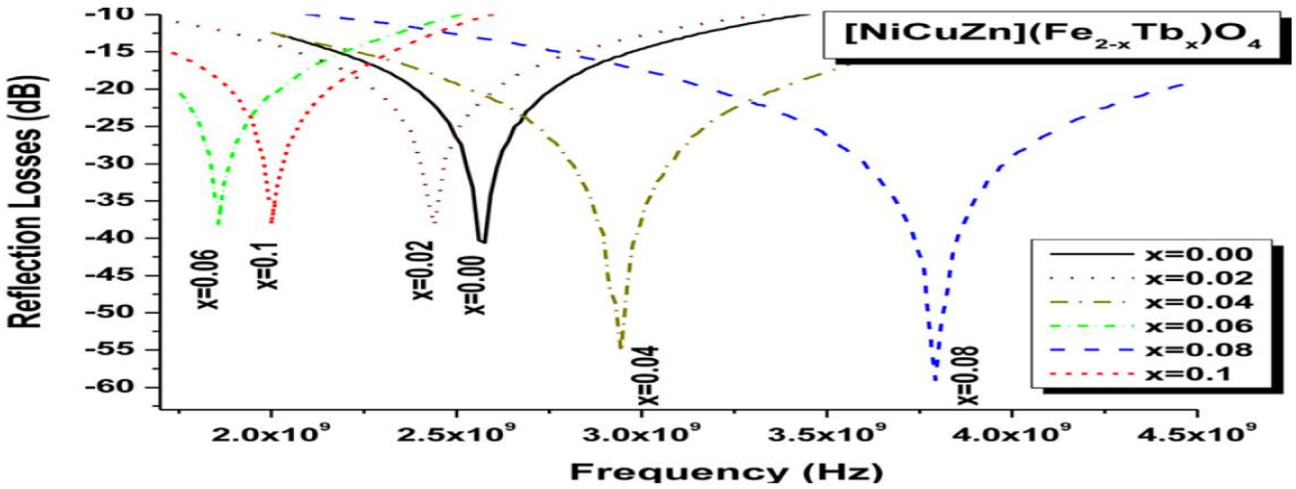

Figure 1.5 – RL as a function of the EM wave frequency of $Ni_{0.4}Cu_{0.2}Zn_{0.4}Tb_xFe_{2-x}O_4$ ($0.0 \leq x \leq 0.10$)

1.8 Incorporation of CPs with ferrite nanoparticles to absorb microwaves

Spinel and hexagonal ferrites have been well-known for their integral MA characteristics [78,79]. However, these ferrites are restrained because of high density, lower dielectric loss, and limited absorption band, which makes use of these ferrites inefficient, particularly when wideband absorption is required [80,81]. To find solutions for these shortcomings, dielectric loss materials are added, such as polyaniline, polypyrrole, carbon nanotubes, carbon black, etc. The results have shown the synergistic impact of combining magnetic loss and dielectric loss material together [82]. Many researchers have conducted studies of the MA characteristics of ferrite nanoparticles containing CPs. Researchers have tried to enhance the absorption BW_{-10dB} by designing nanocomposites with a construction (core/shell). The magnetic core is coated with CPs shell [83,84]. According to this, PANI/NiZn ferrite nanocomposites in the frequency range of 2–40 GHz were designed by Ting et al. [85]. The 67% w/w of the nanocomposites was dispersed in an ER matrix. The outcomes showed that by rising PANI content in NiZn ferrite, a wide absorption $BW_{-10\ dB}$ could be acquired. Li et al. investigated the MA properties of PANI/NiZn ferrite nanorods. The 70% w/w of the nanorods was dispersed in a paraffin wax matrix. The MA properties were studied in the frequency range of 2-18 GHz. The results displayed that RL_{min} was -27.5 dB at 6.2 GHz for a thickness of 2 mm, and the absorption $BW_{-10\ dB}$ was 3 GHz [86]. Yang et al. investigated the MA properties of PANI/NiZn ferrite nanocomposites. The nanocomposites were synthesized by in-situ polymerization. The 75% w/w of the

nanocomposites was dispersed in a paraffin wax matrix. The molar ratios of PANI/NiZn ferrite nanocomposites were 3:1, 2:1, 1:1, 1:2, and 1:3. The results displayed that RL_{min} was -41 dB at 12.8 GHz for a thickness of 2.6 mm and the absorption $BW_{-10\ dB}$ was 5 GHz for PANI/NiZn (1:2) as shown in Figure 1.6. [87]. Xie et al. synthesized NiZn ferrite/PANI nanocomposites by hydrothermal technique. The MA properties were studied in the 2–18 GHz range. The results displayed that RL_{min} was -17 dB at 11.1 GHz and the absorption $BW_{-10\ dB}$ was 5 GHz [88]. Ma et al. have reported the MA properties of PANI/$Co_{0.5}Zn_{0.5}Fe_2O_4$ nanocomposite. The MA properties were studied in the 8.2–26.5 GHz range. The absorbents were synthesized by in-situ polymerization technique. They found that the absorbers had broadband, and minimal reflection loss, where the results indicated that the absorber had a RL_{min} of -39.9 dB at 22.4 GHz and the absorption $BW_{-10\ dB}$ was 5 GHz for 2 mm thickness [89]. However, in various cases, the PANI/F nanocomposites can be incorporated with carbon materials as well, e.g. core-shell F/GO/PANI [90], Fe3O4@C@PANI [[91], F/G/PANI [92], and so on. These nanocomposites can possess special MA performance due to the connection absorbent mechanism in each part. From the above of these studies, we can summarize that the PANI-based nanocomposites are the premium RL of PANI-based nanocomposites produced essentially from the impacts of conduction, magnetic, and dielectric losses. Where combining PANI and other waste substances can improve the absorption $BW_{-10\ dB}$ and enhance the RL values. The EM wave attenuation performance of PANI-based nanocomposites can also be developed by adjusting their architectures.

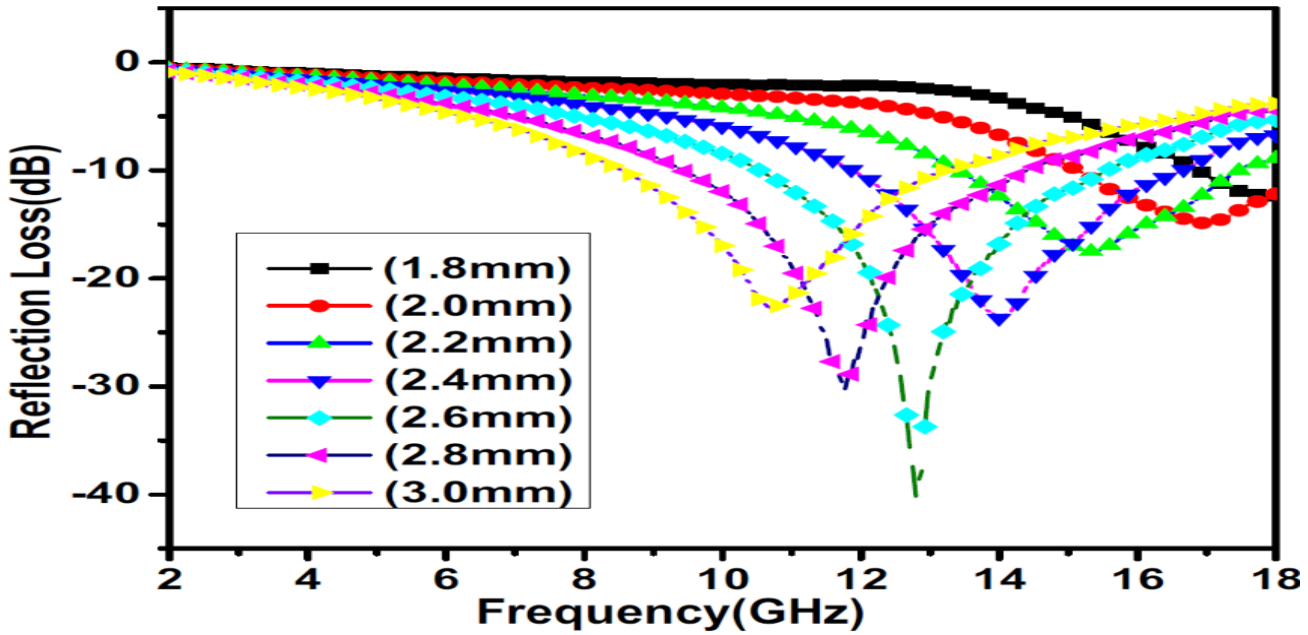

Figure 1.6 – RL as a function of the EM wave frequency of PANI/NiZn (1:2) nanocomposites with different thicknesses

1.9 MA behavior of carbon-based nanomaterials

These days, new carbon nanomaterials are showing and presenting excellent microwave-absorbing characteristics. CNS-based substances have attracted significant attention for microwave absorption lately because of the unique structure and the characteristics of the physical and chemical of carbon, for example, high permittivity, high specified surface region, unique electronic conductivity, huge interface, etc. [93,94]. Accordingly, carbon nanomaterials are usually created to fit the requirements of elevated-effective microwave attenuation substances. When ferrites are incorporated with CB, the MA properties of the resultant absorber are expected to improve. According to this, CB/$Zn_{0.8}Ni_{0.2}Fe_2O_4$ nanocomposites dispersed in a silicon dioxide matrix were prepared by Dan et al. [95]. The results of $Zn_{0.8}Ni_{0.2}Fe_2O_4$ nanoparticles range of 0–1.75 wt% and different coating thicknesses (1–2.5 mm) on MA behavior in the frequency range of 8–12 GHz have been studied. The results referred that a model of 1.5 wt% $Zn_{0.8}Ni_{0.2}Fe_2O_4$ nanoparticles displayed the highest MA at 10 GHz. Higher coating thicknesses (1–2.5 mm) displayed a bigger MA and reached a RL_{min} of 2 mm thickness. On the other hand, Chakradhary et al. [96] designed strontium ferrite epoxy (SrF) NC and CB-loaded (CBSrF) NC. The RL_{min} for the SrF NC is -25.19 dB at 13.32 GHz for 10.5 mm thickness, whereas for (CBSrF) NC the RL_{min} is -31.15 dB at 10.32 GHz for 9.5 mm thickness. Therefore, the CB-loaded (SrF) NC displays higher attenuation efficiency than the (SrF) NC. On the other hand, Peng et al. prepared a collection of CNTs filled with Fe, which induced a rise in the reaction with EM radiation from the absorber substance. The amount of normal carbon permeability exceeds 1. The outcome of this conjugation was that the amount of RL was -24.8 dB at 10.9 GHz for a thickness of 1.2mm, and the absorption $(BW)_{-10\ dB}$ was 16.0 GHz [97]. Zhu et al. prepared the carbon nanotubes/iron nanowires compounds and the maximum reflection loss (RL_m) of the compounds was -22.73 dB [98]. The carbon nanotubes/cobalt nanoparticles compounds were manufactured and the symmetric cobalt nanoparticles were well scattered on the carbon nanotubes surface [99]. The RL_m of the compounds was -36.5 dB. Several magnetic metal alloy compounds, like rod-like FeCo/CNTs were studied [100]. The RL_m of FeCo/CNTs compounds was -46.5 dB at 12.56 GHz and the active absorption $(BW)_{-10dB}$ reached 3.92 GHz. The RL_m of carbon nanotubes/ carbonyl iron particle compounds was -33.3 dB at 11.4 GHz.

On the other hand, many scientists have studied the impact of CF on ferrite. For example, Hou et al. [101] studied carbon fiber@cobalt iron oxide and carbon fiber@cobalt iron oxide@manganese(iv) oxide composites by the sol-gel method. Carbon fiber@cobalt iron oxide@manganese(iv) oxide composite exhibits excellent MA performance due to reasonable EM matching, and its RL_m value equals -34 dB with a

sample thickness of 1.5 mm. Figure 1.7 illustrates RL shapes of carbon fiber (a), carbon fiber@cobalt iron oxide (b), and carbon fiber@cobalt iron oxide@manganese(iv) oxide composites (c) at different thicknesses, the efficient absorption BW of carbon fiber@cobalt iron oxide@manganese(iv) oxide composite (d) [78]. Figure 1.7 shows that the RL attenuation peaks of samples moved to lower frequencies with increasing sample thickness. This phenomenon may be defined by the quarter-wavelength ($\lambda/4$) cancellation model, as shown in equation (1.5). The insert of impurities into the carbon fibers scope in several states created diversities in the magnetic reaction to EM wave via the nanomaterial, [102] for example, by ferromagnetism, [103] although some cases, like the Fe_3O_4/mineral-coated by carbon fibers, [104] the examined substance only showed perversion in response to the electronic reaction of the substance, appearing in an essential electronic loss role compared to a small magnetic loss [104].

From the above of these studies, we can summarize that the carbon-based nanocomposites are the premium reflection loss of carbon-based nanocomposites produced from the impacts of conduction, magnetic, and dielectric losses. Combining carbon and other waste substances can improve the absorption $BW_{-10\ dB}$ and enhance the RL values. Carbon-based nanocomposites' electromagnetic wave attenuation performance can be developed by adjusting their architectures.

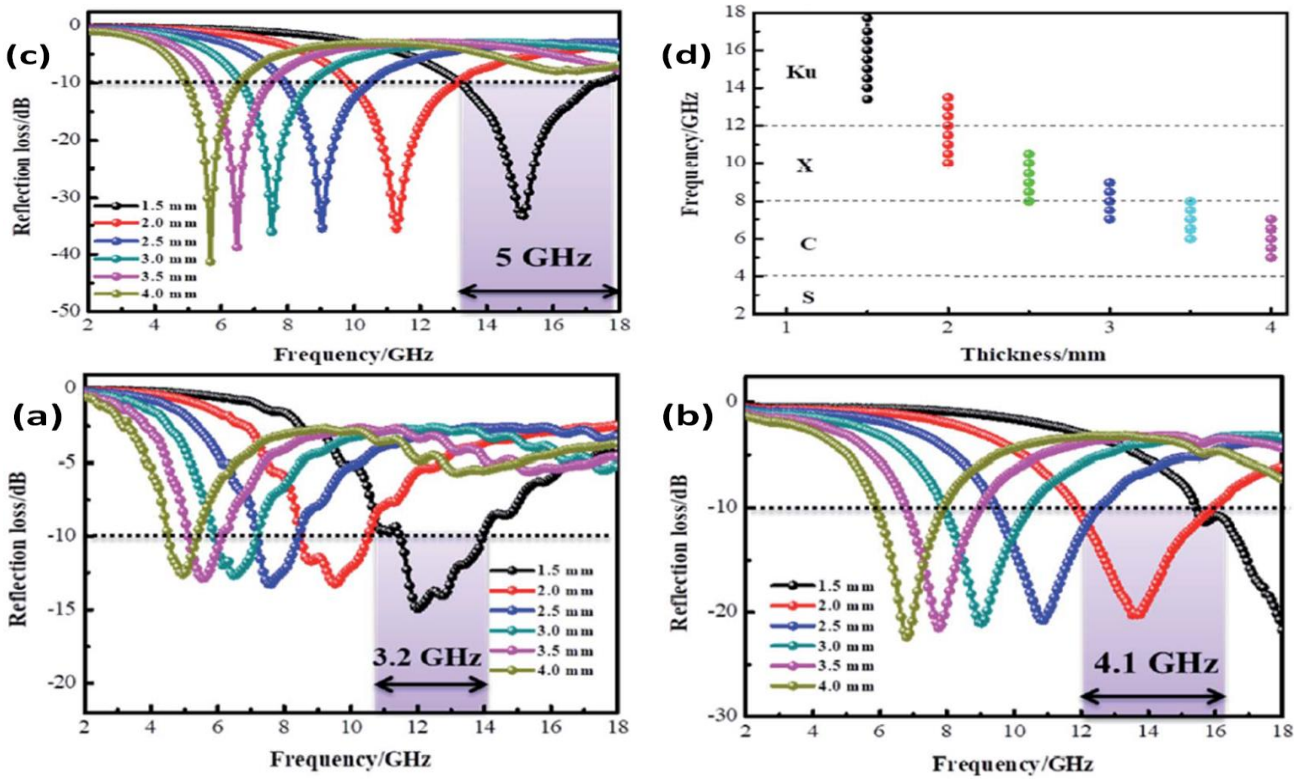

Figure 1.7 – RL shapes for carbon fiber (a), carbon fiber@cobalt iron oxide (b) and carbon fiber@cobalt iron oxide@manganese(iv) oxide composites (c) at different thicknesses the

efficient absorption $(BW)_{-10dB}$ of carbon fiber@cobalt iron oxide@manganese(iv) oxide composite (d) [78]

From the above of these studies, we can summarize that the carbon-based nanocomposites are the premium reflection loss of carbon-based nanocomposites produced from the impacts of conduction, magnetic, and dielectric losses. Combining carbon and other waste substances can improve the absorption $BW_{-10\ dB}$ and enhance the RL values. Carbon-based nanocomposites' electromagnetic wave attenuation performance can be developed by adjusting their architectures.

2 Chapter 2: Practical part

2.1 Chemicals, raw and commercial materials

Ferrites were prepared in this research by different methods (physical and chemical), starting from metal oxides (physical method) and metal salts (chemical methods: citrate precursor, self-combustion). The preparation of the nanocomposite (PANI/SF, PANI/HF, PANI/CI, PANI/CB, etc.) required different chemicals (monomers, oxidizers, and various chemicals). Table 2.1 shows the specifications of the chemicals used to accomplish this research.

Table 2.1 – Chemicals used in laboratory work and their specifications

Chemicals	Formula	molar mass (g/mole)	Purity (%)	Melting point (°C)	Appearance	Source
Iron(III) oxide	Fe_2O_3	159.69	98.7	1565	Solid	Mosreactive company
Zinc(II) oxide	ZnO	81.380	78.3	1975	Solid	
Nickel(II) oxide	NiO	74.6928	77.6	1955	Solid	
Nickel(III) oxide	Ni_2O_3	165.390	77.2	600	Solid	
Copper(II) oxide	CuO	79.545	78.5	1326	Solid	
Manganese(II) oxide	MnO	70.937	80.7	1945	Solid	
Paraffin wax	–	–	Commercial	–	Solid	Market
Iron(III) nitrate nonahydrate	$Fe(NO_3)_3.9H_2O$	403.95	98.3	47	Solid	TRADING COMPANY ANT
Nickel(II) nitrate hexahydrate	$Ni(NO_3)_2{\cdot}6H_2O$	290.81	98.3	56	Solid	
Zinc nitrate hexahydrate	$Zn(NO_3)_2{\cdot}6H_2O$	297.5	98.7	36.4	Solid	
Manganese(II) chloride tetrahydrate	$MnCl_2 .4H_2O$	197.90	97.5	87.5	Solid	
Polyvinyl alcohol	$[-CH_2CHOH-]_n$	MW: 70000	92.4	200	Solid	
Sucrose	$C_{12}H_{22}O_{11}$	342.3	Commercial	–	Solid	Market

Sodium dodecyl sulfate (SDS)	$C_{12}H_{25}NaO_4S$	288.38	92.2%	206	Solid	TRADING COMPANY ANT
Ethanol	C_2H_5OH	46.07	Commercial	–	Liquid	Market
Hydrochloric acid	HCl 37%	36.46	Commercial	–	Liquid	Market
Aniline	$C_6H_5NH_2$	93.13	99.5%	–	Solid	Sigma Aldrich Company
Ammonium persulfate (APS)	$(NH_4)_2S_2O_8$	228.20	95.3%	–	Solid	TRADING COMPANY ANT
Citric acid	$C_6H_8O_7$	192.12	99.0%	–	Solid	Sigma
Ammonium hydroxide	NH_4OH	35.05	99.8%	–	Liquid	Commercial
Carbonyl iron	CI		99.6%	1538	Solid	Cabot Norit Company
Carbon black	CB	12.011	99.5%	3550	Solid	
Activated carbon	AC	12.011	Commercial	3500	Solid	Market
Graphite	C	12.011	Commercial	3652	Solid	Market

2.2 Tools and equipment used for sample preparation

Table 2.2 shows the laboratory's tools and equipment used to prepare microwave absorbers.

Table 2.2 – Tools and equipment used for sample preparation

Tool/Equipment	Manufacture Company
Sensitive scale	Hochoice electronic
Sieve shaker	Fritsch
Ball mill	Fritsch
Glassware	–
Homogenizer	Fritsch
Vacuum pump	jinteng
Büchner funnel	–
Digital magnetic hot plate stirrer	CAPPRondo
Heat treatment oven	GIMA
Digital pH meter	Benchtop

Dryer	Henan Touch

2.3 Characterization devices

The prepared samples were structurally characterized using XRD, FTIR, TGA, and EDX. A powder X-ray diffractometer (XRD, Rigaku Miniflex 600, Cu-Ka) was used to define the crystal structures of the powders. The X-ray diffraction patterns of the prepared samples were recorded at 2θ =10 - 90°. Fourier Transform IR (FTIR) spectra of the prepared samples were recorded on a Perkin Elmer 65 FTIR spectrometer in the 400–4000 cm^{-1}. Thermogravimetric analysis (TGA) curve of the prepared samples were recorded on a thermal analyzer (NETZSCH 449F3A-0372-M) under a nitrogen atmosphere, from room temperature to 1000°C under a constant heating rate of 10 °C/min. Energy-dispersive X-ray spectroscopy (EDX, Quanta 200 3D) was used to know the chemical composition of some of the prepared samples. A scanning electron microscope (SEM, FEI Quanta 200 3D) was utilized to define the morphology of some of the prepared powders. The prepared samples were functionally characterized using the horn antenna connected to an oscilloscope (AKTAKOM ADS-2221M).

The samples' microwave absorption and electromagnetic interference shielding properties were estimated with the free-space technique. A microwave generator generates EM waves at the X-band frequency, where a microwave generator is connected by a WR90 waveguide instrument (IEC Standard R100, X Band). EM waves are detected by using a waveguide microwave detector circuit (Figure 2.1), which is attached to the pyramidal horn antenna. The measurement results in this method are verified by using a reference sample, which is an aluminum plate with previously known microwave properties. The incident EM waves (p_{in}) are measured by the pyramidal horn antenna connected to an oscilloscope (Figure 2.2), then the prepared sample perpendicularly is placed between a microwave generator and the pyramidal horn antenna to measure the transmitted power of the EM waves (p_T) by an oscilloscope. As a result, SE can be calculated for the EMI shielding by applying the equation (2.1) [105]:

$$\boldsymbol{SE\ (dB) = SE_R + SE_A + SE_M = 10\ log \frac{p_{in}}{p_T}} \quad (2.1)$$

It is significant to note that the multiple reflection loss (SE_M) can be ignored if the absorption shielding (SE_A) of EMI shielding material is higher than 10 dB and equation (2.1) then can be rewritten as [105]:

$$\boldsymbol{SE\ (dB) = SE_R + SE_A + SE_M = 10\ log \frac{p_{in}}{p_T}} \quad (2.2)$$

In addition to that, the reflected power of the EM waves (p_{ref}) is measured when the EM waves are incident on the sample surface at an angle of 45° by an oscilloscope. As a result,

the shielding by reflection (SE_R) can be calculated for the EMI shielding by applying equation (2.3).

$$\boldsymbol{SE_R\,(dB) = -10\log(1-R) = -10\log\left(1-\frac{p_{ref}}{p_{in}}\right)} \quad (2.3)$$

Finally, the shielding by absorption (SE_A) is calculated by equation (2.4) [106,107]:

$$\boldsymbol{SE_A\,(dB) = -10\log\left(\frac{T}{1-R}\right) = -10\log\left(\frac{p_T}{p_{in}-p_{ref}}\right)} \quad (2.4)$$

For the microwave absorption method, the prepared sample is placed on the metal plate at an angle of 45° to measure the reflected power of the EM waves (p_{ref}) by an oscilloscope, as shown in Figure 2.3. As a result, the RL can be calculated by applying the equation (2.5) [106,107]:

$$\boldsymbol{Rl\,(dB) = 10log\frac{p_{in}}{p_{ref}}} \quad (2.5)$$

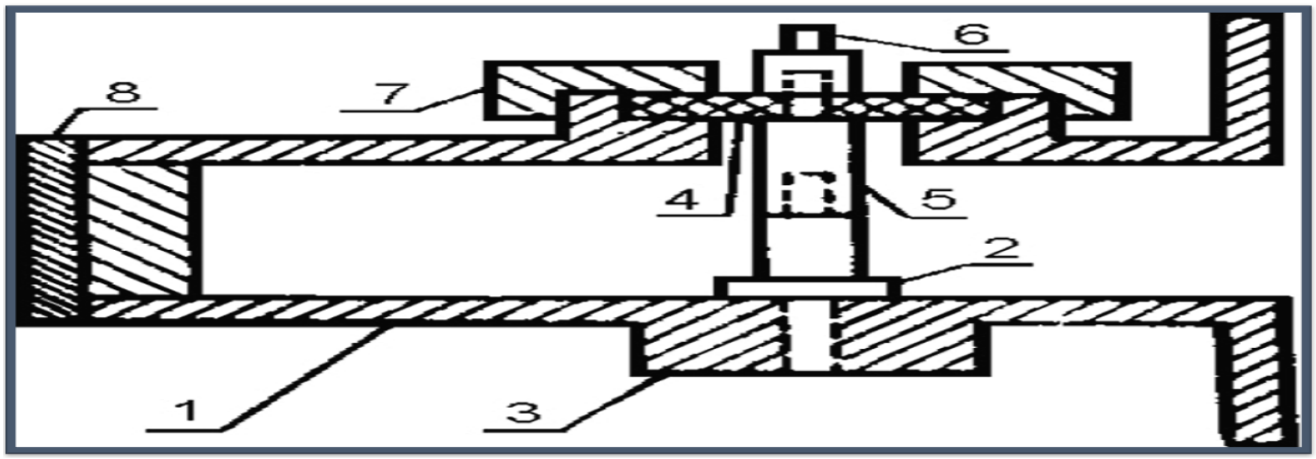

Figure 2.1 – Waveguide microwave detector circuit consists of: (1) waveguide segment, (2) cathode of the microwave diode, (3) bronze bushing, (4) dielectric sleeve, (5) rod, (6) output terminal signal, (7) coupling nut and (8) piston

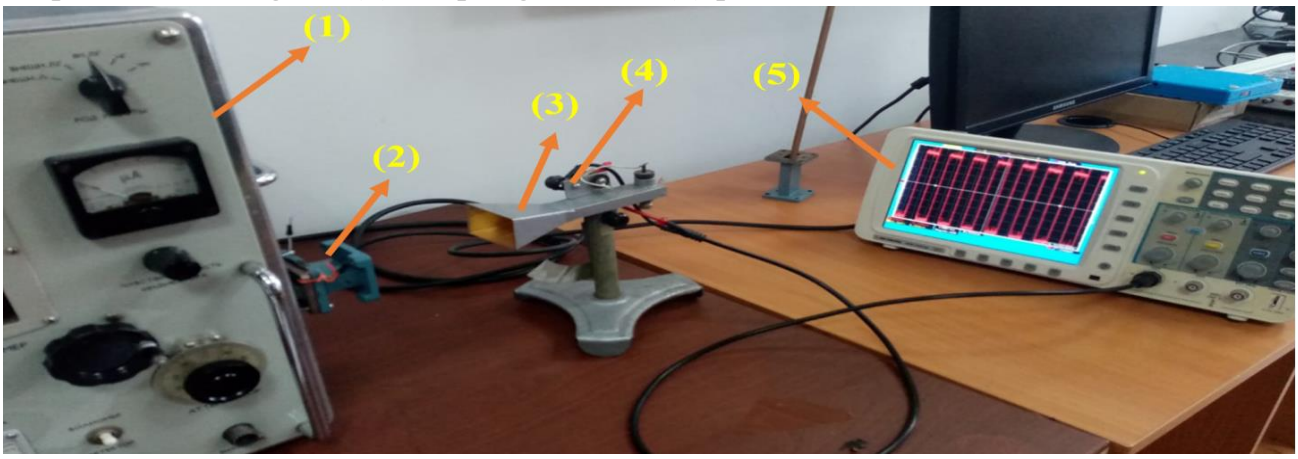

Figure 2.2 – Experimental setup for studying the EMI and MA properties of the prepared samples by the free-space technique. From left to right: (1) microwave generator, (2)

waveguide instrument, (3) horn antenna, (4) waveguide microwave detector circuit and (5) oscilloscope

Figure 2.3 – Experimental setup for measuring the reflected power of the EM waves for the microwave absorption model

2.4 Sample preparation

Different methods have prepared ferrite powders and ferrite-based composites:

2.4.1 Preparation of ferrite powders

2.4.1.1 Preparation of ferrite powders by the ceramic sintering method

Ferrites were prepared by the ceramic sintering technique from metallic oxides to study the effect of substitution on radar absorption properties. The raw materials were blended with ethanol solution by a weight ratio (2:1) using the grinding balls for 8 h at 200 rpm; then, the whole mixture was transferred to the furnace for disposal of the ethanol for 24 h at 70 °C. After that, the mixture was sintered for 3 h at 1100 °C. Finally, the prepared ferrite was milled again in the presence of ethanol solution for 4 h at 200 rpm and the whole mixture was transferred to the furnace for disposal of the ethanol for 24 h at 70 °C. Table 2.3 and equations (2.6-2.12) show the prepared ferrites and the raw materials included in the preparation of these ferrites.

Table 2.3 – Prepared ferrites by the ceramic sintering technique

Ferrite	Composition
1	$NiFe_2O_4$
2	$ZnFe_2O_4$
3	$MnFe_2O_4$
4	$CuFe_2O_4$
5	$Mn_{0.3}Zn_{0.7}Fe_2O_4$
6	$Mn_{0.6}Zn_{0.4}Fe_2O_4$
7	$Mn_{0.9}Zn_{0.1}Fe_2O_4$

8	$Ni_{0.25}Zn_{0.75}Fe_2O_4$
9	$Ni_{0.5}Zn_{0.5}Fe_2O_4$
10	$Ni_{0.75}Zn_{0.25}Fe_2O_4$
11	$Ni_{0.5}Zn_{0.4}Mn_{0.1}Fe_2O_4$
12	$Ni_{0.6}Zn_{0.3}Mn_{0.1}Fe_2O_4$
13	$Ni_{0.7}Zn_{0.2}Mn_{0.1}Fe_2O_4$
14	$Ni^{3+}_{0.25}Ni^{2+}_{0.375}Zn^{2+}_{0.25}Fe_2O_4$
15	$Cu^{2+}_{0.1}Ni^{3+}_{0.15}Ni^{2+}_{0.225}Zn^{2+}_{0.45}Fe_2O_4$
16	$BaNiZnFe_{16}O_{27}$

$MO + Fe_2O_3 \rightarrow MFe_2O_4$ (M: Mn, Ni and Zn) 2.6)

$xMnO + (1-x)ZnO + Fe_2O_3 \rightarrow Mn_xZn_{(1-x)}Fe_2O_4$ (x= 0.3, 0.6 and 0.9) 2.7)

$xNiO + (1-x)ZnO + Fe_2O_3 \rightarrow Ni_xZn_{(1-x)}Fe_2O_4$ (x= 0.25, 0.5 and 0.75) (2.8)

$0.1MnO + (0.4+x)NiO + (0.5-x)ZnO + Fe_2O_3 \rightarrow Mn_{0.1}Ni_{(0.4+x)}Zn_{(0.5-x)}Fe_2O_4$ (x= 0.1, 0.2 and 0.3) 2.9)

$0.125Ni_2O_3 + 0.375NiO + 0.25ZnO + Fe_2O_3 \rightarrow Ni^{3+}_{0.25}Ni^{2+}_{0.375}Zn^{2+}_{0.25}Fe_2O_4$ 2.10)

$0.1CuO + 0.075Ni_2O_3 + 0.225NiO + 0.45ZnO + Fe_2O_3 \rightarrow Cu^{2+}_{0.1}Ni^{3+}_{0.15}Ni^{2+}_{0.225}Zn^{2+}_{0.45}Fe_2O_4$2.11)

$BaCO_3 + NiO + ZnO + 8Fe_2O_3 \rightarrow BaNiZn\ Fe_{16}O_{27} + CO_2$ 2.12)

2.4.1.2 Preparation of NiZn ferrite nanoparticles by citrate precursor method

Ferrite nanoparticles were prepared by citrate precursor method. The effect of the different molar ratios of the metal ions to citrate acid (1:1, 2:1, and 3:1) and the different calcination temperatures (650, 800, and 950 °C) were studied on the ferrite properties. The flow chart for ferrite synthesis using a citrate precursor technique is shown in Figure 2.4. In this method, citric acid played the role of a chelating agent (chemical compound that reacts with metal ions to form stable, water-soluble metal complexes). The symbols of ferrite nanoparticle samples are detailed in Table 2.4. Typical images of a prepared ferrite by citrate precursor method are shown in Figure 2.5.

Table 2.4 – Symbols of ferrite nanoparticle samples

Ferrite	Citric acid: cation	Calcination temperature (°C)	Sample symbol
$Ni_{0.5}Zn_{0.5}Fe_2O_4$	1:1	650	NZ_{11} - 650
	1:2		NZ_{12} - 650
	1:3		NZ_{13} - 650
	1:1	800	NZ_{11} - 800
	1:2		NZ_{12} - 800

	1:3		NZ_{13} - 800
	1:1	950	NZ_{11} - 950
	1:2		NZ_{12} - 950
	1:3		NZ_{13} - 950

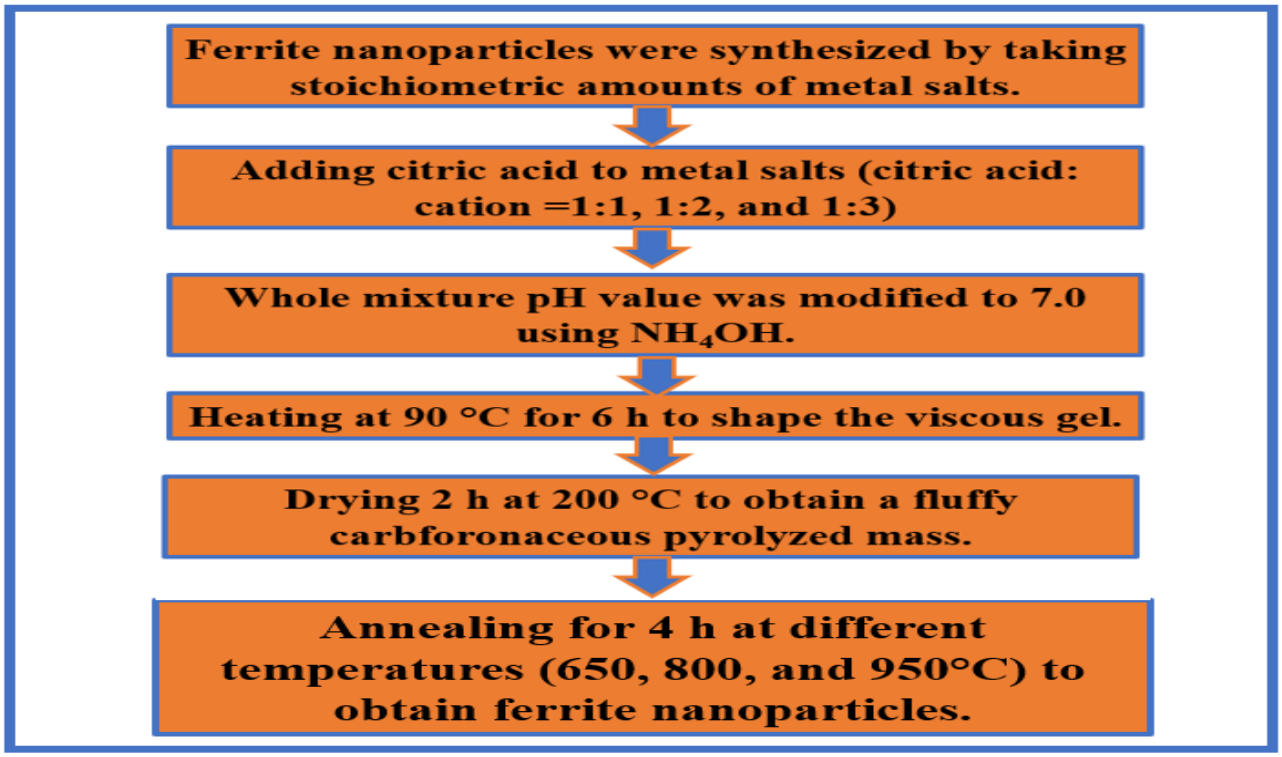

Figure 2.4 – Flow chart for the synthesis of ferrite utilizing a citrate precursor technique

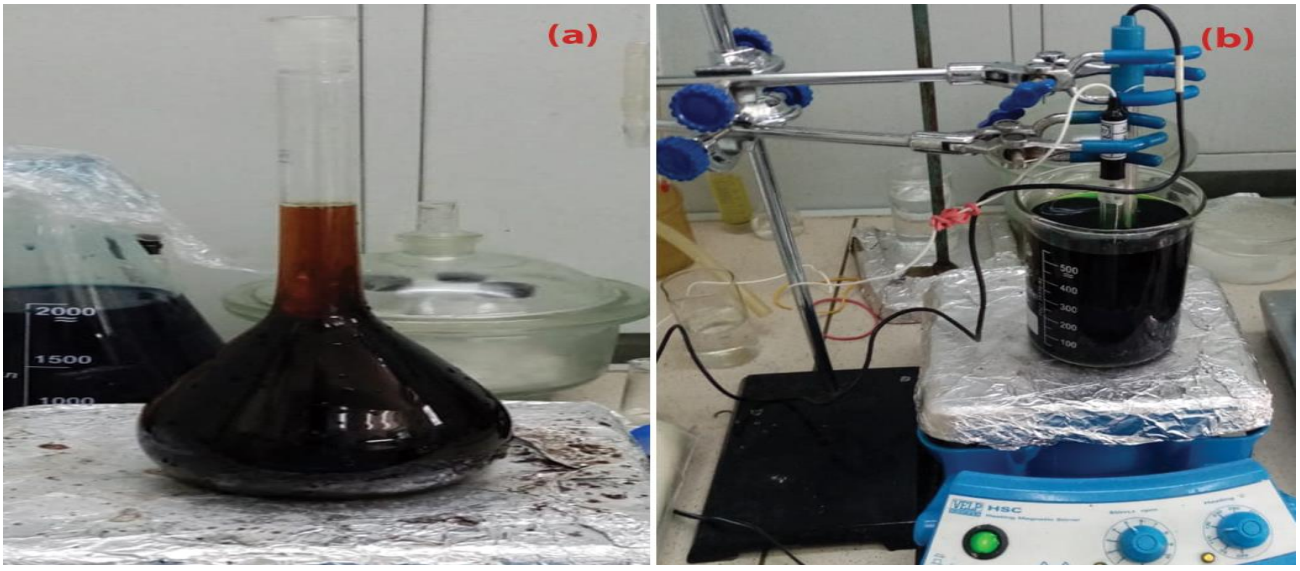

Figure 2.5 – Synthesis of $Ni_{0.5}Zn_{0.5}Fe_2O_4$ nanoparticles by citrate precursor method: (a) the metal salts aqueous solution in the flask, (b) using NH_4OH to maintain the pH of the solution at 7, (c) heating the solution at 90 °C for 6 h, (d) formation the viscous gel, (e) formation a fluffy carbonaceous pyrolyzed mass and (f) obtaining nanoparticles ferrite

2.4.1.3 Preparation of NiZn ferrite nanoparticles by self-combustion method

$Ni_{0.5}Zn_{0.5}Fe_2O_4$ nanoparticles were prepared by self-combustion method. Ferrite nanoparticles were synthesized by taking stoichiometric amounts of metal salts. Metal salts were blended with an aqueous sucrose solution (2 moles per metal ion). The effect of the different aqueous solutions of PVA (1%, 4%, and 6%) and the different calcinates (650, 800, and 950°C) was studied on the MA properties. The flow chart for ferrite synthesis using a self-combustion technique is shown in Figure 2.6. In this method, sucrose played the role of fuel. The symbols of ferrite nanoparticle samples are detailed in Table 2.5. Typical images of a prepared ferrite by self-combustion method are shown in Figure 2.7.

Table 2.5 – Symbols of ferrite nanoparticle samples

Ferrite	PVA concentration (%)	Calcination temperature (°C)	Sample symbol
$Ni_{0.5}Zn_{0.5}Fe_2O_4$	1	650	NSC_{11} - 650
	4		NSC_{12} - 650
	6		NSC_{13} - 650
	1	800	NSC_{11} - 800
	4		NSC_{12} - 800
	6		NSC_{13} - 800
	1	950	NSC_{11} - 950
	4		NSC_{12} - 950
	6		NSC_{13} - 950

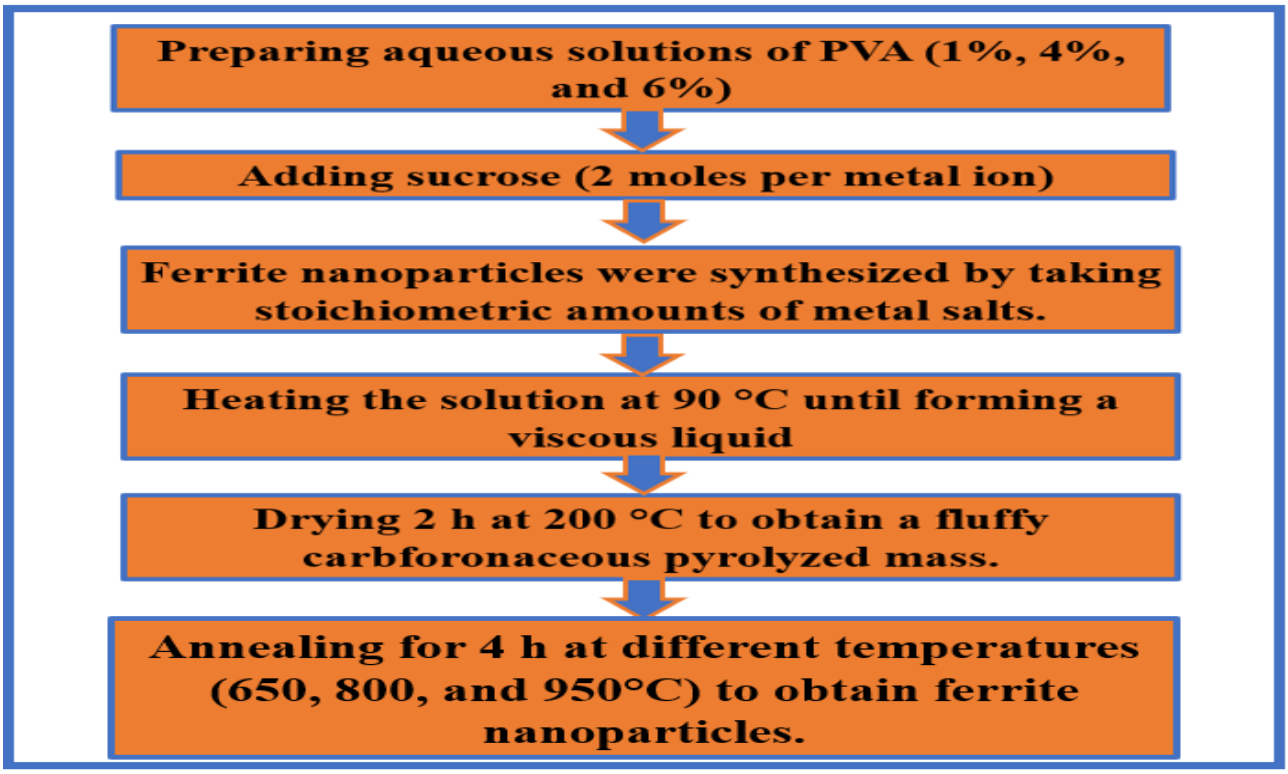

Figure 2.6 – Flow chart for the synthesis of ferrite utilizing self-combustion method

Figure 2.7 – Synthesis of NiZn ferrite nanoparticles by self-combustion method: (a) the metal salts aqueous solution in the flask, (b) blending the whole mixture, (c) heating the solution at 90 °C, (d) formation of a viscous liquid, (e) formation a fluffy carbonaceous pyrolyzed mass, and (f) obtaining nanoparticles ferrite

2.4.2 Preparation of microwave nanocomposites

2.4.2.1 Preparation of CB/F nanocomposites

$Ni_{0.5}Zn_{0.5}Fe_2O_4$ and $Mn_{0.1}Ni_{0.5}Zn_{0.4}Fe_2O_4$ nanoparticles were synthesized by citrate precursor and self-combustion method. Nanocomposites were synthesized by mixing ferrite nanoparticles with carbon black using a ball mill. Three different weight ratios of CB/$Ni_{0.5}Zn_{0.5}Fe_2O_4$ and CB/$Mn_{0.1}Ni_{0.5}Zn_{0.4}Fe_2O_4$ (1:1, 2:1, and 3:1) were prepared. The CB/F nanocomposites were ball-milled for 1 h at 300 rpm. Table 2.6 shows the symbols of nanocomposite samples. The practical steps of preparing the CB/F samples are shown in Figure 2.9.

Table 2.6 – Symbols of nanocomposite samples

Nanocomposite	CB: F	Calcination temperature for ferrite (°C)	Sample symbol
CB/$Ni_{0.5}Zn_{0.5}Fe_2O_4$	1:1	650	CB/F-11
	2:1		CB/F-21
	3:1		CB/F-31
CB/$Mn_{0.1}Ni_{0.5}Zn_{0.4}Fe_2O_4$	1:1	750	CB/MF-11
	2:1		CB/MF-21
	3:1		CB/MF-31

2.4.2.2 Preparation of CI/F nanocomposites

$Ni_{0.5}Zn_{0.5}Fe_2O_4$ nanoparticles were synthesized by self-combustion method. Nanocomposites were synthesized by mixing ferrite nanoparticles with carbon black using a ball mill. Three different weight ratios of CI/$Ni_{0.5}Zn_{0.5}Fe_2O_4$ (1:1, 2:1, and 3:1) were prepared. The CI/F nanocomposites were ball-milled for 1 h at 300 rpm. Table 3.8 shows the symbols of nanocomposite samples.

Table 2.7 – Symbols of nanocomposite samples

Nanocomposite	CI: F	Calcination temperature for ferrite (°C)	Sample symbol
CI/$Ni_{0.5}Zn_{0.5}Fe_2O_4$	1:1	650	CI/F-11
	2:1		CI/F-21
	3:1		CI/F-31

2.4.2.3 Preparation of F/CI/CB nanocomposites

$Ni_{0.5}Zn_{0.5}Fe_2O_4$ nanoparticles were synthesized by self-combustion method. Nanocomposites were synthesized by mixing ferrite nanoparticles and carbonyl iron with carbon black using a ball mill. Three different weight ratios of F/CI/CB (1:1:1, 1:1:2, and

2:1:1) were prepared. The F/CI/CB nanocomposites were ball-milled for 1 h at 300 rpm. Table 2.8 shows the symbols of nanocomposite samples.

Table 2.8 – Symbols of nanocomposite samples

Sample symbols	Weight ratio		
	$Ni_{0.5}Zn_{0.5}Fe_2O_4$	CI	CB
F/CI/CB-111	1	1	1
F/CI/CB-112	1	1	2
F/CI/CB-211	2	1	1

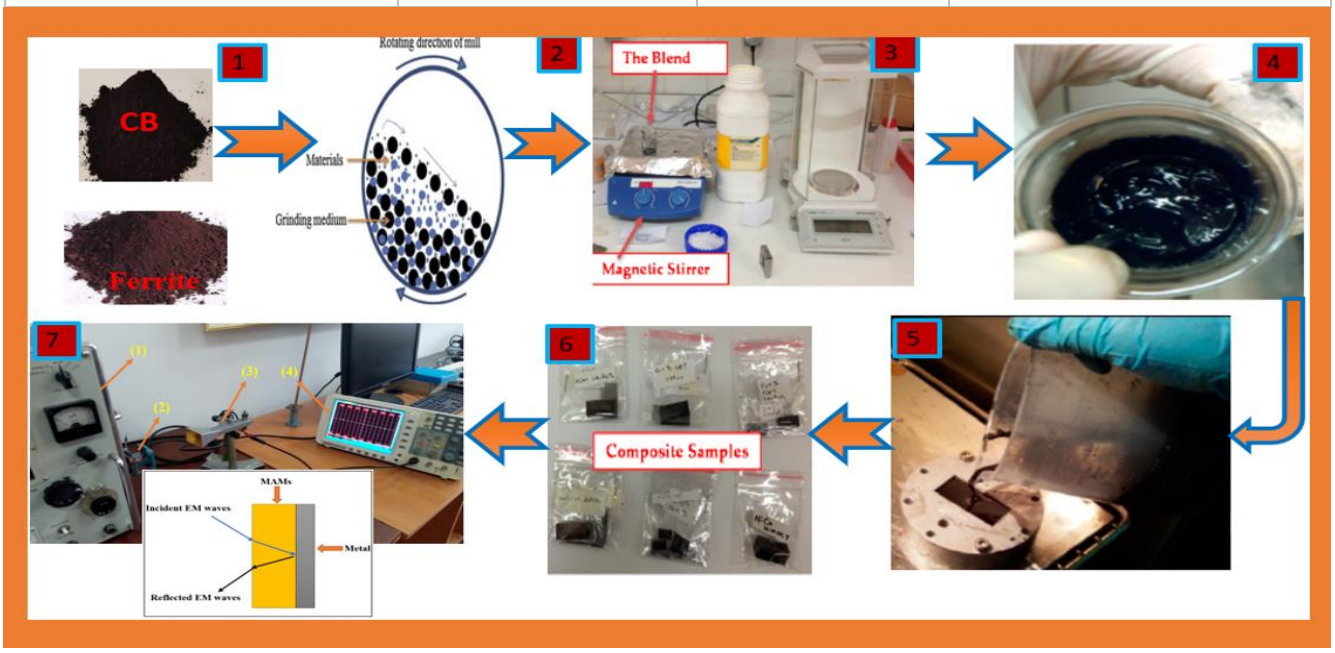

Figure 2.8 – Experimental steps of preparing the CB/F samples. From left to right: (1) preparing CB and F nanopowders, (2) mixing CB and F through ball mills, (3) blending CB and F with paraffin wax by a magnetic stirrer, (4) preparing mixture, (5) pouring the prepared mixture into the special mold (22.86 mm * 10.16 mm), (6) prepared samples, and (7) measuring the MA properties of the prepared samples

2.4.2.4 Preparing double-layer of AC/F

$Mn_{0.1}Ni_{0.5}Zn_{0.4}Fe_2O_4$ nanoparticles were synthesized by self-combustion method. Radar absorption characteristics were studied for double-layer activated carbon/paraffin wax (AC) and $Ni_{0.5}Zn_{0.4}Mn_{0.1}Fe_2O_4$/paraffin wax (F) nanocomposites in the frequency range of 8.8 to 12 GHz. The loading ratio of $Mn_{0.1}Ni_{0.5}Zn_{0.4}Fe_2O_4$ within a paraffin wax matrix (50% w/w). On the other hand, the loading ratio of activated carbon within a paraffin wax matrix (30% w/w). The materials were later combined into paraffin wax to manufacture double-layer composite structures with whole thicknesses of 3 and 4 mm. For a better figure and illustration of the NC structures and their naming, the layering structures are displayed in Figure 2.10 and Table 2.9.

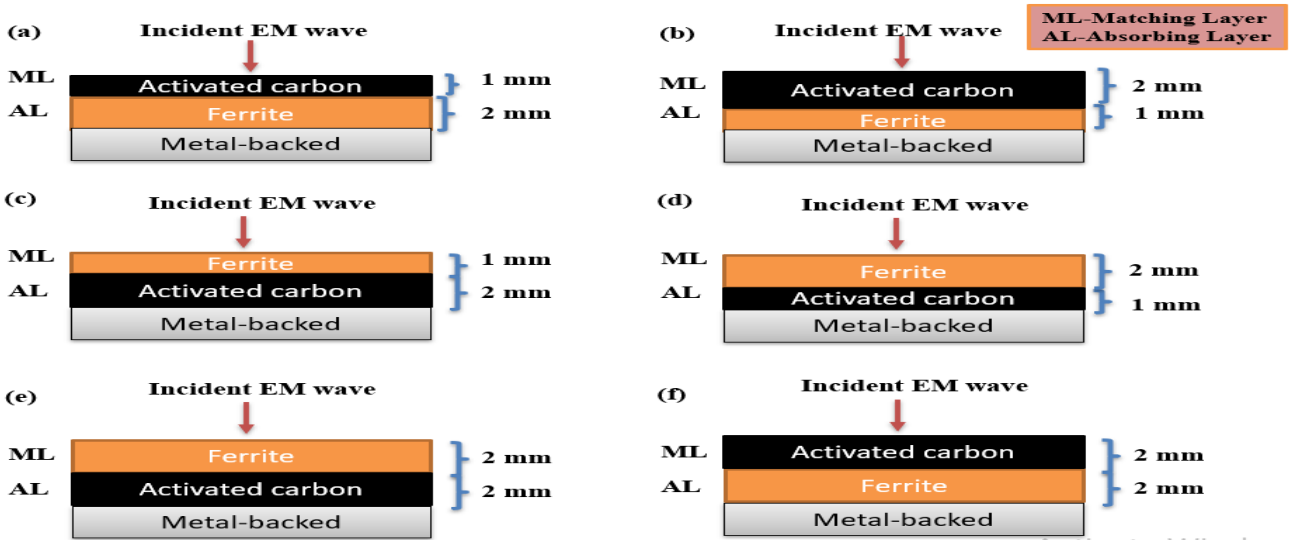

Figure 2.9 – DL structure of AC/F Cs with (a) 1 mm AC/1 mm F (AC/F-11), (b) 2 mm AC/1 mm F (AC/F-21), (c) 1 mm F/2 mm AC (F/AC-12), (d) 2 mm F/1 mm AC (F/AC-21), (e) 2 mm F/2 mm AC (F/AC-22), and (f) 2 mm AC/2 mm F (AC/F-22) thickness

Table 2.9 – Specifics on the DL structure of AC/F Cs

Sample symbols	ML	T(mm)	AL	T(mm)
AC/F-11	Activated carbon	1	$Ni_{0.5}Zn_{0.4}Mn_{0.1}Fe_2O_4$	1
AC/F-21	Activated carbon	2	$Ni_{0.5}Zn_{0.4}Mn_{0.1}Fe_2O_4$	1
F/AC-12	$Ni_{0.5}Zn_{0.4}Mn_{0.1}Fe_2O_4$	1	Activated carbon	2
F/AC-21	$Ni_{0.5}Zn_{0.4}Mn_{0.1}Fe_2O_4$	2	Activated carbon	1
F/AC-22	$Ni_{0.5}Zn_{0.4}Mn_{0.1}Fe_2O_4$	2	Activated carbon	2
AC/F-22	Activated carbon	2	$Ni_{0.5}Zn_{0.4}Mn_{0.1}Fe_2O_4$	2

2.4.2.5 Preparation of graphite/ferrite nanocompsoites

$Ni^{3+}_{0.25}Ni^{2+}_{0.375}Zn^{2+}_{0.25}Fe_2O_4$ nanoparticles were synthesized by a ceramic sintering method. Nanocomposites were synthesized by mixing ferrite nanoparticles with graphite using a ball mill. Three different weight ratios of graphite/$Ni^{3+}_{0.25}Ni^{2+}_{0.375}Zn^{2+}_{0.25}Fe_2O_4$ (1:1, 2:1, and 3:1) were prepared. The C/F nanocomposites were ball-milled for 1 h at 300 rpm. Table 2.10 shows the symbols of nanocomposite samples.

Table 2.10 – Symbols of nanocomposite samples

Nanocomposite	C: F	Heat treatment for ferrite (°C)	Sample symbol
C/ $Ni^{3+}_{0.25}Ni^{2+}_{0.375}Zn^{2+}_{0.25}Fe_2O_4$	1:1	1100	C/F-11
	2:1		C/F-21
	3:1		C/F-31

2.4.3 Preparation of hybrid nanocomposites

2.4.3.1 Coating NiZn spinel nanoferrite with PANI

The flow chart for the synthesis of PANI utilizing in-situ polymerization technique is shown in Figure 2.10. Firstly, sodium dodecyl sulfate and aniline were added to the distilled water while keeping mechanical stirring for 1 h. After that, HCl solution was added to the solution under stirring for 1 h. Finally, APS was dissolved in an aqueous solution utilized as an oxidizing agent and added slowly dropwise into the solution to start the polymerization. The polymerization was allowed to proceed for 6 h with stirring in an ice bath. The PANI was filtered and washed many times with distilled water and ethanol and then dried for 8 h in the furnace at 70 °C. NiZn ferrite nanoparticles were coated with polyaniline via the in-situ polymerization technique. The flow chart for the synthesis of PANI/F utilizing in-situ polymerization technique is shown in Figure 2.11. Three various weight ratios of aniline/$Ni^{3+}_{0.25}Ni^{2+}_{0.375}Zn^{2+}_{0.25}Fe_2O_4$ (1:1, 2:1, and 3:1) were synthesized. The nanocomposite ratios of $Ni^{3+}_{0.25}Ni^{2+}_{0.375}Zn^{2+}_{0.25}Fe_2O_4$ and aniline in weight were 1:1 (PANI/F.1), 2:1 (PANI/F.2) and 3:1 (PANI/F.3), respectively. The circular samples were formed using a special 50 mm diameter mold to measure MA and EMI properties.

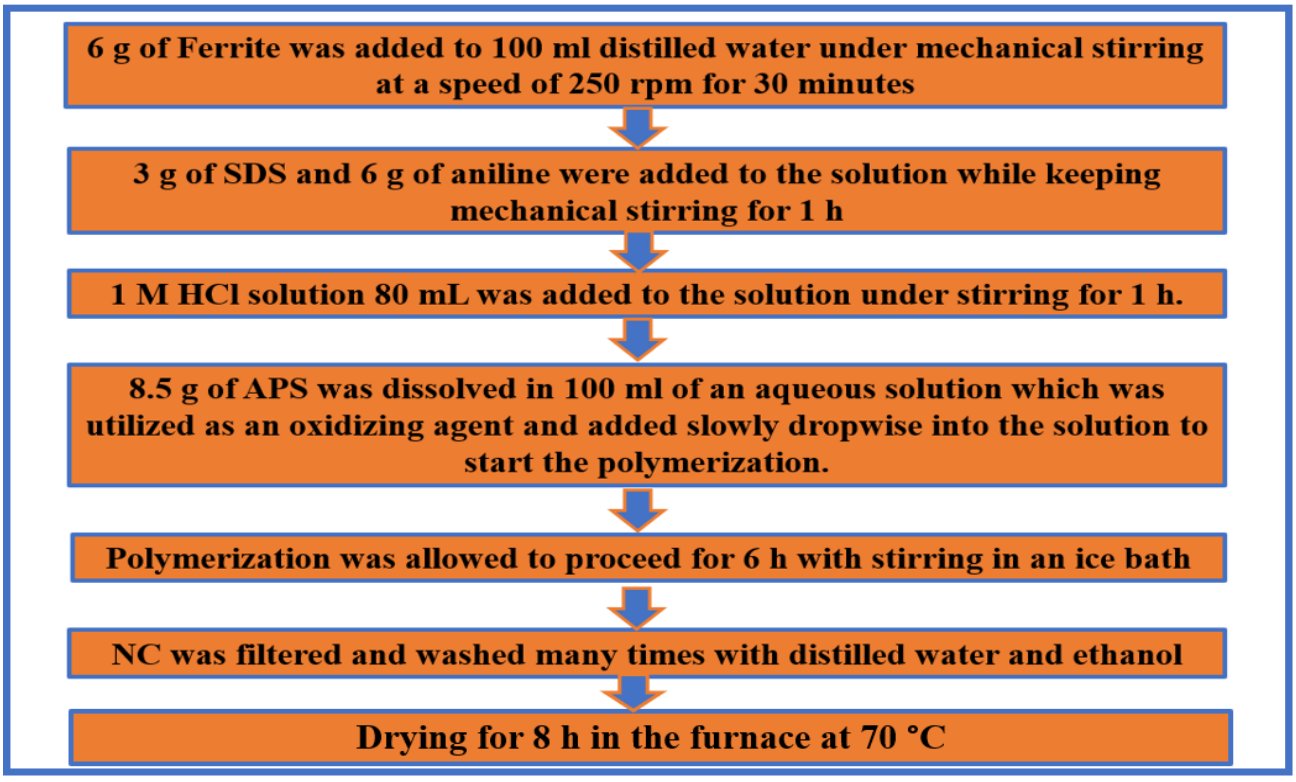

Figure 2.10 – Flow chart for the synthesis of PANI/F utilizing in-situ polymerization technique

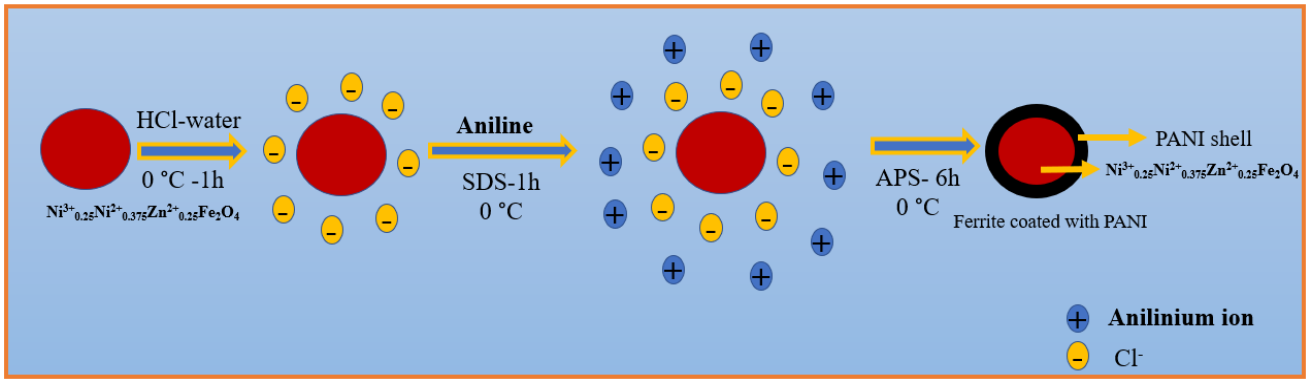

Figure 2.11 – Schematic diagram of a polyaniline/NiZn ferrite by the in-situ polymerization technique

2.4.3.2 Preparation of PANI/CI and PANI/F/CI

PANI/CI nanocomposites were prepared using in-situ polymerization technique of PANI in the CI. The weight ratio of aniline/CI (1/1) was synthesized. On the other hand, Ternary composites of polyaniline/NiZn ferrite/carbonyl iron (PANI/F/CI) were prepared in two stages: Firstly, $Ni_{0.5}Zn_{0.5}Fe_2O_4$ were prepared using citrate precursor method. After that, PANI/90%F/10%CI composites were prepared using in-situ polymerization technique of PANI in the $Ni_{0.5}Zn_{0.5}Fe_2O_4$ and CI. The flow chart for the synthesis of PANI/F/CI utilizing in-situ polymerization technique is shown in Figure 2.12. The weight ratio of aniline/(F-CI) (1/1) was synthesized.

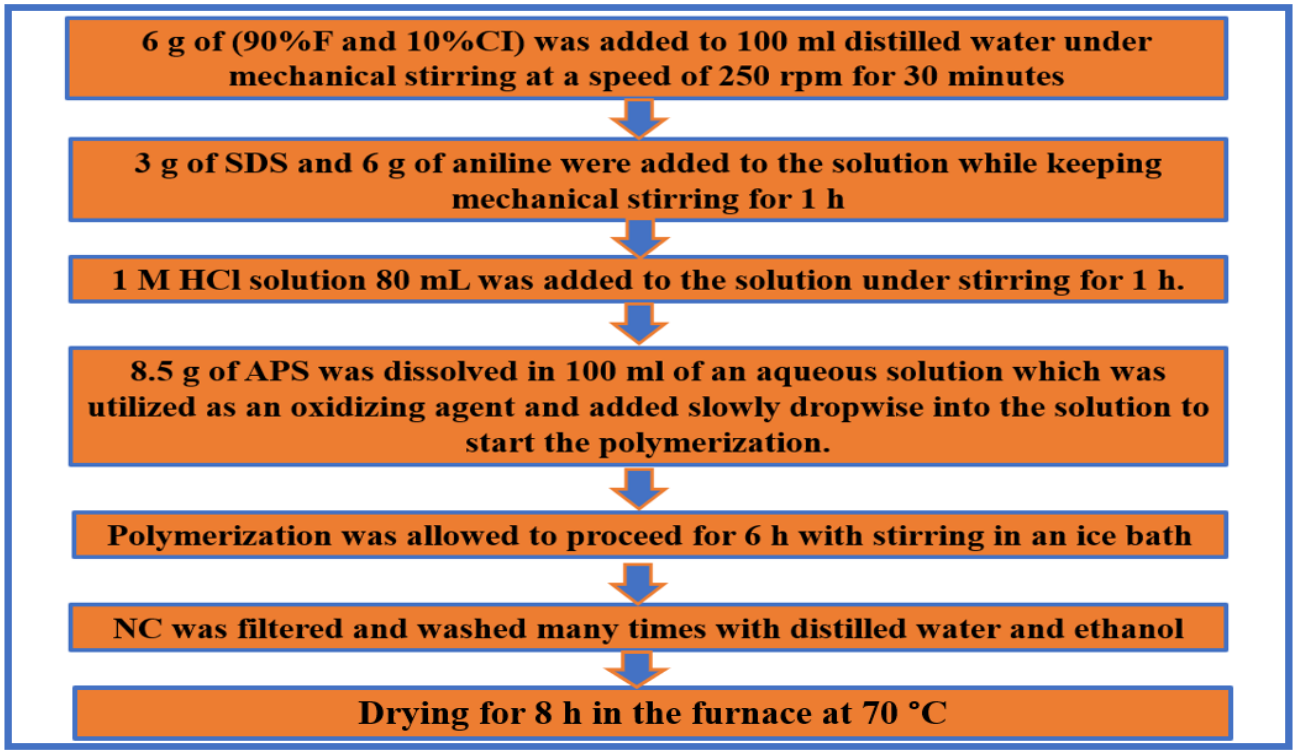

Figure 2.12 – Flow chart for the synthesis of PANI/F/CI utilizing in-situ polymerization technique

2.4.3.3 Preparation of PANI/CB and PANI/F/CB

PANI/CB nanocomposites were prepared using in-situ polymerization technique of PANI in the existence of the CB. The weight ratio of aniline/CB (1/1) was synthesized. On the other hand, Ternary composites of polyaniline/NiZn ferrite/carbon black (PANI/F/CB) were prepared via two stages: Firstly, $Ni^{3+}_{0.25}Ni^{2+}_{0.375}Zn^{2+}_{0.25}Fe_2O_4$ was prepared using a ceramic sintering method. After that, PANI/F/CB composites are prepared using in-situ polymerization technique of PANI in the existence of the $Ni^{3+}_{0.25}Ni^{2+}_{0.375}Zn^{2+}_{0.25}Fe_2O_4$ and CB. The weight ratio of aniline/ (90%,70% and 50%F-10%,30% and 50%CB) (1/1) was synthesized. The flow chart for the synthesis of PANI/F/CB utilizing in-situ polymerization technique is shown in Figure 2.13.

2.4.3.4 Coating $BaNiZnFe_{16}O_{27}$ hexagonal nano ferrite with PANI

$BaNiZnFe_{16}O_{27}$ nanoparticles were coated with polyaniline via the in-situ polymerization technique. The flow chart for the synthesis of PANI/HF utilizing in-situ polymerization technique is shown in Figure 2.10. Three weight ratios of aniline/$BaNiZnFe_{16}O_{27}$ (1:1, 1:2, and 1:3) were synthesized. The nanocomposite ratios of $BaNiZnFe_{16}O_{27}$ and aniline in weight were 1:1 (PANI/HF.1), 1:2 (PANI/HF.2) and 1:3 (PANI/HF.3), respectively.

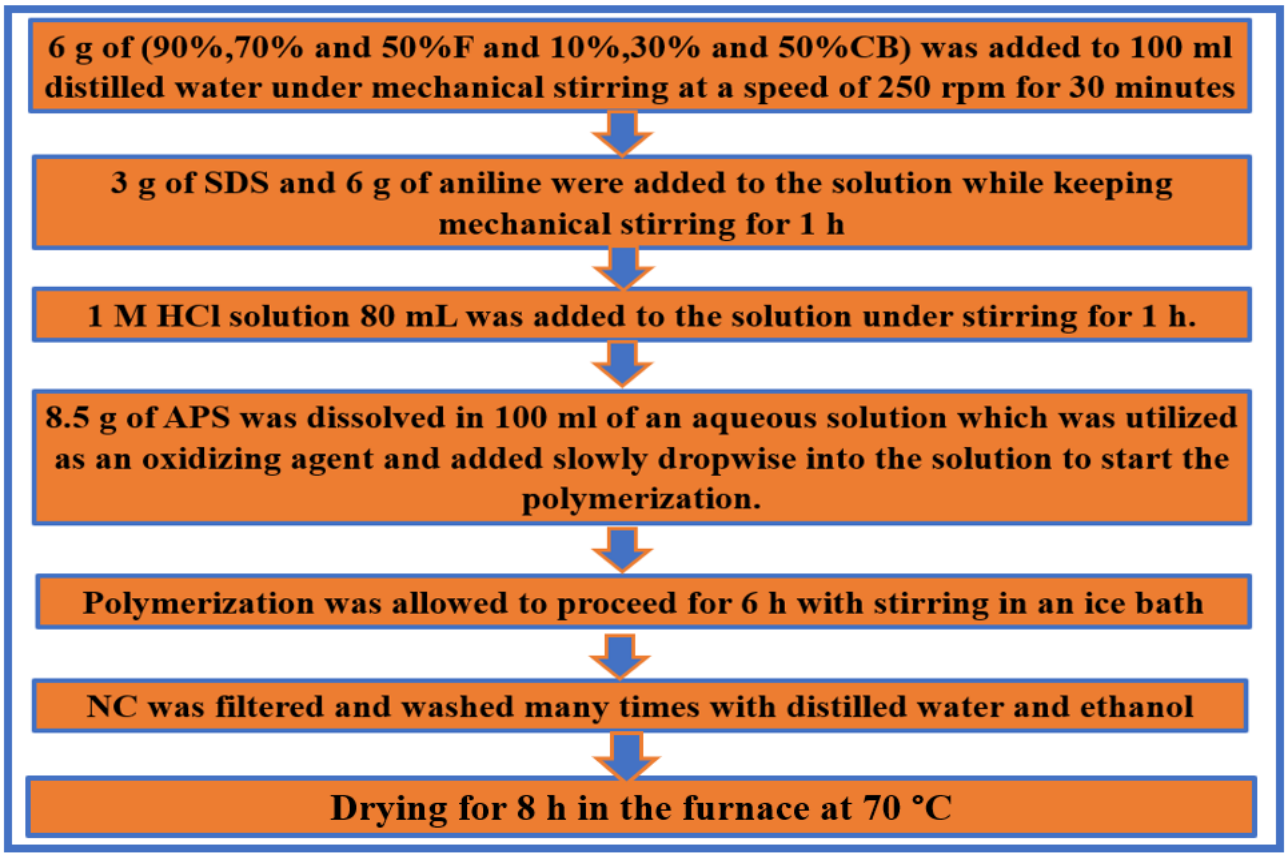

Figure 2.13 – Flow chart for the synthesis of PANI/F/CB utilizing in-situ polymerization technique

2.4.3.5 Preparation of PANI/SF/HF and PANI/SF/HF/CB

Ternary composites of polyaniline/$Ni^{3+}_{0.25}Ni^{2+}_{0.375}Zn^{2+}_{0.25}Fe_2O_4$/$BaNiZnFe_{16}O_{27}$ (PANI/SF/HF) were prepared via two stages: Firstly, $Ni^{3+}_{0.25}Ni^{2+}_{0.375}Zn^{2+}_{0.25}Fe_2O_4$ and $BaNiZnFe_{16}O_{27}$ were prepared using the ceramic sintering method. After that, PANI/50%SF/50%HF nanocomposites were prepared using in-situ polymerization technique of PANI in the existence of the $Ni_{0.5}Zn_{0.5}Fe_2O_4$ and $BaNiZnFe_{16}O_{27}$. The weight ratio of aniline/(SF-HF) (1/1) was synthesized. On the other hand, PANI/45%SF/45%HF/10%CB was also prepared using in-situ polymerization technique. The weight ratio of aniline/(SF-HF-CB) (1/1) was synthesized.

3 Chapter 3: Results and discussion

3.1 XRD patterns

3.1.1 X-ray diffraction of undoped ferrites

Figure 3.1 shows the XRD patterns of the $NiFe_2O_4$, $ZnFe_2O_4$, $MnFe_2O_4$ and $CuFe_2O_4$. For undoped ferrites pattern, six diffraction peaks were detected, which conform to (hkl) planes of (220), (311), (400), (422), (511) and (440), respectively. The XRD figures of ferrites showed the formation of a single-phase cubic spinel structure with no impurity peaks. The XRD patterns of undoped ferrites were totally matched with the reference XRD patterns (JCPDS, PDF no. 01-086–2267, JCPDS, PDF. no. 00-022-012, and JCPDS, PDF. no. 00-010–0319).

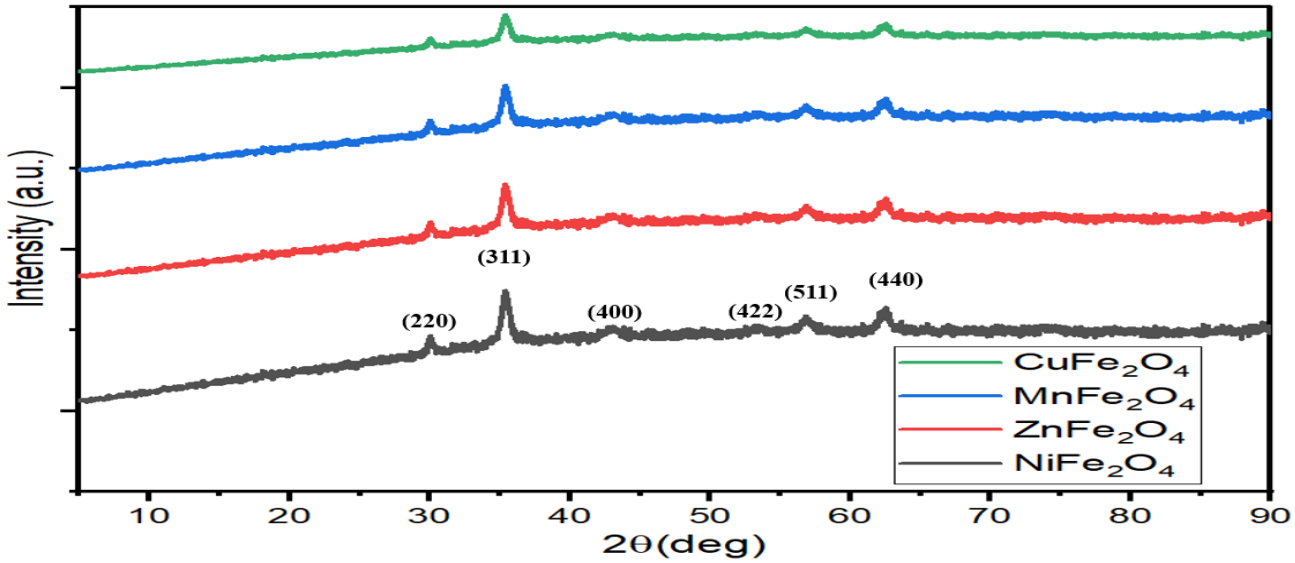

Figure 3.1 – XRD patterns of the $NiFe_2O_4$, $ZnFe_2O_4$, $MnFe_2O_4$ and $CuFe_2O_4$

3.1.2 X-ray diffraction of doped ferrites samples prepared by the ceramic sintering technique

Figure 3.2 shows the XRD patterns of the $Mn_xZn_{(1-x)}Fe_2O_4$ (x= 0.3, 0.6, 0.9), $Ni_xZn_{(1-x)}Fe_2O_4$ (x= 0.25, 0.5, 0.75), $Mn_{0.1}Ni_{(0.4+x)}Zn_{(0.5-x)}Fe_2O_4$ (x= 0.0, 0.1, 0.2), $Ni^{3+}_{0.25}Ni^{2+}_{0.375}Zn^{2+}_{0.25}Fe_2O_4$, $Cu^{2+}_{0.1}Ni^{3+}_{0.15}Ni^{2+}_{0.225}Zn^{2+}_{0.45}Fe_2O_4$ and $BaNiZnFe_{16}O_{27}$. For $Mn_xZn_{(1-x)}Fe_2O_4$ and $Ni_xZn_{(1-x)}Fe_2O_4$ pattern, six diffraction peaks were detected, which conform to (hkl) planes of (220), (311), (400), (422), (511) and (440), respectively. On the other hand, for $Mn_{0.1}Ni_{(0.4+x)}Zn_{(0.5-x)}Fe_2O_4$, $Ni^{3+}_{0.25}Ni^{2+}_{0.375}Zn^{2+}_{0.25}Fe_2O_4$ and $Cu^{2+}_{0.1}Ni^{3+}_{0.15}Ni^{2+}_{0.225}Zn^{2+}_{0.45}Fe_2O_4$ patterns, nine diffraction peaks were noticed, which conform to (hkl) planes of (111), (220), (311), (222), (400), (422), (511), (440) and (533), respectively. The XRD figures of spinel ferrites indicated the formation of a single-phase cubic spinel structure with no impurity peaks. All the observed peaks of the spinel ferrites were matched with the standard XRD pattern (JCPDS, PDF no. 00-008-0234). For the

$BaNiZnFe_{16}O_{27}$ pattern, eleven diffraction peaks were noticed, which conform to (hkil) planes of (110), (1010), (116), (0114), (107), (203), (208), (209), (2015), (2111) and (220), respectively. The hexagonal ferrites' observed peaks were matched with the standard XRD pattern (JCPDS, PDF no. 51-1877). The size of the ferrite grains (hkl (311)) has been evaluated with Scherrer's equation, $D=0.9\ \lambda/\beta\ \cos\theta$, where D is the crystallite size (nm), λ is the X-ray wavelength, β is the bandwidth at half-height, and θ is the diffraction angle in degree. Table 3.1 displays the calculated crystallite size of $Ni_{0.5}Zn_{0.5}Fe_2O_4$.

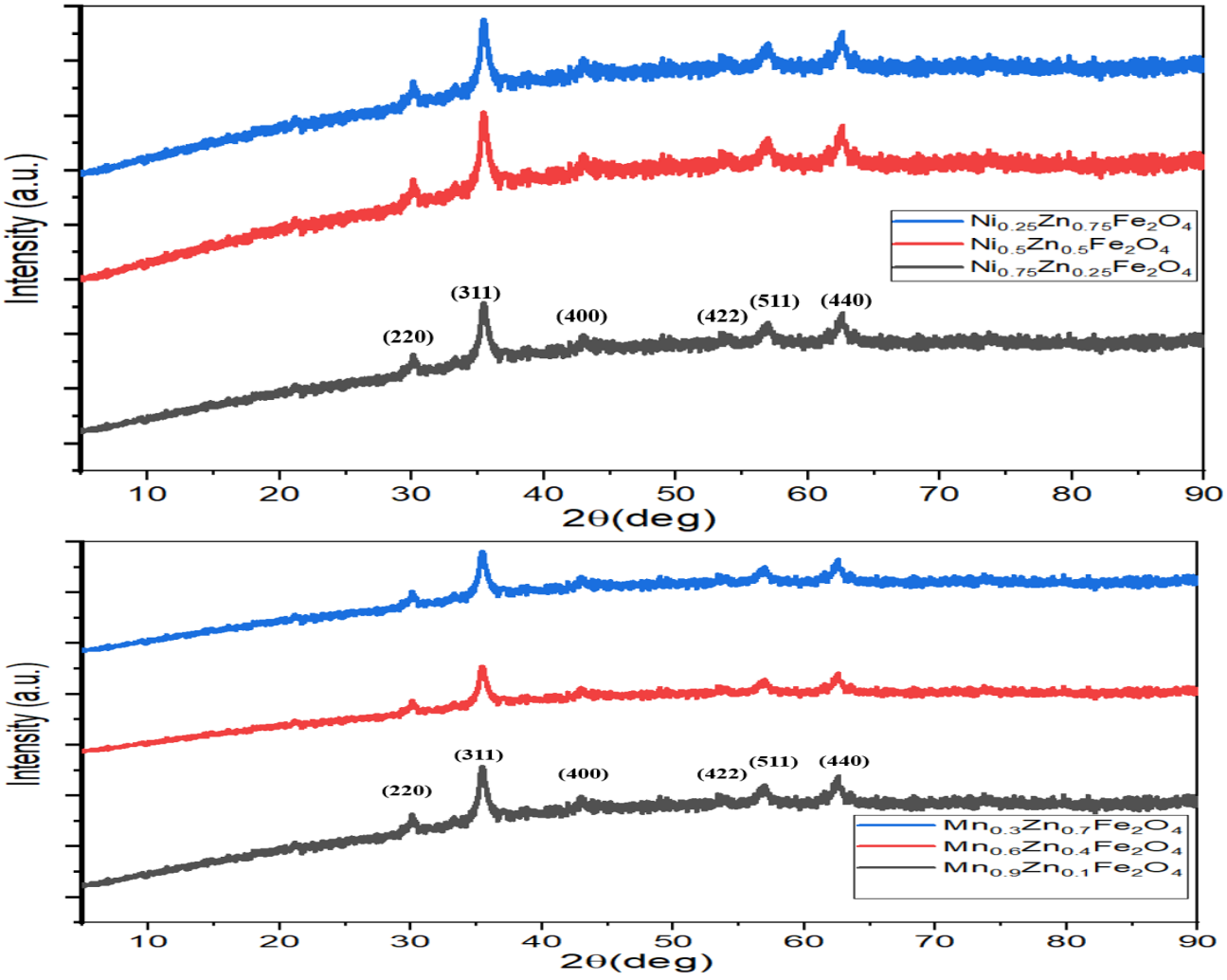

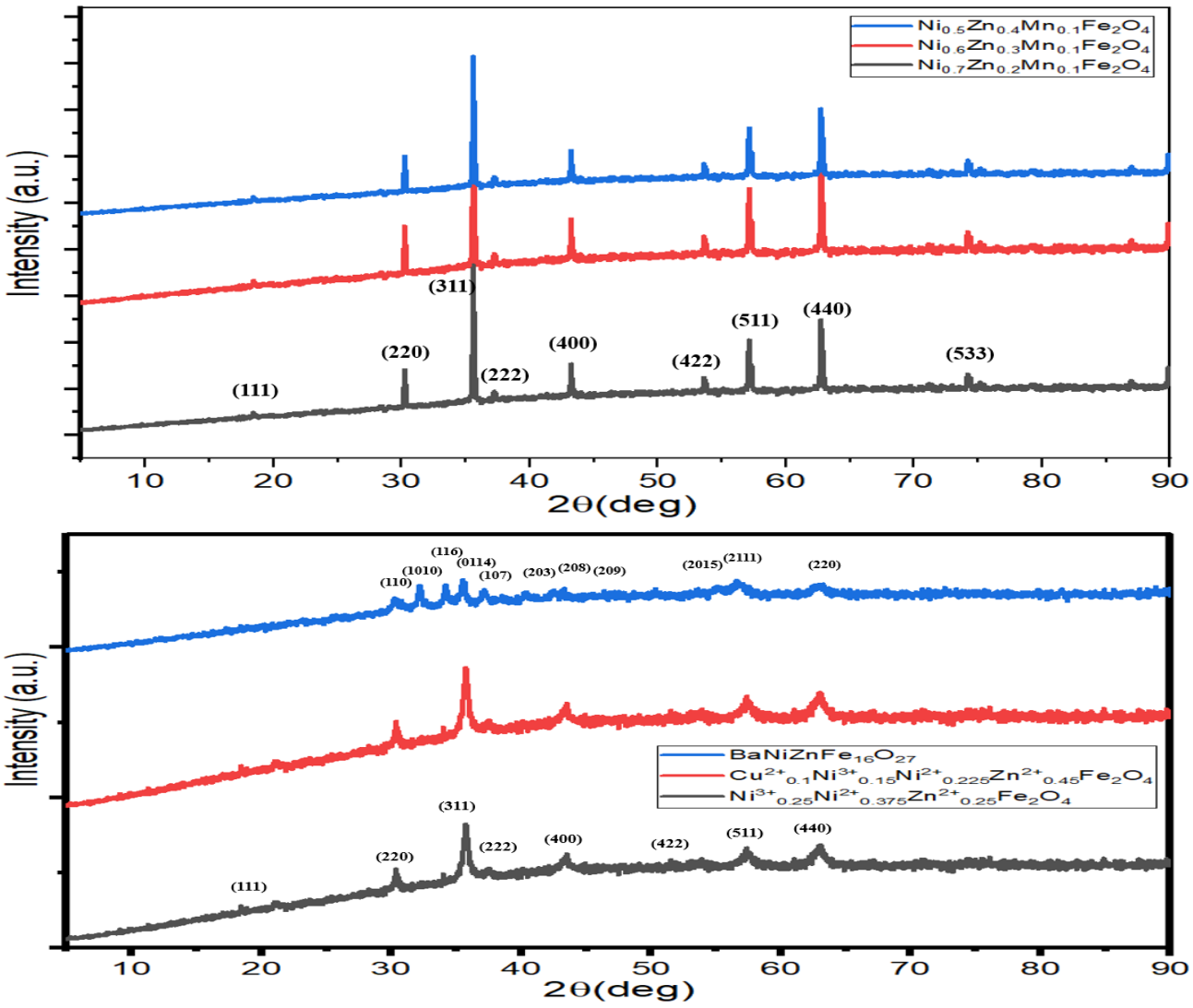

Figure 3.2 – XRD patterns of the $Mn_xZn_{(1-x)}Fe_2O_4$ (x= 0.3, 0.6, 0.9), $Ni_xZn_{(1-x)}Fe_2O_4$ (x= 0.25, 0.5, 0.75), $Mn_{0.1}Ni_{(0.4+x)}Zn_{(0.5-x)}Fe_2O_4$ (x= 0.1, 0.2, 0.3), $Ni^{3+}{}_{0.25}Ni^{2+}{}_{0.375}Zn^{2+}{}_{0.25}Fe_2O_4$, $Cu^{2+}{}_{0.1}Ni^{3+}{}_{0.15}Ni^{2+}{}_{0.225}Zn^{2+}{}_{0.45}Fe_2O_4$ and $BaNiZnFe_{16}O_{27}$

Table 3.1 – Crystallite size of doped ferrites

Sample	K	λ (A)	2Θ (°)	FWHM (°)	Crystallite size (nm)
$Ni_{0.25}Zn_{0.75}Fe_2O_4$	0.94	1.54178	35.41	0.16447	52.9
$Ni_{0.5}Zn_{0.5}Fe_2O_4$	0.94	1.54178	35.45	0.16842	51.7
$Ni_{0.75}Zn_{0.25}Fe_2O_4$	0.94	1.54178	35.51	0.17931	48.6
$Mn_{0.3}Zn_{0.7}Fe_2O_4$	0.94	1.54178	35.62	0.18421	47.3
$Mn_{0.6}Zn_{0.4}Fe_2O_4$	0.94	1.54178	35.42	0.16362	53.2
$Mn_{0.9}Zn_{0.1}Fe_2O_4$	0.94	1.54178	35.61	0.15834	55.1
$Ni_{0.5}Zn_{0.4}Mn_{0.1}Fe_2O_4$	0.94	1.54178	35.65	0.16379	53.2

$Ni_{0.6}Zn_{0.3}Mn_{0.1}Fe_2O_4$	0.94	1.54178	35.43	0.17027	51.2
$Ni_{0.7}Zn_{0.2}Mn_{0.1}Fe_2O_4$	0.94	1.54178	35.55	0.16447	53.1
$Ni^{3+}_{0.25}Ni^{2+}_{0.375}Zn^{2+}_{0.25}Fe_2O_4$	0.94	1.54178	35.48	0.17471	49.9
$Cu^{2+}_{0.1}Ni^{3+}_{0.15}Ni^{2+}_{0.225}Zn^{2+}_{0.45}Fe_2O_4$	0.94	1.54178	35.53	0.16323	53.4

3.1.2.1 X-ray diffraction of ferrite samples prepared by citrate precursor technique

Figure 3.3 displays the XRD patterns of $Ni_{0.5}Zn_{0.5}Fe_2O_4$. The effect of the different molar ratios of the metal ion/citrate acid (1:1, 2:1 and 3:1) and the different calcination temperatures (650, 800 and 950°C) was investigated on the ferrite properties. The XRD Figures of ferrites showed the formation of a single-phase cubic spinel structure with no impurity peaks [108]. All the observed peaks of the NiZn ferrite were matched with the standard XRD pattern (JCPDS, PDF no. 08–0234). The size of the NiZn ferrite grains (hkl (311)) has been evaluated with Scherrer's equation, $D=0.9\ \lambda/\beta\ \cos\theta$. Table 3.2 displays the calculated crystallite size of $Ni_{0.5}Zn_{0.5}Fe_2O_4$. The XRD patterns showed that the crystallite size of nickel-zinc ferrite increased by increasing the calcination temperature, as shown in Table 3.2 and Figure 3.4. One can observe that the crystallite size of nickel-zinc ferrite increased by increasing the metal ion concentrations during the preparation process of the ferrite, regardless of the calcination temperature, which will impact its EMI shielding and MA properties, as will be clarified later.

Table 3.2 – Crystallite size of $Ni_{0.5}Zn_{0.5}Fe_2O_4$

Sample	K	λ (A)	2Θ (°)	FWHM (°)	Crystallite size (nm)
NZ_{11} - 650	0.94	1.54178	35.44	0.31603	27.5
NZ_{12} - 650	0.94	1.54178	35.43	0.28904	30.1
NZ_{13} - 650	0.94	1.54178	35.62	0.21431	40.7
NZ_{11} - 800	0.94	1.54178	35.37	0.27702	31.5
NZ_{12} - 800	0.94	1.54178	35.54	0.25410	34.3
NZ_{13} - 800	0.94	1.54178	35.62	0.19422	44.9
NZ_{11} - 950	0.94	1.54178	35.46	0.26351	33.1
NZ_{12} - 950	0.94	1.54178	35.41	0.23678	36.8
NZ_{13} - 950	0.94	1.54178	35.56	0.17982	48.5

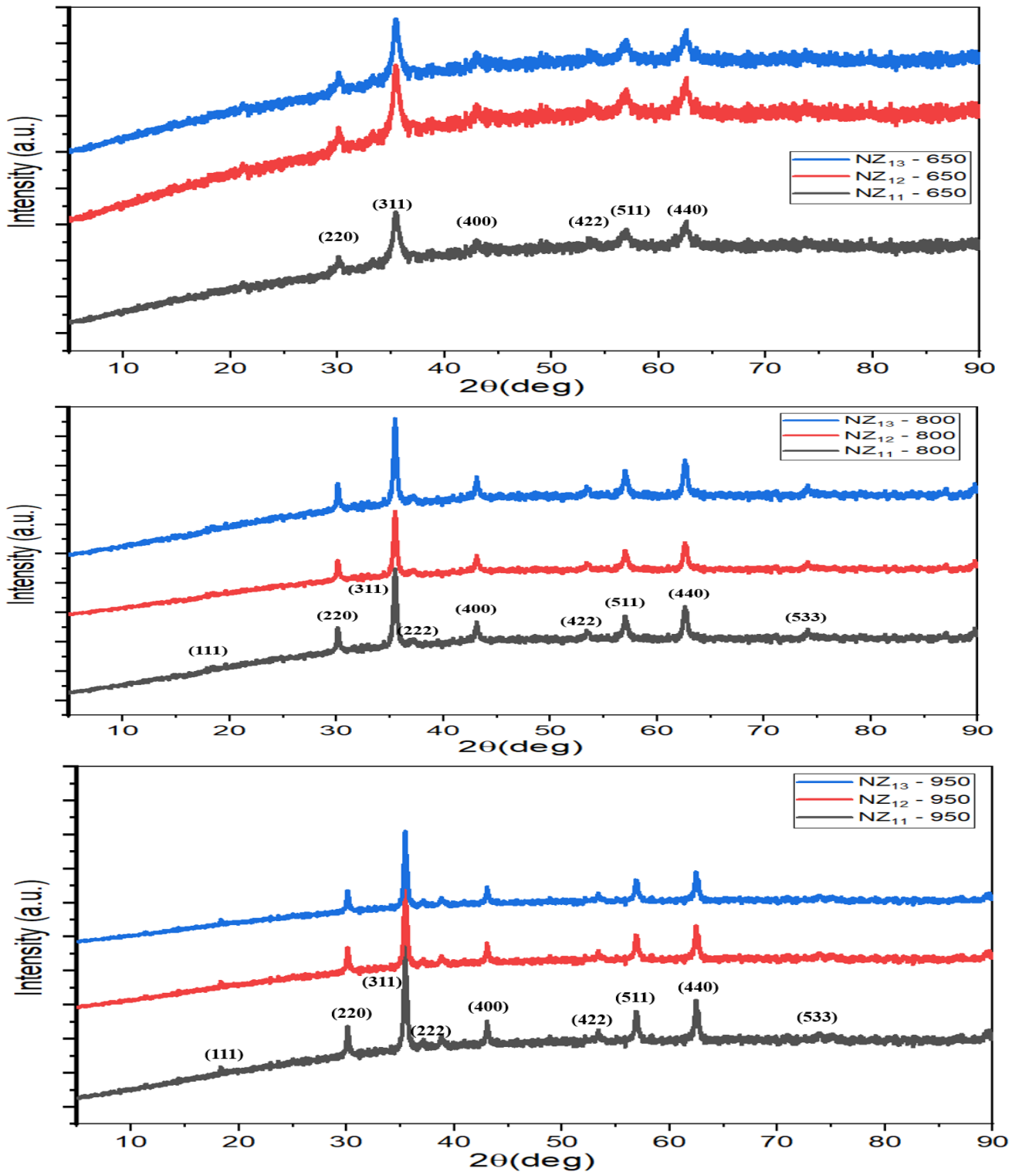

Figure 3.3 – XRD patterns at $Ni_{0.5}Zn_{0.5}Fe_2O_4$ of the different molar ratios of the metal ion/citrate acid (1:1, 2:1, and 3:1) at the different calcination temperatures (650, 800, and 950°C)

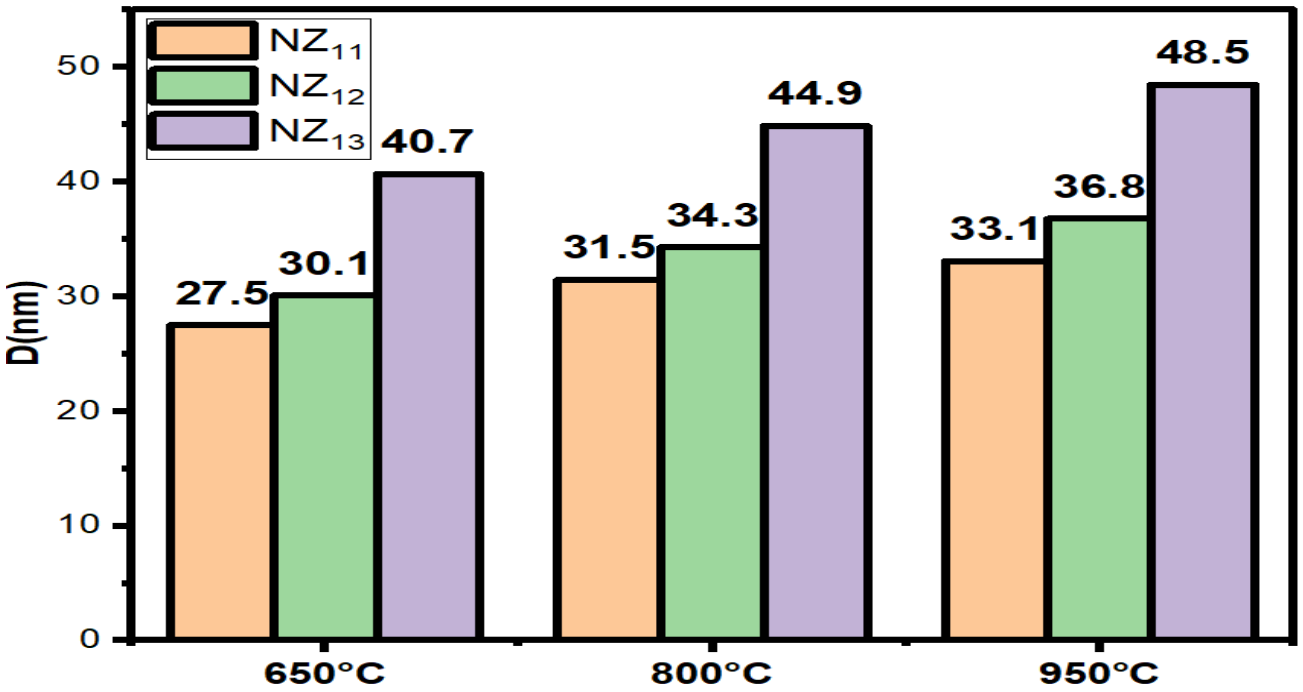

Figure 3.4 – Change of crystallite size of nickel-zinc ferrite prepared by citrate precursor method by changing the preparation conditions (calcination temperatures, metal ion concentrations)

3.1.2.2 X-ray diffraction of ferrite samples prepared by the self-combustion technique

Figure 3.5 displays the XRD patterns of $Ni_{0.5}Zn_{0.5}Fe_2O_4$. The effect of the different aqueous solutions of PVA (1%, 4% and 6%) and the different calcination temperatures (650, 800 and 950°C) were studied on the ferrite properties. The XRD Figures of ferrites showed the formation of a single-phase cubic spinel structure with no impurity peaks [108]. All the observed peaks of the NiZn ferrite were matched with the standard XRD pattern (JCPDS, PDF no. 08–0234). The size of the NiZn ferrite grains (hkl (311)) has been evaluated with Scherrer's equation. Table 3.3 shows the calculated crystallite size of $Ni_{0.5}Zn_{0.5}Fe_2O_4$. The XRD patterns results showed that the crystallite size of nickel-zinc ferrite increased by increasing the calcination temperature, as shown in Table 3.3 and Figure 3.6. One can notice that the crystallite size of nickel-zinc ferrite increased by increasing the PVA concentrations during the preparation process of the ferrite, regardless of calcination temperature, which will affect its EMI shielding and MA properties, as will be explained later.

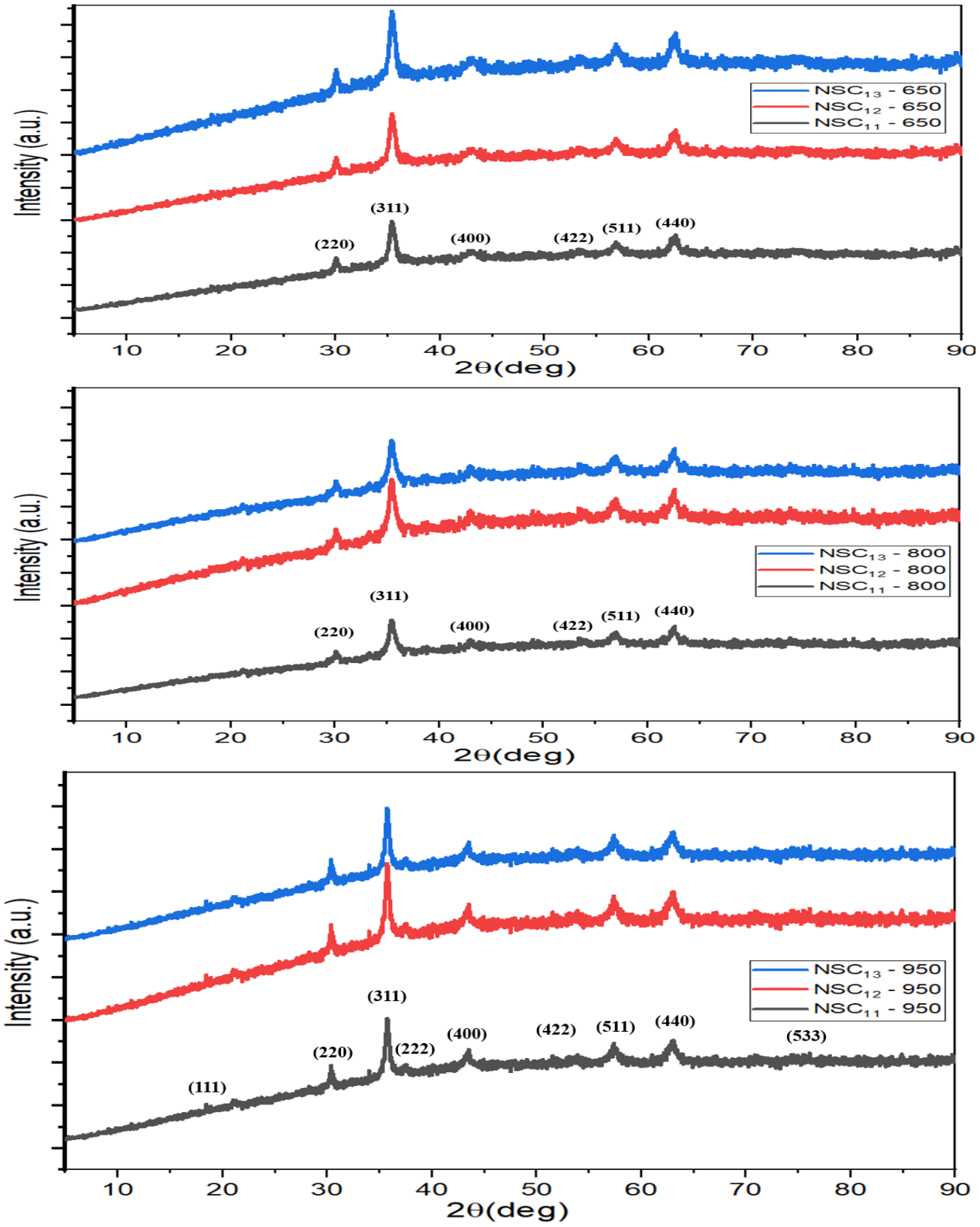

Figure 3.5 – XRD patterns of $Ni_{0.5}Zn_{0.5}Fe_2O_4$ at the different aqueous solutions of PVA (1%, 4%, and 6%) at the different calcination temperatures (650, 800, and 950°C)

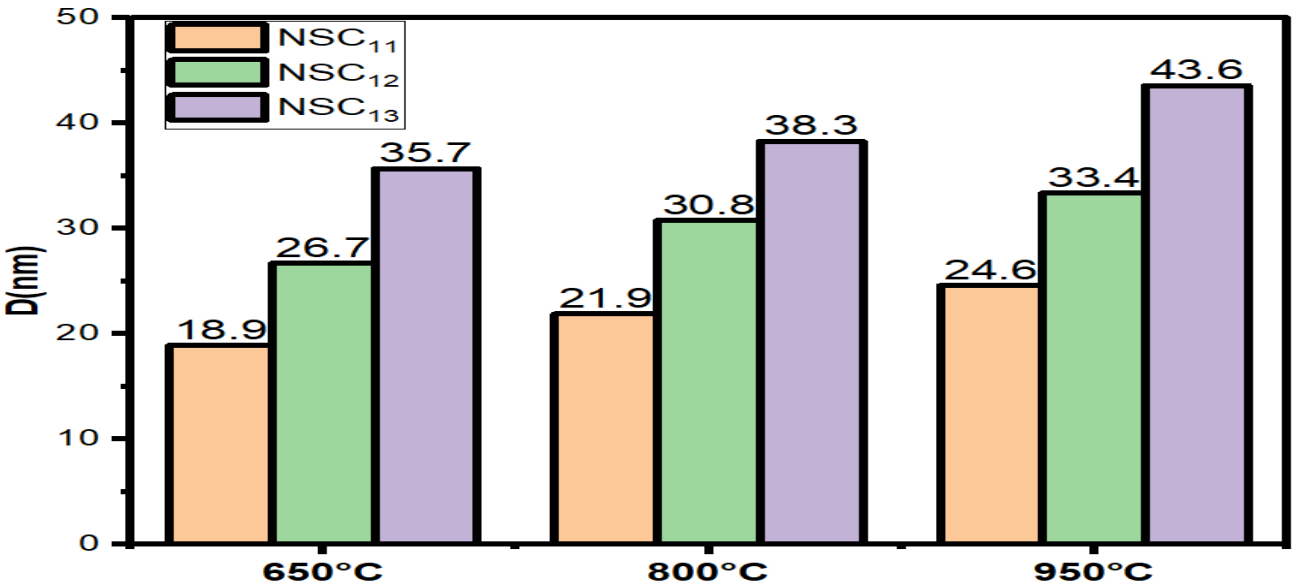

Figure 3.6 – Change of crystallite size of ferrites prepared by self-combustion method by changing the preparation conditions (calcination temperatures, PVA concentrations)

Table 3.3 – Crystallite size of $Ni_{0.5}Zn_{0.5}Fe_2O_4$

Sample	K	λ (A)	2Θ (°)	FWHM (°)	Crystallite size (nm)
NSC_{11} - 650	0.94	1.54178	35.46	0.46131	18.9
NSC_{12} - 650	0.94	1.54178	35.49	0.32637	26.7
NSC_{13} - 650	0.94	1.54178	35.51	0.24416	35.7
NSC_{11} - 800	0.94	1.54178	35.47	0.39641	21.9
NSC_{12} - 800	0.94	1.54178	35.61	0.28230	30.8
NSC_{13} - 800	0.94	1.54178	35.52	0.22735	38.3
NSC_{11} - 950	0.94	1.54178	35.45	0.35471	24.6
NSC_{12} - 950	0.94	1.54178	35.48	0.26129	33.4
NSC_{13} - 950	0.94	1.54178	35.49	0.19521	43.6

3.1.2.3 X-ray diffraction of carbon black, activated carbon, graphite and carbonyl iron

Figure 3.7 shows the XRD patterns of carbon black, activated carbon, graphite and carbonyl iron. For the CB pattern, two diffraction peaks were detected at 2θ values of 22.88°and 43.22°. As well, for the AC pattern, two diffraction peaks were noticed at 2θ values of 22.85° and 43.19°, which conform to (hkl) planes of (002) and (100), respectively [109]. On the other hand, for the graphite pattern, five characteristic peaks were detected at 2θ values of 26.36°, 42.65°, 54.17°, 77.52°, and 82.94°, which conform to (hkl) planes of (002), (100), (004), (110) and (112), respectively. Finally, for the carbonyl iron pattern, three characteristic peaks were noticed at 2θ values of 44.61°,

64.26° and 82.33°, which conform to (hkl) planes of (100), (200), and (211), respectively. The XRD pattern of carbonyl iron resembles crystallites in which the sample mainly contains the α-Fe phase [110]. All the observed peaks of CI were matched with the standard XRD pattern (JCPDS, PDF no. 06-0696).

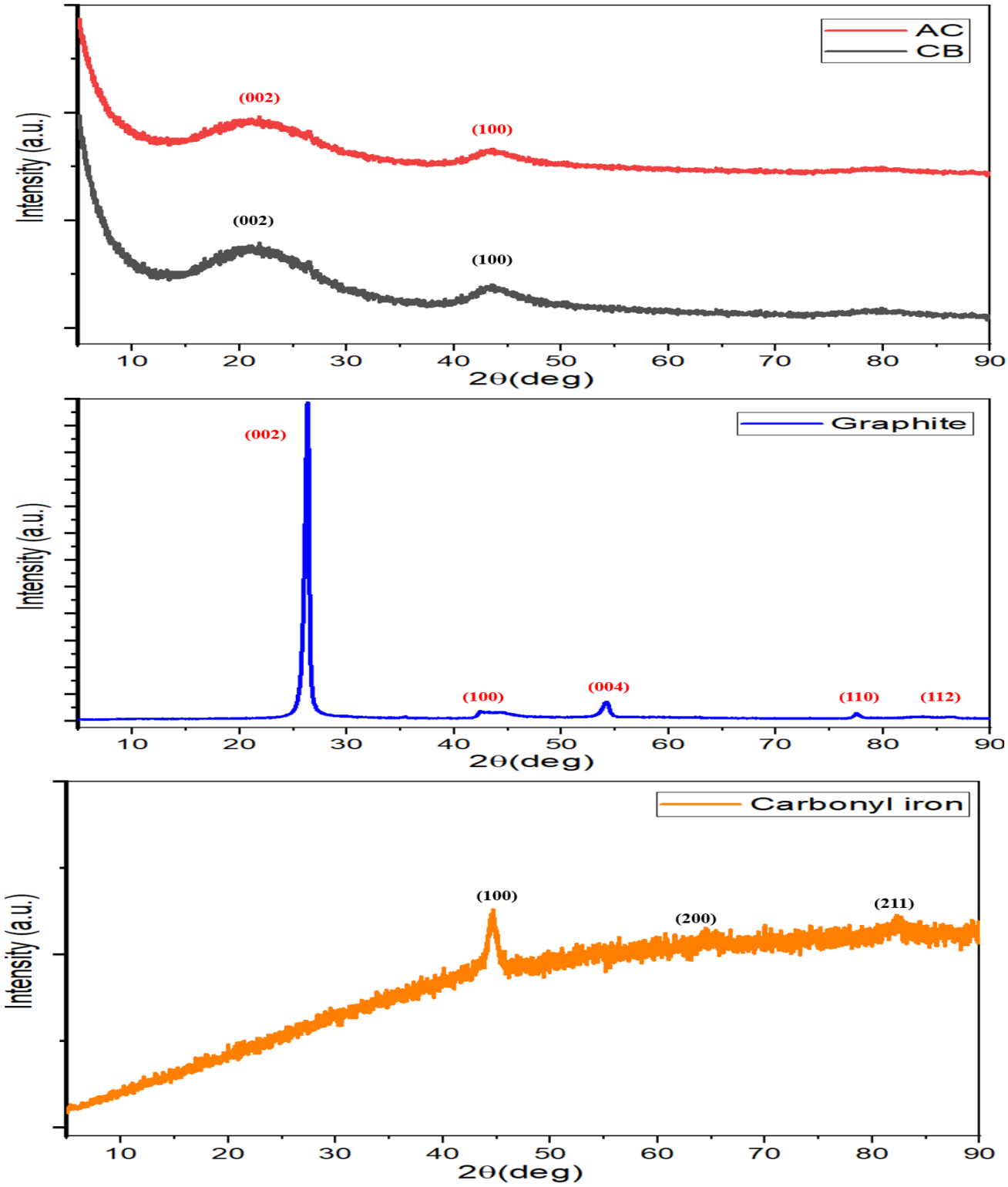

Figure 3.7 – XRD patterns of CB, AC, C and CI

3.1.2.4 X-ray diffraction of PANI-based nanocomposites

Figure 3.8 displays the XRD patterns of the $Ni^{3+}_{0.25}Ni^{2+}_{0.375}Zn^{2+}_{0.25}Fe_2O_4$, PANI/F nanocomposites and PANI. The characteristic peaks of PANI/F hybrid nanocomposites matched the characteristic peaks of $Ni^{3+}_{0.25}Ni^{2+}_{0.375}Zn^{2+}_{0.25}Fe_2O_4$ core as mentioned above. This revealed when the $Ni^{3+}_{0.25}Ni^{2+}_{0.375}Zn^{2+}_{0.25}Fe_2O_4$ magnetic core was coated with PANI, the spinel structure of the $Ni^{3+}_{0.25}Ni^{2+}_{0.375}Zn^{2+}_{0.25}Fe_2O_4$ magnetic core remained intact. As shown in Figure 3.8, the XRD pattern of the pure PANI displayed an amorphous structure with two characteristic peaks at 20.22° and 25.36°, which were attributed to the periodicity parallel to the polymer chains of PANI [111,112]. The XRD patterns of the PANI/$Ni^{3+}_{0.25}Ni^{2+}_{0.375}Zn^{2+}_{0.25}Fe_2O_4$ nanocomposites displayed crystalline peaks because of the existence of NiZn ferrite in these nanocomposites. The two characteristic peaks of the PANI disappeared due to the $Ni^{3+}_{0.25}Ni^{2+}_{0.375}Zn^{2+}_{0.25}Fe_2O_4$ nanoparticles [113,114].

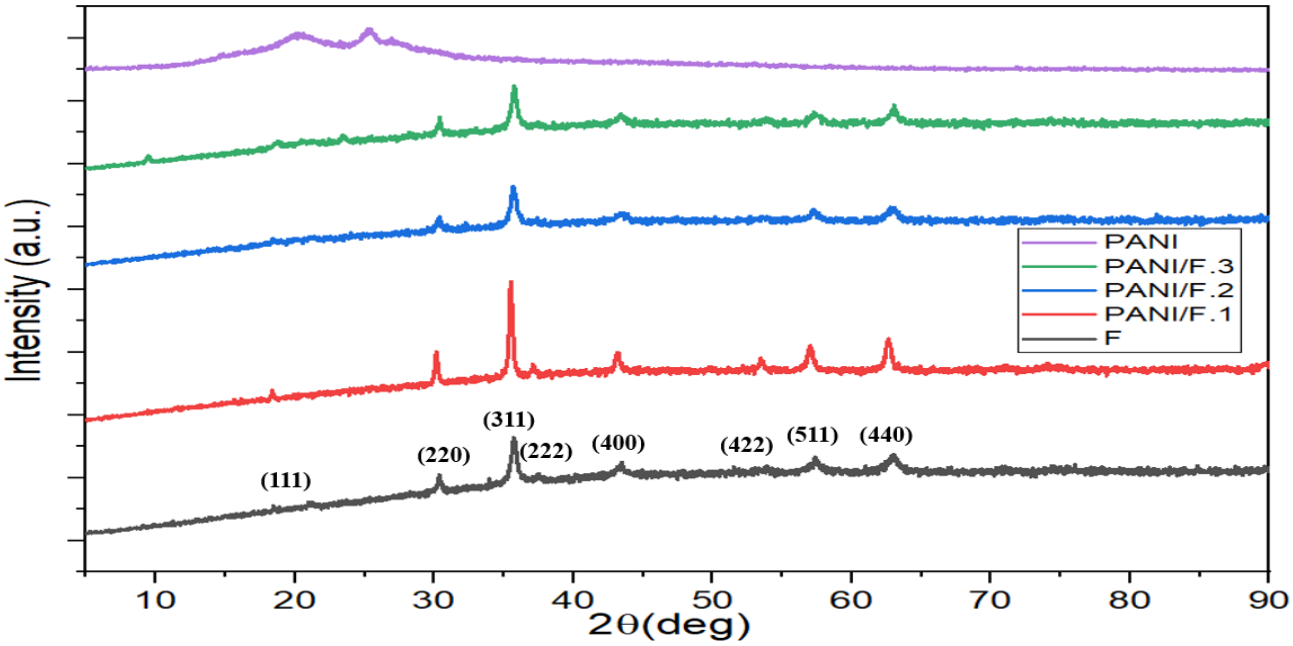

Figure 3.8 – XRD patterns of $Ni^{3+}_{0.25}Ni^{2+}_{0.375}Zn^{2+}_{0.25}Fe_2O_4$, PANI/$Ni^{3+}_{0.25}Ni^{2+}_{0.375}Zn^{2+}_{0.25}Fe_2O_4$ nanocomposites and pure PANI

The XRD patterns of $Ni_{0.5}Zn_{0.5}Fe_2O_4$, CI, PANI/CI and PANI/F/CI nanocomposite are shown in Figure 3.9. The characteristic peaks of the PANI/F/CI hybrid nanocomposite showed matching the characteristic peaks of $Ni_{0.5}Zn_{0.5}Fe_2O_4$ as cited above. The XRD patterns of the PANI/F/CI hybrid nanocomposite showed crystalline peaks because of the existence of NiZn ferrite in this composite.

Figure 3.10 displays the XRD patterns of the PANI/CB, PANI/90%F/10%CB, PANI/70%F/30%CB and PANI/50%F/50%CB hybrid nanocomposite. For the PANI/F/CB patterns, eight diffraction peaks were detected, which conform to (hkl)

planes of (111), (220), (311), (222), (400), (422), (511) and (440), respectively. The characteristic peaks of PANI/F/CB nanocomposites matched the characteristic peaks of $Ni^{3+}_{0.25}Ni^{2+}_{0.375}Zn^{2+}_{0.25}Fe_2O_4$ as mentioned above. For PANI/CB pattern, two diffraction peaks were noticed, which conform to (hkl) planes of (002) and (100), respectively. The characteristic peaks of PANI/CB nanocomposites matched the characteristic peaks of carbon black, as cited above.

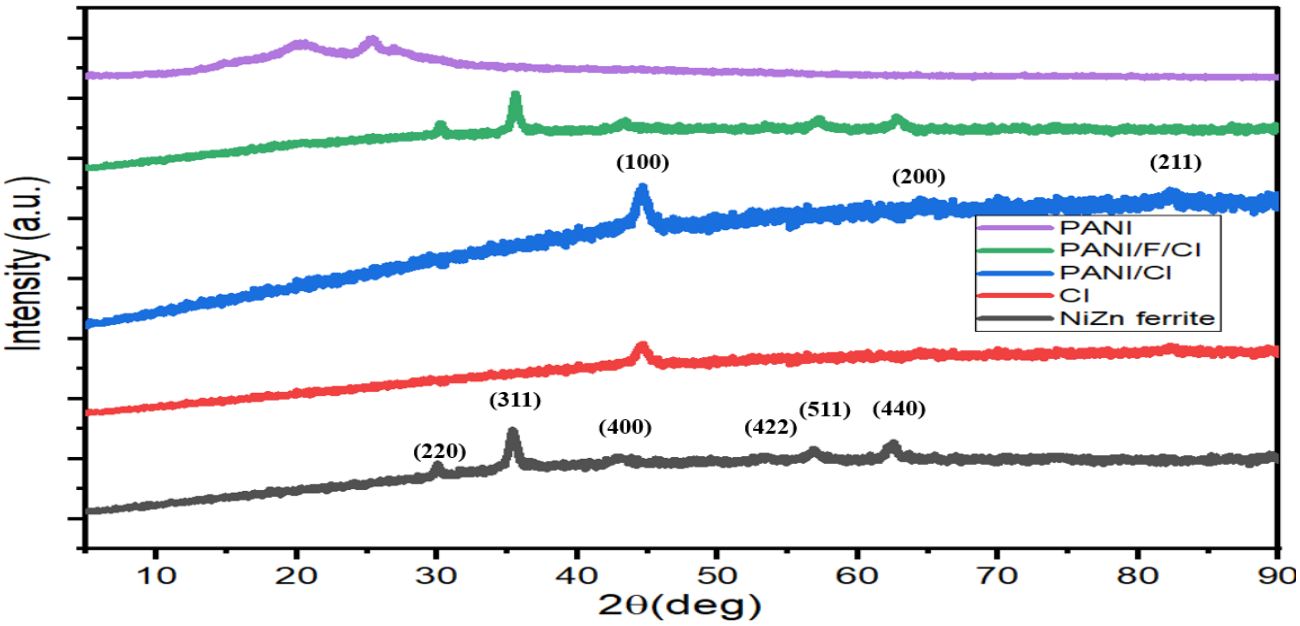

Figure 3.9 – XRD patterns of $Ni_{0.5}Zn_{0.5}Fe_2O_4$, CI, PANI/F/CI, PANI/F/CI nanocomposites and pure PANI

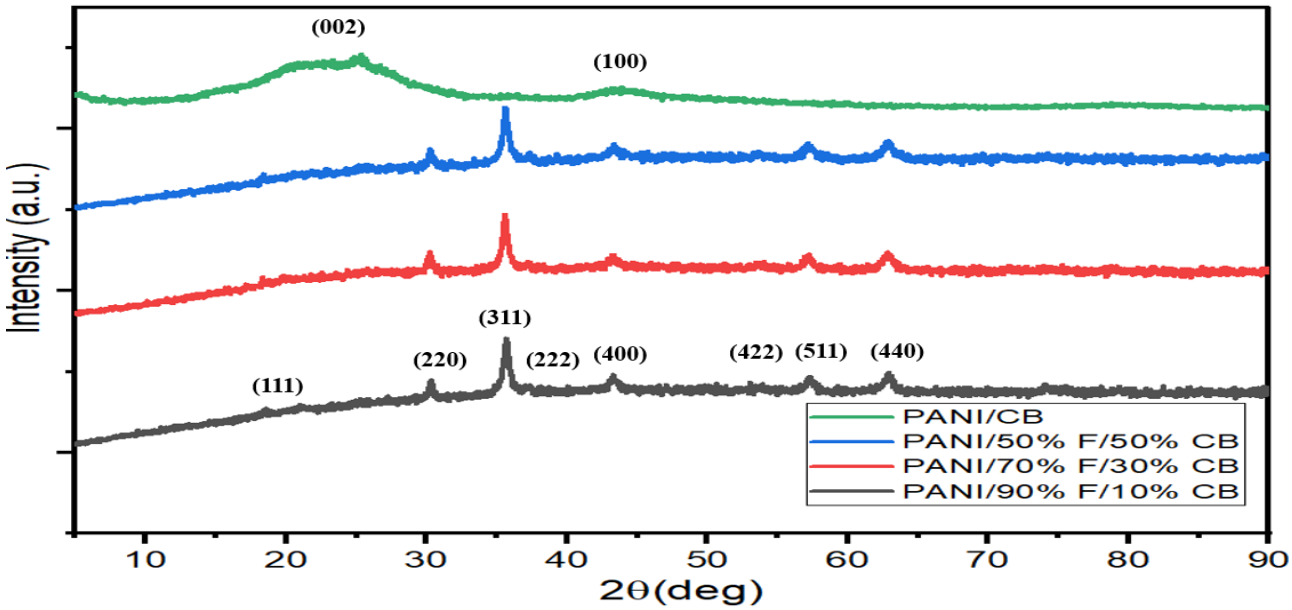

Figure 3.10 – XRD patterns of PANI/F/CB and PANI/CB hybrid nanocomposites

Figure 3.11 shows the XRD patterns of the HF and PANI/HF nanocomposites. The characteristic peaks of PANI/HF nanocomposites showed matching the characteristic

peaks of the $BaNiZnFe_{16}O_{27}$ core as cited above. This was shown when the $BaNiZnFe_{16}O_{27}$ magnetic core was coated with PANI. The hexagonal structure of the $BaNiZnFe_{16}O_{27}$ magnetic core remained intact. The XRD patterns of the PANI/$BaNiZnFe_{16}O_{27}$ nanocomposites displayed crystalline peaks because of the existence of $BaNiZnFe_{16}O_{27}$ in these nanocomposites. The XRD patterns of PANI/SF/HF and PANI/SF/HF/CB hybrid nanocomposite are shown in Figure 3.11. For the PANI/SF/HF and PANI/SF/HF/CB patterns, eleven diffraction peaks were detected, which conform to (110), (1010), (116), (0114), (107), (203), (208), (209), (2015), (2111) and (220), respectively.

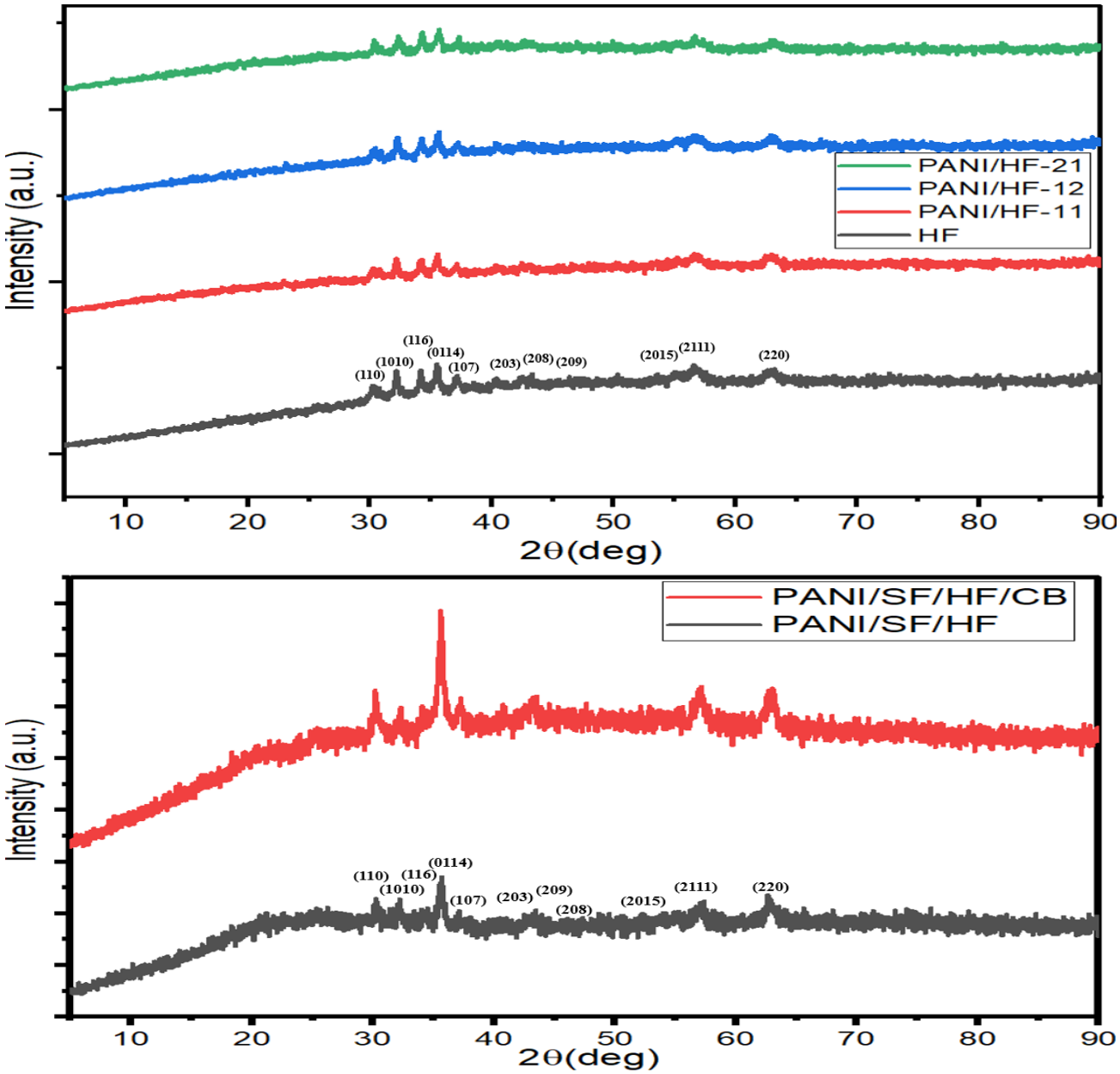

Figure 3.11 – XRD patterns of HF, PANI/HF, PANI/SF/HF and PANI/SF/HF/CB

3.2 FTIR spectra

3.2.1 FTIR spectra of ferrites prepared by the ceramic sintering technique

Figure 3.12 displays the FTIR spectra of the undoped and doped ferrites. The peaks within the range (550–590 cm^{-1}) were due to the stretching vibration of (Fe-O) at the tetrahedral sites, while the peaks located in the sites less than 460 cm^{-1} were due to the stretching vibration of (Fe-O) at the octahedral sites [115].

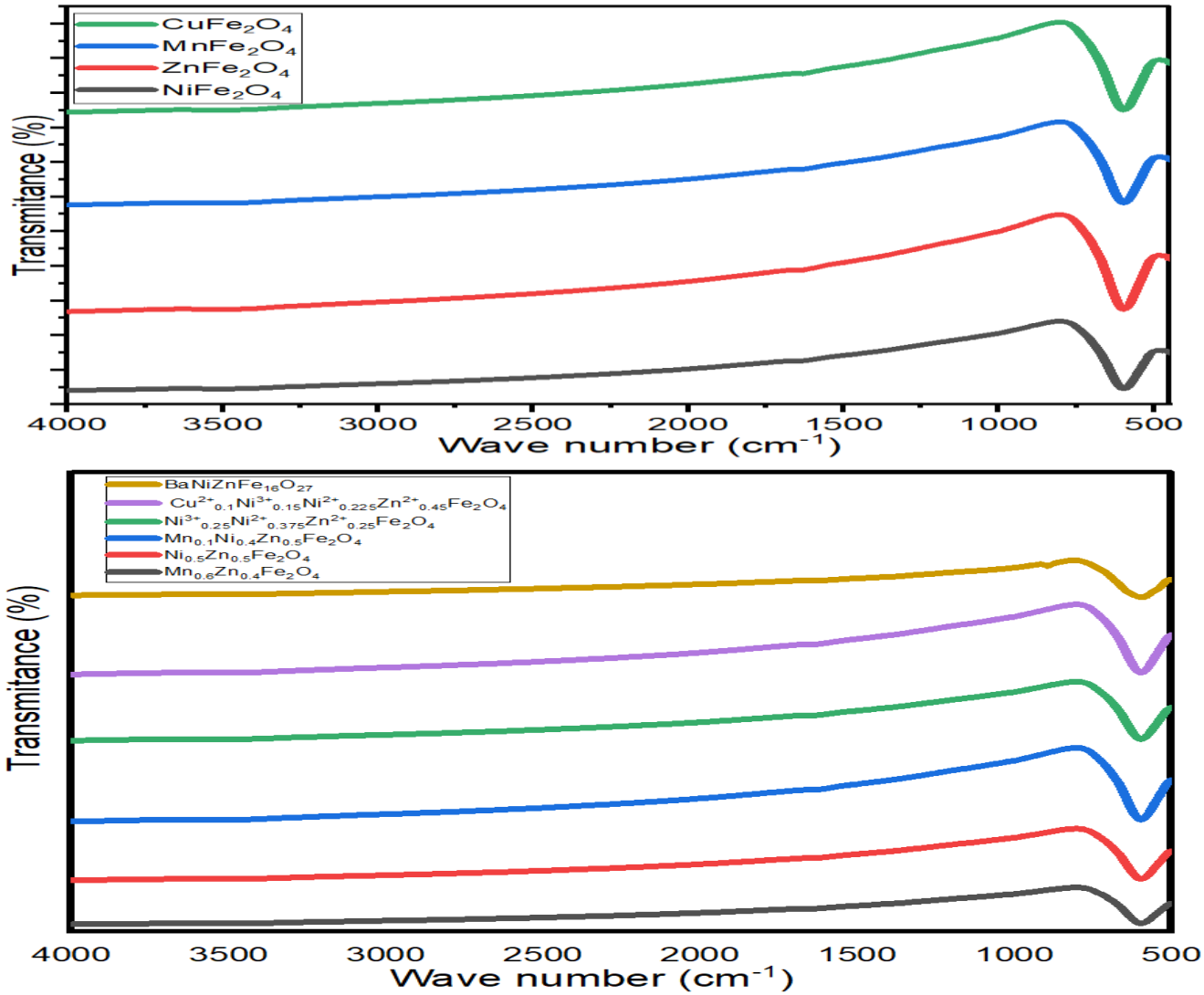

Figure 3.12 – FTIR spectra of undoped and doped ferrites

3.2.2 FTIR spectra of ferrite samples prepared by citrate precursor and self-combustion technique

Figure 4.13 and Figures 4.14 show the FTIR spectra of $Ni_{0.5}Zn_{0.5}Fe_2O_4$ prepared by citrate precursor and self-combustion technique. The peaks within the range (560–590 cm^{-1}) were due to the stretching vibration of (Fe-O) at the tetrahedral sites, while the peaks located in the sites less than 460 cm^{-1} were due to the stretching vibration of (Fe-O) at the octahedral sites [115]. In addition, the peaks within the range (1630–1640 cm^{-}

[1]) were due to the stretching vibration of C=O and the peaks at 2348 cm^{-1} and 3452 cm^{-1} referred to O-H stretching vibration [116,117].

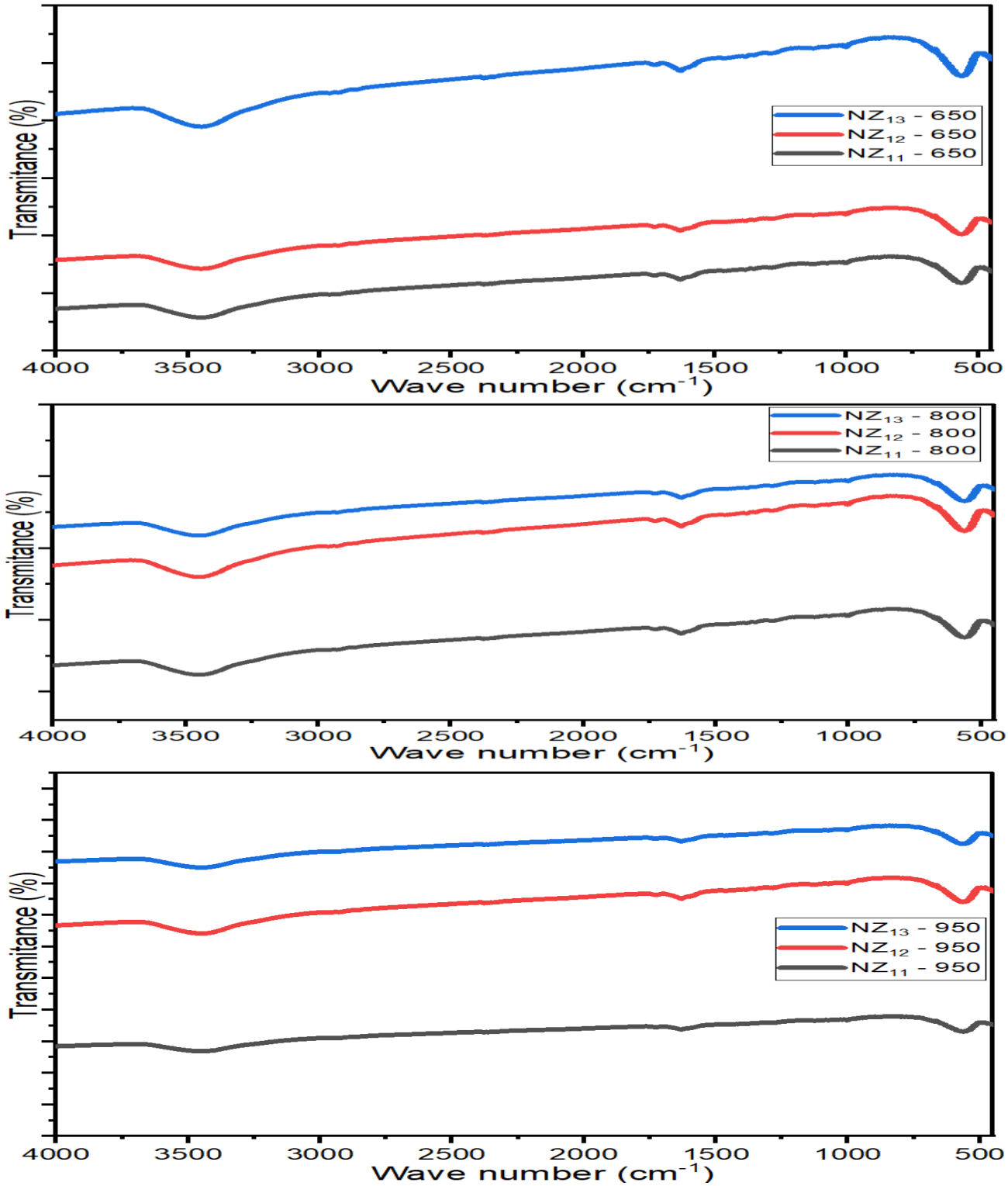

Figure 3.13 – FTIR spectra of $Ni_{0.5}Zn_{0.5}Fe_2O_4$ at the different molar ratios of the metal ion/citrate acid (1:1, 2:1 and 3:1) at the different calcination temperatures (650, 800 and 950°C)

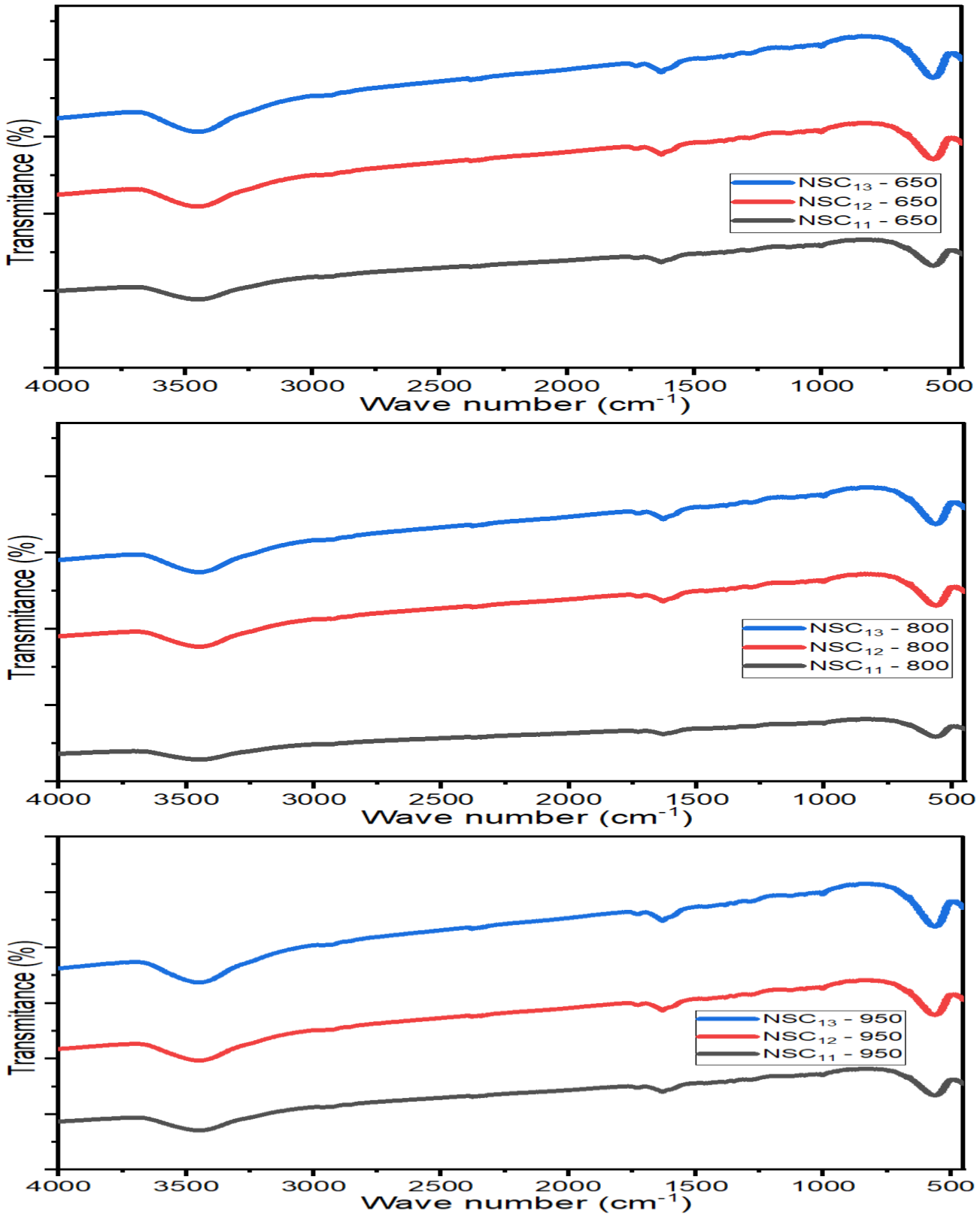

Figure 3.14 – FTIR spectra of $Ni_{0.5}Zn_{0.5}Fe_2O_4$ at the different aqueous solutions of PVA (1%, 4% and 6%) at the different calcination temperatures (650, 800 and 950°C)

3.2.3 FTIR spectra of carbon black, activated carbon, graphite and carbonyl iron

Figure 3.15 exhibits the FTIR spectra of CB, AC, C and CI. The peak at 1630.4 cm^{-1} was due to the stretching vibration of C=O, while the peaks at 2348 cm^{-1} and 3452 cm^{-1} were due to the stretching vibration of O-H [116,117].

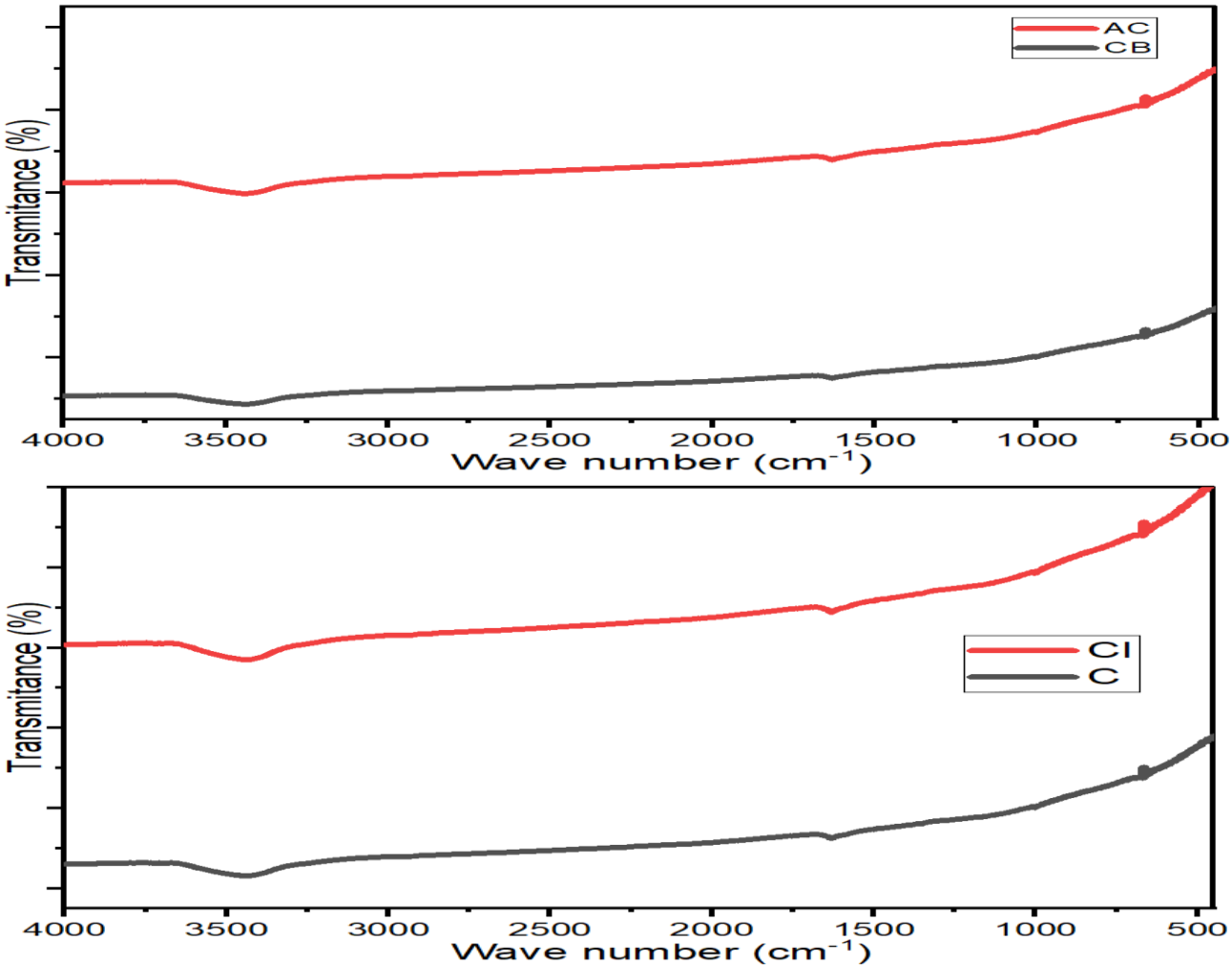

Figure 3.15 – FTIR spectra of CB and AC, C and CI

3.2.4 FTIR spectra of PANI-based nanocomposites

Figures 3.16 exhibits the FTIR spectra of the PANI-based nanocomposites. The peaks within the range (1568–1580 cm^{-1}) and (1475–1489 cm^{-1}) were due to the C=N and C=C stretching modes of vibration for the quinonoid and benzenoid units of the polymer, while the peaks within the range (1290 –1298 cm^{-1}) and (1475–1489 cm^{-1}) were due to N-H bending and asymmetric C-H stretching of the benzenoid ring, respectively [118,119]. Finally, the peaks within the range (1113 –1125 cm^{-1}) and (790–800 cm^{-1}) were due to N-H bending and asymmetric C-H stretching of the benzenoid ring, respectively [87,113]. In addition, the characteristic peaks within the range (563–585 cm-1) of the PANI-based nanocomposites matched the characteristic peak of ferrite, as cited

above. This indicates the stretching vibration of (Fe-O), which confirms the formation of the metal-oxygen in the PANI-based nanocomposites.

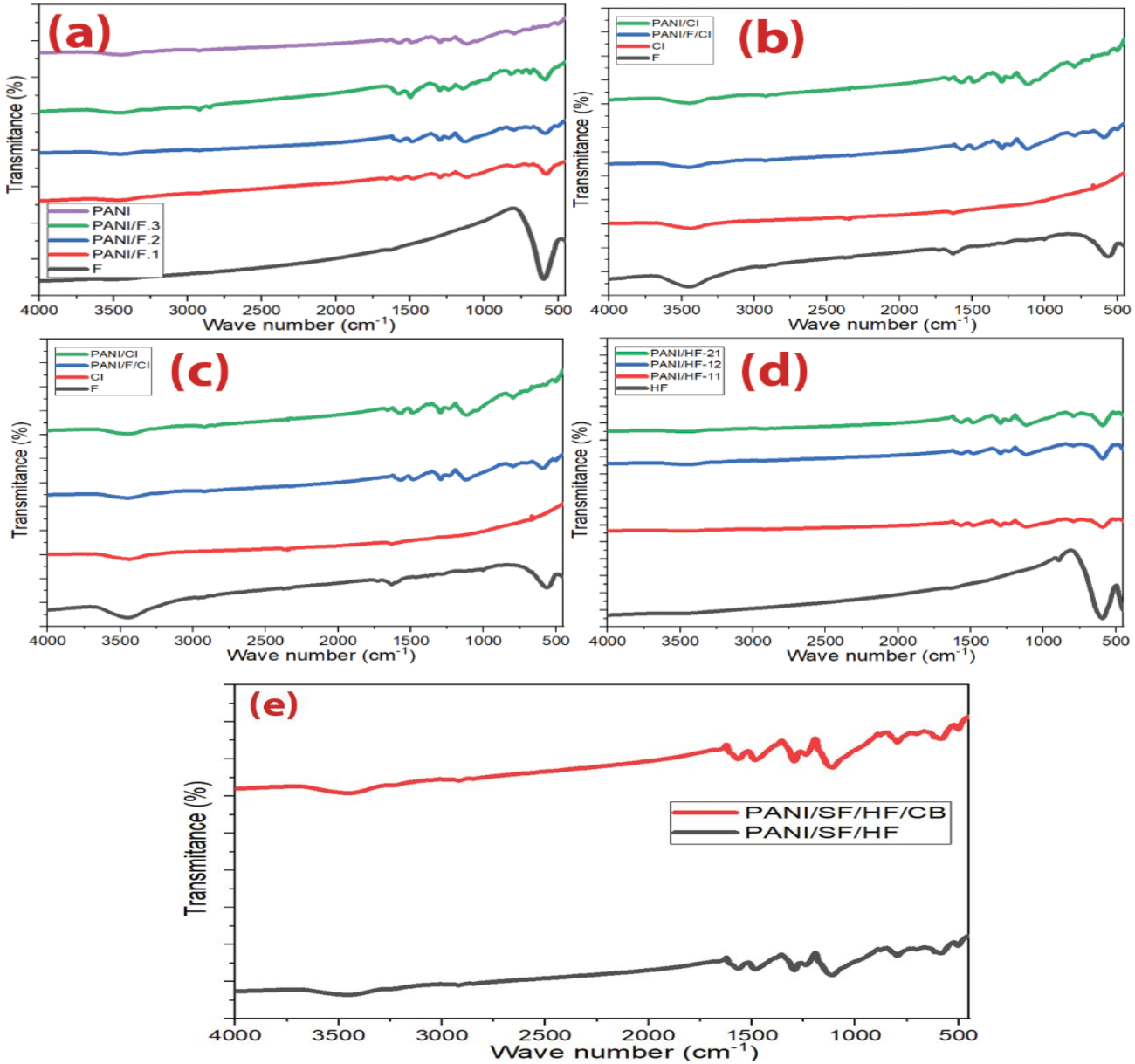

Figure 3.16 – FTIR spectra of (a) $Ni^{3+}_{0.25}Ni^{2+}_{0.375}Zn^{2+}_{0.25}Fe_2O_4$, PANI/$Ni^{3+}_{0.25}Ni^{2+}_{0.375}Zn^{2+}_{0.25}Fe_2O_4$ nanocomposites and pure PANI, (b) $Ni_{0.5}Zn_{0.5}Fe_2O_4$, CI, PANI/CI and PANI/F/CI nanocomposites, (c) PANI/CB and PANI/F/CB nanocomposites, (d) HF and PANI/HF nanocomposites and (e) PANI/SF/HF and PANI/SF/HF/CB hybrid nanocomposites

3.3 Energy-dispersive X-ray spectroscopy (EDX) analysis

3.3.1 EDX analysis for some spinel ferrites and hexagonal ferrite

EDX analysis of $Ni^{3+}_{0.25}Ni^{2+}_{0.375}Zn^{2+}_{0.25}Fe_2O_4$, $Ni_{0.5}Zn_{0.5}Fe_2O_4$ nanoparticles prepared by citrate precursor and self-combustion methods and $BaNiZnFe_{16}O_{27}$ nanoparticles is shown

in Figure 3.17 and Table 3.4. The presence of C, O, Cl, S, Fe, Ni, Al and Zn elements in the spinel ferrites EDX spectrums was noticed. On the other hand, the presence of C, O, Ba, Cl, Fe, Ni, and Zn elements in the hexagonal ferrite ($BaNiZnFe_{16}O_{27}$) EDX spectrum was found.

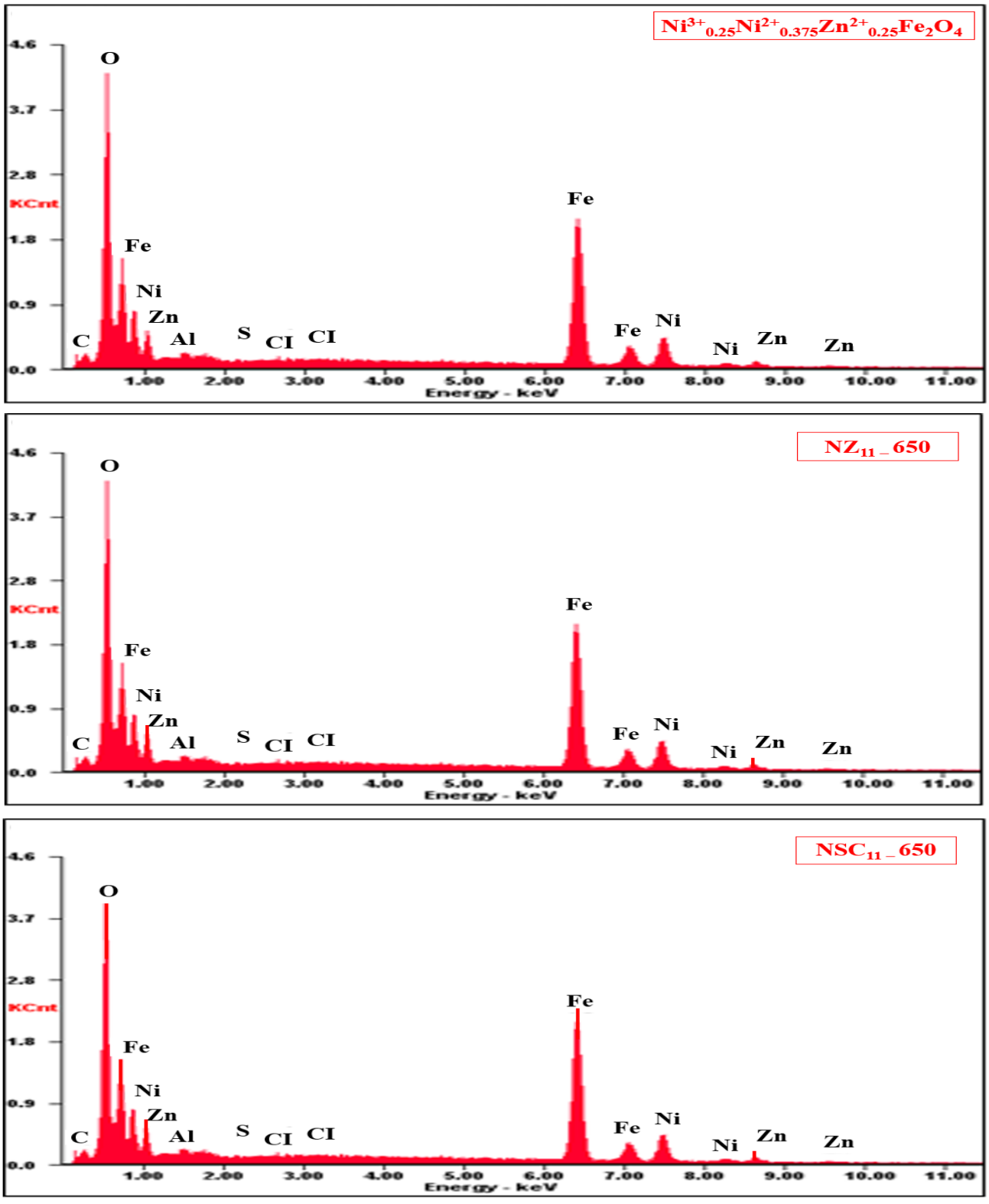

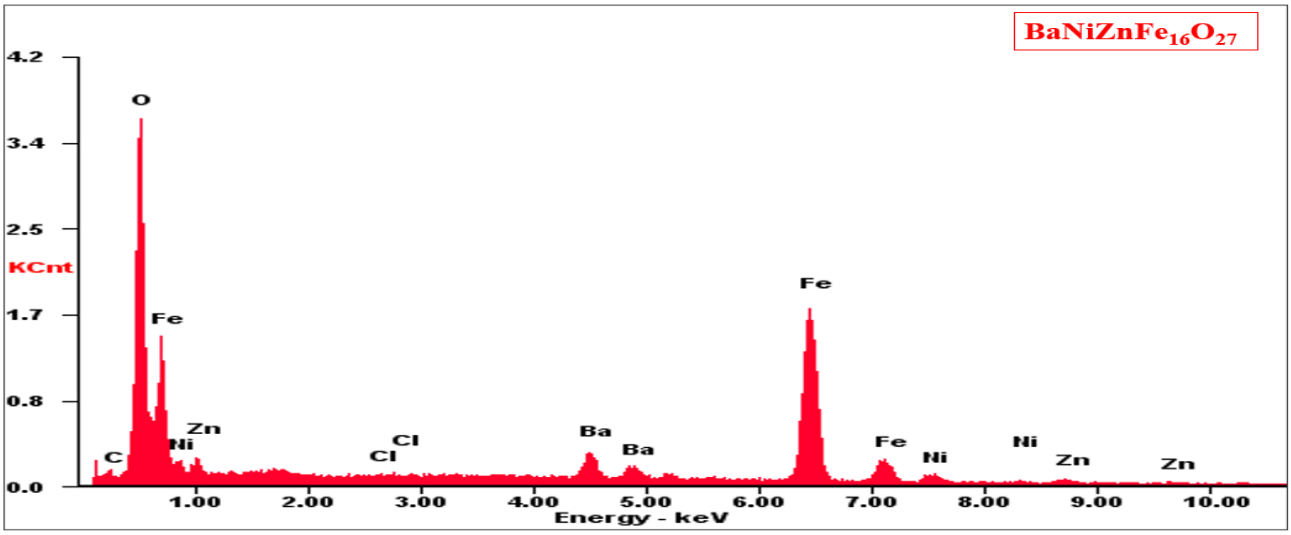

Figure 3.17 – EDX of spinel ferrites and hexagonal ferrite

Table 3.4 – EDX element composition of spinel ferrites and hexagonal ferrite

Element	C	Cl	O	S	Ba	Al	Fe	Ni	Zn
$Ni^{3+}_{0.25}Ni^{2+}_{0.375}Zn^{2+}_{0.25}Fe_2O_4$ (wt%)	3.28	0.15	19.28	0.03	-	0.39	53.04	18.02	5.81
$NZ_{11\_}650$ (wt%)	3.30	0.13	19.26	0.02	-	0.41	53.02	13.04	10.82
$NSC_{11\_}650$ (wt%)	3.50	0.17	18.92	0.01	-	0.39	54.01	12.79	10.21
$BaNiZnFe_{16}O_{27}$ (wt%)	1.8	0.16	20.72	-	9.88	-	59.34	4.24	3.86

3.3.2 EDX analysis of PANI-based nanocomposites

EDX analysis of PANI and PANI-based nanocomposites are shown in Figures (3.18-3.19) and Table 3.5. The presence of C, O, S and Cl elements in the PANI EDX spectrum is found. The elemental Cl and S presence can be attributed to doping agents' hydrochloric acid and sodium dodecyl sulfate. On the other hand, the presence of C, O, Cl, S, Fe, Ba, Zn, Al and Ni elements in the PANI-based nanocomposites EDX spectrum was observed. One can observe with increasing the PANI in nanocomposites, the carbon will increase and iron will decrease inside them, which will impact its EMI shielding and MA properties, as will be clarified later.

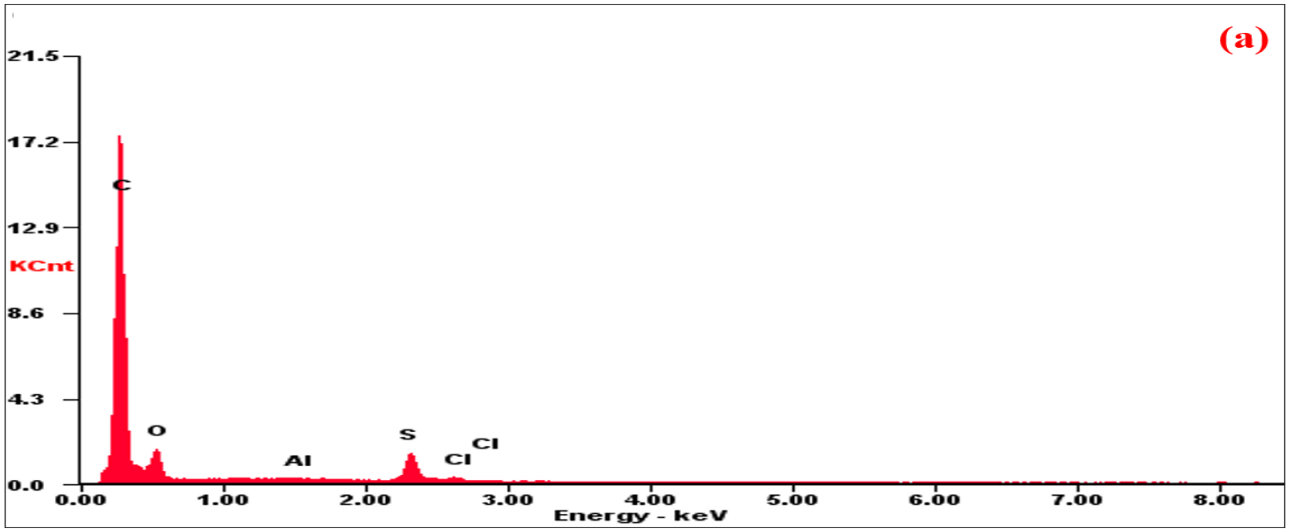
(a)
21.5
17.2
12.9
KCnt
8.6
4.3
0.0
C
O
Al
S
Cl
Cl
0.00
1.00
2.00
3.00
4.00
5.00
6.00
7.00
8.00
Energy - keV

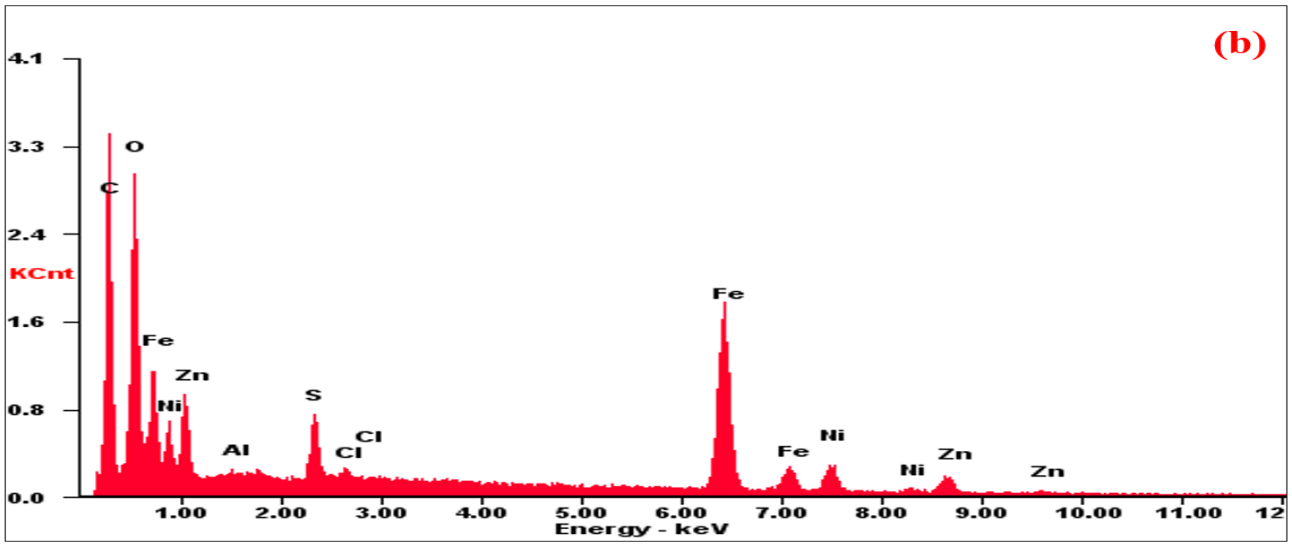
(b)
4.1
3.3
2.4
KCnt
1.6
0.8
0.0
C
O
Fe
Zn
Ni
Al
S
Cl
Cl
Fe
Ni
Ni
Zn
Zn
1.00
2.00
3.00
4.00
5.00
6.00
7.00
8.00
9.00
10.00
11.00
12
Energy - keV

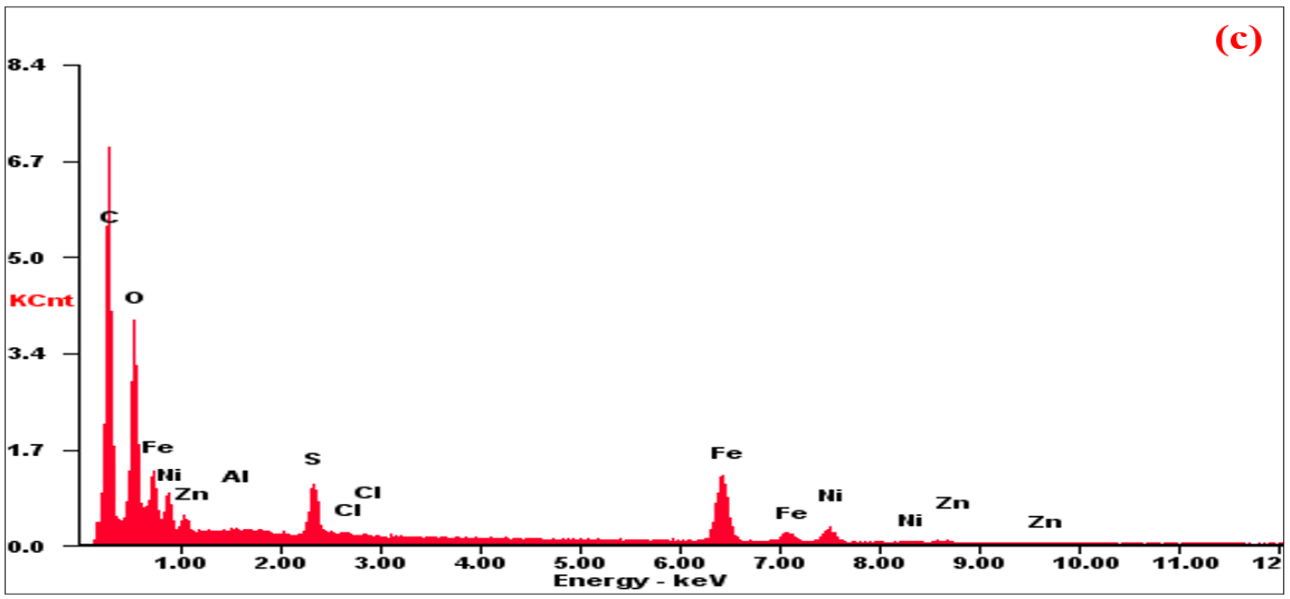
(c)
8.4
6.7
5.0
KCnt
3.4
1.7
0.0
C
O
Fe
Ni
Zn
Al
S
Cl
Cl
Fe
Ni
Ni
Zn
Zn
1.00
2.00
3.00
4.00
5.00
6.00
7.00
8.00
9.00
10.00
11.00
12
Energy - keV

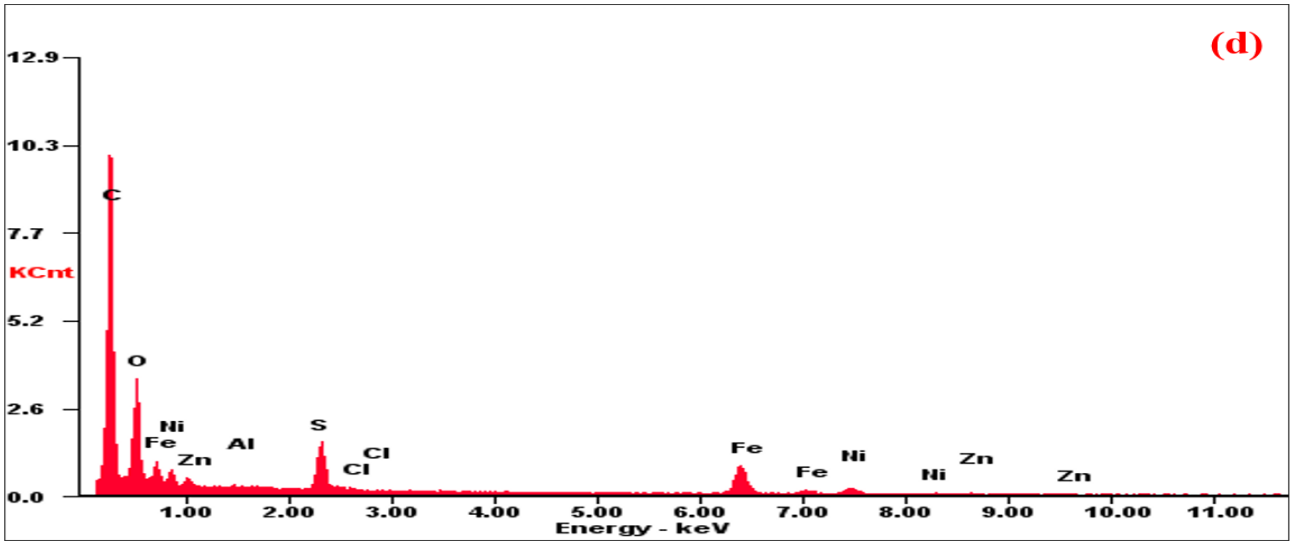

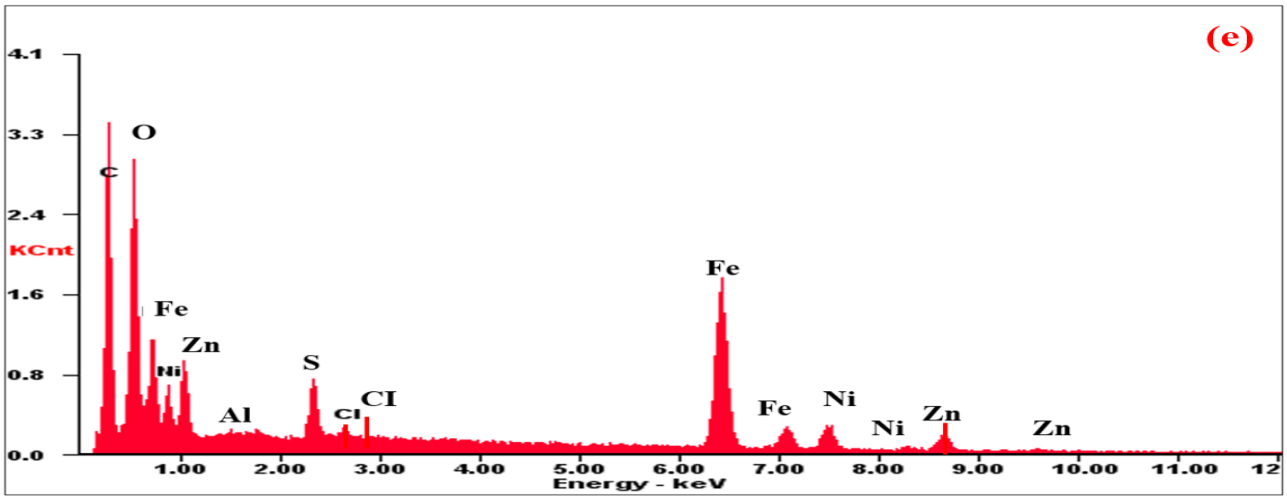

Figure 3.18 – EDX of (a) PANI, (b) PANI/F.1, (c) PANI/F.2, (d) PANI/F.3 and (e) PANI/F/CI hybrid nanocomposites

Table 3.5 – EDX element composition of PANI and PANI-based nanocomposites

Element	C	Cl	O	S	Al	Fe	Ni	Zn	Ba
PANI (wt%)	84.52	0.45	11.81	3.17	0.05	0	0	0	0
PANI/F.1 (wt%)	37.29	0.32	15.2	1.75	0.12	28.6	7.67	9.05	0
PANI/F.2 (wt%)	51.76	0.22	19.27	2.42	0.08	17.95	6.32	1.98	0
PANI/F.3 (wt%)	63.01	0.18	17.30	2.93	0.08	11.17	3.96	1.37	0
PANI/F/CI (wt%)	51.72	0.51	19.23	2.02	0.08	17.15	5.32	3.97	0
PANI/HF.1 (wt%)	53.44	0.30	14.63	2.63	0	21.02	2.63	1.60	3.75
PANI/HF.2 (wt%)	59.02	0.67	15.31	3.14	0	15.69	2.29	1.09	2.79

PANI/HF.3 (wt%)	66.91	0.18	15.94	2.91	0	9.65	1.61	0.59	2.21
PANI/SF/HF (wt%)	61.27	0.73	12.42	4.51	0	13.97	4.64	1.42	1.04
PANI/SF/HF/CB (wt%)	75.44	0.85	12.44	3.65	0	4.45	2.31	0.47	0.39

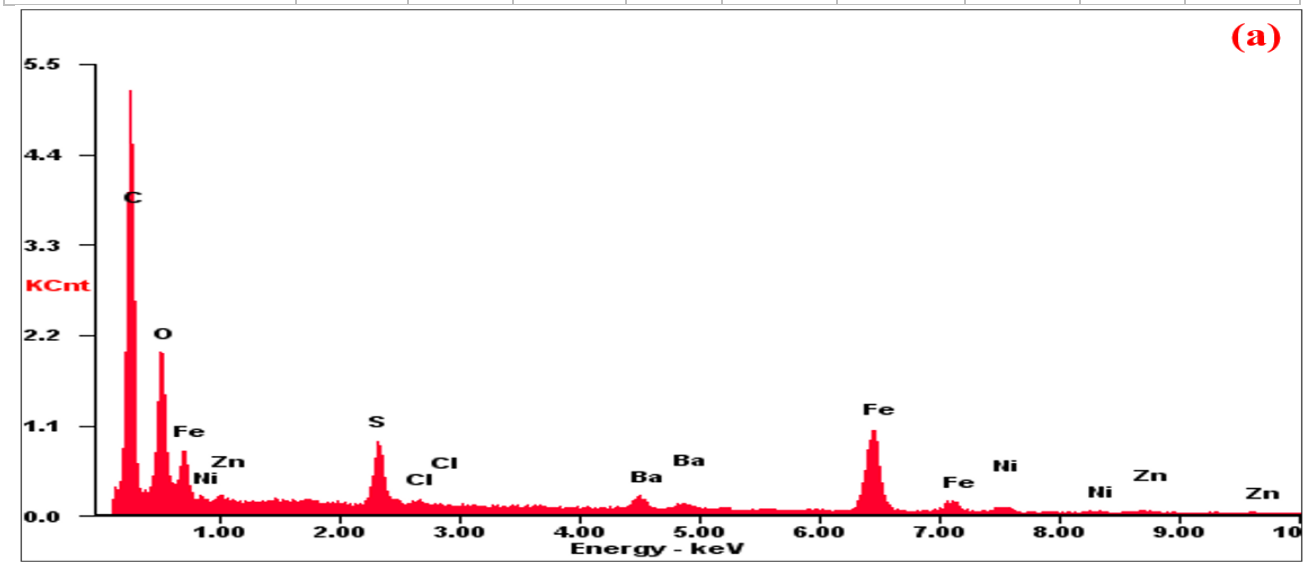

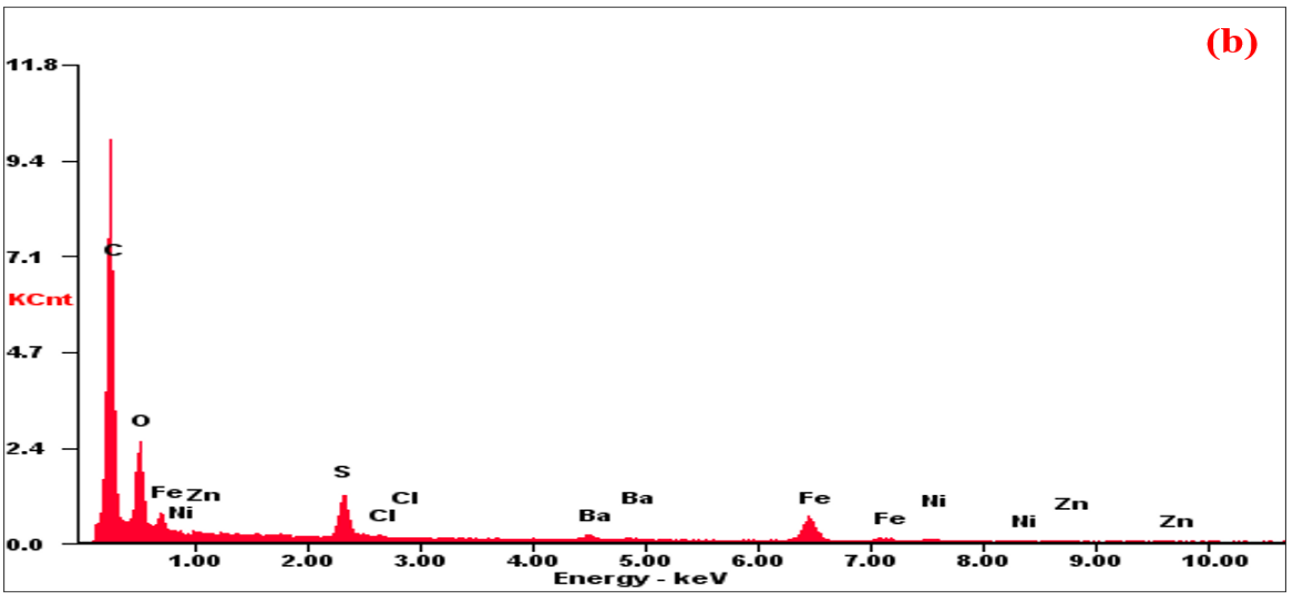

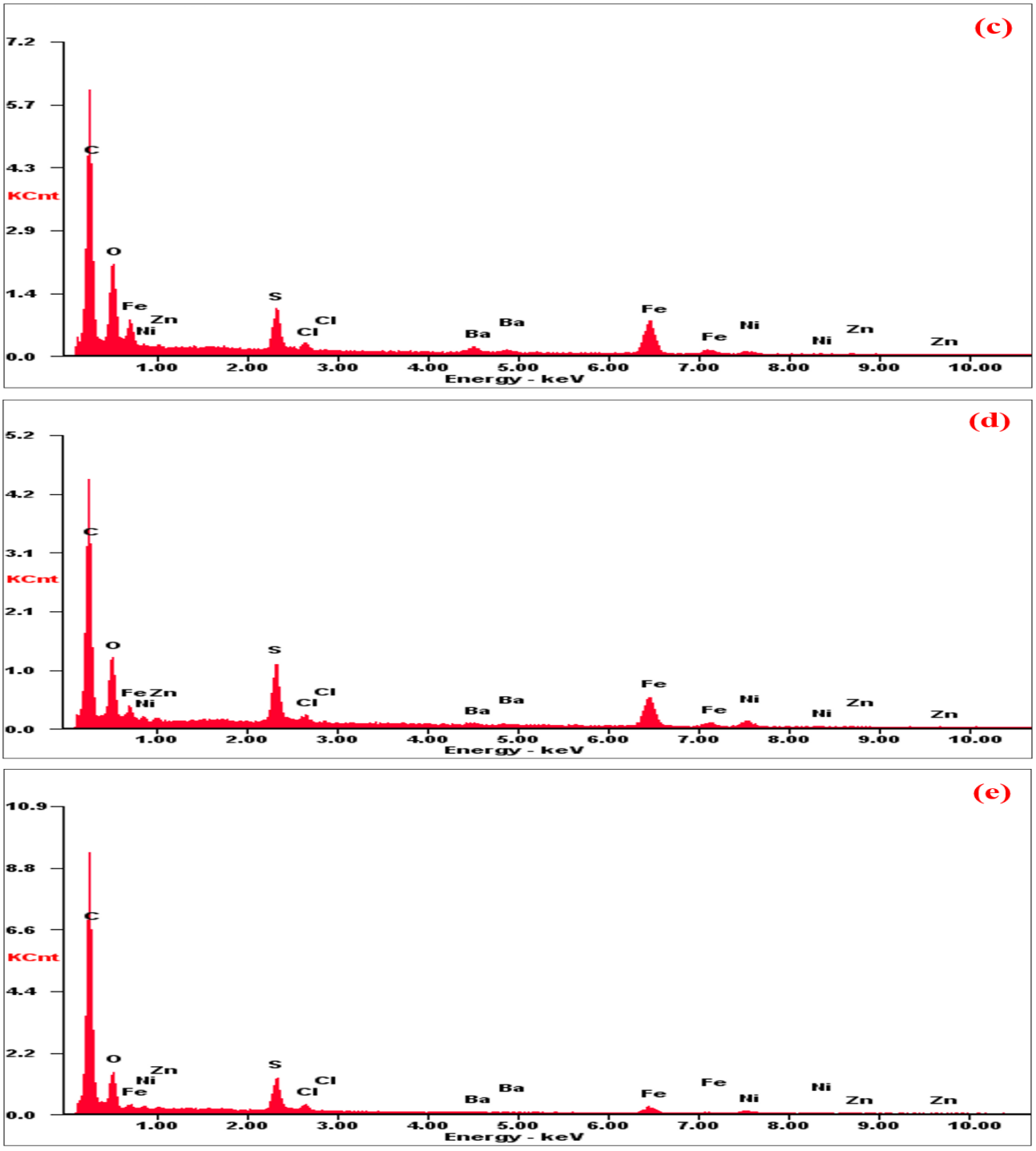

Figure 3.19 – EDX of (a) PANI/HF-11, (b) PANI/HF-21, (c) PANI/HF-12, (d) PANI/SF/HF and (e) PANI/SF/HF/CB hybrid nanocomposites

3.4 Morphology investigations

3.4.1 Morphology investigations for some spinel ferrites and hexagonal ferrite

The morphology of the $Ni^{3+}_{0.25}Ni^{2+}_{0.375}Zn^{2+}_{0.25}Fe_2O_4$, $NZ_{11-}650$, $NSC_{11-}650$ and $BaNiZnFe_{16}O_{27}$ are shown in Figure 3.20. The agglomerated spherical particles of spinel and hexagonal ferrites are noticed. The average diameters of the spherical-shaped

particles are observed for the $Ni^{3+}_{0.25}Ni^{2+}_{0.375}Zn^{2+}_{0.25}Fe_2O_4$, $NZ_{11-}650$, $NSC_{11-}650$ and $BaNiZnFe_{16}O_{27}$ to be ranging between 18–93 nm, 27–63 nm, 18–52 nm, and 15-110 nm, respectively.

3.4.2 Morphology investigations of PANI-based nanocomposites

The morphology of the (a) PANI and PANI/F nanocomposites are shown in Figure 3.21. The combination of rough surface sheets and short rods connected to each other of PANI were noticed, distributed in the range between 60–220 nm. After coating by polyaniline, a continued overlayer of PANI was created on the $Ni^{3+}_{0.25}Ni^{2+}_{0.375}Zn^{2+}_{0.25}Fe_2O_4$ nanoparticles. The $Ni^{3+}_{0.25}Ni^{2+}_{0.375}Zn^{2+}_{0.25}Fe_2O_4$ nanocomposites images exhibit that the $Ni^{3+}_{0.25}Ni^{2+}_{0.375}Zn^{2+}_{0.25}Fe_2O_4$ nanoparticles were coated with PANI to create the composite structure. In addition to that, agglomerated rod-like particle formation was noticed in the PANI/F nanocomposites, and this was due to the increased percentage of PANI content in the nanocomposites. One can observe that the percentage of PANI in the PANI/F hybrid nanocomposites has a significant role in specifying the definitive morphology of the nanocomposite, which will impact its EMI shielding and MA properties, as will be clarified later.

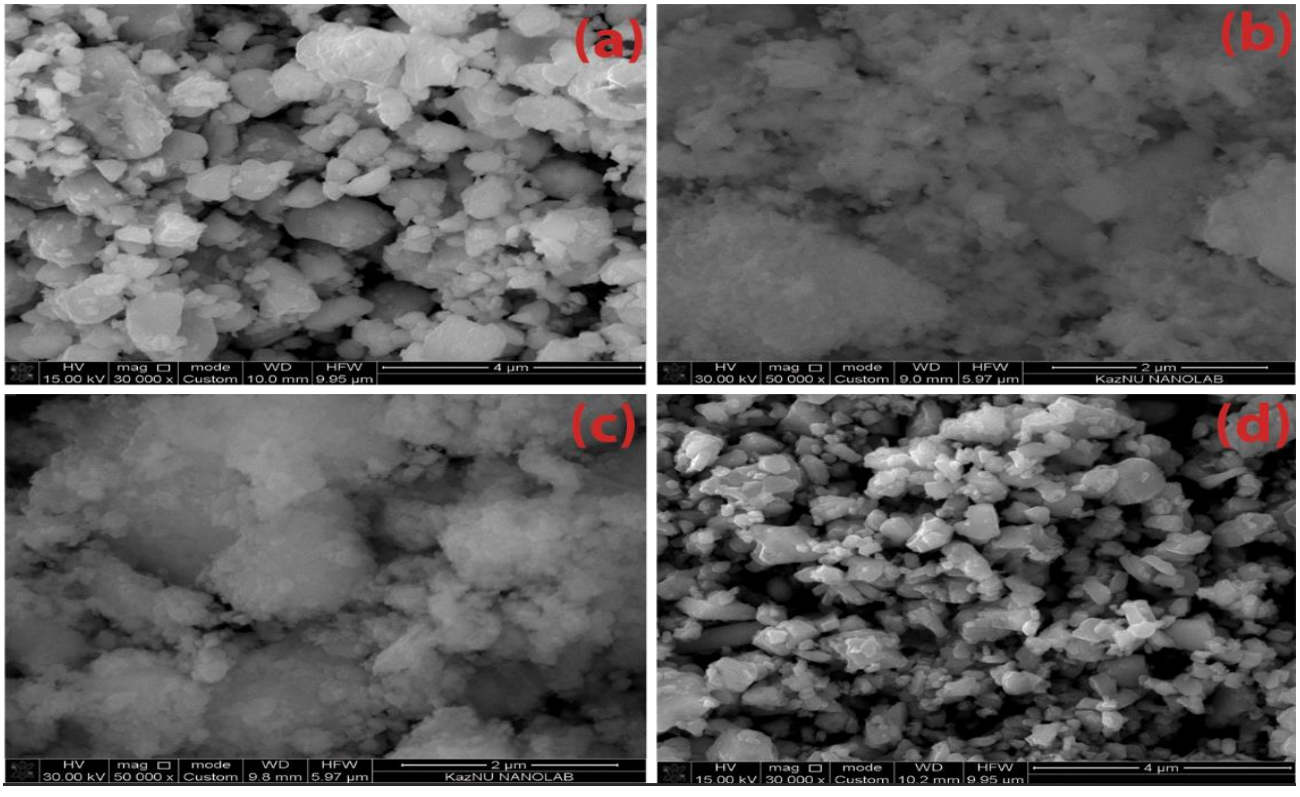

Figure 3.20 – SEM images of (a) $Ni^{3+}_{0.25}Ni^{2+}_{0.375}Zn^{2+}_{0.25}Fe_2O_4$, (b) $NZ_{11-}650$, (c) $NSC_{11-}650$, and (d) $BaNiZnFe_{16}O_{27}$

The morphology of the CI and PANI/F/CI composite is shown in Figure 3.22. The spherical particles of carbonyl iron are observed with average diameters to be ranging

between 0.2–2.4 μm. On the other hand, after coating with polyaniline, a continued overlayer of PANI is created on the CI and $Ni_{0.5}Zn_{0.5}Fe_2O_4$ nanoparticles' surface.

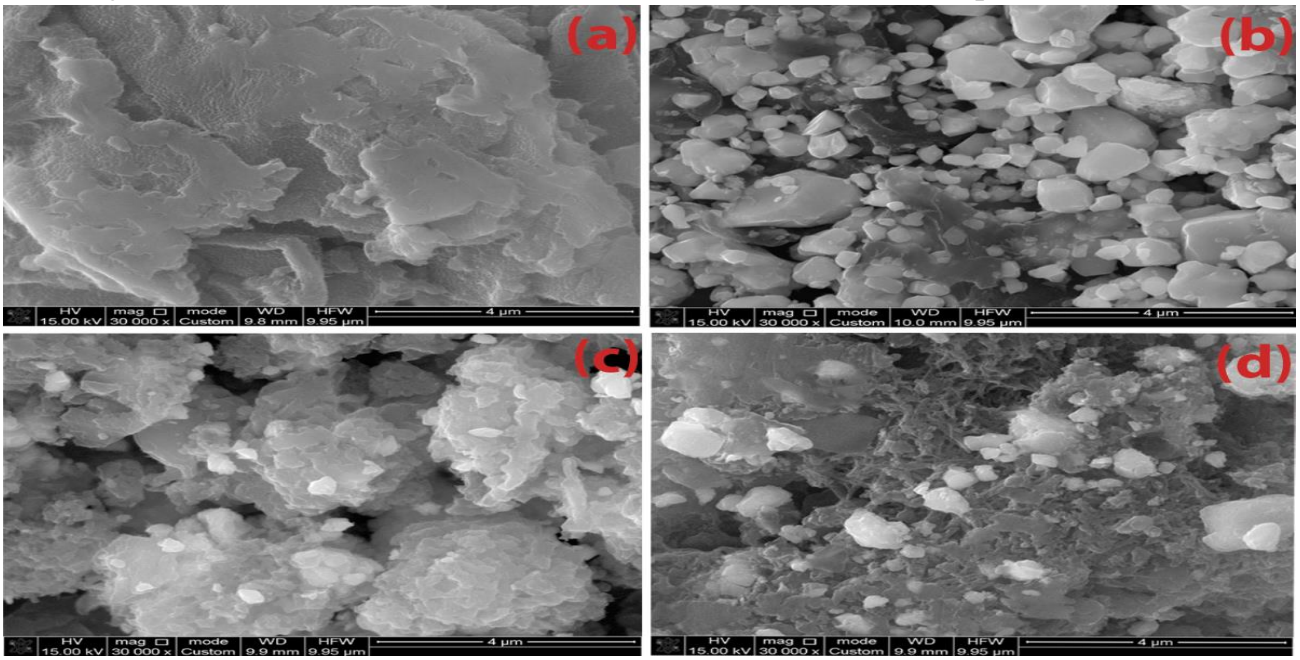

Figure 3.21 – SEM images of (a) PANI, (b) PANI/F.1, (c) PANI/F.2 and (d) PANI/F.3

The morphology of various samples of PANI/HF hybrid nanocomposites is shown in Figure (3.23–3.24). After coating by polyaniline, a continued overlayer of PANI is created on the $BaNiZnFe_{16}O_{27}$ nanoparticles' surface. The $BaNiZnFe_{16}O_{27}$ nanocomposite images exhibit that the $BaNiZnFe_{16}O_{27}$ nanoparticles are coated with PANI to create the composite structure. In addition, agglomerated rod-like particle formation is noticed in the PANI/HF hybrid nanocomposites. This is due to the increased percentage of PANI content in the nanocomposites. One can notice that the percentage of PANI in the PANI/HF hybrid nanocomposites has a significant role in specifying the definitive morphology of the nanocomposite, which will affect its EMI shielding and MA conduct, as will be explained later.

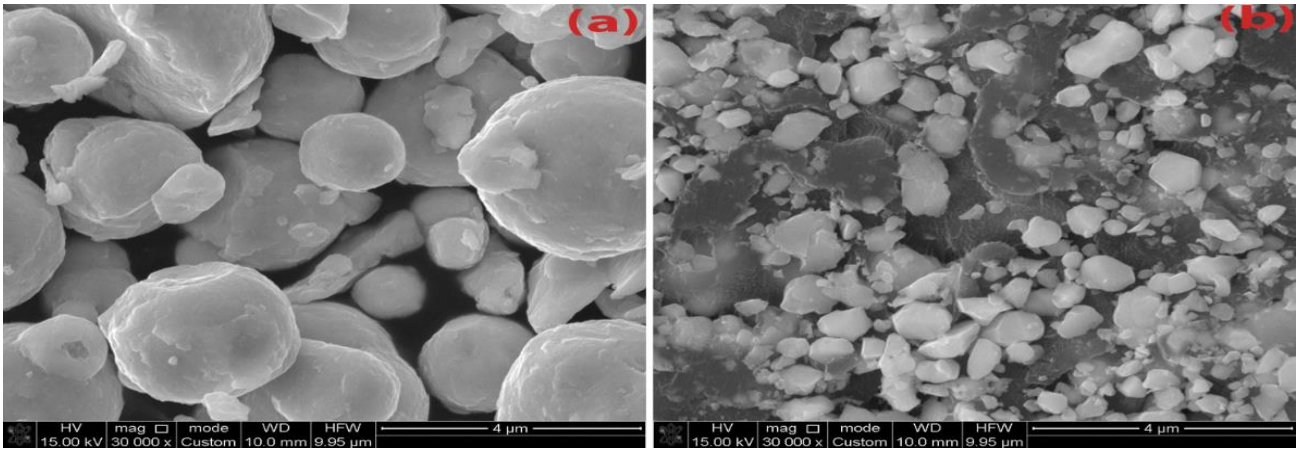

Figure 3.22 – SEM images of (a) CI and (c) PANI/F/CI composite

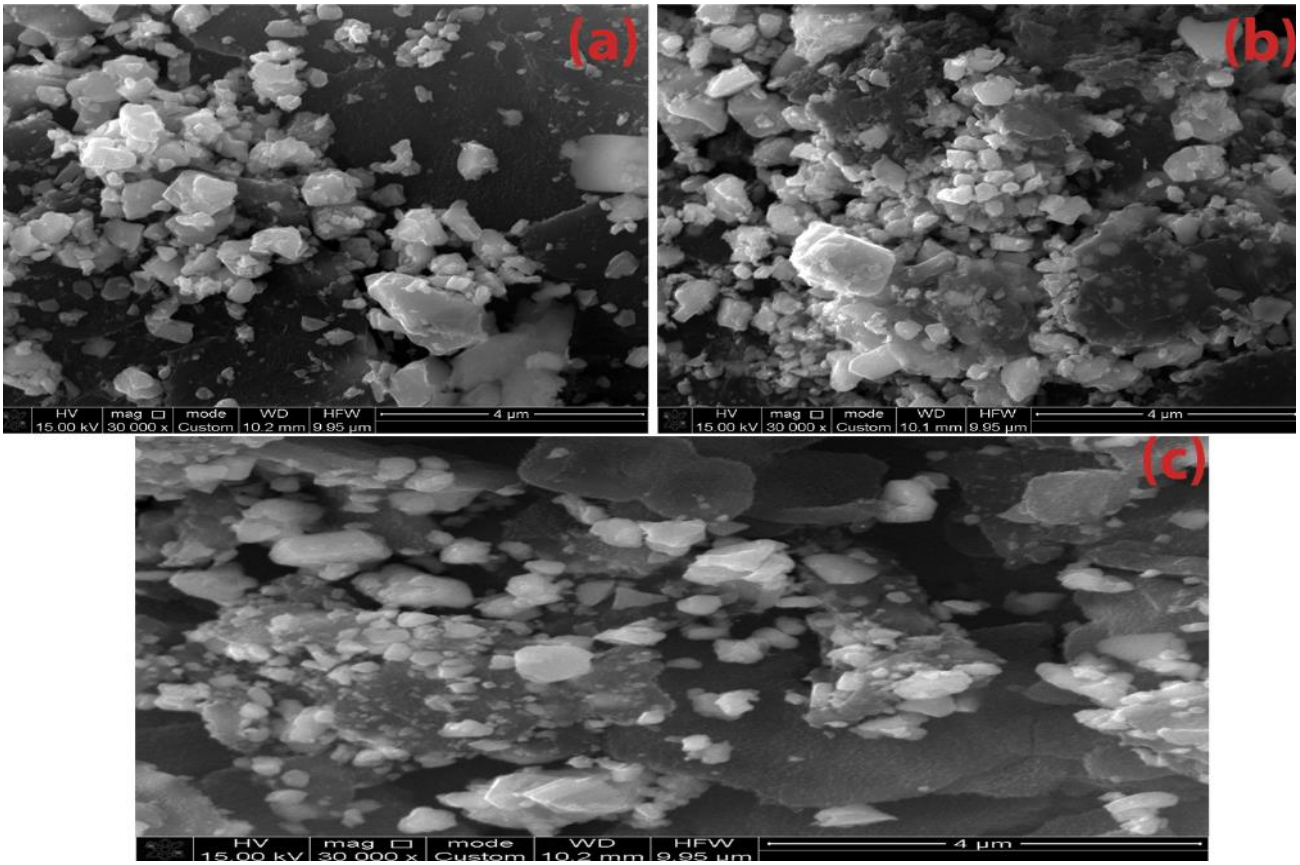

Figure 3.23 – SEM images of PANI/HF.1, PANI/HF. 2 and PANI/HF.3 nanocomposites

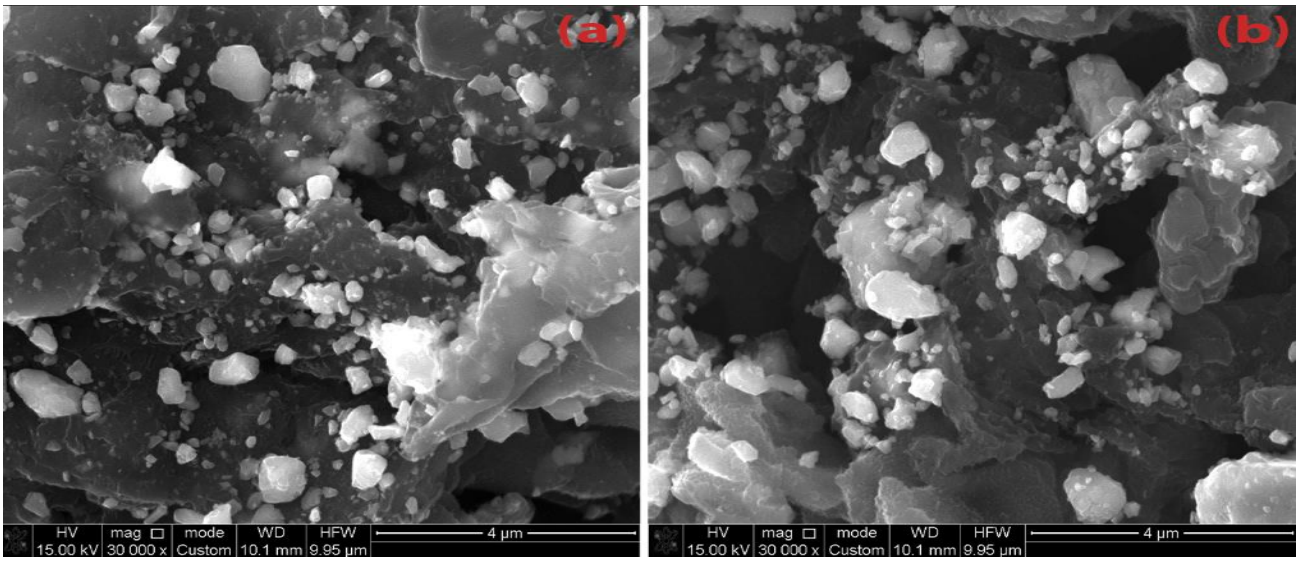

Figure 3.24 – SEM images of PANI/SF/HF and PANI/SF/HF/CB nanocomposites

3.5 TGA analysis

3.5.1 TGA analysis of PANI-based nanocomposites

The TGA curves of the $Ni^{3+}_{0.25}Ni^{2+}_{0.375}Zn^{2+}_{0.25}Fe_2O_4$, $Ni_{0.5}Zn_{0.5}Fe_2O_4$, $BaNiZnFe_{16}O_{27}$, PANI/$Ni^{3+}_{0.25}Ni^{2+}_{0.375}Zn^{2+}_{0.25}Fe_2O_4$, PANI/CB, PANI/F/CB, PANI/F/CI, PANI/$BaNiZnFe_{16}O_{27}$, PANI/SF/HF and PANI/SF/HF/CB are shown in Figure 3.25.

$Ni^{3+}_{0.25}Ni^{2+}_{0.375}Zn^{2+}_{0.25}Fe_2O_4$, $Ni_{0.5}Zn_{0.5}Fe_2O_4$, and $BaNiZnFe_{16}O_{27}$ nanoparticles, no mass loss is noticed over the whole temperature range. PANI loses 4.87% of its weight in the field of 110–130 °C, which is due to the evaporation of moisture in the PANI. The thermal decomposition of the PANI is shown in the range of 230–1000 °C and had a big weight loss of 65.12%. On the other hand, PANI-based nanocomposites can be evaluated from the TGA curves, as shown in Table 3.6.

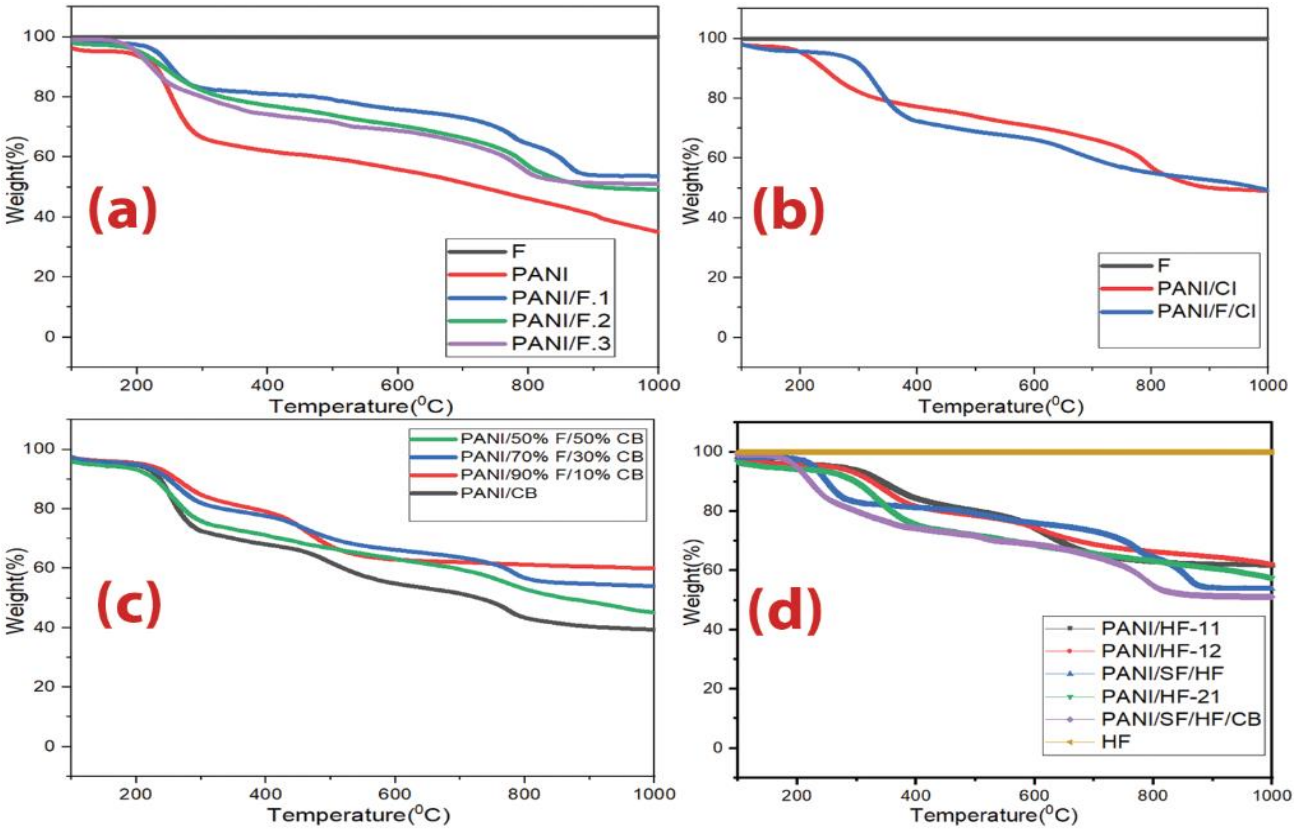

Figure 3.25 – TGA thermograms of (a) $Ni^{3+}_{0.25}Ni^{2+}_{0.375}Zn^{2+}_{0.25}Fe_2O_4$, PANI/$Ni^{3+}_{0.25}Ni^{2+}_{0.375}Zn^{2+}_{0.25}Fe_2O_4$ nanocomposites and pure PANI, (b) $Ni_{0.5}Zn_{0.5}Fe_2O_4$, PANI/CI and PANI/F/CI nanocomposites, (c) PANI/CB and PANI/F/CB hybrid nanocomposites and (d) HF, PANI/, PANI/SF/HF and PANI/SF/HF/CB nanocomposites

Table 3.6 – TGA measurements of the PANI-based nanocomposites

Sample	Calculated PANI percentage	Evaluated PANI percentage utilizing TGA
PANI/F.1	50%	53.8%
PANI/F.2	66.7%	49.5%
PANI/F.3	75%	51.2%
PANI/CI	50%	49.0%
PANI/F/CI	50%	49.5%
PANI/CB	50%	39.7%

PANI/90%F/10%CB	50%	45.4%
PANI/70%F/30%CB	50%	54.3%
PANI/50%F/50%CB	50%	60.1%
PANI/HF-11	50%	61.7%
PANI/HF-12	33.3%	62.4%
PANI/HF-21	66.7%	58.5%
PANI/SF/HF	50%	53.8%
PANI/SH/HF/CB	50%	51.3%

3.6 Microwave absorption properties of prepared samples

3.6.1 Microwave absorption properties of ferrite samples prepared by the ceramic sintering technique

Several variables that affect MA properties were studied, as follows: effect of ferrite type, substitution with several metal ions, the concentration of metal ions, absorbent layer thickness, and loading percentage of ferrite in the paraffin matrix.

3.6.1.1 Microwave absorption properties of undoped ferrites

EMI shielding and MA properties of $NiFe_2O_4$, $ZnFe_2O_4$, $MnFe_2O_4$ and $CuFe_2O_4$ were studied. The results of this investigation are exhibited in Figure 3.26. The thickness of the prepared samples was 6 mm. The results showed that the absorbers with a loading percentage within a paraffin matrix of 75% w/w had weak reflection loss and low shielding efficiency. Hence, substitutions with suitable metal ions are needed to improve microwave absorption properties.

3.6.1.2 Microwave absorption properties of doped ferrites

EMI shielding and MA properties of $Mn_xZn_{(1-x)}Fe_2O_4$ (x= 0.3, 0.6 and 0.9), $Ni_xZn_{(1-x)}Fe_2O_4$ (x= 0.25, 0.5 and 0.75), $Ni_{(0.4+x)}Zn_{(0.5-x)}Mn_{0.1}Fe_2O_4$ (x= 0.1, 0.2 and 0.3), $Ni^{3+}_{0.25}Ni^{2+}_{0.375}Zn^{2+}_{0.25}Fe_2O_4$, $Cu^{2+}_{0.1}Ni^{3+}_{0.15}Ni^{2+}_{0.225}Zn^{2+}_{0.45}Fe_2O_4$ and $BaNiZnFe_{16}O_{27}$ were investigated at a constant loading percentage of 65% w/w within a paraffin matrix with different thicknesses (3, 5 and 7 mm). The absorbers were molded to measure RL and SE at the range of 8.8-12 GHz. For $Mn_xZn_{(1-x)}Fe_2O_4$ (x= 0.3, 0.6 and 0.9), the effect of Mn^{2+} ion substitution and substitution concentrations on the EMI shielding and MA properties was studied. Figures (3.27-3.28) and Table 3.7 show the MA properties of the prepared samples. The results displayed weak RL and low SE for $Mn_{0.3}Zn_{0.7}Fe_2O_4$ and $Mn_{0.6}Zn_{0.4}Fe_2O_4$. Also, the results indicated that a RL_{min} was -11.7 dB at 9.2 GHz for a thickness of 5 mm, absorbing $BW_{-10\,dB}$ is 0.7 GHz and the SE_{max} was 13.3 dB at 9.6 GHz for $Mn_{0.9}Zn_{0.1}Fe_2O_4$ as shown in Figure 3.27. Figure 3.28 illustrates that the RL attenuation peaks of samples moved to lower frequencies with increasing sample thickness. This phenomenon may be defined by the quarter-wavelength ($\lambda/4$) cancellation

model, as shown in equation (1.5) [66–68]. On the other hand, for $Ni_xZn_{(1-x)}Fe_2O_4$ (x= 0.25, 0.5 and 0.75), the effect of Ni^{2+} ion substitution and substitution concentrations on the EMI shielding and MA properties was investigated. Table 3.7 shows the MA properties of the absorbers. Figure 3.29 demonstrates a comparison of the MA curves of the absorbers at a thickness of 5 mm. The results displayed weak RL and low SE for $Ni_{0.25}Zn_{0.75}Fe_2O_4$. As well, the results displayed that $Ni_{0.5}Zn_{0.5}Fe_2O_4$ and $Ni_{0.75}Zn_{0.25}Fe_2O_4$ exceeded the -10 dB threshold, as shown in Figure 3.29, which demonstrates that the RL attenuation peaks of samples moved to lower frequencies with increasing sample thickness. The results also indicate that the RL_{min} shifted to higher frequencies by increasing the substitution with several metal ions on ferrite. The SE_{max} was 13.7 dB at 10.4 GHz for $Ni_{0.5}Zn_{0.5}Fe_2O_4$.

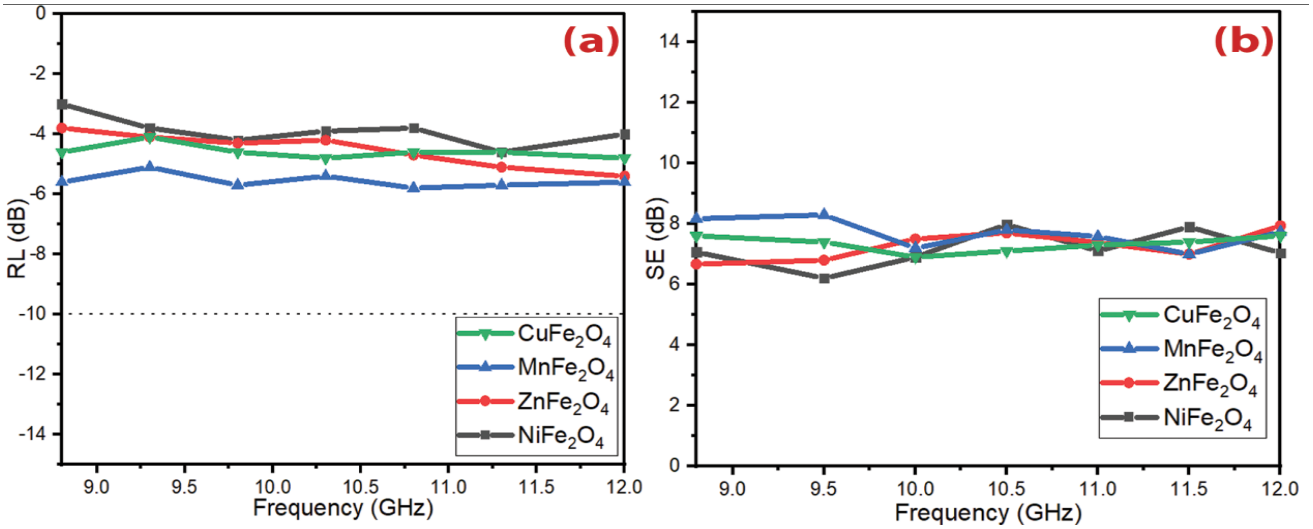

Figure 3.26 (a, b) – RL and SE curves of $NiFe_2O_4$, $ZnFe_2O_4$, $MnFe_2O_4$ and $CuFe_2O_4$ at 6 mm thickness

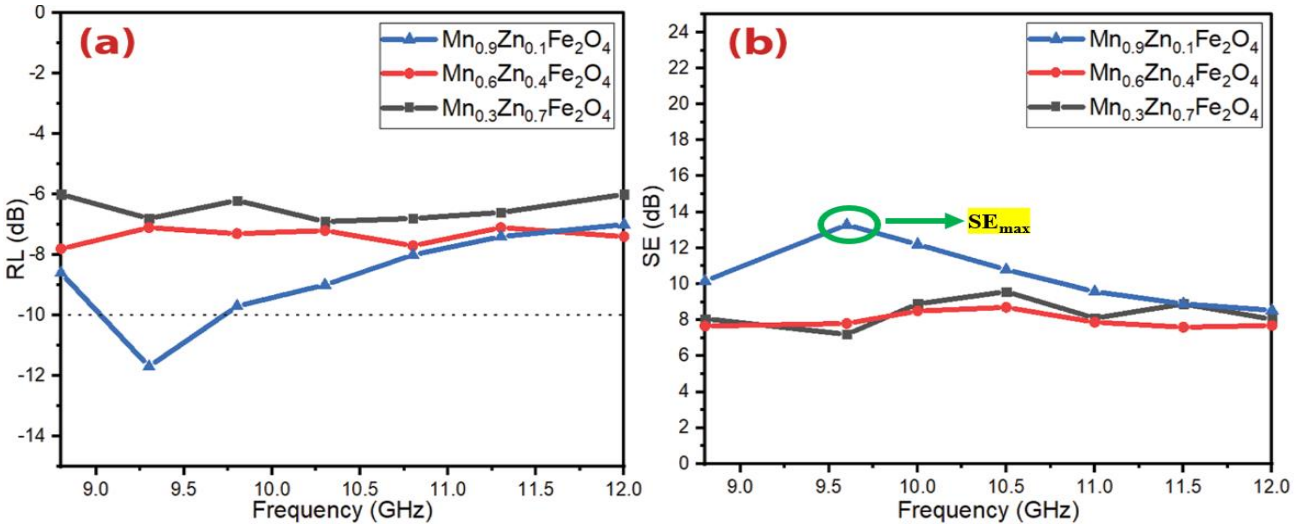

Figure 3.27 (a, b) – RL and SE curves of $Mn_xZn_{(1-x)}Fe_2O_4$ (x= 0.3, 0.6 and 0.9) at 5 mm thickness

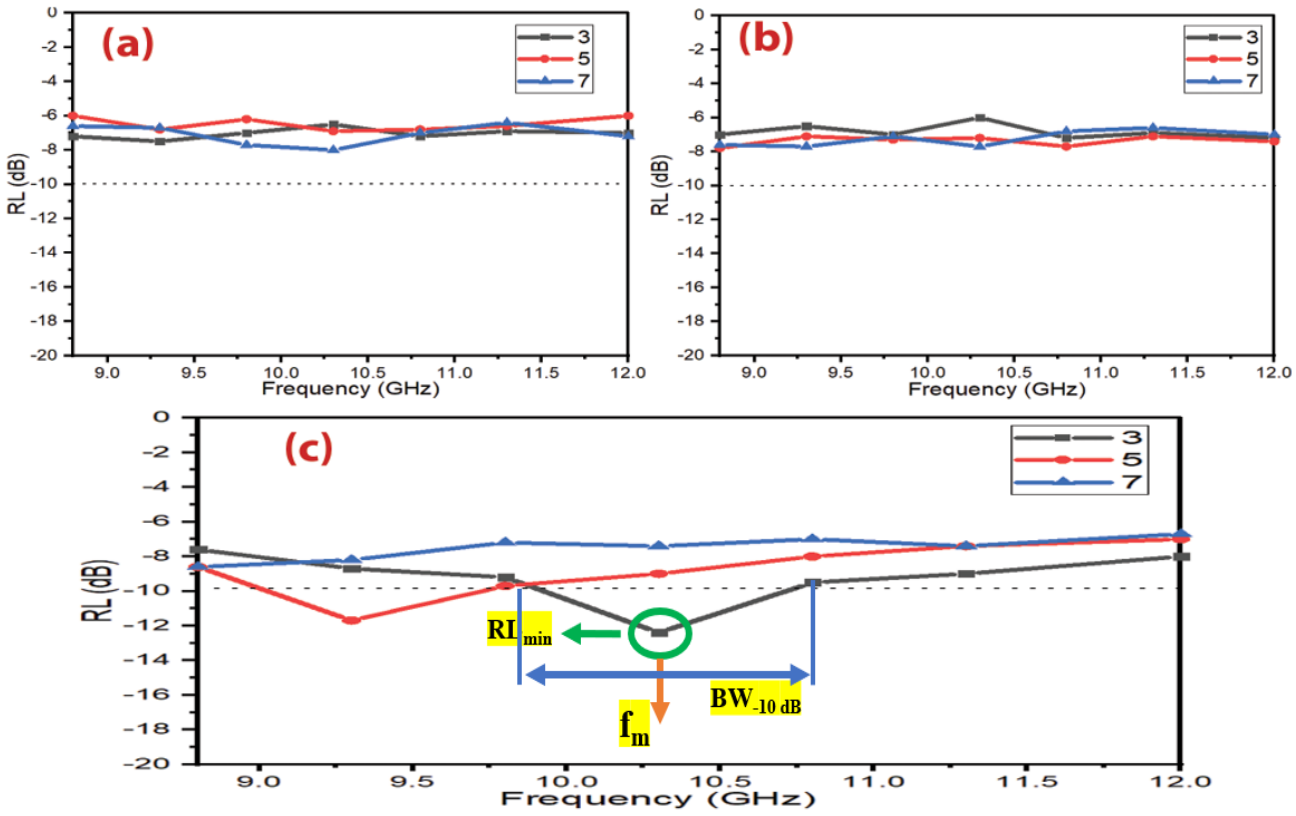

Figure 3.28 – RL curves of (a) $Mn_{0.3}Zn_{0.7}Fe_2O_4$, (b) $Mn_{0.6}Zn_{0.4}Fe_2O_4$ and (c) $Mn_{0.9}Zn_{0.1}Fe_2O_4$ at different thicknesses

Table 3.7 – MA behavior of doped ferrites at different thicknesses

Samples	t (mm)	RL_{min} (dB)	f_m (GHz)	$BW_{-10\ dB}$ (GHz)
$Mn_{0.3}Zn_{0.7}Fe_2O_4$	3	-7.5	9.2	0
	5	-6.9	10.3	0
	7	-7.7	9.8	0
$Mn_{0.6}Zn_{0.4}Fe_2O_4$	3	-7.2	10.2	0
	5	-7.8	8.2	0
	7	-7.5	9.3	0
$Mn_{0.9}Zn_{0.1}Fe_2O_4$	3	-12.4	10.3	0.9
	5	-11.7	9.2	0.7
	7	-8.6	8.8	0
$Ni_{0.25}Zn_{0.75}Fe_2O_4$	3	-7.5	11.0	0
	5	-7.4	12.0	0
	7	-8.2	11.4	0
$Ni_{0.5}Zn_{0.5}Fe_2O_4$	3	-11.5	10.1	0.5
	5	-12.2	9.6	0.8

	7	-8.4	8.8	0
$Ni_{0.75}Zn_{0.25}Fe_2O_4$	3	-12.3	11.1	0.7
	5	-13.5	10.0	0.8
	7	-11.4	9.5	0.8
$Ni_{0.5}Zn_{0.4}Mn_{0.1}Fe_2O_4$	3	-12.2	10.7	0.9
	5	-11.8	10.2	0.8
	7	-11.1	9.4	0.8
$Ni_{0.6}Zn_{0.3}Mn_{0.1}Fe_2O_4$	3	-11.4	11.3	0.7
	5	-13.7	10.6	1.0
	7	-12.5	10.2	1.3
$Ni_{0.7}Zn_{0.2}Mn_{0.1}Fe_2O_4$	3	-11.7	12.0	1.0
	5	-12.5	11.3	0.9
	7	-11.8	10.7	0.5
$Ni^{3+}_{0.25}Ni^{2+}_{0.375}Zn^{2+}_{0.25}Fe_2O_4$	3	-13.3	9.8	1.3
	5	-12.7	10.3	1.2
	7	-12.5	10.7	1.3
$Cu^{2+}_{0.1}Ni^{3+}_{0.15}Ni^{2+}_{0.225}Zn^{2+}_{0.45}Fe_2O_4$	3	-11.6	11.0	0.8
	5	-12.1	10.5	0.8
	7	-11.8	11	0.7
$BaNiZnFe_{16}O_{27}$	3	-8.4	12.0	0
	5	-8.0	12.0	0
	7	-8.8	12.0	0

Table 3.8 illustrates a comparison of MA characteristics of some lately informed ferrite absorbers with different preparation methods and loading percentages. The results of the literature show these ferrites are good in the C-band and Ku-band frequencies and weak in the X-band frequency. The presently prepared ferrites display in this research better MA in the X-band frequency. The distinct of these prepared ferrites have a lower loading percentage and thickness of the absorbers compared with the other literature.

Table 3.8 – Comparison of MA properties of the present prepared ferrites with similar ferrites in the other research

Sample	Preparation method	t (mm)	f_m (GHz)	$BW_{-10\ dB}$ (GHz) (C-band)	$BW_{-10\ dB}$ (GHz) (X-band)	$BW_{-10\ dB}$ (GHz) (Ku-band)	Loading percentage (%)	Ref
$Ni_{0.5}Zn_{0.5}Fe_2O_4$	Combustion	5.92	3.16	1.65	0	0	80	[120]

$Ni_{0.5}Zn_{0.5}Fe_2O_4$	Iron oxide catalysts	5.5	6.1	3.2	0	0	70	[121]
$Ni_{0.5}Zn_{0.5}Fe_2O_4$	Combustion	5.0	5.82	1.6	0	0	80	[122]
$Mn_{0.5}Zn_{0.5}Fe_2O_4$	Sol-gel	20	6.0	1.2	0	0	66.66	[123]
$Ni_{0.5}Zn_{0.5}Fe_2O_4$	-	7.10	2.19	6.0	2.0	0	73	[78]
$Ni_{0.5}Zn_{0.5}Fe_2O_4$	nitrate-citrate precursor	5.0	8.52	-	0.41	-	80	[69]

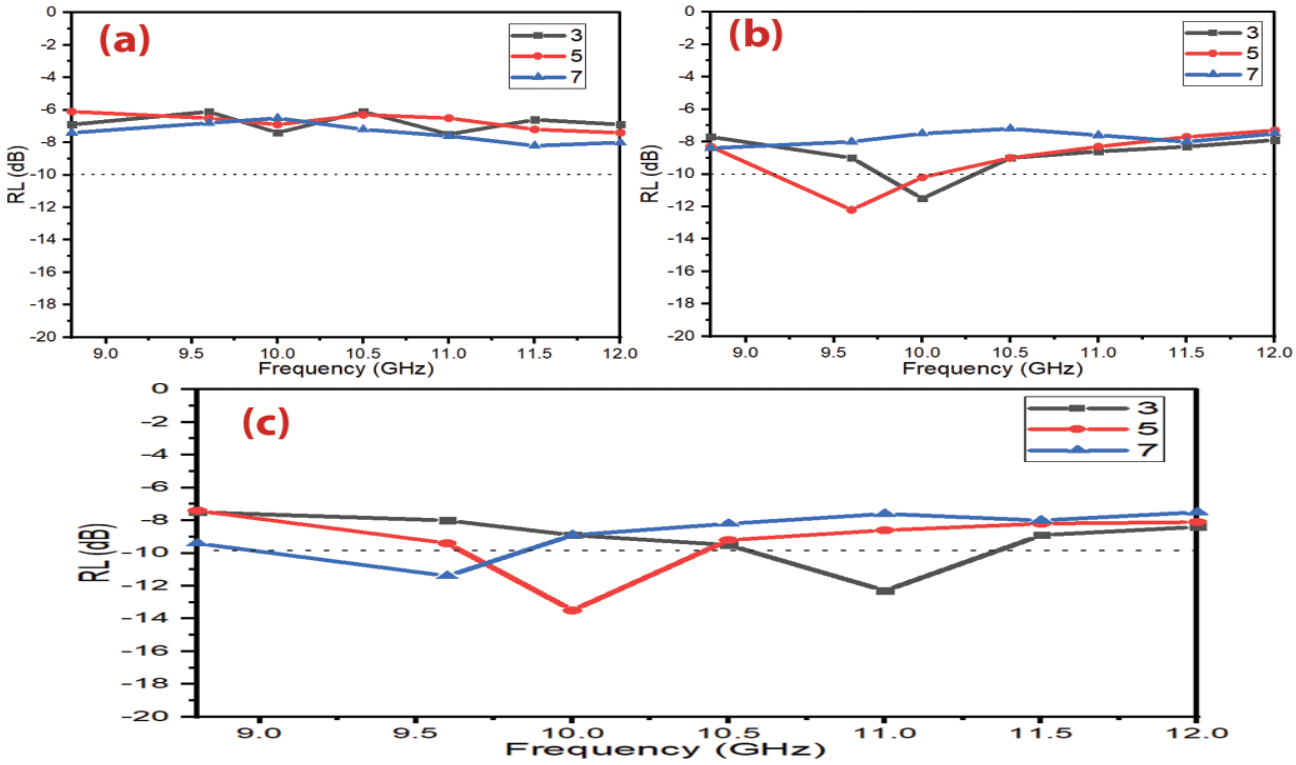

Figure 3.29 – RL curves of (a) $Ni_{0.25}Zn_{0.75}Fe_2O_4$, (b) $Ni_{0.5}Zn_{0.5}Fe_2O_4$ and (c) $Ni_{0.75}Zn_{0.25}Fe_2O_4$ at different thicknesses

On the other hand, Ni-doped manganese zinc ferrite ($Ni_{(0.4+x)}Zn_{(0.5-x)}Mn_{0.1}Fe_2O_4$ (x= 0.1, 0.2 and 0.3)) was studied. Table 3.9 demonstrate the MA properties of the prepared samples. Figure 3.30 displays a comparison of the MA and EMI properties of the prepared samples at a thickness of 5 mm. The results indicated that the $Ni_{(0.4+x)}Zn_{(0.5-x)}Mn_{0.1}Fe_2O_4$ (x= 0.1, 0.2 and 0.3) exceeded the -10 dB threshold, as shown in Figure 3.31, which illustrates that the RL attenuation peaks of samples moved to lower frequencies by increasing sample thickness. This phenomenon may be defined by the quarter-wavelength ($\lambda/4$) cancellation model, as shown in equation (1.12). The results also demonstrated that the RL_{min} shifted to higher frequencies by increasing the substitution with several metal ions on ferrite. The SE_{max} was 14.8 dB at 11.3 GHz for $Ni_{0.6}Zn_{0.3}Mn_{0.1}Fe_2O_4$ as shown in Figure 3.32.

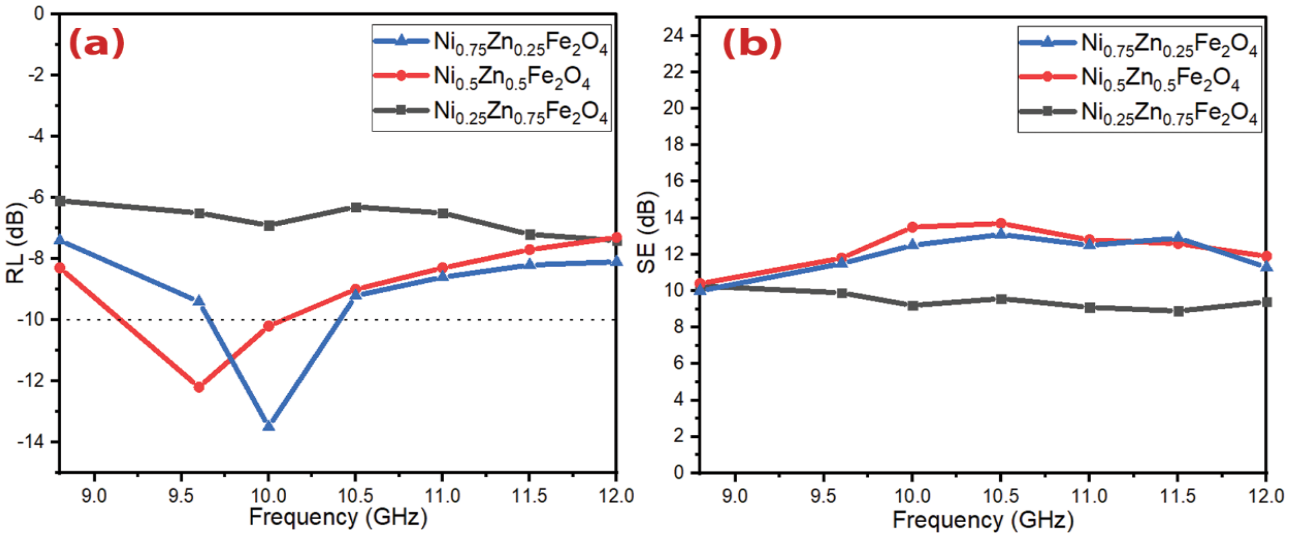

Figure 3.30 (a, b) – RL and SE curves of $Ni_xZn_{(1-x)}Fe_2O_4$ (x= 0.25, 0.5 and 0.75) at 5 mm thickness**.**

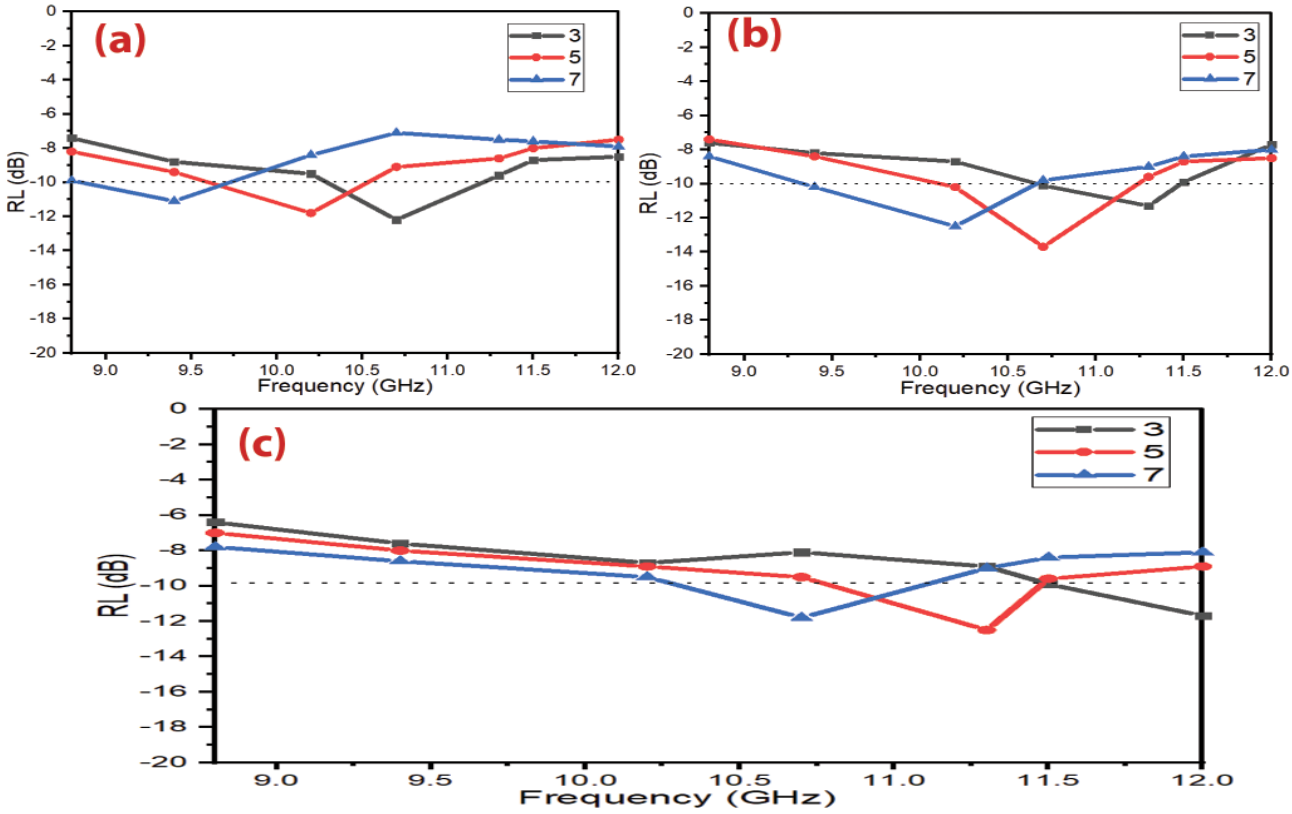

Figure 3.31 – RL curves of (a) $Ni_{0.5}Zn_{0.4}Mn_{0.1}Fe_2O_4$, (b) $Ni_{0.6}Zn_{0.3}Mn_{0.1}Fe_2O_4$ and (c) $Ni_{0.7}Zn_{0.2}Mn_{0.1}Fe_2O_4$ at different thicknesses

The effect of the triple nickel (Ni^{3+}) ion substitution on the EMI shielding and MA properties was investigated. Table 3.9 shows the prepared samples' MA properties. Figure 3.33 illustrates a comparison of the MA curves with different loading percentages (60% w/w, 65% w/w and 70% w/w) at 5 mm thickness and shows the SE_R and SE_A of $Ni^{3+}{}_{0.25}Ni^{2+}{}_{0.375}Zn^{2+}{}_{0.25}Fe_2O_4$ with a thickness of 5 mm at the frequency of 11.5 GHz. The

absorption results demonstrate that the MA properties improved by entering the triple nickel into the nickel-zinc ferrite composition. This substitution process increased the absorption $BW_{-10\ dB}$ of the Ni-Zn ferrite and improved the RL_{min} and SE_{max}. The results indicated that the $Ni^{3+}_{0.25}Ni^{2+}_{0.375}Zn^{2+}_{0.25}Fe_2O_4$ exceeded the -10 dB threshold, which illustrates that the RL attenuation peaks of samples moved to lower frequencies by increasing sample thickness and loading percentage of absorber within a paraffin matrix. On the other hand, the substitution process increased the SE_{max}, as shown in Figure 3.33.

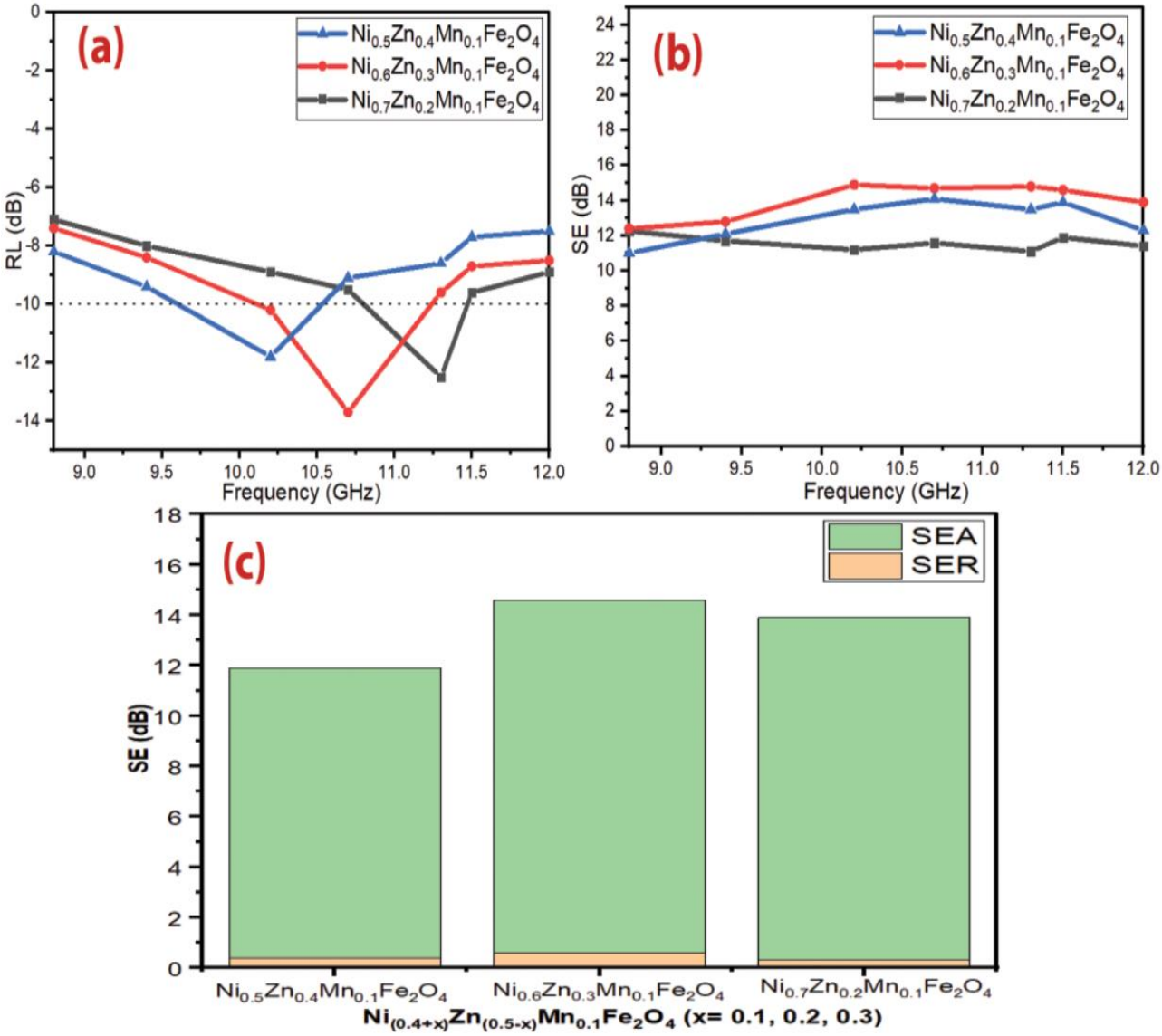

Figure 3.32 (a, b) – RL and SE curves of $Ni_{(0.4+x)}Zn_{(0.5-x)}Mn_{0.1}Fe_2O_4$ (x= 0.1, 0.2 and 0.3) at 5 mm thickness and (c) Bar plot for individual components of SE_R and SE_A of $Ni_{(0.4+x)}Zn_{(0.5-x)}Mn_{0.1}Fe_2O_4$ (x= 0.1, 0.2 and 0.3) with a thickness of 5 mm at the frequency of 11.5 GHz

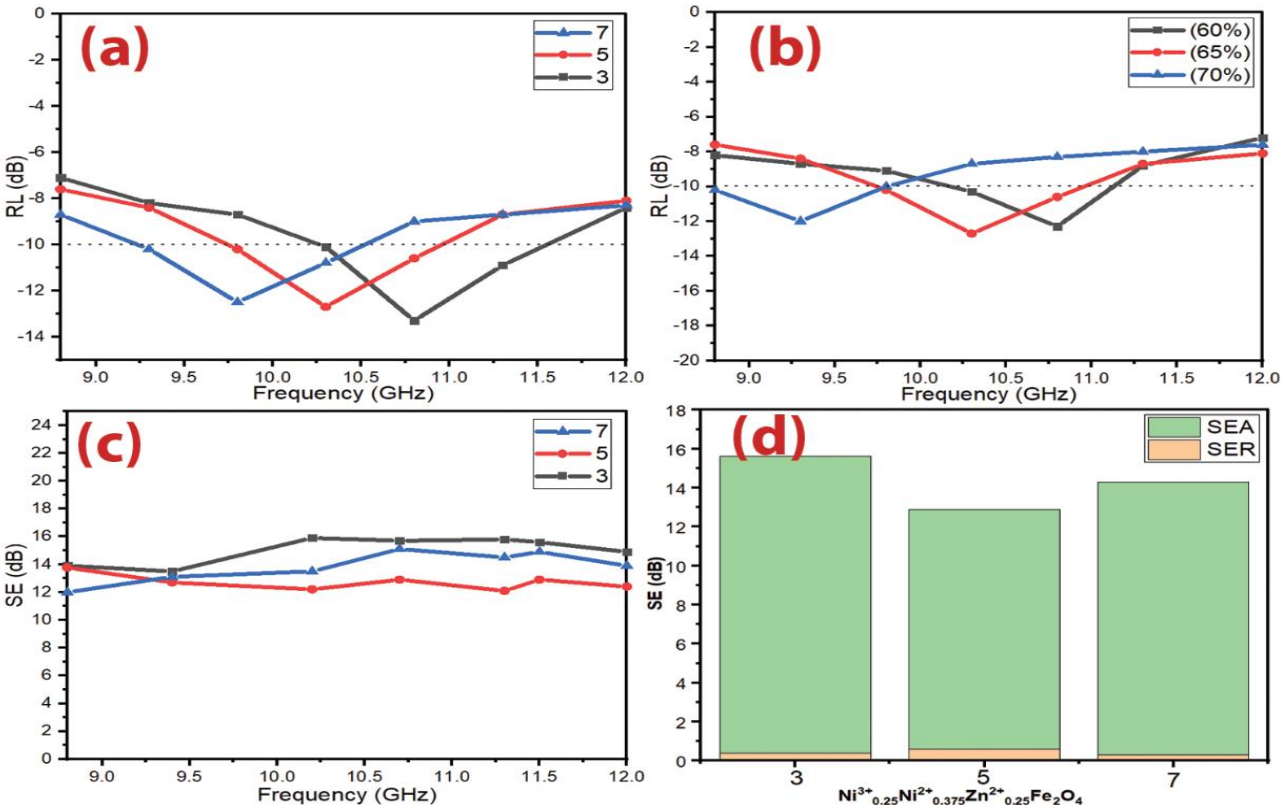

Figure 3.33 (a,b) – RL curves of $Ni^{3+}_{0.25}Ni^{2+}_{0.375}Zn^{2+}_{0.25}Fe_2O_4$ at different thicknesses and different loading percentages (60% w/w, 65% w/w and 70% w/w mm) at 5 mm thickness, (c) SE curves of $Ni^{3+}_{0.25}Ni^{2+}_{0.375}Zn^{2+}_{0.25}Fe_2O_4$ at different thicknesses and (d) bar plot for individual components of SE_R and SE_A with a thickness of 5 mm at the frequency of 11.5 GHz

On the other hand, Cu-doped nickel zinc ferrite ($Cu^{2+}_{0.1}Ni^{3+}_{0.15}Ni^{2+}_{0.225}Zn^{2+}_{0.45}Fe_2O_4$) was studied. Table 3.9 shows the prepared samples' MA properties. Figure 3.34 also shows a comparison of the MA curves with different loading percentages (60% w/w, 65% w/w and 70% w/w) at 5 mm thickness. Finally, Figure 3.34 shows the SE_R and SE_A of $Cu^{2+}_{0.1}Ni^{3+}_{0.15}Ni^{2+}_{0.225}Zn^{2+}_{0.45}Fe_2O_4$ with a thickness of 5 mm at the frequency of 11.5 GHz. The results show that the MA properties decreased by entering the Cu^{2+} into $Ni^{3+}_{0.25}Ni^{2+}_{0.375}Zn^{2+}_{0.25}Fe_2O_4$. This substitution process decreased the absorption bandwidth of $Ni^{3+}_{0.25}Ni^{2+}_{0.375}Zn^{2+}_{0.25}Fe_2O_4$, as shown in Table 3.9. The results indicated that the $Cu^{2+}_{0.1}Ni^{3+}_{0.15}Ni^{2+}_{0.225}Zn^{2+}_{0.45}Fe_2O_4$ exceeded the -10 dB threshold, as shown in Figure 3.34, which illustrates that the RL attenuation peaks of samples moved to lower frequencies by increasing sample thickness and loading percentage. On the other hand, the substitution process decreased the SE_{max}, as shown in Figure 3.34.

Table 3.9 – MA behavior of $Ni^{3+}_{0.25}Ni^{2+}_{0.375}Zn^{2+}_{0.25}Fe_2O_4$ and $Cu^{2+}_{0.1}Ni^{3+}_{0.15}Ni^{2+}_{0.225}Zn^{2+}_{0.45}Fe_2O_4$ with different loading percentages (60% w/w, 65% w/w and 70% w/w mm) at 5 mm thickness

Samples	Loading percentage (%)	RL_{min} (dB)	f_m (GHz)	$BW_{-10\ dB}$ (GHz)
$Ni^{3+}_{0.25}Ni^{2+}_{0.375}Zn^{2+}_{0.25}Fe_2O_4$	60	-12.3	10.7	1.1
	65	-12.7	10.3	1.2
	70	-12.0	9.2	1.0
$Cu^{2+}_{0.1}Ni^{3+}_{0.15}Ni^{2+}_{0.225}Zn^{2+}_{0.45}Fe_2O_4$	60	-11.1	11.5	0.8
	65	-12.1	10.5	0.9
	70	-11.8	10.0	0.9

EMI shielding and MA properties of $BaNiZnFe_{16}O_{27}$ were investigated. The results of this investigation are exhibited in Figure 2.34. The results showed that the absorbers with a loading percentage within a paraffin matrix of 65% w/w had weak RL and low SE. As a result, there is a need to incorporate $BaNiZnFe_{16}O_{27}$ with dielectric loss materials such as PANI and CB to improve the radar absorption properties, as will be clarified later.

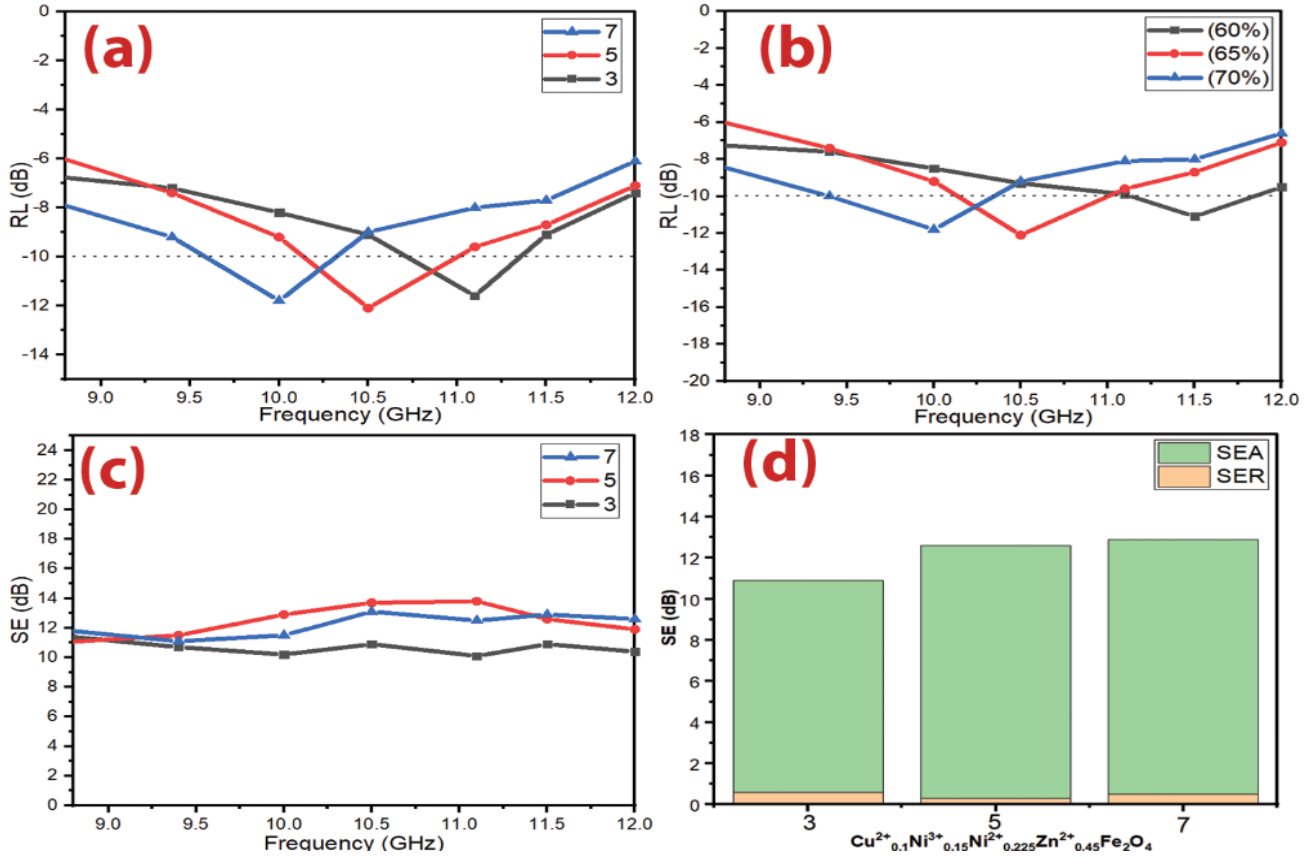

Figure 3.34 (a,b) – RL curves of $Cu^{2+}_{0.1}Ni^{3+}_{0.15}Ni^{2+}_{0.225}Zn^{2+}_{0.45}Fe_2O_4$ at different thicknesses and different loading percentages (60% w/w, 65% w/w and 70% w/w mm) at

5 mm thickness, (c) SE curves of $Cu^{2+}_{0.1}Ni^{3+}_{0.15}Ni^{2+}_{0.225}Zn^{2+}_{0.45}Fe_2O_4$ at different thicknesses and (d) bar plot for individual components of SE_R and SE_A with a thickness of 5 mm at the frequency of 11.5 GHz.

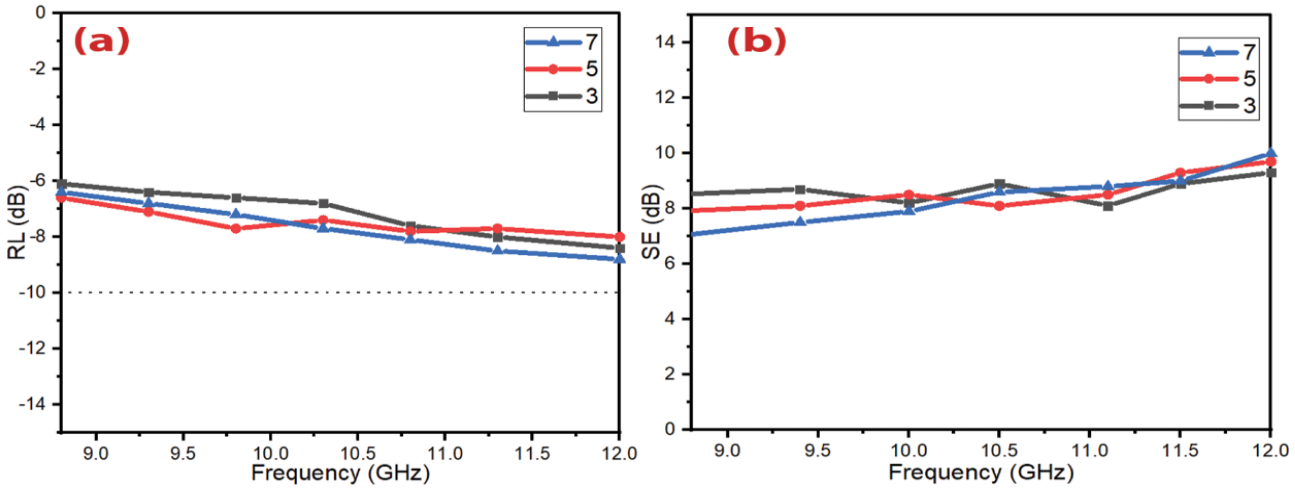

Figure 3.35 (a,b) – RL and SE curves of $BaNiZnFe_{16}O_{27}$ at different thicknesses

Table 3.10 illustrates a comparison of MA characteristics of some lately informed ferrite absorbers with different preparation methods and loading percentages. The results of the literature show these ferrites are good in the C-band and Ku-band frequencies and weak in the X-band frequency. The presently prepared ferrites display in this research better MA in the X-band frequency. The distinct of these prepared ferrites have a lower loading percentage and thickness of the absorbers compared with the other literature. The best result obtained at this stage was by using $Ni^{3+}_{0.25}Ni^{2+}_{0.375}Zn^{2+}_{0.25}Fe_2O_4$. A RL_{min} indicated -13.3 dB at 9.8 GHz and bandwidth $BW_{-10\ dB}$ was 1.3 GHz for a thickness of 3 mm. Also, the SE_{max} attained 15.9 dB at 10.2 GHz.

Table 3.10 – Comparison of MA properties of the present prepared ferrites with similar ferrites in the other research

Sample	Preparation method	t (mm)	$BW_{-10\ dB}$ (GHz) (C-band)	$BW_{-10\ dB}$ (GHz) (X-band)	$BW_{-10\ dB}$ (GHz) (Ku-band)	Loading percentage (%)	Ref
$Mn_{0.5}Zn_{0.5}Fe_2O_4$	Sol-gel	20	1.2	0	0	66.66	[123]
$Cu_{0.2}Ni_{0.45}Zn_{0.35}Fe_2O_4$	Co-Precipitation	7.35	1.1	0	0	100	[124]
$Cu_{0.3}Ni_{0.2}Zn_{0.5}Fe_2O_4$	Nitrate-citrate precursor	6.2	0	0.6	0	70	[125]
$Ni_{0.4}Zn_{0.4}Mn_{0.2}Fe_2O_4$		5.0	-	0.8	-	80	[69]

$Ni_{0.4}Zn_{0.4}Cu_{0.2}Fe_2O_4$	Nitrate-citrate precursor		-	1.2	-		
$Ni_{0.4}Zn_{0.4}Mg_{0.2}Fe_2O_4$			-	0.7	-		
$Ni_{0.4}Cu_{0.2}Zn_{0.4}Tb_{0.8}Fe_{1.2}O_4$	Sonochemical	8.0	2.1	-	-	70	[73]
$Ni_{0.4}Cu_{0.2}Zn_{0.4}Eu_{0.8}Fe_{1.2}O_4$	Sol-gel	7.0	1.5	-	-	70	[74]
$Cu_{0.2}Ni_{0.4}Zn_{0.4}Fe_2O_4$	Ceramic	9.2	1.5	0	0	85	[44]

3.6.2 Microwave absorption properties of ferrite samples prepared by citrate precursor technique

Several variables that affect MA properties were studied: molar ratio of the metal ion to citrate acid, calcination temperature, absorber thickness and loading percentage.

3.6.2.1 Microwave absorption properties of $Ni_{0.5}Zn_{0.5}Fe_2O_4$ nanoparticles

The effect of the different molar ratios of the metal ions to citrate acid (1:1, 2:1, and 3:1) and calcination temperatures (650, 800, and 950°C) on the properties of $Ni_{0.5}Zn_{0.5}Fe_2O_4$ was studied. Samples were prepared with a thickness of 5 mm and a loading percentage of 65%. The results indicated that the RL attenuation peaks of samples moved to lower frequencies with increasing the metal ions to citrate acid and calcination temperature as shown in Figure 3.36. This may be due to the change in the crystallite size of the ferrite nanoparticles. The results of XRD patterns indicated that the crystallite size of nickel-zinc ferrite increased by increasing the calcination temperature and the metal ion concentration. The best result obtained at this stage was by using $NZ_{11}-650$ as shown in Figure 3.37 and Table 3.101.

Table 3.11 – MA behavior of $Ni_{0.5}Zn_{0.5}Fe_2O_4$ nanoparticles

Samples	T (°C)	RL_{min} (dB)	f_m (GHz)	$BW_{-10\,dB}$ (GHz)
NZ_{11} - 650	650	-12.9	10.5	1.3
NZ_{12} - 650		-12.3	10.0	0.8
NZ_{13} - 650		-11.7	9.5	1.2
NZ_{11} - 800	800	-12.2	10.1	1.1
NZ_{12} - 800		-12.0	9.5	0.9
NZ_{13} - 800		-8.4	11.4	0
NZ_{11} - 950	950	-11.9	9.6	0.8
NZ_{12} - 950		-7.9	9.9	0
NZ_{13} - 950		-7.7	110.4	0

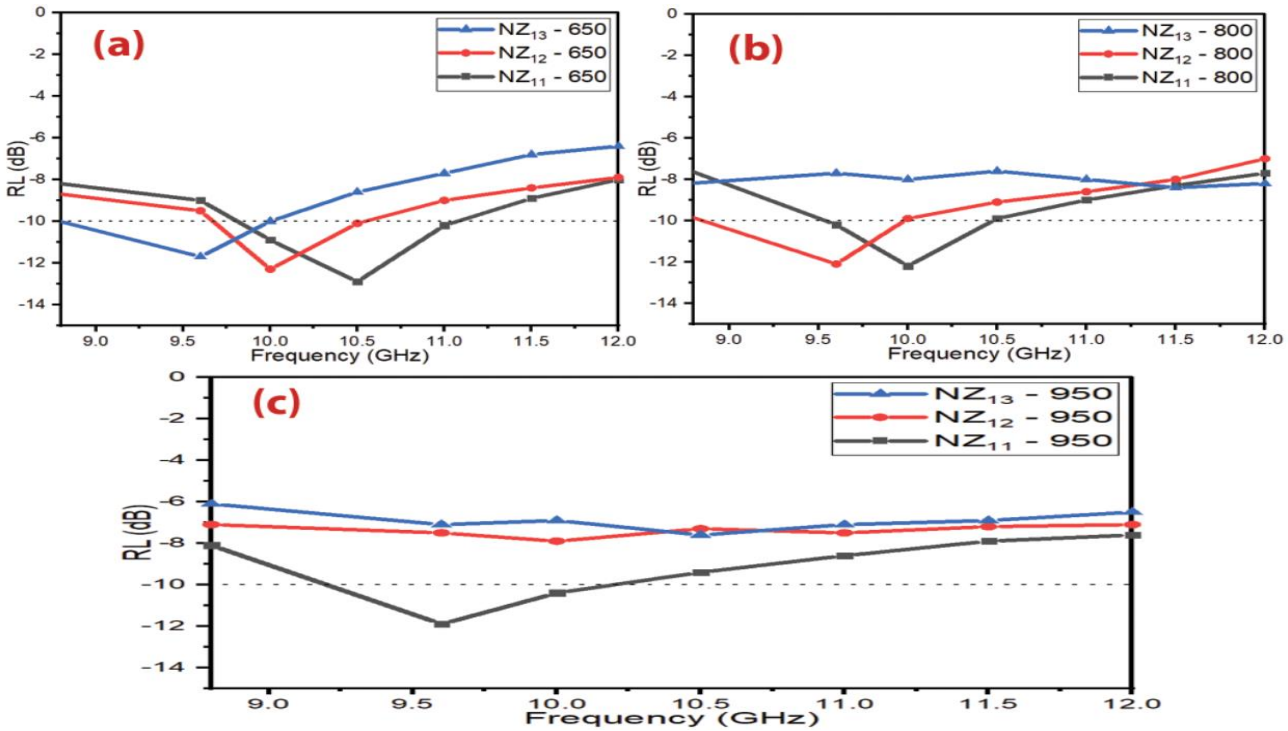

Figure 3.36 – RL curves of $Ni_{0.5}Zn_{0.5}Fe_2O_4$ nanoparticles at (a) 650 °C, (b) 800 °C and (c) 950 °C

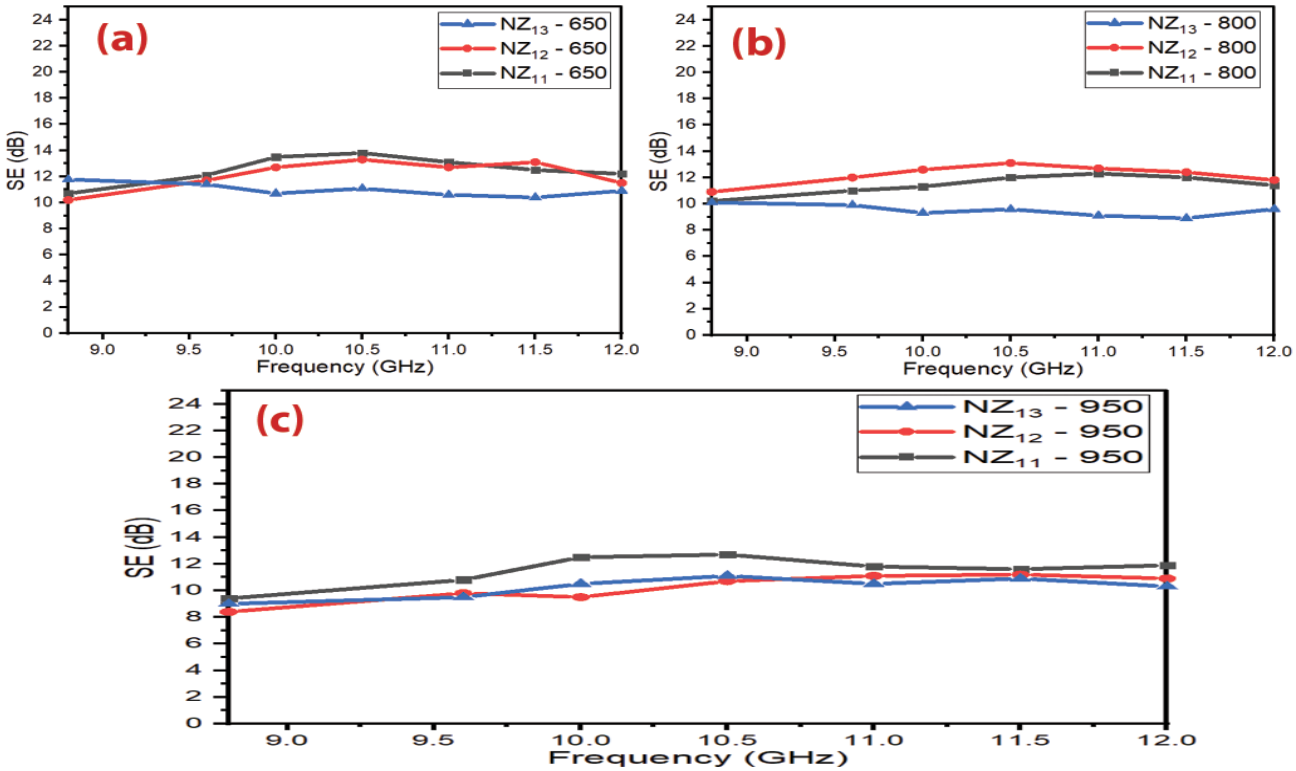

Figure 3.37 – SE curves of $Ni_{0.5}Zn_{0.5}Fe_2O_4$ nanoparticles (a) 650 °C, (b) 800 °C and (c) 950 °C.

3.6.2.2 Influence of sample thickness and loading percentage on the f_m

The influence of the different loading percentages (60, 65 and 70% w/w) and thicknesses (3, 5 and 6 mm) on NZ11 – 650 properties were investigated. Figure 3.38 shows that the RL moved gradually to a lower frequency with the increased loading percentage. Also, the same phenomenon was noticed by increasing the thickness of an absorber. These results may be defined by the quarter-wavelength (λ/4) cancellation model, as shown in equation (1.5) [66–68]. The results indicated a RL_{min} of -13.7 dB at 11.0 GHz for a thickness of 5 mm for NZ_{11} – 60%. The SE_{max} was 14.2 dB at 10.4 GHz for NZ_{11} – 65%. From the above studies, we found the f_m position controllability of ferrite nanoparticles prepared with the citrate precursor technique.

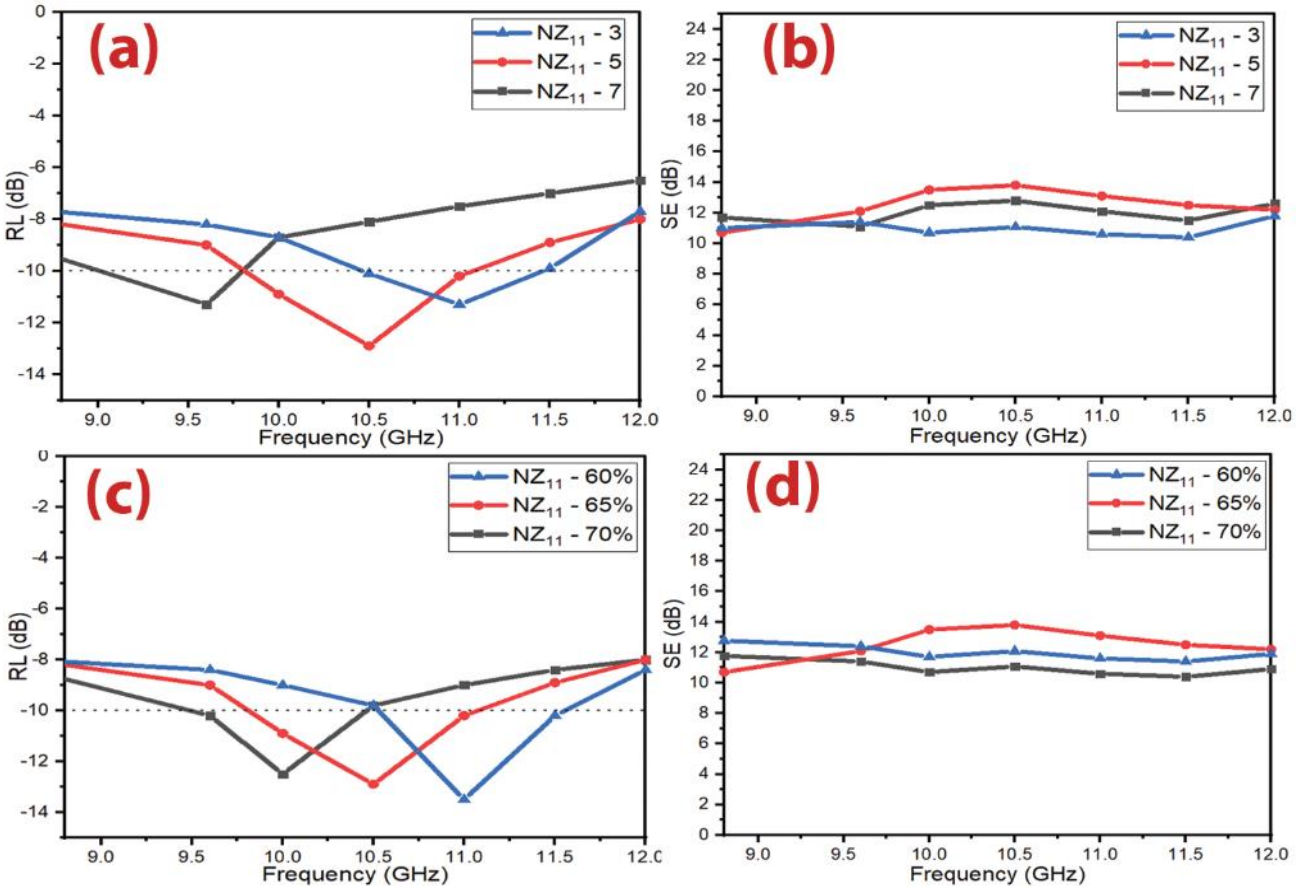

Figure 3.38 (a,b) – RL and SE curves of $Ni_{0.5}Zn_{0.5}Fe_2O_4$ nanoparticles at different thicknesses and (d,c) RL and SE curves of $Ni_{0.5}Zn_{0.5}Fe_2O_4$ nanoparticles with varying percentages of loading (60% w/w, 65% w/w and 70% w/w mm) at 5 mm thickness

3.6.3 Microwave absorption properties of ferrite samples prepared by the self-combustion technique

Several variables that affect MA properties were studied: PVA concentration, calcination temperature, absorber thickness and loading percentage of ferrite in the host matrix.

3.6.3.1 Microwave absorption properties of $Ni_{0.5}Zn_{0.5}Fe_2O_4$ nanoparticles

The effect of the different aqueous solutions of PVA (1%, 4%, and 6%) and calcination temperatures (650, 800, and 950°C) on the properties of $Ni_{0.5}Zn_{0.5}Fe_2O_4$ was studied. Samples were prepared with a thickness of 5 mm and a loading percentage of 65%. The results indicated that the RL attenuation peaks of samples shifted to lower frequencies with increasing PVA concentration and calcination temperature as shown in Figure 3.39. This may be due to the change in the crystallite size of the ferrite nanoparticles. The results of XRD patterns indicated that the crystallite size of nickel-zinc ferrite increased by increasing the calcination temperature and PVA concentration. The best result obtained was by using $NSC_{11} - 800$ as shown in Figure 3.40 and Table 3.12.

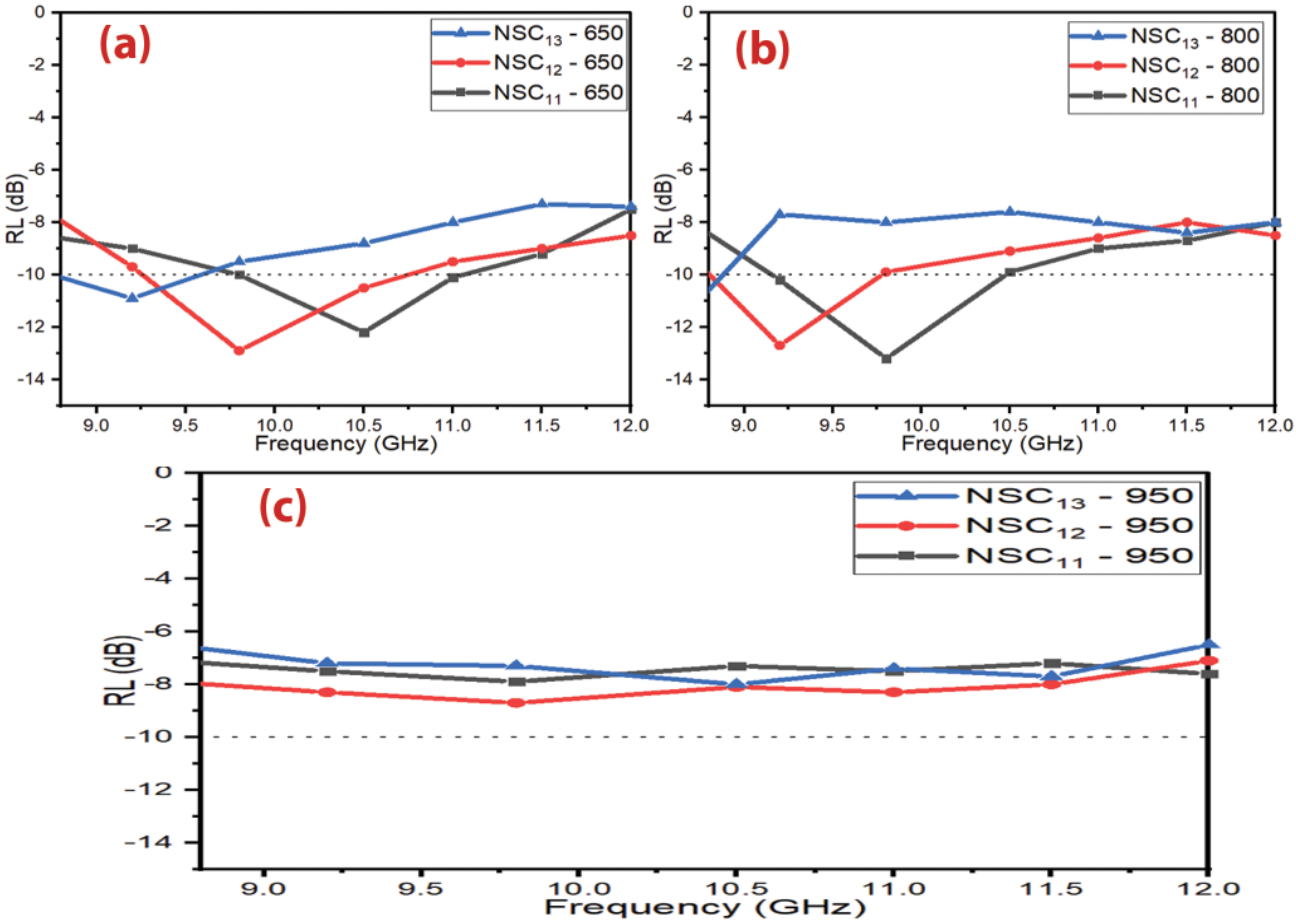

Figure 3.39 – RL curves of $Ni_{0.5}Zn_{0.5}Fe_2O_4$ nanoparticles at (a) 650 °C, (b) 800 °C and (c) 950 °C

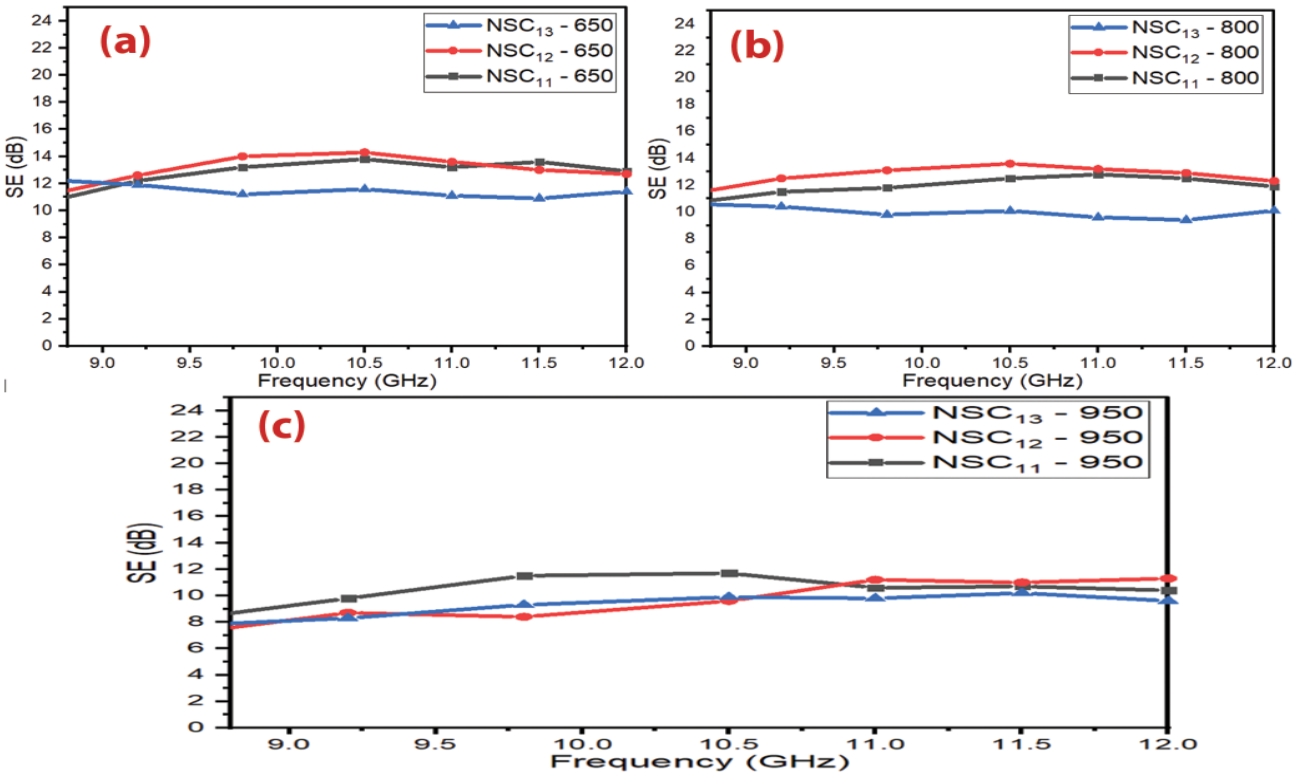

Figure 3.40 – SE curves of $Ni_{0.5}Zn_{0.5}Fe_2O_4$ nanoparticles at (a) 650 °C, (b) 800 °C and (c) 950 °C

Table 3.12 – MA behavior of $Ni_{0.5}Zn_{0.5}Fe_2O_4$ nanoparticles

Samples	T (°C)	RL_{min} (dB)	f_m (GHz)	$BW_{-10\ dB}$ (GHz)
NSC_{11} - 650	650	-12.2	10.5	1.3
NSC_{12} - 650		-12.9	9.8	1.5
NSC_{13} - 650		-10.9	9.2	0.8
NSC_{11} - 800	800	-13.2	9.7	1.2
NSC_{12} - 800		-12.7	9.3	1.0
NSC_{13} - 800		-11.3	8.8	0.2
NSC_{11} - 950	950	-7.9	9.5	0
NSC_{12} - 950		-8.0	11.0	0
NSC_{13} - 950		-8.1	10.5	0

3.6.3.2 Influence of sample thickness and loading percentage on the f_m

The influence of the different loading percentages (60, 65 and 70% w/w) and thicknesses (3, 5 and 6 mm) on NZ11 – 650 properties were investigated. Figure 3.41 shows that the RL moved gradually to a lower frequency with the increased loading percentage. Also, the same phenomenon was noticed by increasing the thickness of an absorber. These results may be defined by the quarter-wavelength (λ/4) cancellation

model, as shown in equation (1.5) [66–68]. The results indicated a RL_{min} of -12.9 dB at 10.0 GHz and absorption $BW_{-10\,dB}$ of 0.7 GHz for 5 mm thickness for NSC_{11} – 70%. The SE_{max} was 14.4 dB at 8.8 GHz. From the above studies, we found the f_m position controllability of ferrite nanoparticles prepared with the self-combustion.

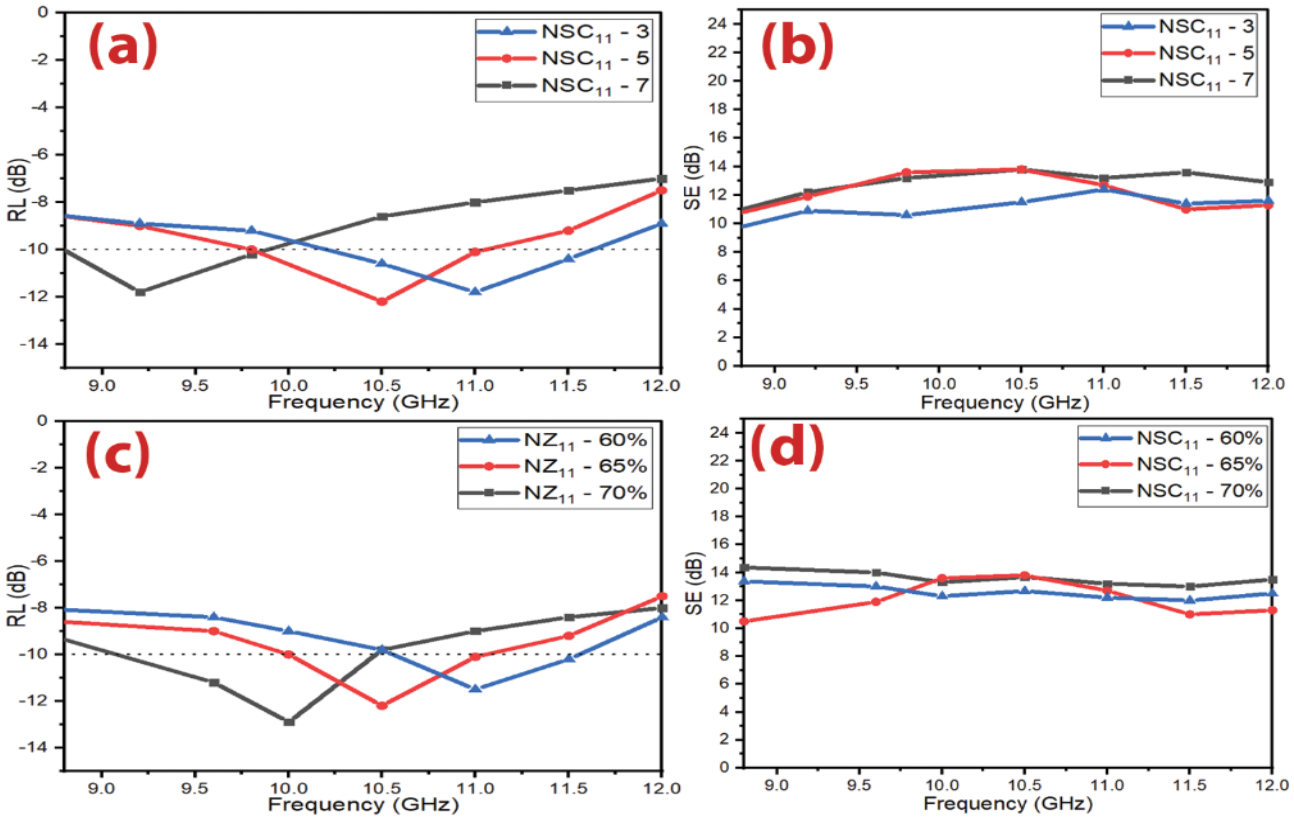

Figure 3.41 (a,b) – RL and SE curves of $Ni_{0.5}Zn_{0.5}Fe_2O_4$ nanoparticles at different thicknesses and (c,d) RL and SE curves of $Ni_{0.5}Zn_{0.5}Fe_2O_4$ nanoparticles with different loading percentages (60% w/w, 65% w/w and 70% w/w mm) at 5 mm thickness

From the above studies, One can notice that MA properties were changed with the variation of the synthesis method. The best result was obtained by using the $Ni_{0.5}Zn_{0.5}Fe_2O_4$ nanoparticles with a loading percentage of 60% at a constant calcination temperature of 650° C prepared by the citrate precursor method. This improvement is due to the fact that these processes will affect the MA capacity by changing the complex permeability and permittivity. However, the defects of these prepared absorbers are that they have a limited absorption $BW_{-10\,dB}$ and high loading percentage. This necessitated working to decrease the loading percentage and increase the absorption $BW_{-10\,dB}$ of the absorbers to cover most of the X-band frequency by incorporating magnetic loss and dielectric loss materials.

3.6.4 Microwave absorption properties of ferrite nanocomposites

Several variables that affect MA properties were studied, as follows: ferrite nanocomposite type, the weight ratio of CB/$Ni_{0.5}Zn_{0.5}Fe_2O_4$, CB/$Mn_{0.1}Ni_{0.5}Zn_{0.4}Fe_2O_4$, C/$Ni^{3+}_{0.25}Ni^{2+}_{0.375}Zn^{2+}_{0.25}Fe_2O_4$ and $Ni_{0.5}Zn_{0.5}Fe_2O_4$/CI/CB, and loading percentage.

3.6.4.1 Microwave absorption properties of carbon black/NiZn ferrite nanocomposites

EMI shielding and MA properties of CB/$Ni_{0.5}Zn_{0.5}Fe_2O_4$ nanocomposites were studied at a loading percentage of 45% w/w with the different weight ratios of CB/$Ni_{0.5}Zn_{0.5}Fe_2O_4$ (1:1, 2:1, and 3:1). Figure 3.42 displays the RL of the prepared samples with different thicknesses (2–4–6 mm). The results show that the RL attenuation peaks of samples moved to lower frequencies with increasing sample thickness. This phenomenon may be defined by the quarter-wavelength (λ/4) cancellation model, as shown in equation (1.5). The results demonstrated that the absorber of 3.2 GHz bandwidth had a RL_{min} of -18.2 dB at the f_m of 9.9 GHz with a thickness of 6 mm for CB/F-21. Figure 3.43 represents the SE of the prepared samples. The SE_{max} was 18 dB at 11.5 GHz with a thickness of 2 mm. Figure 3.44 shows the SE_R and SE_A of the prepared samples at the frequency of 11.5 GHz. The results revealed the impact of incorporating $Ni_{0.5}Zn_{0.5}Fe_2O_4$ (magnetic loss material) and CB (dielectric loss material) on the SD, RL_{min}, SE_{max}, and $BW_{-10\ dB}$ of the prepared absorber. This incorporation leads to an effective and low SD absorber with a wide $BW_{-10\ dB}$ compared to a pure CB absorber as shown in Table 3.13.

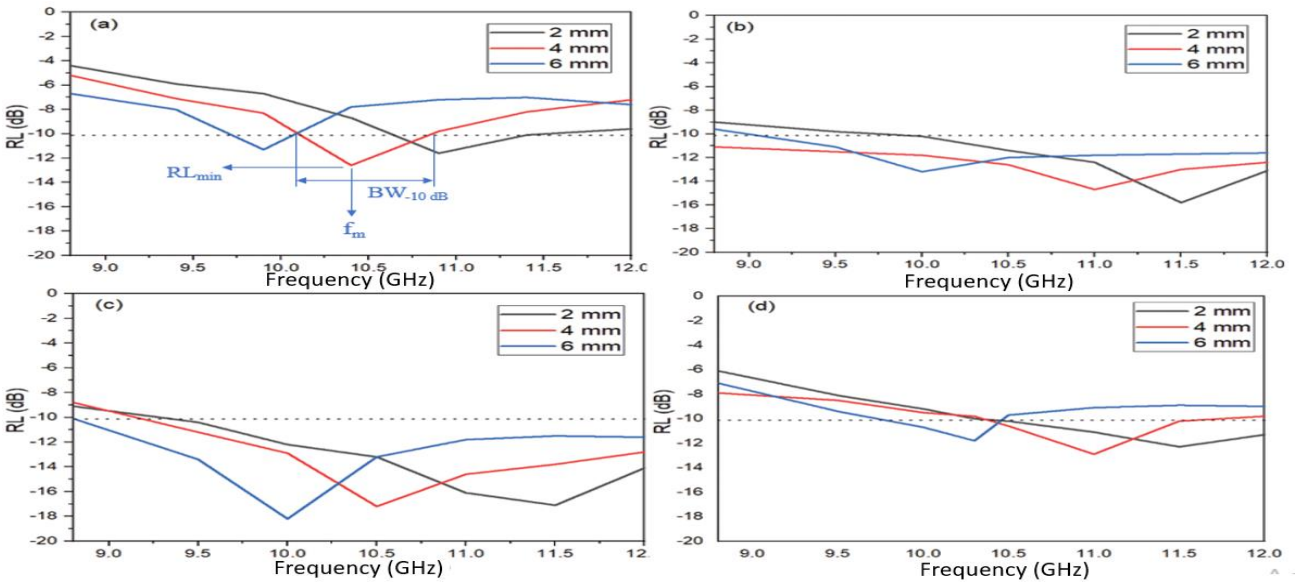

Figure 3.42 – RL curves of (a) pure CB nanopowder, (b) CB/F-11 nanocomposite, (c) CB/F-21 nanocomposite and (d) CB/F-31 nanocomposite at different thicknesses (2–4–6 mm)

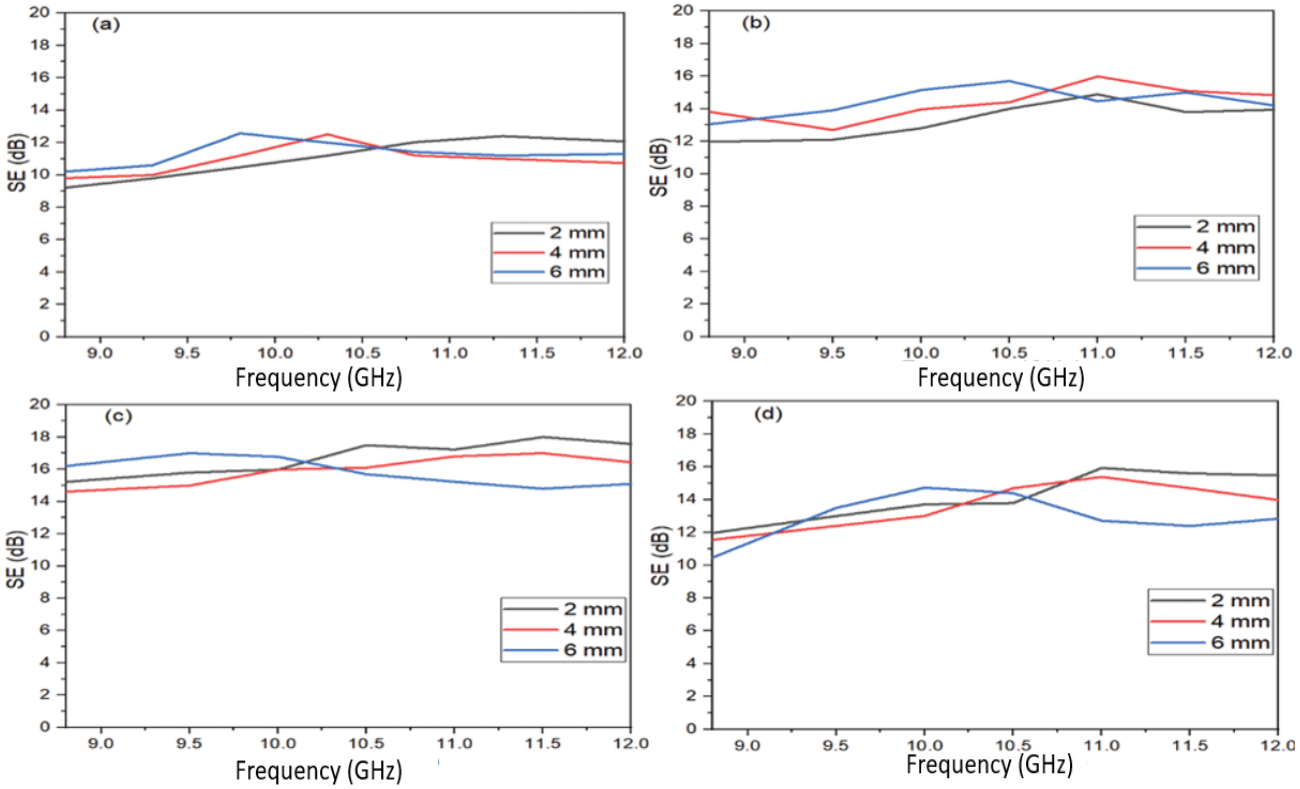

Figure 3.43 – SE curves of (a) pure CB nanopowder, (b) CB/F-11 nanocomposite, (c) CB/F-21 nanocomposite and (d) CB/F-31 nanocomposite at different thicknesses (2–4–6 mm)

Table 3.13 – MA behavior of CB/$Ni_{0.5}Zn_{0.5}Fe_2O_4$ nanocomposites and pure CB nanopowder at different thicknesses (2–4–6 mm)

Nanocomposite samples	t (mm)	RL_{min} (dB)	f_m (GHz)	$BW_{-10\ dB}$ (GHz)	SD (kg/m^2)
CB	2	-11.6	10.9	0.7	2.91
	4	-12.5	10.4	0.8	2.92
	6	-11.3	9.8	0.3	2.94
CB/F-11	2	-15.8	11.6	2.1	3.72
	4	-14.7	10.9	3.2	3.74
	6	-13.2	10.2	2.8	3.75
CB/F-21	2	-17.1	11.4	2.6	3.49
	4	-17.2	10.5	2.8	3.50
	6	-18.2	9.9	3.2	3.52
CB/F-31	2	-11.9	11.6	1.6	3.18
	4	-11.8	11.1	1.8	3.20
	6	-11.2	10.3	2.3	3.21

3.6.4.2 Microwave absorption properties of carbon black/MnNiZn ferrite nanocomposites

EMI shielding and MA properties of CB/$Mn_{0.1}Ni_{0.5}Zn_{0.4}Fe_2O_4$ nanocomposites were studied at a constant loading percentage of 40% w/w with the different weight ratios of CB/$Mn_{0.1}Ni_{0.5}Zn_{0.4}Fe_2O_4$ (1:1, 2:1, and 3:1). Figure 3.45 illustrates the RL of the prepared samples with different thicknesses (2–4–6 mm). The results demonstrated the RL attenuation peaks of samples moved to lower frequencies with increasing sample thickness. Table 3.14 shows the results of all the prepared absorbers. The best result obtained at this stage was by using CB/MF-21 nanocomposite. Figure 3.46 and Figure 3.47 represent the SE, SE_R and SE_A of the prepared samples.

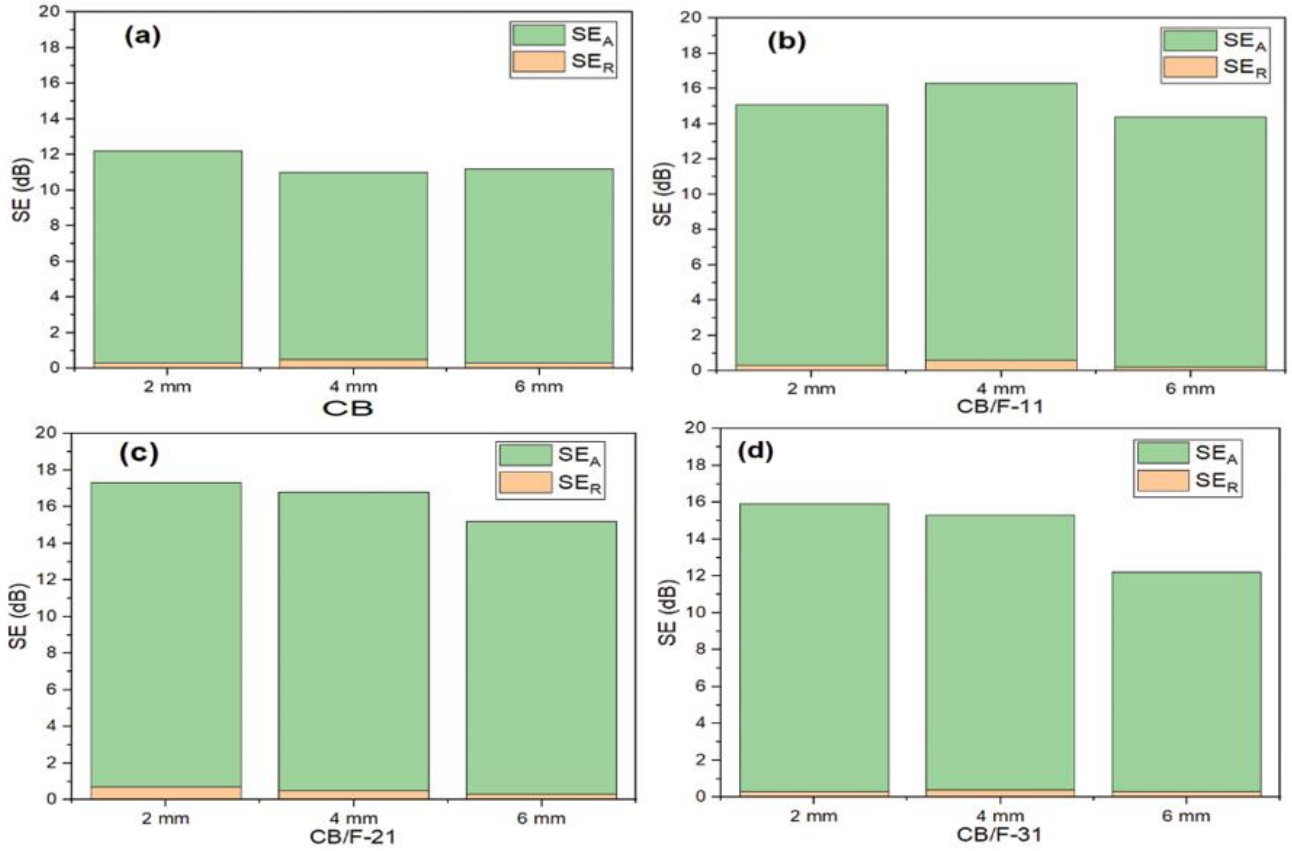

Figure 3.44 – Bar plot for individual components of SE_R and SE_A of (a) pure CB nanopowder, (b) CB/F-11 nanocomposite, (c) CB/F-21 nanocomposite and (d) CB/F-31 nanocomposite with different thicknesses (2–4–6 mm) at the frequency of 11 GHz

From the above studies, One can notice that the RL_{min}, SE_{max}, and $BW_{-10\ dB}$ were changed with the variation of the ferrite type used with carbon black. The best result was obtained by using the CB/$Mn_{0.1}Ni_{0.5}Zn_{0.4}Fe_2O_4$ nanocomposite (1:1) with a thickness of 2 mm. This improvement is due to the fact that these processes will affect the MA capacity by changing the complex permeability and permittivity.

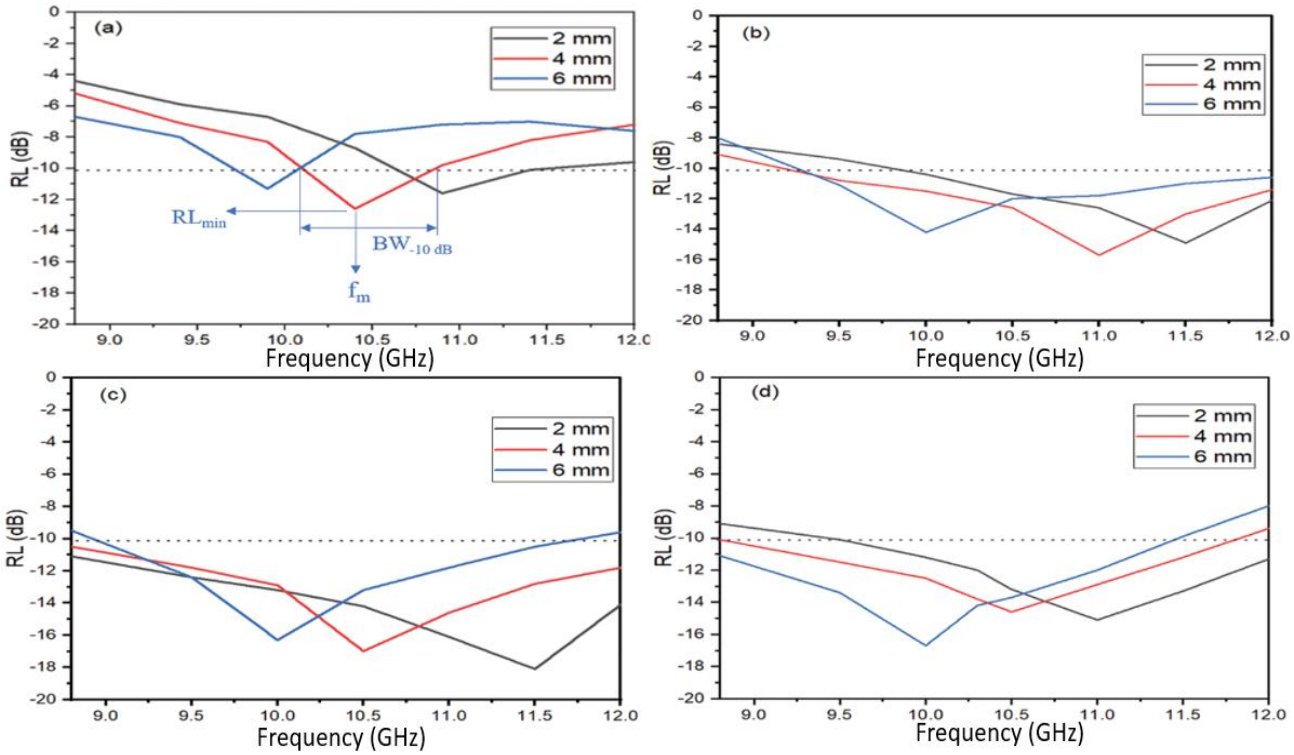

Figure 3.45 – RL curves of (a) pure CB nanopowder, (b) CB/MF-11 nanocomposite, (c) CB/MF-21 nanocomposite, and (d) CB/MF-31 nanocomposite at various thicknesses (2–4–6 mm)

Table 3.14 – MA behavior of CB/$Mn_{0.1}Ni_{0.5}Zn_{0.4}Fe_2O_4$ nanocomposites at various thicknesses (2–4–6 mm)

Nanocomposite samples	t (mm)	RL_{min} (dB)	f_m (GHz)	$BW_{-10\ dB}$ (GHz)	SD (kg/m^2)
CB	2	-11.6	10.9	0.7	2.91
	4	-12.5	10.4	0.8	2.92
	6	-11.3	9.8	0.3	2.94
CB/MF-11	2	-14.7	11.5	2.0	3.63
	4	-15.8	11.0	3.2	3.65
	6	-13.9	10.1	2.9	3.66
CB/MF-21	2	-18.3	11.4	3.2	3.40
	4	-17.2	10.5	3.2	3.41
	6	-17.1	10.0	2.8	3.43
CB/MF-31	2	-15.1	11.0	2.5	3.09
	4	-14.6	10.6	2.9	3.11
	6	-16.7	9.9	2.6	3.12

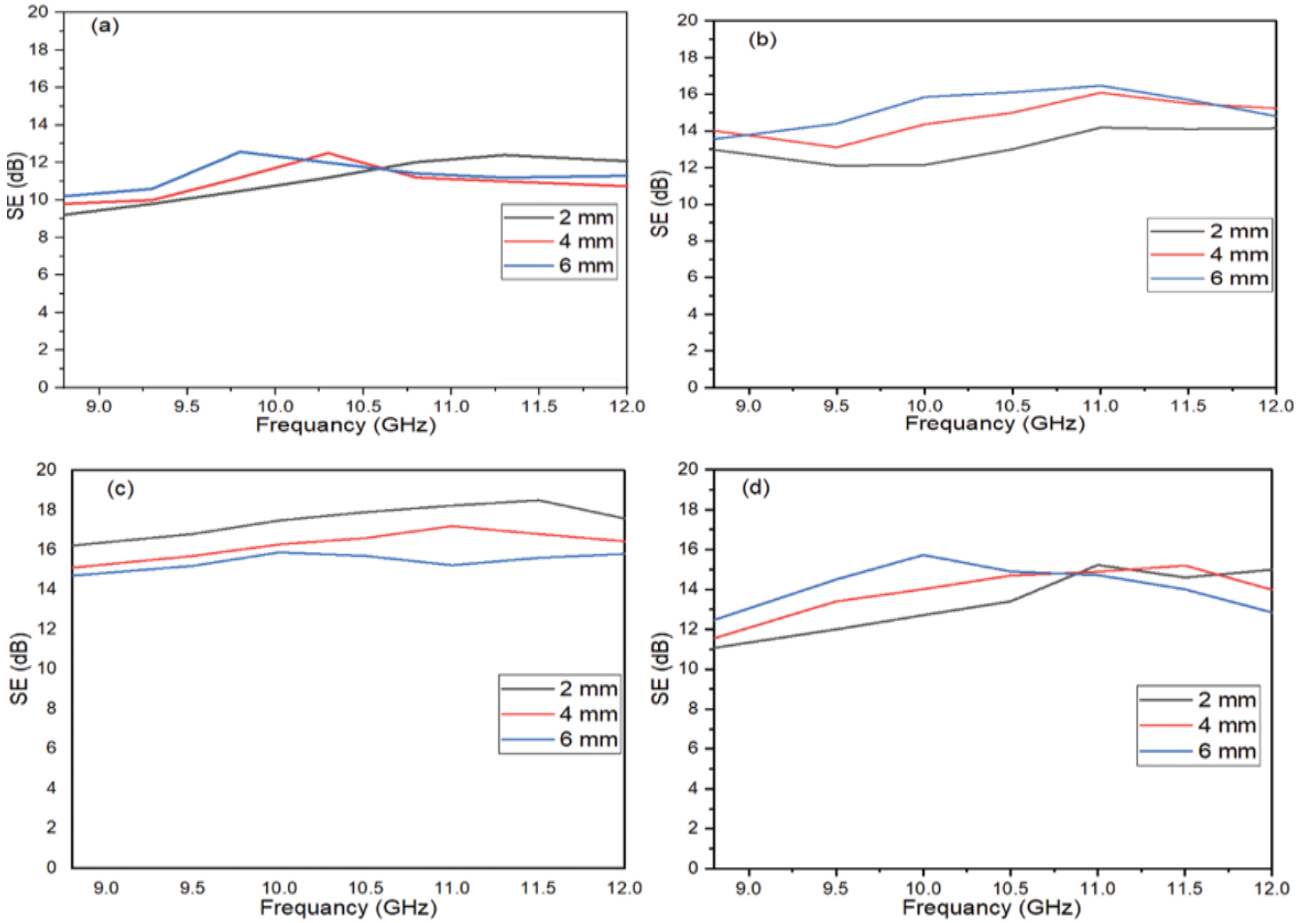

Figure 3.46 – SE curves of (a) pure CB nanopowder, (b) CB/MF-11 nanocomposite, (c) CB/MF-21 nanocomposite and (d) CB/MF-31 nanocomposite at various thicknesses (2–4–6 mm)

3.6.4.3 Microwave absorption properties of graphite/NiZn ferrite composites

EMI shielding and MA properties of C/$Ni^{3+}_{0.25}Ni^{2+}_{0.375}Zn^{2+}_{0.25}Fe_2O_4$ nanocomposites were studied at a constant loading percentage of 45% w/w with the different weight ratios of C/$Ni^{3+}_{0.25}Ni^{2+}_{0.375}Zn^{2+}_{0.25}Fe_2O_4$ (1:1, 2:1, and 3:1). Figure 3.48 displays the RL of the prepared samples with different thicknesses (2–4–6 mm). The results demonstrated the RL attenuation peaks of samples moved to lower frequencies with increasing sample thickness. Table 3.15 and Figure 3.49 show the results of all the prepared absorbers. The results revealed the impact of incorporating $Ni^{3+}_{0.25}Ni^{2+}_{0.375}Zn^{2+}_{0.25}Fe_2O_4$ and C on the SD, RL_{min}, SE_{max}, and $BW_{-10\,dB}$ of the prepared absorber. The best result obtained at this stage was by using the C/F-31 nanocomposite.

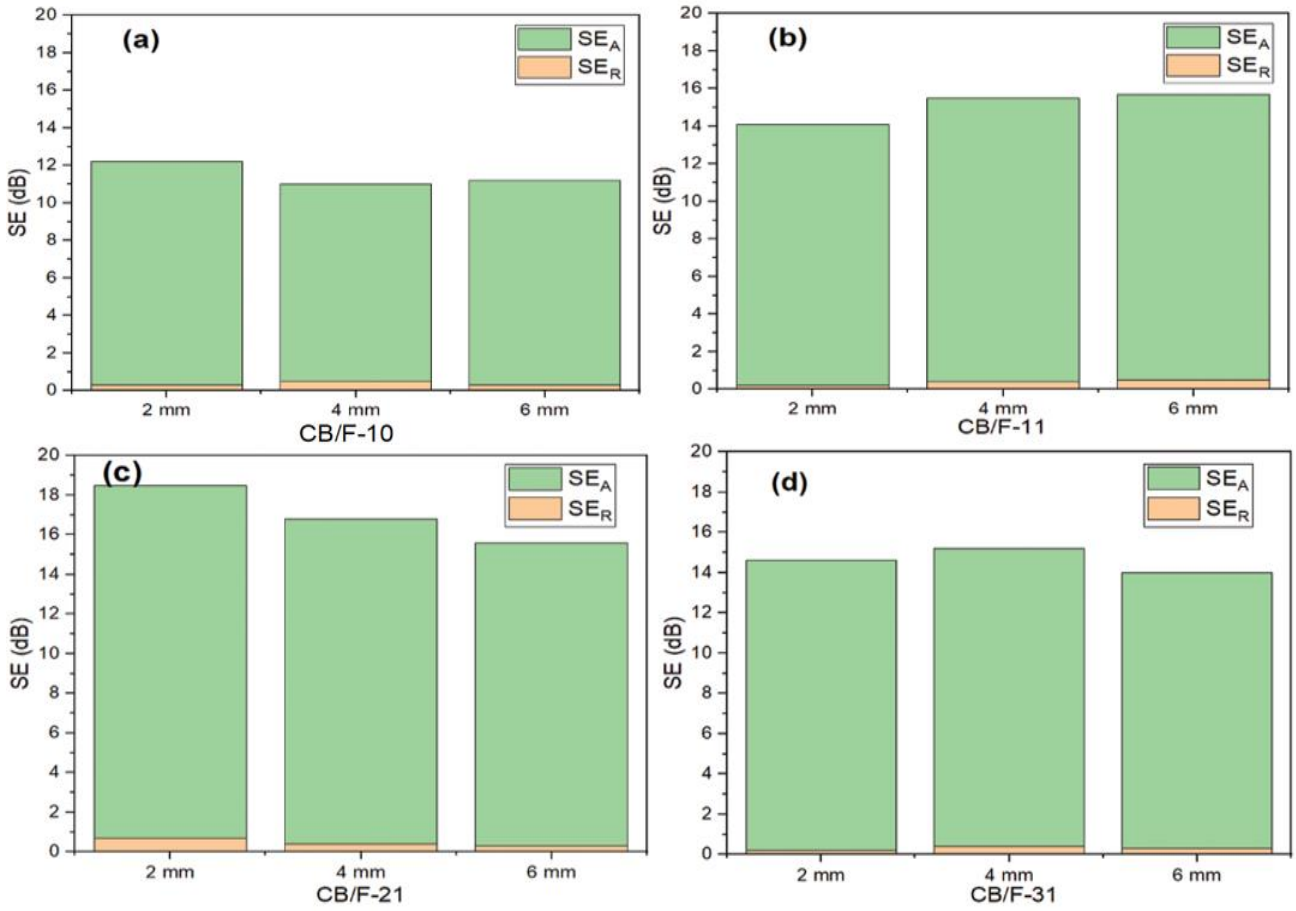

Figure 3.47 – Bar plot for individual components of SE_R and SE_A of (a) pure CB nanopowder, (b) CB/MF-11 nanocomposite, (c) CB/MF-21 nanocomposite and (d) CB/MF-31 nanocomposite with various thicknesses (2–4–6 mm) at the frequency of 11.5 GHz

Table 3.15 – MA behavior of $C/Ni^{3+}_{0.25}Ni^{2+}_{0.375}Zn^{2+}_{0.25}Fe_2O_4$ composites at different thicknesses (2–4–6 mm)

Nanocomposite samples	t (mm)	RL_{min} (dB)	f_m (GHz)	$BW_{-10\ dB}$ (GHz)	SD (kg/m^2)
C/F-11	2	-13.8	11.5	1.1	3.71
	4	-12.7	11.0	1.8	3.73
	6	-11.2	9.8	1.3	3.74
C/F-21	2	-13.1	11.0	1.9	3.51
	4	-12.7	10.6	1.6	3.52
	6	-14.8	10.1	2.2	3.54
C/F-31	2	-15.1	11.5	1.6	3.17
	4	-15.2	10.5	2.3	3.19
	6	-16.2	10.0	2.0	3.21

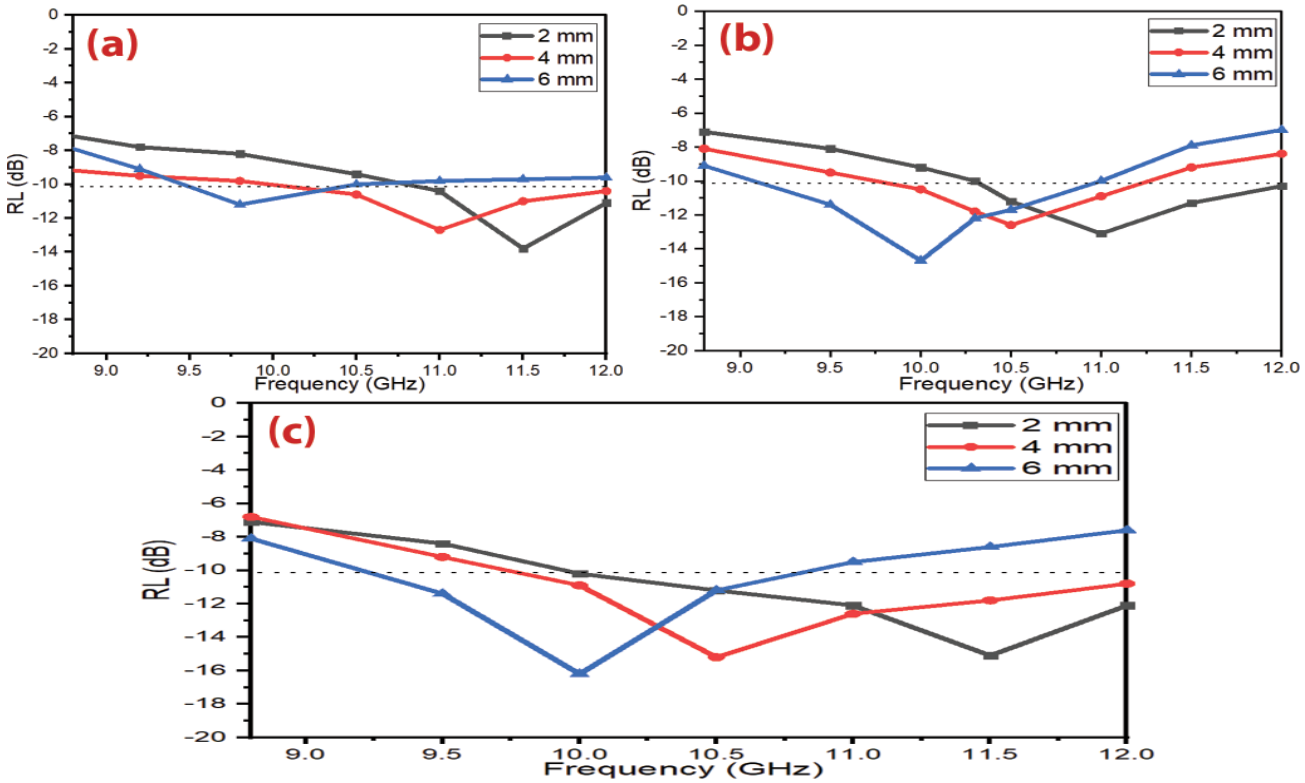

Figure 3.48 – RL curves of (a) C/F-11 composite, (c) C/F-21 composite, and (d) C/F-31 composite at various thicknesses (2–4–6 mm)

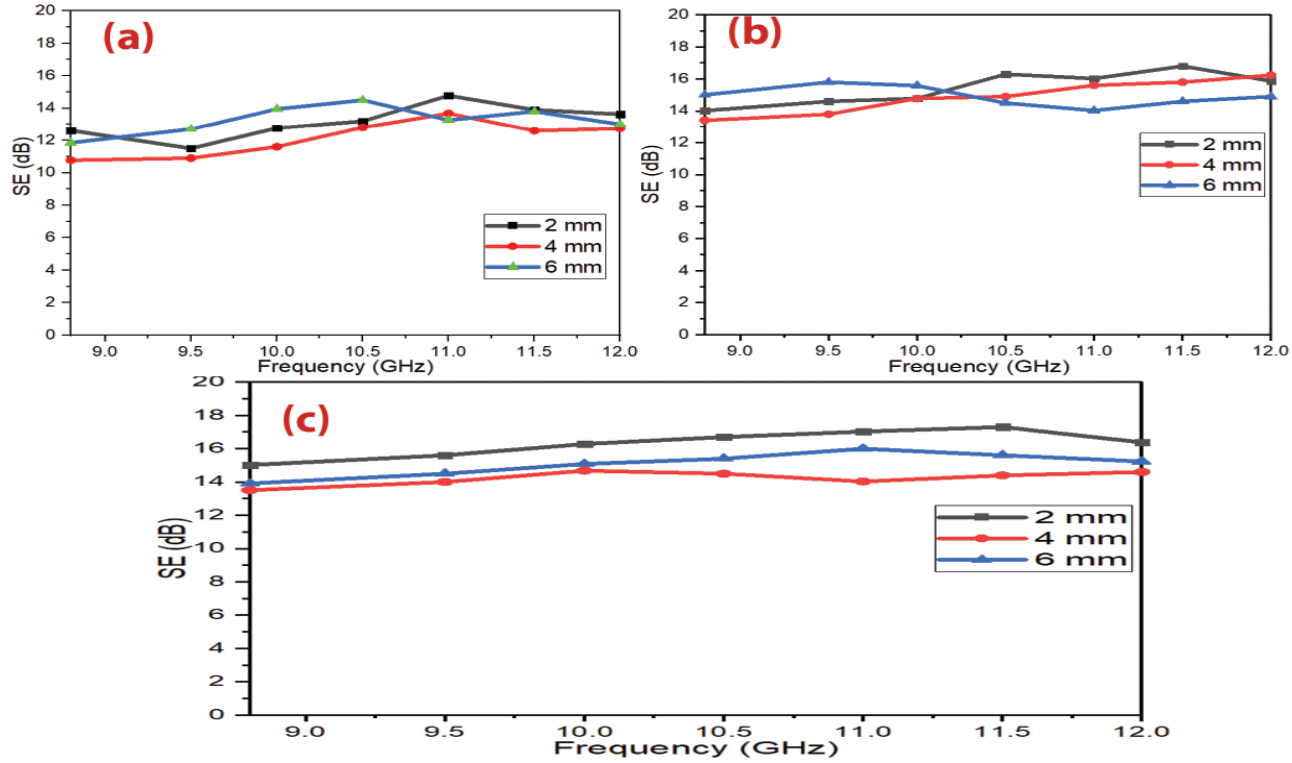

Figure 3.49 – SE curves of (a) C/F-11 composite, (b) C/F-21 composite, and (c) C/F-31 composite at various thicknesses (2–4–6 mm)

3.6.4.4 Microwave absorption properties of carbonyl iron/NiZn ferrite nanocomposites

EMI shielding and MA properties of CI/$Ni_{0.5}Zn_{0.5}Fe_2O_4$ nanocomposites were investigated at a loading percentage of 45% w/w with the different weight ratios of C/$Ni^{3+}_{0.25}Ni^{2+}_{0.375}Zn^{2+}_{0.25}Fe_2O_4$ (1:1, 2:1, and 3:1). Figure 3.50 displays the RL of the prepared samples with different thicknesses (2–4–6 mm). The results demonstrated the RL attenuation peaks of samples moved to lower frequencies with increasing sample thickness. Table 3.16 and Figure 3.51 represent the results of all the prepared absorbers. The results indicated a RL_{min} of -16.1 dB at 9.8 GHz for a thickness of 6 mm for the CI/F-21 nanocomposite sample. The SE_{max} was 16.5 dB at 11.2 GHz for the CI/F-21 nanocomposite sample. The results revealed the impact of incorporating $Ni_{0.5}Zn_{0.5}Fe_2O_4$ (magnetic loss material) and CI (magnetic loss material) on the SD, RL_{min}, SE_{max}, and $BW_{-10\ dB}$ of the prepared absorber. The defects of these absorbers are that they have a limited absorption $BW_{-10\ dB}$. This is due to the fact that the absorbers have a high complex relative permeability and low complex relative permittivity. This necessitated working to add CB to NiZn ferrite/carbonyl iron to increase the absorption $BW_{-10\ dB}$ to cover most of the X-band frequency and low the SD.

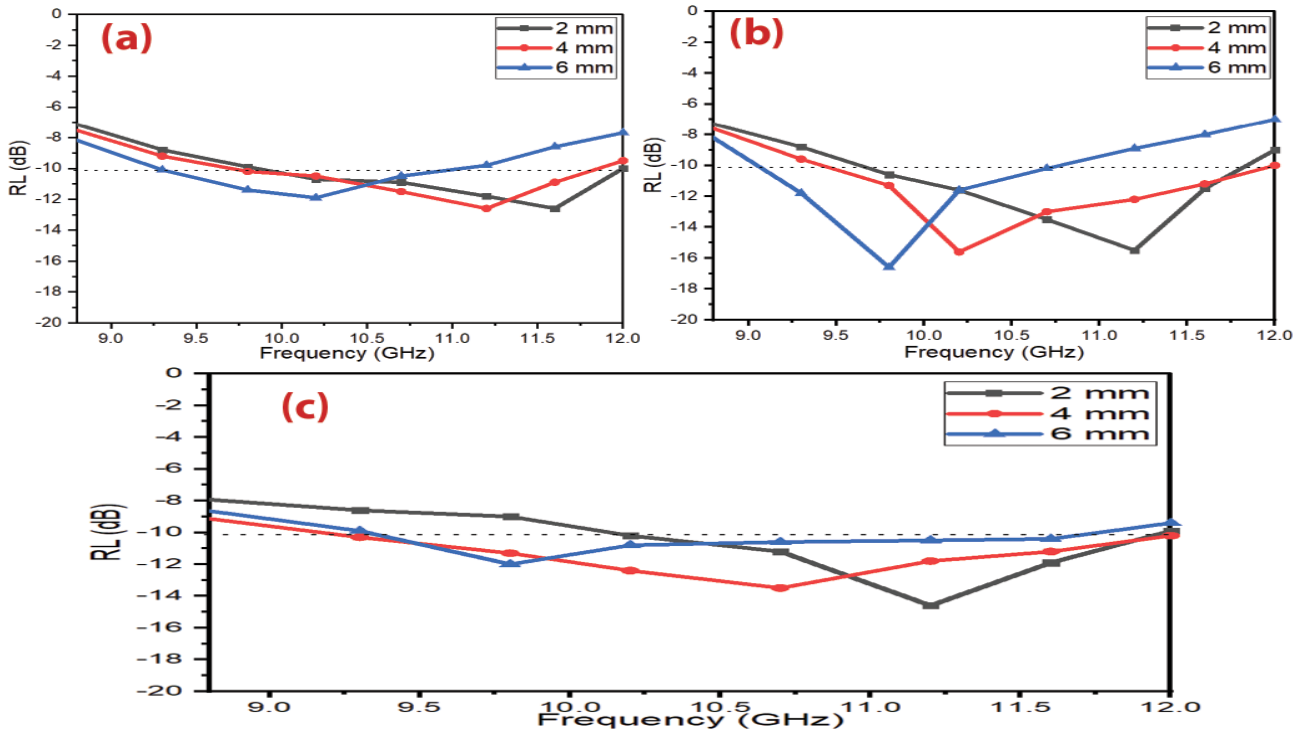

Figure 3.50 – RL curves of (a) CI/F-11 nanocomposite, (b) CI/F-21 nanocomposite and (c) CI/F-31 nanocomposite at different thicknesses (2–4–6 mm)

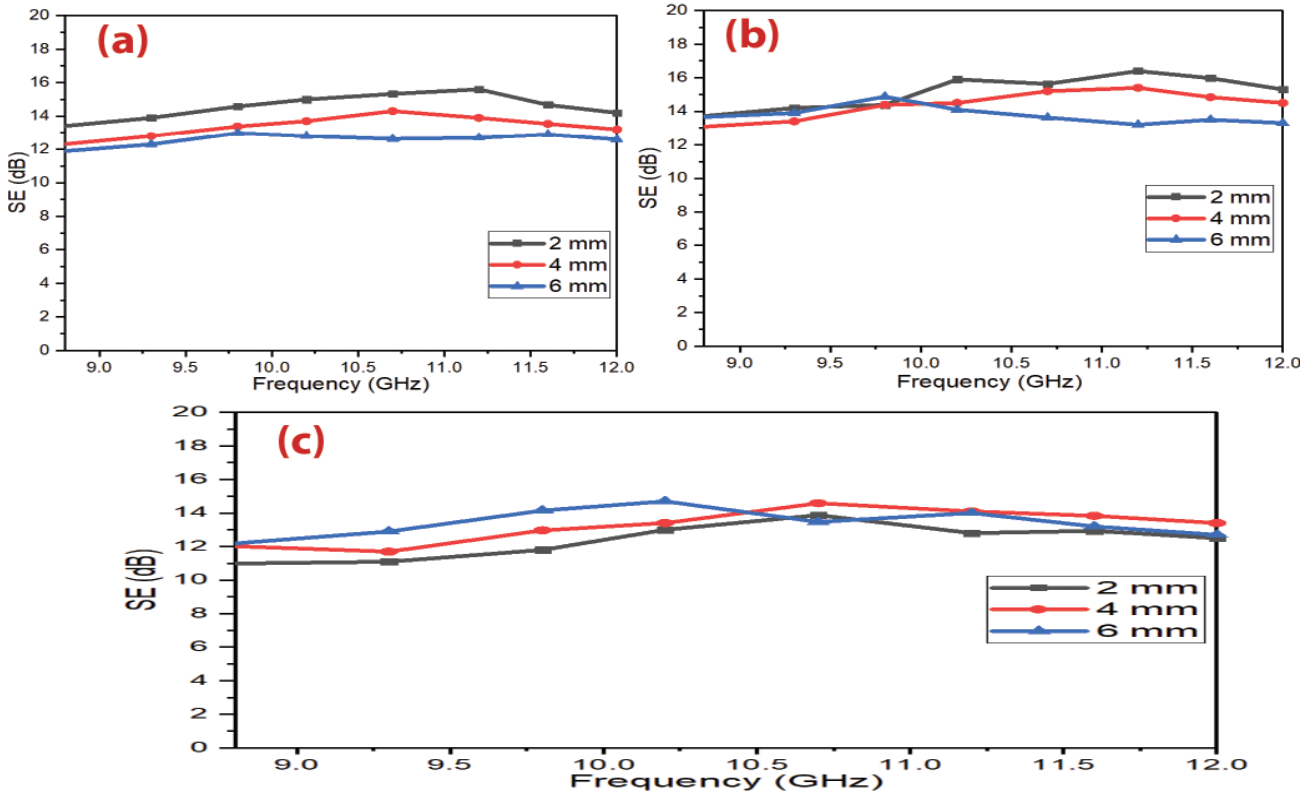

Figure 3.51 – SE curves of (a) CI/F-11 nanocomposite, (b) CI/F-21 nanocomposite and (c) CI/F-31 nanocomposite at different thicknesses (2–4–6 mm)

Table 3.16 – MA behavior of CI/$Ni_{0.5}Zn_{0.5}Fe_2O_4$ nanocomposites at different thicknesses (2–4–6 mm)

Nanocomposite samples	t (mm)	RL_{min} (dB)	f_m (GHz)	$BW_{-10\ dB}$ (GHz)	SD (kg/m^2)
CI/F-11	2	-12.6	11.6	2.2	4.52
	4	-12.5	11.2	2.0	4.54
	6	-11.9	10.2	1.8	4.55
CI/F-21	2	-15.5	11.2	2.1	4.76
	4	-15.6	10.2	2.5	4.77
	6	-16.1	9.8	1.8	4.79
CI/F-31	2	-14.6	11.2	1.8	4.91
	4	-13.5	10.7	2.8	4.92
	6	-12.0	9.8	2.2	4.94

3.6.4.5 Microwave absorption properties of ternary nanocomposites of NiZn ferrite/carbonyl iron/carbon black

EMI shielding and MA properties of $Ni_{0.5}Zn_{0.5}Fe_2O_4$/CI/CB nanocomposites were investigated at a loading percentage of 40% w/w with the different weight ratios of

$Ni_{0.5}Zn_{0.5}Fe_2O_4$/CI/CB (1:1:1, 1:1:2, and 2:1:1). Figure 3.52 displays the RL of the prepared samples with different thicknesses (2–4–6 mm). The results demonstrated the RL attenuation peaks of samples moved to lower frequencies with increasing sample thickness. Table 3.17 and Figure 3.53 represent the results of all the prepared absorbers. The results revealed the impact of incorporating $Ni_{0.5}Zn_{0.5}Fe_2O_4$, CI (magnetic loss materials) and CB (dielectric loss material) on the SD, RL_{min}, SE_{max}, and $BW_{-10\ dB}$ of the prepared absorber. This incorporation leads to obtaining a wider $BW_{-10\ dB}$, lower SD absorber, and loading percentage compared to the $Ni_{0.5}Zn_{0.5}Fe_2O_4$/CI absorber. The best result was obtained by using the F/CI/CB-211 nanocomposite sample. In order to evaluate the beneficial impact of adding CB to the F/CI on the microwave properties, Table 3.18 shows a comparison of the radar absorption properties of some lately reported carbon-based nanomaterials. The results of the literature show these composites are good in the C-band and Ku-band frequencies and limited in the X-band frequency. The presently prepared nanocomposites display in this research better MA in the X-band frequency. The distinct of these prepared nanocomposites have a lower loading percentage and thickness of the absorbers compared with the other literature.

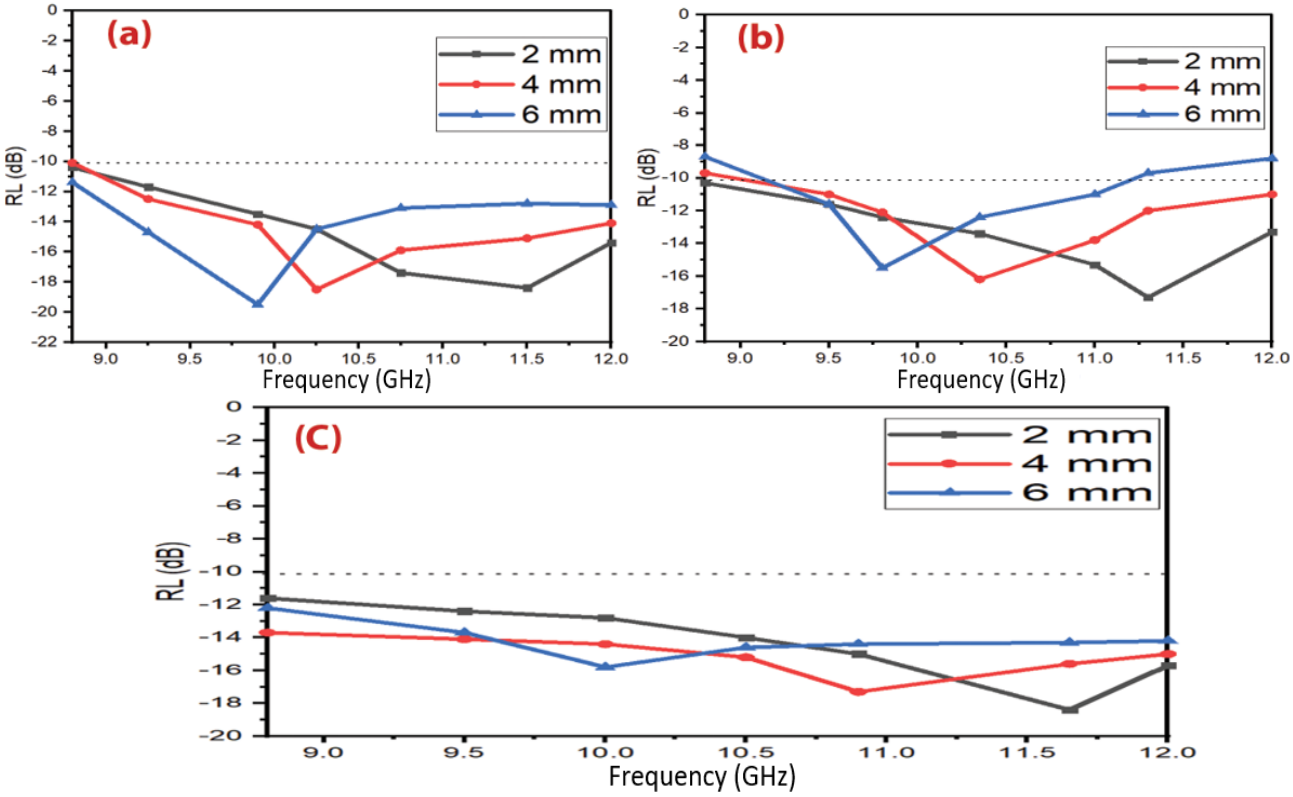

Figure 3.52 – RL curves of (a) F/CI/CB-111 composite, (b) F/CI/CB-112 composite and (c) F/CI/CB-211 composite at various thicknesses (2–4–6 mm)

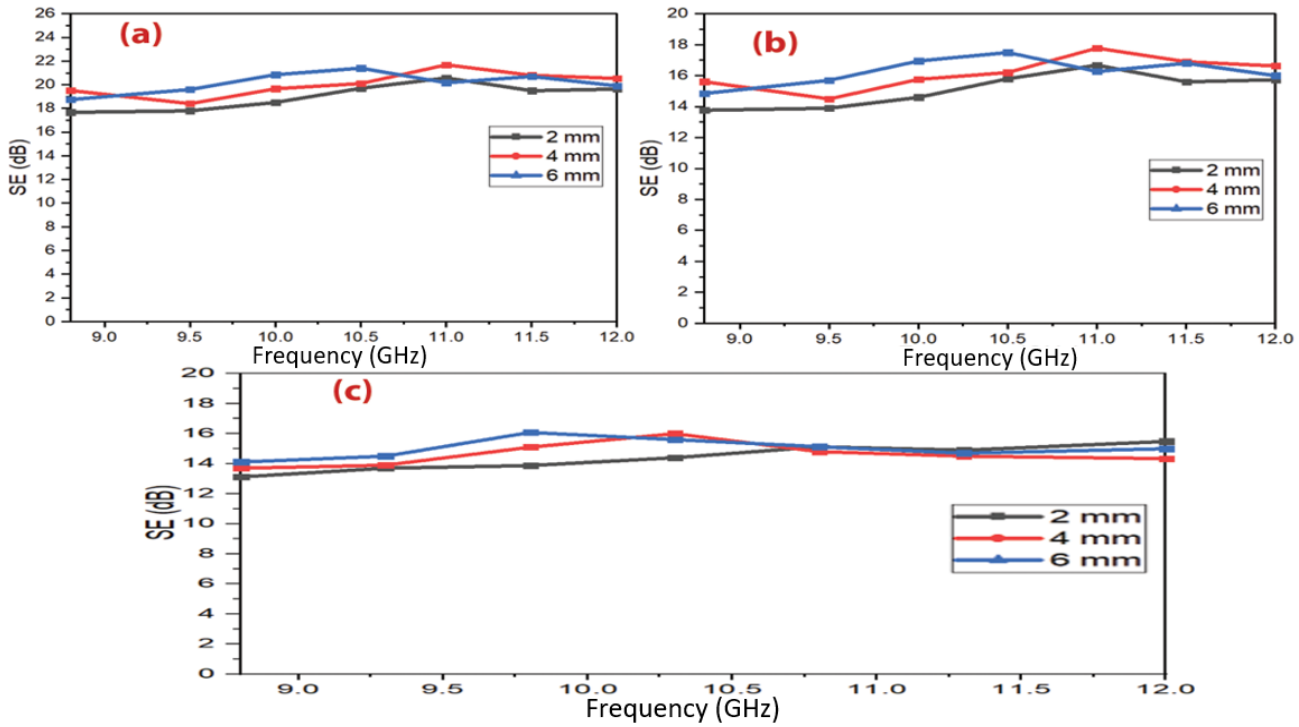

Figure 3.53 – SE curves of (a) F/CI/CB-111 composite, (b) F/CI/CB-112 composite and (c) F/CI/CB-211 composite at various thicknesses (2–4–6 mm)

Table 3.17 – MA behavior of $Ni_{0.5}Zn_{0.5}Fe_2O_4$/CI/CB composites at various thicknesses (2–4–6 mm)

Nanocomposite samples	t (mm)	RL_{min} (dB)	f_m (GHz)	$BW_{-10\ dB}$ (GHz)	SD (kg/m^2)
F/CI/CB-111	2	-18.3	11.5	3.2	3.86
	4	-18.5	10.3	3.2	3.87
	6	-19.4	9.9	3.2	3.89
F/CI/CB-112	2	-17.3	11.3	3.2	3.62
	4	-16.3	10.4	2.9	3.64
	6	-15.5	9.8	2.8	3.65
F/CI/CB-211	2	-18.4	11.7	3.2	4.01
	4	-17.3	10.9	3.2	4.02
	6	-15.8	10.0	3.2	4.04

3.6.4.6 Microwave absorption properties of double-layer of AC/F

Microwave absorption characteristics were studied for double-layer activated carbon/paraffin wax (AC) and $Mn_{0.1}Ni_{0.5}Zn_{0.4}Fe_2O_4$/paraffin wax (F) nanocomposites as shown in Figure 3.54. The AC/F-21 (activated carbon as a matching layer with a thickness of 1 mm and activated carbon as an absorbing layer with a thickness of 2 mm) exhibited a minimal reflection loss of -21.4 dB at 10.35 GHz and the absorption $BW_{-10\ dB}$

of 2.3 GHz. While the F/AC-12 (MnNiZn ferrite as a matching layer with a thickness of 1 mm and activated carbon as an absorbing layer with a thickness of 2 mm) exhibited a minimal reflection loss of -16.2 dB at 10.2 GHz and the absorption $BW_{-10\ dB}$ of 1.9 GHz. The results showed the significant effects of the layer positions of the absorbers on their MA characteristics are systematically studied by adjusting the matching and absorbing layers.

Table 3.18 – Radar absorption properties of carbon-based nanomaterials

Sample	t (mm)	f (GHz)	$BW_{-10\ dB}$ (GHz) (C-band)	$BW_{-10\ dB}$ (GHz) (X-band)	$BW_{-10\ dB}$ (GHz) (Ku-band)	Ref
$ZnFe_2O_4$/rGO	2.5	9.3	1.6	1.0	0	[126]
$NiFe_2O_4$/rGO	1.9	14.5	0	1.4	3.8	[127]
$CoFe_2O_4$/rGO	1.6	14.7	0	0	4.5	[128]
MWCNT/$Ni_{0.5}Zn_{0.5}Fe_2O_4$	2	10.40	0.08	0	0	[129]
CF/Fe_3O_4/BN	3.0	12.5	0	0.8	3.4	[130]
Ni/MWNT	4	7.2	2.2	1.2	0	[131]
Sm_2O_3/MWCNT	2	9.4	1.1	0.5	0	[132]
Fe/Fe_3C/MWCNT	2	9	1.6	0.8	0	[133]
	3.5	4.6	2.3	0	0	
Fe/CNTs	3.5	11.4	0	2.9	0	[134]
CoNC/CNTs	4.7	5.2	2.2	0	0	[135]
FeCo@CFs	1.6	16.6	0	3.5	0.9	[136]

Table 3.19 shows the radar absorption properties of double-layer activated carbon/paraffin wax (AC) and $Mn_{0.1}Ni_{0.5}Zn_{0.4}Fe_2O_4$/paraffin wax (F) nanocomposites. As a result, one can observe the effect of combining $Mn_{0.1}Ni_{0.5}Zn_{0.4}Fe_2O_4$ (magnetic loss material) and AC (dielectric loss material) on the EMI and MA properties of the prepared absorber. This incorporation leads to an effective and low-thickness absorber with a wide bandwidth. This is due to the fact that layer positions of the absorbers will affect the MA capacity by changing the complex permeability and permittivity.

Table 3.19 – Radar absorption properties of double-layer of AC/F nanocomposites

Sample symbols	t (mm)	RL_{min} (dB)	f_m (GHz)	$BW_{-10\ dB}$ (GHz)
AC/F-12	3	-13.1	11.0	1.9
AC/F-21	3	-21.4	10.35	2.3
AC/F-22	4	-13.6	11.2	1.4

F/AC12	3	-16.2	10.2	1.9
F/AC-21	3	-6.5	10.8	0
F/AC-22	4	-6.9	9.6	0

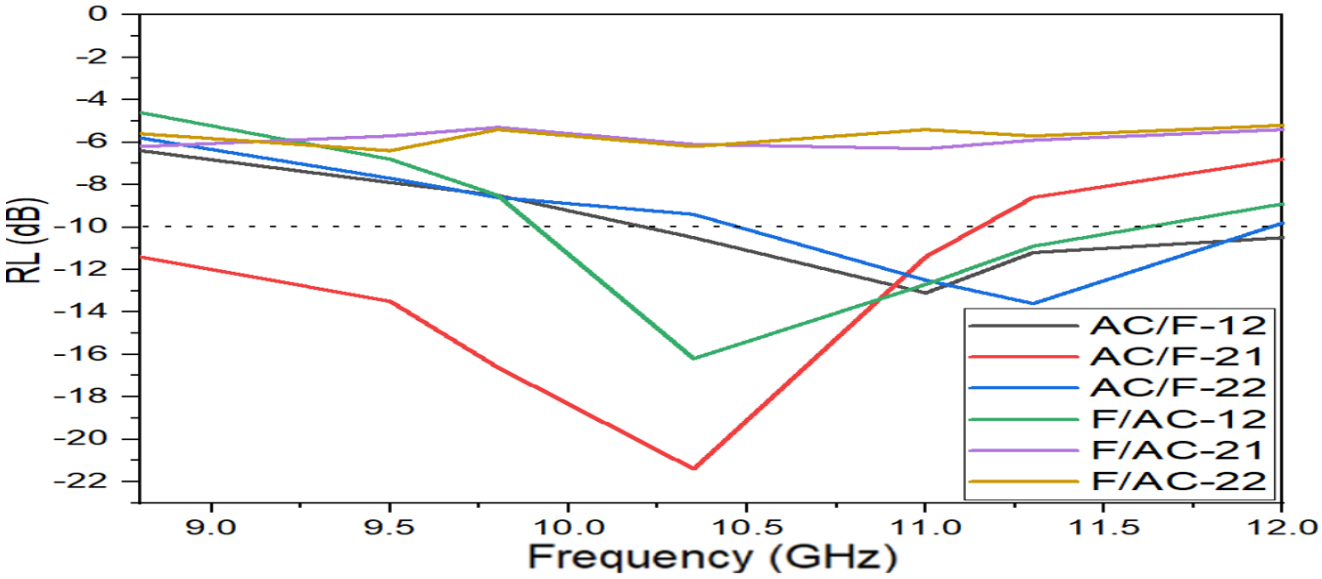

Figure 3.54 – RL curves of double-layer of AC/F nanocomposites at the frequency range of 8.8 to 12 GHz

3.6.5 Microwave absorption properties of PANI-based nanocomposites

Several variables that affect microwave absorption properties were studied, as follows: PANI-based nanocomposites type, weight ratios of PANI/$Ni^{3+}_{0.25}Ni^{2+}_{0.375}Zn^{2+}_{0.25}Fe_2O_4$, and PANI/$BaNiZnFe_{16}O_{27}$, and adding CB and CI to hybrid nanocomposites.

3.6.5.1 Effect of PANI/$Ni^{3+}_{0.25}Ni^{2+}_{0.375}Zn^{2+}_{0.25}Fe_2O_4$ hybrid nanocomposites morphology on the RL and the SE

EMI shielding and MA properties of the $Ni^{3+}_{0.25}Ni^{2+}_{0.375}Zn^{2+}_{0.25}Fe_2O_4$, PANI/F nanocomposites and PANI were studied. The results of this investigation are exhibited in Figure 3.55 and Table 3.20. Figure 3.55 illustrates the changing of the RL and SE as a function of the EM wave frequency for various weight ratios of PANI/$Ni^{3+}_{0.25}Ni^{2+}_{0.375}Zn^{2+}_{0.25}Fe_2O_4$ (1:1, 2:1, and 3:1). The thickness of the prepared samples was 2.90 mm. As illustrated in Figure 3.55, for the $Ni^{3+}_{0.25}Ni^{2+}_{0.375}Zn^{2+}_{0.25}Fe_2O_4$ nanoparticles, weak RL and low SE were observed. On the other hand, for the pure PANI, the RL was between 6.2–8.1 dB and the SE was between 9.6–12.5 dB. Furthermore, when PANI was incorporated with $Ni^{3+}_{0.25}Ni^{2+}_{0.375}Zn^{2+}_{0.25}Fe_2O_4$ nanoparticles, the RL increased to −18.6 dB at 11.3 GHz for PANI/F.2 nanocomposite and the SE increased to 23.18 dB at 11.1 GHz. As for the PANI/F.1 nanocomposite, the RL increased to −15.4 dB at 10.3 GHz and the SE increased to 22.1 dB at 11.0 GHz. This indicated a synergistic influence

in incorporating $Ni^{3+}_{0.25}Ni^{2+}_{0.375}Zn^{2+}_{0.25}Fe_2O_4$ nanoparticles and PANI. Nevertheless, this increase in RL and SE was not noticed for the PANI/F.3 composite. This referred to the MA and EMI shielding properties related to the nanocomposite morphology. One can observe from the EDX spectrum with increasing the PANI in nanocomposites, the carbon will increase and iron will decrease inside them which will affect the morphology of the particles. The mixture of agglomerated particles and rod-like morphology appeared to show the best MA and EMI shielding properties. The absorption BW_{-10dB} was 1.8 GHz with a SD of 3.04 for the PANI/F.2 nanocomposite. In contrast, the absorption BW_{-10dB} was 1.9 GHz with a SD of 3.22 for the PANI/F.1 nanocomposite. While no absorption BW_{-10dB} was noticed for PANI, $Ni^{3+}_{0.25}Ni^{2+}_{0.375}Zn^{2+}_{0.25}Fe_2O_4$ and PANI/F.3 nanocomposite. Figure 3.55 shows the SE_R and SE_A of PANI/F nanocomposites with a thickness of 2.90 mm at the frequency of 11.0 GHz.

3.6.5.2 Effect of sample thickness on the RL

Figure 3.56 illustrates the RL of PANI/F.2 nanocomposite with different thicknesses at the loading percentage of 25% w/w. Figure 4.56 illustrates that the RL attenuation peaks of samples moved to lower frequencies with increasing sample thickness. This phenomenon may be defined by the quarter-wavelength (λ/4) cancellation model, as shown in equation (1.5).

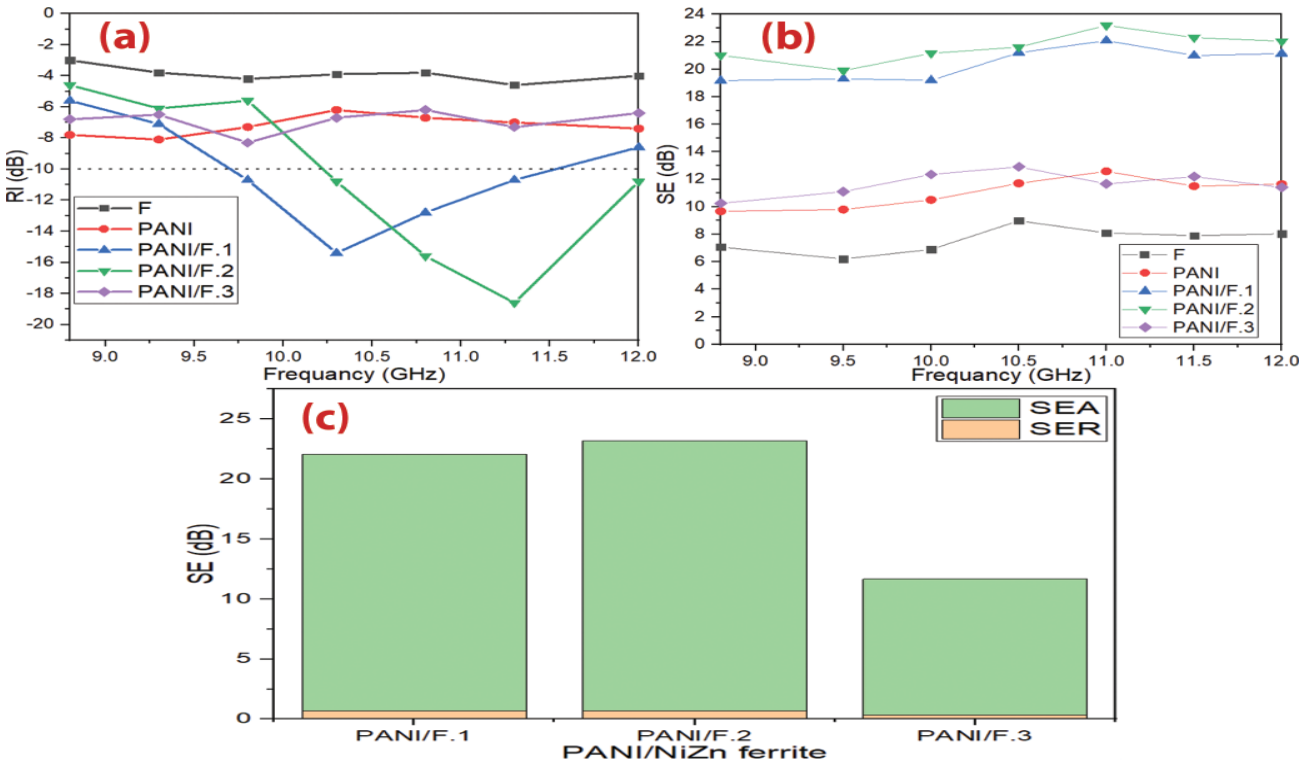

Figure 3.55 (a,b) – RL and SE curves of $Ni^{3+}_{0.25}Ni^{2+}_{0.375}Zn^{2+}_{0.25}Fe_2O_4$, PANI/$Ni^{3+}_{0.25}Ni^{2+}_{0.375}Zn^{2+}_{0.25}Fe_2O_4$ nanocomposites and pure PANI at 2.9 mm thickness

and (c) bar plot for individual components of SE_R and SE_A with a thickness of 2.90 mm at the frequency of 11.0 GHz

Table 3.20 – MA behavior of $Ni^{3+}_{0.25}Ni^{2+}_{0.375}Zn^{2+}_{0.25}Fe_2O_4$, PANI/$Ni^{3+}_{0.25}Ni^{2+}_{0.375}Zn^{2+}_{0.25}Fe_2O_4$ nanocomposites and pure PANI at 2.9 mm thickness

Samples	RL_{min} (dB)	f_m (GHz)	$BW_{-10\ dB}$ (GHz)	SD (kg/m^2)
$Ni^{3+}_{0.25}Ni^{2+}_{0.375}Zn^{2+}_{0.25}Fe_2O_4$	-4.2	-	-	4.53
PANI	-8.1	-	-	2.21
PANI/F.1	-15.4	10.2	1.9	3.22
PANI/F.2	-18.6	11.3	1.8	3.04
PANI/F.3	-8.3	-	-	2.96

It can be noticed from equation (1.5) that the f_m is inversely proportionate to the thickness of an absorber. One can conclude that the optimal matching and absorption can be accomplished by modifying the thickness of an absorber (Table 3.21).

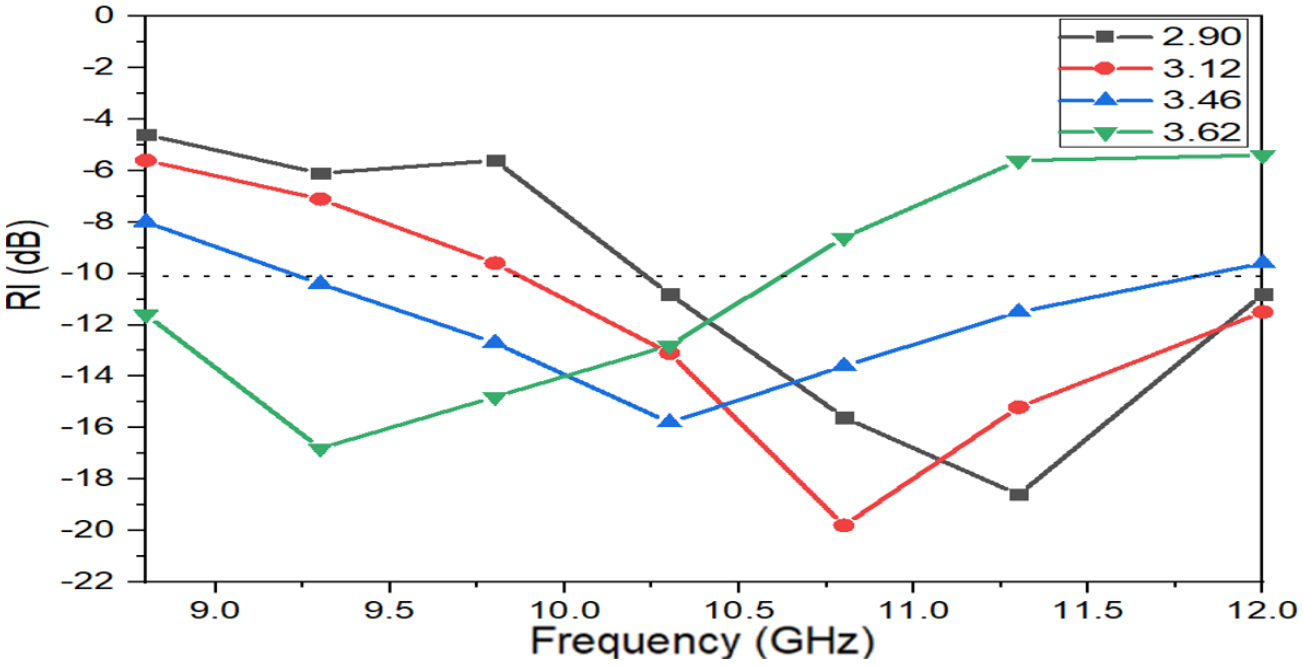

Figure 3.56 – RL curves of PANI/F.2 hybrid nanocomposite at various thicknesses

Table 3.21 – MA behavior of PANI/F.2 hybrid nanocomposite at various thicknesses

PANI/F.2	t (mm)	RL_{min} (dB)	f_m (GHz)	BW_{-10dB} (GHz)	SD (kg/m^2)
	2.90	-18.6	11.3	1.8	3.04
	3.12	-19.8	10.8	2.2	3.07
	3.46	-15.7	10.2	2.7	3.09
	3.62	-16.9	9.3	1.7	3.12

3.6.5.3 Influence of the incorporation of $Ni_{0.5}Zn_{0.5}Fe_2O_4$, CI and PANI on the RL and the SE

EMI shielding and MA properties of the $Ni_{0.5}Zn_{0.5}Fe_2O_4$, CI, PANI, PANI/CI and PANI/F/CI nanocomposite were investigated. The results of this investigation are exhibited in Figure 3.57 and Table 3.22. Figure 3.57 illustrates the changing of the RL and SE as a function of the EM wave frequency for $Ni_{0.5}Zn_{0.5}Fe_2O_4$, CI, PANI, PANI/CI and PANI/F/CI nanocomposite. The thickness of the prepared samples was 3.2 mm. As illustrated in Figure 3.57, for the $Ni_{0.5}Zn_{0.5}Fe_2O_4$ and CI, weak RL and low SE were observed. The defect of the $Ni_{0.5}Zn_{0.5}Fe_2O_4$ and CI are that they have low complex relative permittivity. On the other hand, for the pure PANI, the RL was between 6.6–8.5 dB and the SE was between 9.8–12.9 dB. The defect of the PANI is that it has low complex relative permeability. Furthermore, when PANI was incorporated with ferrite, which was mixed with carbonyl iron, the RL increased to −25.7 dB at 11.3 GHz for PANI/F/CI composite and the SE increased to 30.12 dB at 11.0 GHz. As a result, one can notice the impact of incorporating $Ni_{0.5}Zn_{0.5}Fe_2O_4$ and CI (magnetic loss materials) and PANI (dielectric loss material) on the EMI and MA properties of the prepared absorber. This incorporation leads to an effective and low-thickness absorber with a wide BW_{-10dB} [82]. Figure 3.57 shows the SE_R and SE_A of the $Ni_{0.5}Zn_{0.5}Fe_2O_4$, CI, PANI, PANI/CI and PANI/F/CI composite with a thickness of 3.2 mm at the frequency of 11.0 GHz.

Table 3.22 – MA behavior of $Ni_{0.5}Zn_{0.5}Fe_2O_4$, CI, PANI, PANI/CI and PANI/F/CI composite at 3.2 mm thickness

Samples	RL_{min} (dB)	f_m (GHz)	$BW_{-10\ dB}$ (GHz)	SD (kg/m^2)
$Ni_{0.5}Zn_{0.5}Fe_2O_4$	-4.6	-	-	4.56
CI	-6.5	-	-	5.21
PANI	-8.5	-	-	2.25
PANI/CI	-21.3	10.2	2.7	3.36
PANI/F/CI	-25.7	11.3	2.6	3.31

3.6.5.4 Influence of sample thickness and loading ratio of the absorption material within paraffin on the RL

Figure 3.58 illustrates the RL of PANI/F/CI composite with various thicknesses (3.2, 3.4 and 3.6 mm) at the various loading percentages (30% w/w and 35% w/w). Figure 3.58 shows that the RL attenuation peaks of samples moved to lower frequencies with increasing sample thickness.

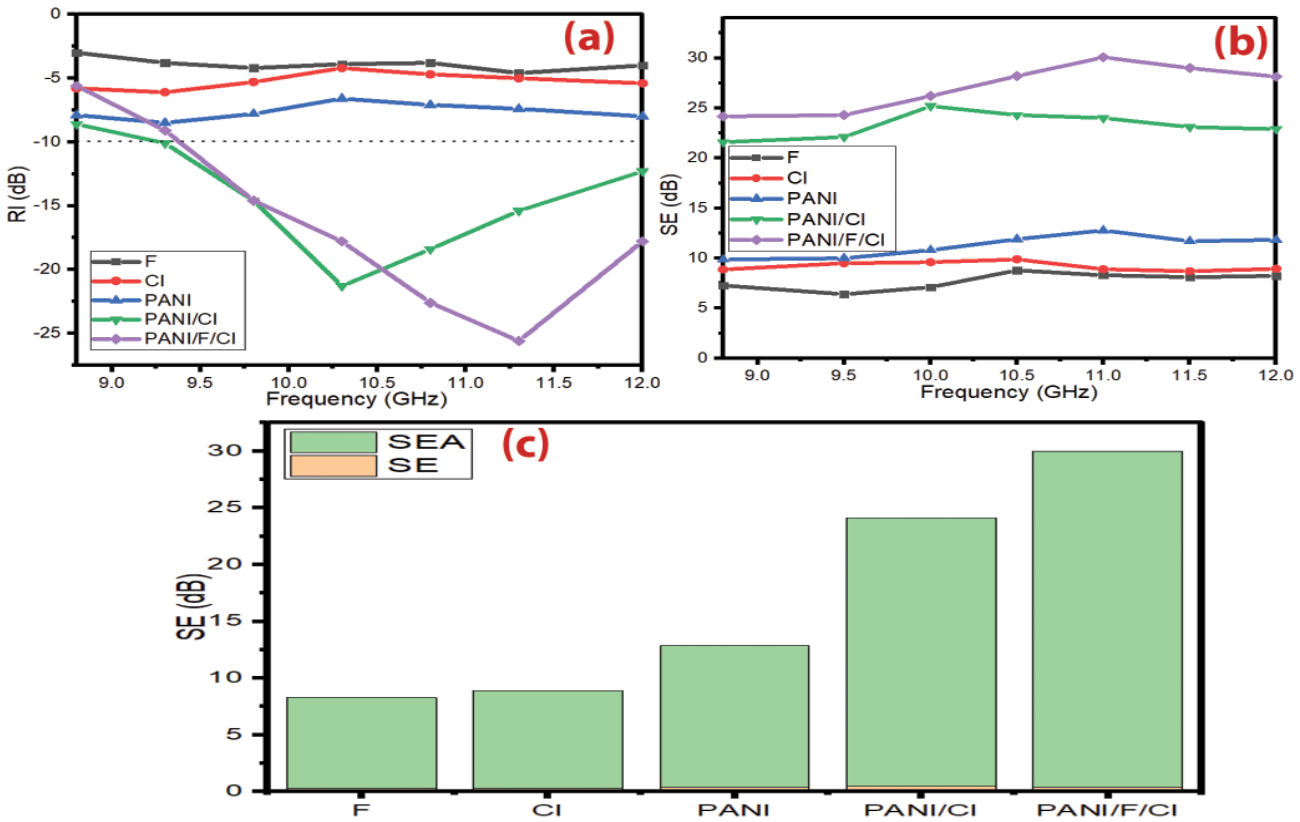

Figure 3.57 (a,b) – RL and SE curves of $Ni_{0.5}Zn_{0.5}Fe_2O_4$, CI, PANI, PANI/CI and PANI/F/CI composite at 3.2 mm thickness. SE curves of $Ni_{0.5}Zn_{0.5}Fe_2O_4$, CI, PANI and PANI/F/CI composite at 3.2 mm thickness and (c) bar plot for individual components of SE_R and SE_A of $Ni_{0.5}Zn_{0.5}Fe_2O_4$, CI, PANI and PANI/F/CI composite with a thickness of 3.2 mm at the frequency of 11.0 GHz

On the other hand, one can notice the RL_{min} moves gradually to a lower frequency with the increase in the loading percentage within a paraffin matrix (Figure 4.124). Furthermore, Table 3.23 shows the PANI/F/CI composites have reasonable SD, ranging from 3.31 to 3.40 kg/m^2, and wide BW_{-10dB} extending from 2.5 to 3.0 GHz. The absorption percentage of microwaves reached about 99.9% with a loading percentage of 30%. One can conclude that optimal absorption can be accomplished by modifying the absorber thickness and the loading percentage.

Table 3.23 – MA behavior of PANI/F/CI composite at various thicknesses and various loading ratios within a paraffin matrix

Loading ratio %	t (mm)	RL_{min} (dB)	f_m (GHz)	BW_{-10dB} (GHz)	SD (kg/m^2)
30%	3.2	-25.7	11.3	2.6	3.31
	3.4	-28.5	10.8	3.0	3.35
	3.6	-26.8	9.8	2.9	3.37

35%	3.2	-28.6	10.8	2.5	3.33
	3.4	-30.8	10.3	2.8	3.38
	3.6	-28.4	9.3	2.6	3.40

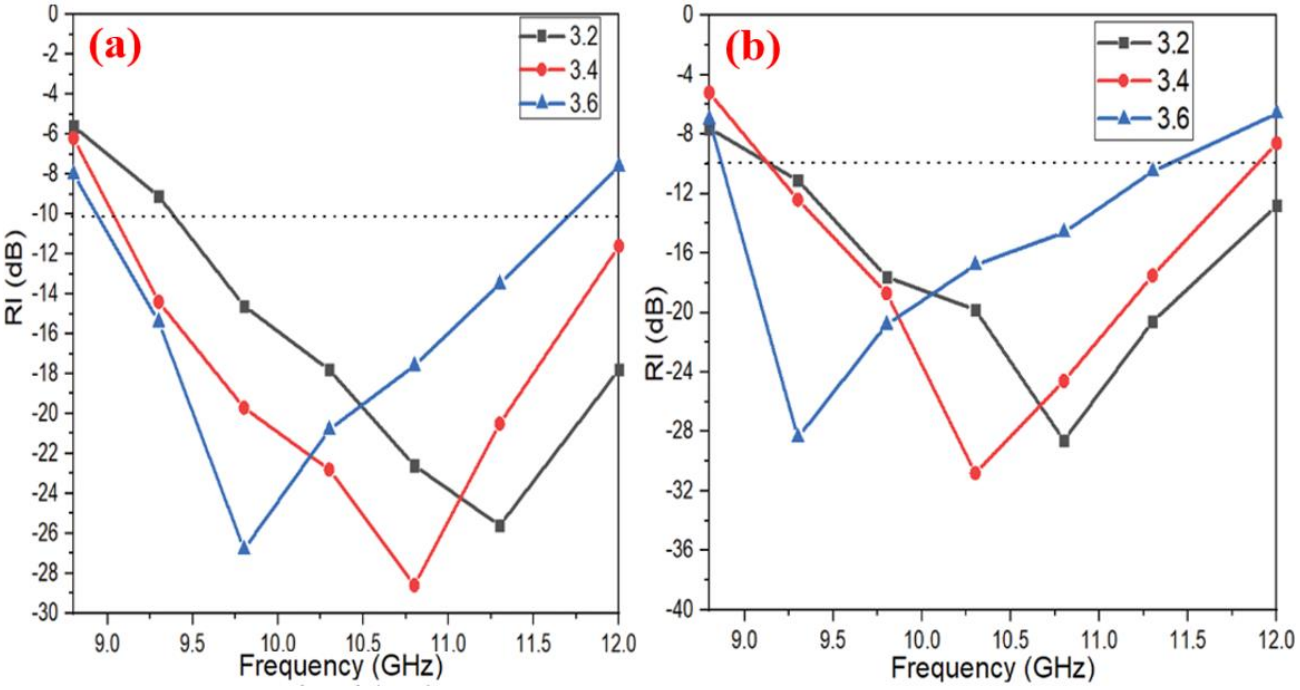

Figure 3.58 – RL curves of PANI/F/CI composite with various thicknesses (3.2, 3.4, 3.6 mm) at the various weight ratios of the absorber within a paraffin matrix (a) 30% and (b) 35%

3.6.5.5 Influence of the incorporation of $Ni^{3+}_{0.25}Ni^{2+}_{0.375}Zn^{2+}_{0.25}Fe_2O_4$, CB and PANI on the RL and the SE

EMI shielding and MA properties of the PANI/CB and PANI/F/CB nanocomposites were studied. The results of this investigation are exhibited in Figures 3.59 and Table 3.24. Figures 3.59 illustrates the changing of the RL and SE as a function of the EM wave frequency for PANI/CB and PANI/F/CB nanocomposites at the loading percentage of 30% w/w. The thickness of the prepared samples was 3.0 mm. As illustrated in Figure 3.59, for the PANI/CB, weak RL and medium SE were observed. The defect of the PANI/CB is that it has low complex relative permeability. On the other hand, when PANI/CB was incorporated with ferrite, the RL increased to −17.2 dB at 9.9 GHz for PANI/70%F/30%CB nanocomposite and the SE increased to 19.7 dB at 11.1 GHz. As a result, this improvement is due to the fact that this combination will affect the MA capacity by changing the complex permeability and permittivity. This combination leads to an effective and low-thickness absorber with a wide BW_{-10dB} [82].

Table 3.24 – MA behavior of PANI/CB and PANI/F/CB nanocomposites at 3.0 mm thickness

Samples	RL_{min} (dB)	f_m (GHz)	$BW_{-10\ dB}$ (GHz)	SD (kg/m^2)
PANI/CB	-8.4	10.5	0	2.62
PANI/50%F/50%CB	-15.6	11.0	2.8	2.91
PANI/70%F/30%CB	-17.2	9.9	2.8	3.02
PANI/90%F/10%CB	-15.1	10.5	3.2	3.15

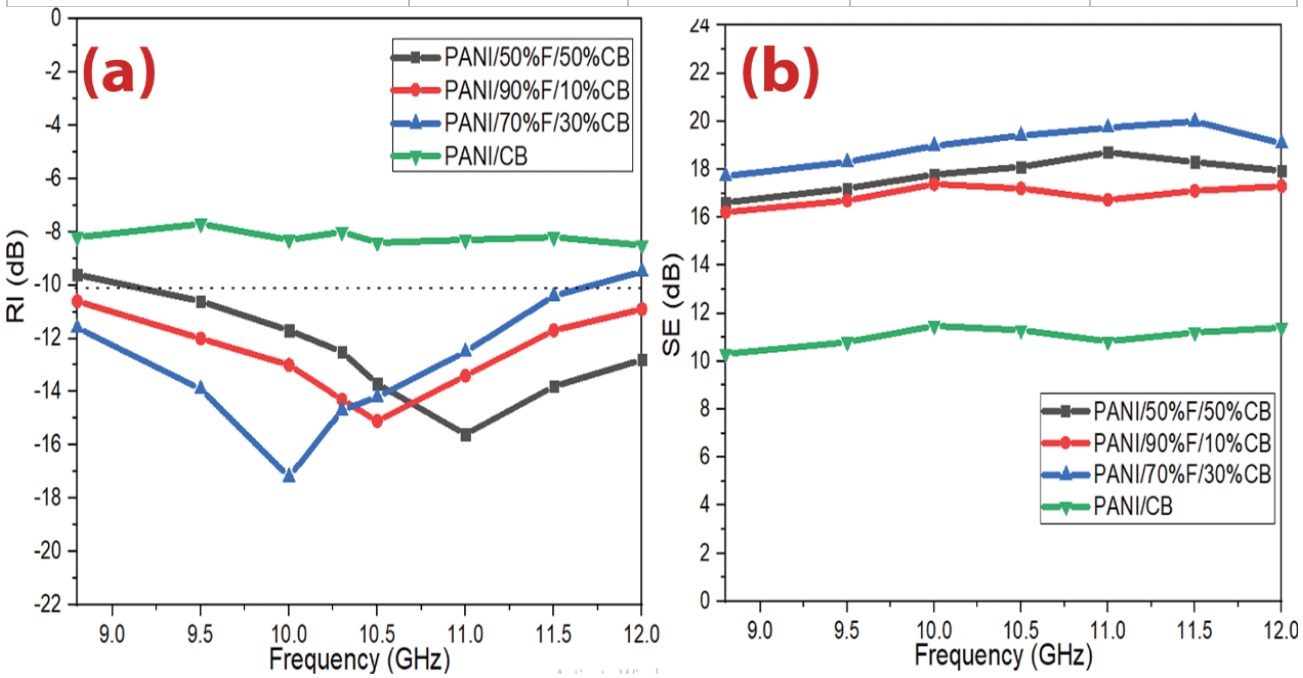

Figure 3.59 (a,b) – RL and SE curves of PANI/CB and PANI/F/CB nanocomposites at 3.0 mm thickness

3.6.5.6 Effect of PANI/$BaNiZnFe_{16}O_{27}$ hybrid nanocomposites morphology on the RL and the SE

EMI shielding and MA properties of the HF and PANI/HF nanocomposites were investigated. The results of this investigation are exhibited in Figure 3.60 and Table 3.25. Figure 3.60 illustrates the changing of the RL and SE as a function of the EM wave frequency for various weight ratios of PANI/HF at the loading percentage of 30% w/w. The thickness of the prepared samples was 3.0 mm. As illustrated in Figure 3.60, for the $BaNiZnFe_{16}O_{27}$ nanoparticles, weak RL and low SE were noticed. That is due to low complex relative permittivity. To improve the RL and SE of $BaNiZnFe_{16}O_{27}$. That requires incorporation with PANI. As a result, the RL increased to −17.0 dB at 11.6 GHz for PANI/HF.2 nanocomposite and the SE increased to 17.9 dB at 10.2 GHz. This refers to the MA and EMI shielding properties being related to the morphology of the

nanocomposite. In reality, the mixture of agglomerated particles and rod-like morphology appears to show the best MA and EMI shielding properties. As a result, one can observe the effect of combining $BaNiZnFe_{16}O_{27}$ (magnetic loss material) and PANI (dielectric loss material) on the EMI and MA properties of the prepared absorber. This incorporation leads to an effective and low-thickness absorber with a wide BW_{-10dB}.

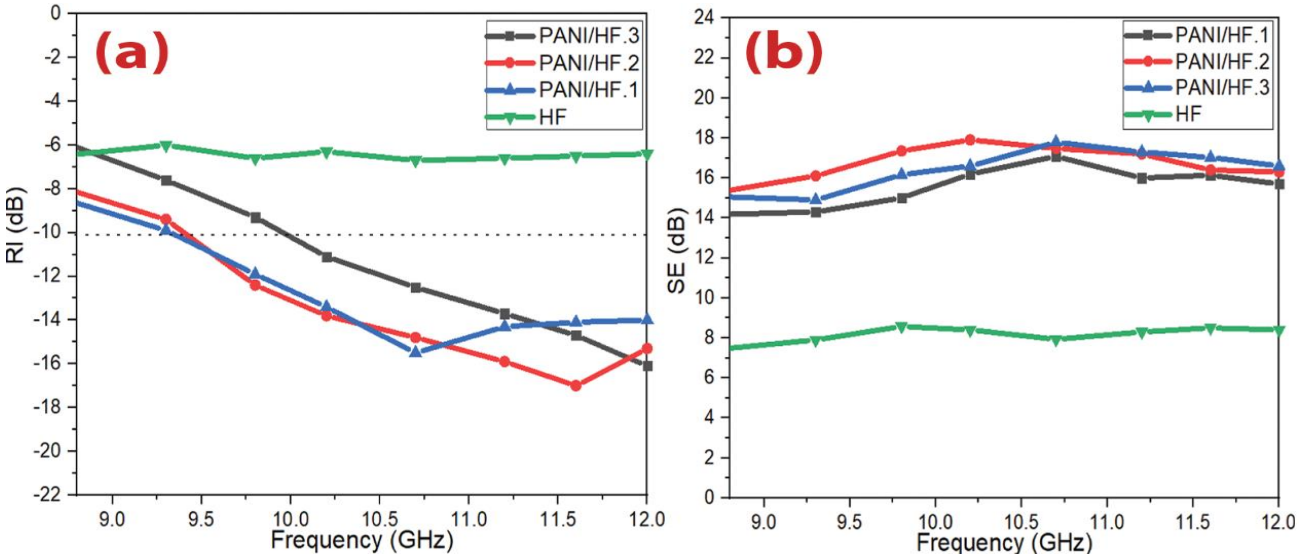

Figure 3.60 (a,b) – RL and SE curves of PANI/HF nanocomposites at 3.0 mm thickness. SE curves of PANI/HF nanocomposites at 3.0 mm thickness

Table 3.25 – MA behavior of HF and PANI/HF nanocomposites at 3.0 mm thickness

Samples	RL_{min} (dB)	f_m (GHz)	$BW_{-10\ dB}$ (GHz)	SD (kg/m^2)
HF	-6.7	10.6	0	4.61
PANI/HF.1	-15.6	10.7	2.7	3.74
PANI/HF.2	-17.0	11.6	2.6	3.57
PANI/HF.3	-16.1	12.0	2.5	3.16

3.6.5.7 Microwave absorption properties of PANI/SF/HF and PANI/SF/HF/CB nanocomposites

EMI shielding and MA properties of the PANI/SF/HF and PANI/SF/HF/CB nanocomposites were studied. The results of this investigation are exhibited in Figure 3.61 and Table 3.26. Figure 3.61 illustrates the changing of the RL and SE as a function of the EM wave frequency for PANI/SF/HF and PANI/SF/HF/CB nanocomposites at the loading percentage of 30% w/w. As illustrated in Figure 3.61, the results illustrate that the PANI/SF/HF with a RL_{min} of -27.1 dB at 11.5 GHz with the SD 3.21 kg/m^2. The SE_{max} was 29.0 dB at 10.2 GHz for a thickness of 3 mm. On the other hand, the results illustrate that the PANI/SF/HF/CB with a RL_{min} of -25.2 dB at 10.5 GHz with the SD

3.14 kg/m^2. The SE_{max} was 26.1 dB at 10.2 GHz for a thickness of 3 mm. This refers to the MA and EMI shielding properties related to the nanocomposite morphology. As a result, this improvement is due to the fact that this incorporation will affect the MA capacity by changing the complex permeability and permittivity. This incorporation leads to an effective and low-thickness absorber with a wide BW_{-10dB}.

Table 3.26 – MA behavior of PANI/SF/HF and PANI/SF/HF/CB nanocomposites at 3.0 mm thickness

Samples	RL_{min} (dB)	f_m (GHz)	$BW_{-10\ dB}$ (GHz)	SD (kg/m^2)
PANI/50%SF/50%HF	-27.1	11.5	3.2	3.21
PANI/45%SF/45%HF/10%CB	-25.2	10.5	3.2	3.14

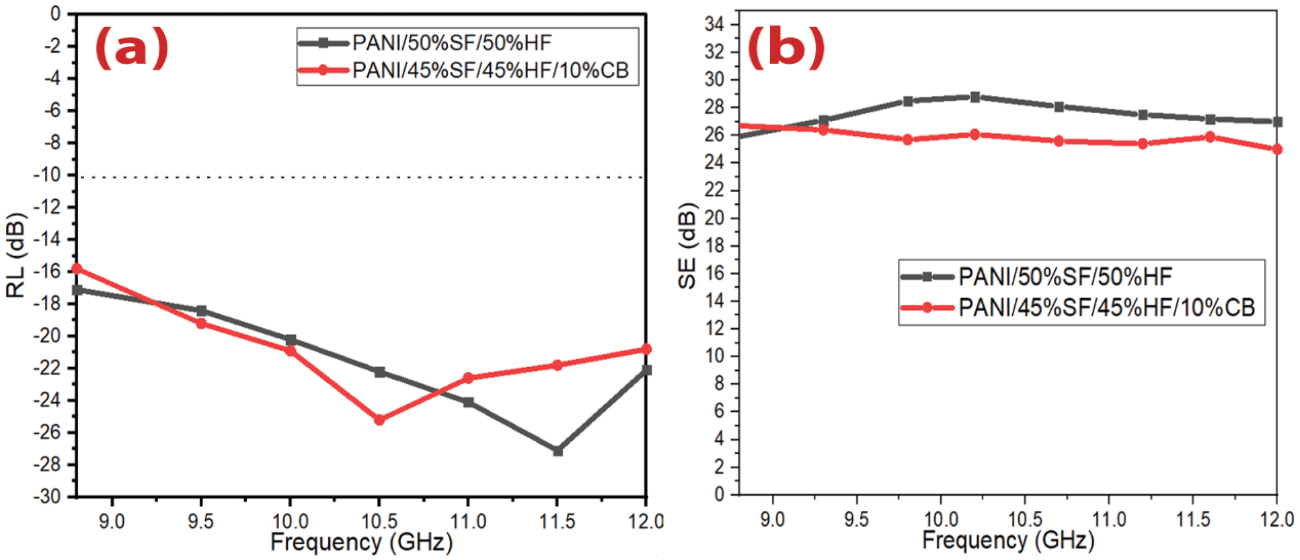

Figure 3.61 (a,b) – RL and SE curves of PANI/SF/HF and PANI/SF/HF/CB nanocomposites at 3.0 mm thickness

Figure 3.62 illustrates the RL of PANI/SF/HF nanocomposites with various thicknesses (3.0, 3.22 and 3.45 mm). Figure 3.62 shows that the RL attenuation peaks of samples moved to lower frequencies with increasing sample thickness. On the other hand, one can notice the RL_{min} moves gradually to a lower frequency with the increase in loading percentage. Furthermore, Table 3.27 shows the PANI/SF/HF nanocomposites have low SD, ranging from 3.21 to 3.26 kg/m^2. The absorption percentage of microwaves reached about 99.9%. One can conclude that optimal absorption can be accomplished by modifying the absorber thickness and the loading percentage. The best result was obtained by using the PANI/SF/HF nanocomposite sample. Figure 3.63 shows the relationship between the number of research that studied the radar absorption properties of PANI/F within the range of 8.0-12.0 GHz and the absorption bandwidth under -10 dB.

It turns out that the number of these research (22), and only four research were able to cover most of the range (8.0-12.0 GHz). In order to evaluate the beneficial impact of the combination of PANI with SF/HF on the radar absorption properties, Table 3.28 shows a comparison of radar absorption properties of some lately reported PANI/NiZn ferrite absorbers with various loading ratios of the composites in the host matrix. The results of the literature show these composites have an elevated loading percentage in the host matrix. This leads to a high surface density and heavy weight of the absorbents. This confirms the distinctiveness of prepared nanocomposites in terms of lower loading percentage compared with this literature.

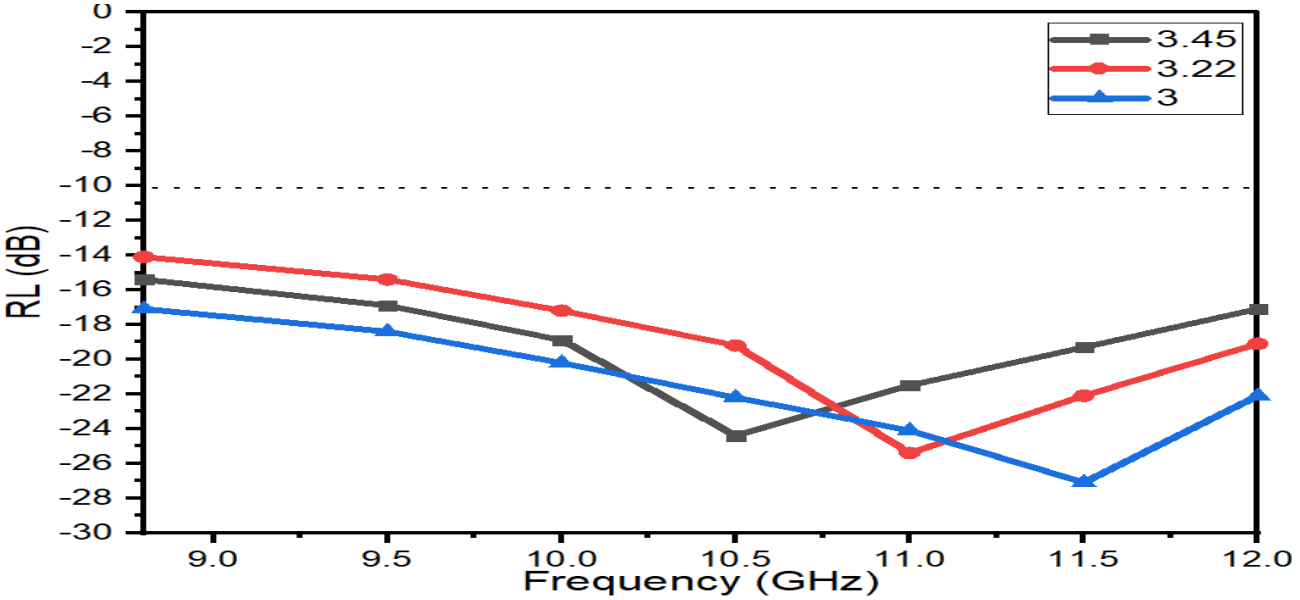

Figure 3.62 – RL curves of PANI/SF/HF with various thicknesses (3.0, 3.22, 3.45 mm)

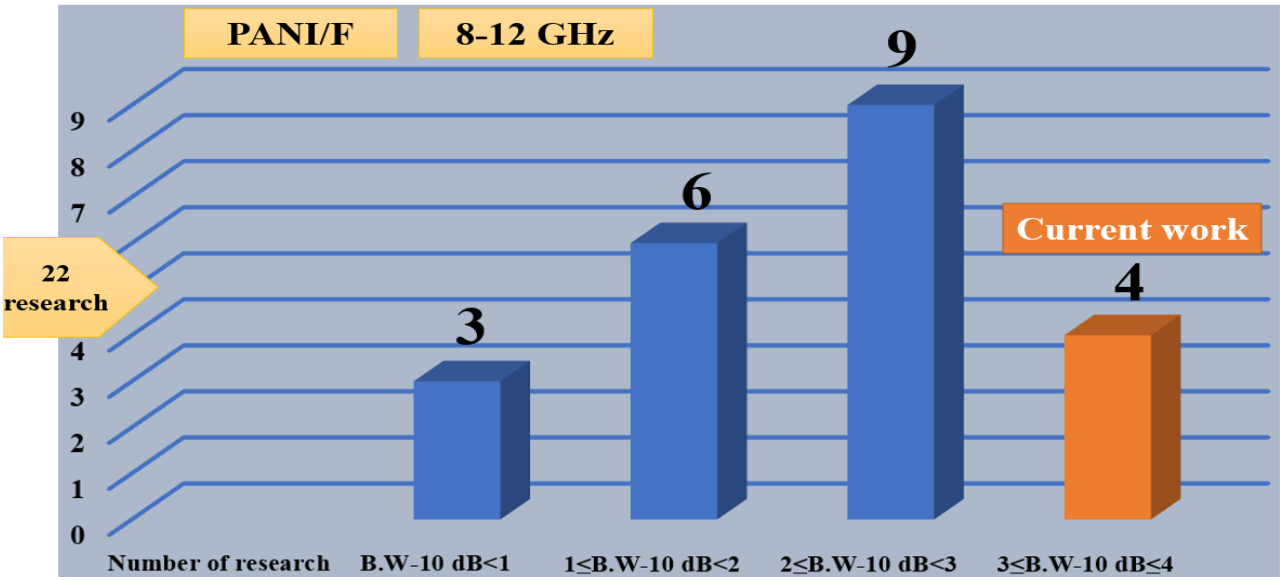

Figure 3.63 – Relationship between the number of research that studied the radar absorption properties of PANI/F and the absorption bandwidth under -10 dB

Table 3.27 – MA behavior of PANI/SF/HF nanocomposites at various thicknesses (3.0, 3.22, 3.45 mm)

Loading ratio %	t (mm)	RL_{min} (dB)	f_m (GHz)	BW_{-10dB} (GHz)	SD (kg/m^2)
30%	3.0	-27.1	11.5	3.2	3.21
	3.22	-25.4	11.0	3.2	3.23
	3.45	-24.3	10.6	3.2	3.26

Table 3.28 – Radar absorption properties of PANI-based nanomaterials

Specimen (relative weight ratio)/host matrix	Loading percentage (%)	t (mm)	RL_{min} (dB)	f_m (GHz)	BW_{-10dB} (GHz)	Ref
NiZn ferrite-PANI(50:50)/Epoxy	67	2.00	-14	11.0	2.6	[85]
NiZn ferrite-PANI(35:65)/Epoxy	20	2.00	-20	9.1	0.5	[137]
NiZn ferrite-PANI(1:3)/Paraffin	75	3.50	-32	9.5	3.8	[87]
NiZn ferrite-PANI(2:1)/Paraffin	70	2.00	-27.5	6.0	3.0	[86]
NiZn ferrite-PANI/Epoxy	67	3.00	-17	11.1	2.8	[88]

Conclusion

According to the results of the dissertation research, the following conclusions are made**:**

1) Received ferrite absorbers from magnetic loss materials. It was found that the RL attenuation peaks of samples were shown to move to lower frequencies with increasing the metal ions to citrate acid, PVA concentration and calcination temperature. This may be due to the change in the crystallite size of the ferrite nanoparticles. The results of XRD patterns indicated that the crystallite size of nickel-zinc ferrite increased by increasing the calcination temperature. As well, the XRD patterns results revealed that the crystallite size of nickel-zinc ferrite increased by increasing the metal ions and PVA concentrations during the preparation process of the ferrite, regardless of the calcination temperature.
2) The effect of CB, CI, AC, and C on the ferrite on the MA and EMI properties were displayed. The best result obtained was by using F/CI/CB-211 composite.

A RL_{min} indicated -18.4 dB at 11.7 GHz and $BW_{-10\ dB}$ was 4.0 GHz for a thickness of 2 mm with a SD of 4.01 kg/m^2.

3) The results of the hybrid nanocomposites revealed that the RL_{min} and SE_{max} improved by obtaining -19.8 dB and 23.18 dB, respectively for PANI/F.2 nanocomposite with loading percentage from 25% which means obtaining lightweight absorbers with distinguished properties.
4) It was detected that PANI/SF/HF and PANI/SF/HF/CB nanocomposites had the best results to absorb EM waves. The absorption percentage of EM waves reached about 99.9% with a loading percentage of 30%.

Assessment of the results of the work

The tasks set in the work are completely reached. Microwave absorbers are obtained competing with commercial absorbers mentioned in the literature in terms of weight, RL, SE, and absorption BW_{-10}. The results are reliable and reasonable since all measurements were carried out on calibrated instruments using standard methods. The prepared samples were structurally characterized using XRD, FTIR, TGA, and EDX. A powder X-ray diffractometer (XRD, Rigaku Miniflex 600, Cu-Ka) was used to define the crystal structures of the powders. The X-ray diffraction patterns of the prepared samples were recorded at 2θ =10 - 90°. Fourier Transform IR (FTIR) spectra of the prepared samples were recorded on a Perkin Elmer 65 FTIR spectrometer in the 400–4000 cm^{-1}. Thermogravimetric analysis (TGA) curve of the prepared samples were recorded on a thermal analyzer (NETZSCH 449F3A-0372-M) under a nitrogen atmosphere, from room temperature to 1000°C under a constant heating rate of 10 °C/min. Energy-dispersive X-ray spectroscopy (EDX, Quanta 200 3D) was used to know the chemical composition of some of the prepared samples. A scanning electron microscope (SEM, FEI Quanta 200 3D) was utilized to define the morphology of some of the prepared powders. The prepared samples were functionally characterized using the free-space technique.

Assessment of technical efficiency proposed in the thesis

The results obtained in the framework of this thesis can be suggested for producing microwave absorbers synthesized based on magnetic loss and dielectric loss materials. An advantage of the work is that obtained absorbers can attenuate about 99.9% of EM waves with low SD and wide absorption BW_{-10}. These microwave absorbers can be used to cover the walls of anechoic chambers and to prevent or reduce EM reflections from large bodies.

Assessment of the scientific level and economic efficiency of the work

Nowadays, most international companies work to fabricate MAMs for reducing the noise produced by electronic circuits and smartphones, removing the noise from the original images on screens and manufacturing protective shields in microwave ovens. As

well as fabricating these materials for military applications to reduce the radar cross-section of some military systems in order to keep them away from the eyes of hostile radars. MAMs consider expensive materials from a commercial point of view (1 Kg of MAMs costs between 900-1200$). This work opens up prospects for the production of effective absorbers in the laboratory as affordable, cheap (e.g., 1 Kg of raw materials of CB/$Mn_{0.1}Ni_{0.5}Zn_{0.4}Fe_2O_4$, PANI/$Ni^{3+}_{0.25}Ni^{2+}_{0.375}Zn^{2+}_{0.25}Fe_2O_4$/CB and PANI/SF/HF cost between 25-40 $, 75-100$, and 90-110$, respectively) with the required international quality. The results obtained are of practical interest for obtaining new improved nanocomposites for absorbing EM waves at the X-band frequency. In addition, the scientific level of the presented thesis complies with international standards for research conducted in the selected field. This is evidenced by a good level of publications, the presentation and the discussion of the results of work at international conferences.

References

1. Zhang J. et al. Preparation and Microwave Absorbing Characteristics of Multi-Walled Carbon Nanotube/Chiral-Polyaniline Composites // Open J. Polym. Chem. 2014. Vol. 04, № 03. P. 62–72.
2. Hosseini S.H., Asadnia A., Moloudi M. Preparation and electromagnetic wave absorption hard-soft Ba ferrite/polypyrrole core-shell nanocomposites // Mater. Res. Innov. 2015. Vol. 19, № 2. P. 107–112.
3. Lv H. et al. A Flexible Microwave Shield with Tunable Frequency-Transmission and Electromagnetic Compatibility // Adv. Funct. Mater. 2019. Vol. 29, № 14. P. 1–8.
4. Liang C. et al. Ultra-light MXene aerogel/wood-derived porous carbon composites with wall-like “mortar/brick” structures for electromagnetic interference shielding // Sci. Bull. Science China Press, 2020. Vol. 65, № 8. P. 616–622.
5. Chen X. et al. Capacitive behavior of MoS2 decorated with FeS2@carbon nanospheres // Chem. Eng. J. 2020. Vol. 379, № July.
6. Chen S. et al. Asymmetric alicyclic amine-polyether amine molecular chain structure for improved energy storage density of high-temperature crosslinked polymer capacitor // Chem. Eng. J. Elsevier B.V., 2020. Vol. 387. P. 123662.
7. Cheng C. et al. Simultaneously improving mode I and mode II fracture toughness of the carbon fiber/epoxy composite laminates via interleaved with uniformly aligned PES fiber webs // Compos. Part A Appl. Sci. Manuf. Elsevier Ltd, 2020. Vol. 129. P. 105696.
8. Xu H. et al. Lightweight Ti 2 CT x MXene/Poly(vinyl alcohol) Composite Foams for Electromagnetic Wave Shielding with Absorption-Dominated Feature // ACS Appl. Mater. Interfaces. 2019. Vol. 11, № 10. P. 10198–10207.
9. Xie X.B. et al. Spinel structured MFe2O4 (M = Fe, Co, Ni, Mn, Zn) and their composites for microwave absorption: A review // Chem. Eng. J. Elsevier B.V., 2022. Vol. 428, № May 2021. P. 131160.
10. Bera P. et al. Solution combustion synthesis, characterization, magnetic, and dielectric properties of CoFe2O4and Co0.5M0.5Fe2O4(M = Mn, Ni, and Zn) // Phys. Chem. Chem. Phys. 2020. Vol. 22, № 35. P. 20087–20106.
11. Shu J.C. et al. Molecular Patching Engineering to Drive Energy Conversion as Efficient and Environment-Friendly Cell toward Wireless Power Transmission // Adv. Funct. Mater. 2020. Vol. 30, № 10. P. 1–10.
12. Cao M.S. et al. Variable-Temperature Electron Transport and Dipole Polarization Turning Flexible Multifunctional Microsensor beyond Electrical and Optical Energy // Adv. Mater. 2020. Vol. 32, № 10. P. 1–8.

13. Ma M. et al. Development, applications, and future directions of triboelectric nanogenerators // Nano Res. 2018. Vol. 11, № 6. P. 2951–2969.

14. Li G. et al. Dynamical Control over Terahertz Electromagnetic Interference Shielding with 2D Ti3C2Ty MXene by Ultrafast Optical Pulses // Nano Lett. 2020. Vol. 20, № 1. P. 636–643.

15. Folgueras L. de C., Alves M.A., Rezende M.C. Microwave absorbing paints and sheets based on carbonyl iron and polyaniline: Measurement and simulation of their properties // J. Aerosp. Technol. Manag. 2010. Vol. 2, № 1. P. 63–70.

16. Af B.A. ADVANCES IN COMPOSITE MATERIALS ECODESIGN AND ANALYSIS Edited by Brahim A tt af. 211AD.

17. Ari Adi W. et al. Metamaterial: Smart Magnetic Material for Microwave Absorbing Material // Electromagn. Fields Waves. 2019. P. 1–18.

18. Griffiths H. et al. Radar spectrum engineering and management: Technical and regulatory issues // Proc. IEEE. IEEE, 2015. Vol. 103, № 1. P. 85–102.

19. Adebayo L.L. et al. Investigation of the broadband microwave absorption of citric acid coated Fe3O4/PVDF composite using finite element method // Appl. Sci. 2019. Vol. 9, № 18.

20. McDowell A.J., Hubing T.H. Analysis and comparison of plane wave shielding effectiveness decompositions // IEEE Trans. Electromagn. Compat. 2014. Vol. 56, № 6. P. 1711–1714.

21. Wang Y. et al. Recent advances in conjugated polymer-based microwave absorbing materials // Polymers (Basel). 2017. Vol. 9, № 1.

22. Zhao B. et al. Recent Advances on the Electromagnetic Wave Absorption Properties of Ni Based Materials // Eng. Sci. 2018. P. 5–40.

23. Drab M. et al. Electric double layer and orientational ordering of water dipoles in narrow channels within a modified Langevin Poisson-Boltzmann model // Entropy. 2020. Vol. 22, № 9.

24. Raju G. Dielectric Loss and Relaxation—I // Dielectrics in Electric Fields, Second Edition. 2016. 83–136 p.

25. Mohamed M.A. et al. The field of an electric dipole and the polarizability of a conducting object embedded in the interface between dielectric materials // Prog. Electromagn. Res. B. 2009. № 16. P. 1–20.

26. Green M. et al. Dielectric, magnetic, and microwave absorption properties of polyoxometalate-based materials // J. Magn. Magn. Mater. Elsevier B.V., 2020. Vol. 497, № September 2019. P. 165974.

27. Pratap V. et al. Electromagnetic and microwave absorbing properties of U-type barium hexaferrite / polyaniline-epoxy composites Electromagnetic and Microwave Absorbing Properties of U- type Barium Hexaferrite / Polyaniline-Epoxy Composites. 2020. Vol. 080003, № May. P. 1–6.

28. Du S., Chen H., Hong R. Preparation and electromagnetic properties characterization of reduced graphene oxide/strontium hexaferrite nanocomposites // Nanotechnol. Rev. 2020. Vol. 9, № 1. P. 105–114.

29. Srivastava R., Yadav B.C. Ferrite materials: Introduction, synthesis techniques, and applications as sensors // Int. J. Green Nanotechnol. Biomed. 2012. Vol. 4, № 2. P. 141–154.

30. Jadhav V. V. et al. Properties of ferrites // Spinel Ferrite Nanostructures for Energy Storage Devices. Elsevier Inc., 2020. № M. 35–50 p.

31. Arora A. Optical and electric field control of magnetism // Univ. Potsdam. 2018. P. 11–20.

32. Dehghan R., Seyyed Ebrahimi S.A., Badiei A. Investigation of the effective parameters on the synthesis of Ni-ferrite nanocrystalline powders by coprecipitation method // J. Non. Cryst. Solids. Elsevier B.V., 2008. Vol. 354, № 47–51. P. 5186–5188.

33. Hankare P.P. et al. Synthesis, characterization and effect of sintering temperature on magnetic properties of MgNi ferrite prepared by co-precipitation method // J. Alloys Compd. 2009. Vol. 475, № 1–2. P. 926–929.

34. Vadivel M. et al. Synthesis, structural, dielectric, magnetic and optical properties of Cr substituted CoFe2O4 nanoparticles by co-precipitation method // J. Magn. Magn. Mater. Elsevier, 2014. Vol. 362. P. 122–129.

35. Jacob B.P. et al. Influence of preparation method on structural and magnetic properties of nickel ferrite nanoparticles // Bull. Mater. Sci. 2011. Vol. 34, № 7. P. 1345–1350.

36. Padmanaban R. et al. Recent Trends in Materials Science (RTMS-2011) // Recent Trends Mater. Sci. Appl. 2017. № October. P. 2011.

37. Ding Z. et al. Synthesis and Characterization of Co-Zn Ferrite Nanoparticles by Hydrothermal Method: A Comparative Study // IEEE Trans. Magn. 2015. Vol. 51, № 11. P. 2–5.

38. Zalite I. et al. Hydrothermal synthesis of cobalt ferrite nanosized powders // IOP Conf. Ser. Mater. Sci. Eng. 2015. Vol. 77, № 1.

39. Praveena K. et al. Microwave absorption studies of magnetic sublattices in microwave sintered Cr3+ doped SrFe12O19 // J. Magn. Magn. Mater. Elsevier, 2017. Vol. 426, № July 2016. P. 604–614.

40. Mallesh S. et al. Structure and magnetic properties of ZnO coated MnZn ferrite nanoparticles // J. Magn. Magn. Mater. Elsevier, 2016. Vol. 418. P. 112–117.

41. Jia P.Y. et al. Sol-gel synthesis and characterization of SiO2@CaWO 4,SiO2@CaWO4:Eu3+/Tb3+ core-shell structured spherical particles // Nanotechnology. 2006. Vol. 17, № 3. P. 734–742.

42. Sulaiman N.H. et al. Superparamagnetic calcium ferrite nanoparticles synthesized using a simple solgel method for targeted drug delivery // Biomed. Mater. Eng. 2015. Vol. 26. P. S103–S110.

43. Panchal N.R., Jotania R.B. Cobalt ferrite nano particles by microemulsion route // Nanotechnology. 2010. Vol. 1, № 1. P. 17–18.

44. Zhao D.L., Lv Q., Shen Z.M. Fabrication and microwave absorbing properties of Ni-Zn spinel ferrites // J. Alloys Compd. 2009. Vol. 480, № 2. P. 634–638.

45. Zhuang L. et al. Temperature sensitive ferrofluid composed of Mn 1-xZn xFe 2O 4 nanoparticles prepared by a modified hydrothermal process // Powder Technol. 2012. Vol. 217. P. 46–49.

46. Fan G. et al. Nanocrystalline zinc ferrite photocatalysts formed using the colloid mill and hydrothermal technique // Chem. Eng. J. 2009. Vol. 155, № 1–2. P. 534–541.

47. Goodarz Naseri M. et al. Superparamagnetic magnesium ferrite nanoparticles fabricated by a simple, thermal-treatment method // J. Magn. Magn. Mater. Elsevier, 2014. Vol. 350. P. 141–147.

48. Milutinović A. et al. The cation inversion and magnetization in nanopowder zinc ferrite obtained by soft mechanochemical processing // Mater. Res. Bull. 2013. Vol. 48, № 11. P. 4759–4768.

49. Biasotto G. et al. A novel synthesis of perovskite bismuth ferrite nanoparticles // Process. Appl. Ceram. 2011. Vol. 5, № 3. P. 171–179.

50. Li S. et al. Ultrafast microwave hydrothermal synthesis of BiFeO3 NANOPLATES // J. Am. Ceram. Soc. 2013. Vol. 96, № 10. P. 3155–3162.

51. Ibrahim A.M., El-Latif M.M.A., Mahmoud M.M. Synthesis and characterization of nano-sized cobalt ferrite prepared via polyol method using conventional and microwave heating techniques // J. Alloys Compd. Elsevier B.V., 2010. Vol. 506, № 1. P. 201–204.

52. Manikandan A. et al. Synthesis, optical and magnetic properties of pure and Co-doped ZnFe 2O4 nanoparticles by microwave combustion method // J. Magn. Magn. Mater. Elsevier, 2014. Vol. 349. P. 249–258.

53. Kaur H., Singh J., Randhawa B.S. Essence of superparamagnetism in cadmium ferrite induced by various organic fuels via novel solution combustion method // Ceram. Int. Elsevier, 2014. Vol. 40, № 8 PART A. P. 12235–12243.

54. Kaur N., Kaur M. Comparative studies on impact of synthesis methods on structural and magnetic properties of magnesium ferrite nanoparticles // Process. Appl. Ceram. 2014. Vol. 8, № 3. P. 137–143.

55. Sharma R., Chandra Agarwala R., Agarwala V. A study on the heat-treatments of nanocrystalline nickel substituted BaW hexaferrite produced by low combustion synthesis method // J. Magn. Magn. Mater. 2007. Vol. 312, № 1. P. 117–125.

56. Huízar-Félix A.M. et al. Sol-gel based Pechini method synthesis and characterization of Sm 1-xCa xFeO 3 perovskite 0.1≤x≤0.5 // Powder Technol. Elsevier B.V., 2012. Vol. 229. P. 290–293.

57. Jacobo S.E., Herme C., Bercoff P.G. Influence of the iron content on the formation process of substituted Co-Nd strontium hexaferrite prepared by the citrate precursor method // J. Alloys Compd. Elsevier B.V., 2010. Vol. 495, № 2. P. 513–515.

58. Martins M.L. et al. Mechanisms of phase formation along the synthesis of Mn-Zn ferrites by the polymeric precursor method // Ceram. Int. Elsevier, 2014. Vol. 40, № 10. P. 16023–16031.

59. Nikolić A.S. et al. Carboxylic acids and polyethylene glycol assisted synthesis of nanocrystalline nickel ferrites // Ceram. Int. 2013. Vol. 39, № 6. P. 6681–6688.

60. Drmota A., Drofenik M., Žnidaršič A. Synthesis and characterization of nano-crystalline strontium hexaferrite using the co-precipitation and microemulsion methods with nitrate precursors // Ceram. Int. 2012. Vol. 38, № 2. P. 973–979.

61. Uskoković V., Drofenik M. A mechanism for the formation of nanostructured NiZn ferrites via a microemulsion-assisted precipitation method // Colloids Surfaces A Physicochem. Eng. Asp. 2005. Vol. 266, № 1–3. P. 168–174.

62. Saini P., Aror M. Microwave Absorption and EMI Shielding Behavior of Nanocomposites Based on Intrinsically Conducting Polymers, Graphene and Carbon Nanotubes // New Polym. Spec. Appl. 2012.

63. Boeva Z.A., Sergeyev V.G. Polyaniline: Synthesis, properties, and application // Polym. Sci. - Ser. C. 2014. Vol. 56, № 1. P. 144–153.

64. Yusuf J.Y. et al. Recent advances and prospect of cobalt based microwave absorbing materials // Ceram. Int. Elsevier Ltd and Techna Group S.r.l., 2020. Vol. 46, № 17. P. 26466–26485.

65. Chen N., Gu M. Microstructure and Microwave Absorption Properties of Y-Substituted Ni-Zn Ferrites // Open J. Met. 2012. Vol. 02, № 02. P. 37–41.

66. Wang S. et al. Synthesis of porous nitrogen-doped graphene decorated by γ-Fe2O3 nanorings for enhancing microwave absorbing performance // Ceram. Int. Elsevier Ltd and Techna Group S.r.l., 2020. Vol. 46, № 1. P. 1002–1010.

67. Shu R. et al. Facile synthesis of nitrogen-doped reduced graphene oxide/nickel-zinc ferrite composites as high-performance microwave absorbers in the X-band // Chem. Eng. J. Elsevier, 2020. Vol. 384, № July 2019. P. 123266.

68. Jaiswal R. et al. EMI and microwave absorbing efficiency of polyaniline-functionalized reduced graphene oxide/γ-Fe2O3/epoxy nanocomposite // Soft Matter. 2020. Vol. 16, № 28. P. 6643–6653.

69. Bueno A.R., Gregori M.L., Nóbrega M.C.S. Microwave-absorbing properties of Ni0.50-xZn0.50-x Me2xFe2O4 (Me=Cu, Mn, Mg) ferrite-wax composite in X-band frequencies // J. Magn. Magn. Mater. 2008. Vol. 320, № 6. P. 864–870.

70. Zinc N. et al. Synthesis and Microwave Absorbing Properties of Cu-Doped. 2013. Vol. 2013.

71. Chen B.Y. et al. Preparation and microwave absorption properties of Ni-Co nanoferrites // J. Alloys Compd. Elsevier B.V., 2015. Vol. 618. P. 222–226.

72. Almessiere M.A. et al. Effect of Nd-Y co-substitution on structural, magnetic, optical and microwave properties of NiCuZn nanospinel ferrites // J. Mater. Res. Technol. Korea Institute of Oriental Medicine, 2020. Vol. 9, № 5. P. 11278–11290.

73. Almessiere M.A. et al. Microstructure, dielectric and microwave features of [Ni0.4Cu0.2Zn0.4](Fe2−xTbx)O4 ($x \leq 0.1$) nanospinel ferrites // J. Mater. Res. Technol. Korea Institute of Oriental Medicine, 2020. Vol. 9, № 5. P. 10608–10623.

74. Almessiere M.A. et al. Impact of Eu3+ ion substitution on structural, magnetic and microwave traits of Ni–Cu–Zn spinel ferrites // Ceram. Int. Techna Group S.r.l., 2020. Vol. 46, № 8. P. 11124–11131.

75. Almessiere M.A. et al. Strong correlation between Dy3+ concentration, structure, magnetic and microwave properties of the [Ni0.5Co0.5](DyxFe2-x)O4 nanosized ferrites // J. Ind. Eng. Chem. The Korean Society of Industrial and Engineering Chemistry, 2020. Vol. 90. P. 251–259.

76. Goel S. et al. Effect of neodymium doping on microwave absorption property of barium hexaferrite in X-band // Mater. Res. Express. IOP Publishing, 2020. Vol. 7, № 1.

77. Ghasemi A. et al. Microwave absorption properties of Mn-Co-Sn doped barium ferrite nanoparticles // IEEE Trans. Magn. 2009. Vol. 45, № 6. P. 2456–2459.

78. Houbi A. et al. Microwave absorbing properties of ferrites and their composites: A review // J. Magn. Magn. Mater. Elsevier B.V., 2021. Vol. 529, № September 2020. P. 167839.

79. Harris V.G. Modern microwave ferrites // IEEE Trans. Magn. 2012. Vol. 48, № 3. P. 1075–1104.

80. Cui G. et al. Excellent microwave absorption properties derived from the synthesis of hollow fe 3 o 4 @reduced graphite oxide (RGO) nanocomposites // Nanomaterials. 2019. Vol. 9, № 2. P. 1–12.

81. Luo J. et al. Excellent microwave absorption properties by tuned electromagnetic parameters in polyaniline-coated Ba0.9La0.1Fe11.9Ni0.1O19/reduced graphene oxide nanocomposites // RSC Adv. Royal Society of Chemistry, 2017. Vol. 7, № 58. P. 36433–36443.

82. Ali N.N. et al. Lightweight broadband microwave absorbers of core–shell (polypyrrole/NiZn ferrite) nanocomposites in the X-band: insights on interfacial polarization // J. Mater. Sci. Mater. Electron. Springer US, 2019. Vol. 30, № 7. P. 6876–6887.

83. Hosseini S.H., Asadnia A. Synthesis, characterization, and microwave-absorbing properties of polypyrrole/MnFe 2O 4 nanocomposite // J. Nanomater. 2012. Vol. 2012.

84. Mostafa N.Y., Hessien M.M., Shaltout A.A. Hydrothermal synthesis and characterizations of Ti substituted Mn-ferrites // J. Alloys Compd. 2012. Vol. 529. P. 29–33.

85. Ting T.H., Yu R.P., Jau Y.N. Synthesis and microwave absorption characteristics of polyaniline/NiZn ferrite composites in 2-40 GHz // Mater. Chem. Phys. 2011. Vol. 126, № 1–2. P. 364–368.

86. Wang C.P. et al. Novel one-dimensional polyaniline/Ni0.5Zn0.5Fe 2O4 hybrid nanostructure: Synthesis, magnetic, and electromagnetic wave absorption properties // J. Nanoparticle Res. 2014. Vol. 16, № 3.

87. Wang M. et al. Controlled synthesis and microwave absorption properties of Ni0.6Zn0.4Fe2O4/PANI composite via an in-situ polymerization process // J. Magn. Magn. Mater. Elsevier, 2015. Vol. 377. P. 52–58.

88. Wang C. et al. Synthesis of novel NiZn-ferrite/Polyaniline nanocomposites and their microwave absorption properties // Mater. Sci. Semicond. Process. Elsevier, 2013. Vol. 16, № 1. P. 77–82.

89. Ma R.T., Zhao H.T., Zhang G. Preparation, characterization and microwave absorption properties of polyaniline/Co0.5Zn0.5Fe2O4 nanocomposite // Mater. Res. Bull. 2010. Vol. 45, № 9. P. 1064–1068.

90. Sun J. et al. Preparation of copper-cobalt-nickel ferrite/graphene oxide/polyaniline composite and its applications in microwave absorption coating // Prog. Org. Coatings. Elsevier, 2020. Vol. 141, № October 2019. P. 105552.

91. Manna K., Srivastava S.K. Fe3O4@Carbon@Polyaniline Trilaminar Core-Shell Composites as Superior Microwave Absorber in Shielding of Electromagnetic Pollution // ACS Sustain. Chem. Eng. 2017. Vol. 5, № 11. P. 10710–10721.

92. Xiong P., Huang H., Wang X. Design and synthesis of ternary cobalt ferrite/graphene/polyaniline hierarchical nanocomposites for high-performance supercapacitors This work is dedicated to Professor MIN Enze on the occasion of his 90th birthday. // J. Power Sources. Elsevier B.V, 2014. Vol. 245. P. 937–946.

93. Mondal K. et al. Carbon Nanostructures for Energy and Sensing Applications // J. Nanotechnol. 2019. Vol. 2019. P. 10–13.

94. Kwiatkowski M. et al. Evaluation of CO2 interactions with S-doped nanoporous carbon and its composites with a reduced GO: Effect of surface features on an apparent physical adsorption mechanism // Carbon N. Y. 2016. Vol. 98. P. 250–258.

95. Anh L.T.Q., Van Dan N. A microwave-absorbing property of super-paramagnetic zinc–nickel ferrite nanoparticles in the frequency range of 8–12 GHz // Appl. Phys. A Mater. Sci. Process. Springer Berlin Heidelberg, 2020. Vol. 126, № 1. P. 1–6.

96. Ri E. et al.) Huulwh Dqg & Duerq % Odfn % Dvhg 1Dqrfrpsrvlwhv Iru. P. 0–3.

97. Che R. et al. Microwave Absorption Enhancement and Complex Permittivity and Permeability of Fe Encapsulated within Carbon Nanotubes // Adv. Mater. 2004. Vol. 16, № 5. P. 401–405.

98. Lin H. et al. Investigation of the microwave-absorbing properties of Fe-filled carbon nanotubes // Mater. Lett. 2007. Vol. 61, № 16. P. 3547–3550.

99. Wu N. et al. Strengthened electromagnetic absorption performance derived from synergistic effect of carbon nanotube hybrid with Co@C beads // Adv. Compos. Hybrid Mater. Advanced Composites and Hybrid Materials, 2018. Vol. 1, № 1. P. 149–159.

100. Yang B. et al. Surface-oxidized FeCo/carbon nanotubes nanorods for lightweight and efficient microwave absorbers // Mater. Des. Elsevier Ltd, 2017. Vol. 136. P. 13–22.

101. Feng A. et al. Synthesis of a hierarchical carbon fiber@cobalt ferrite@manganese dioxide composite and its application as a microwave absorber // RSC Adv. Royal Society of Chemistry, 2020. Vol. 10, № 18. P. 10510–10518.

102. Gholampoor M., Movassagh-Alanagh F., Salimkhani H. Fabrication of nano-Fe3O4 3D structure on carbon fibers as a microwave absorber and EMI shielding composite by modified EPD method // Solid State Sci. Elsevier Masson SAS, 2017. Vol. 64. P. 51–61.

103. Liu Y. et al. Preparation and properties of cobalt oxides coated carbon fibers as microwave-absorbing materials // Appl. Surf. Sci. Elsevier B.V., 2011. Vol. 257, № 17. P. 7678–7683.

104. Meng X. et al. The electrochemical preparation and microwave absorption properties of magnetic carbon fibers coated with Fe 3 O 4 films // Appl. Surf. Sci. Elsevier B.V., 2011. Vol. 257, № 24. P. 10808–10814.

105. Verma P. et al. Electromagnetic interference shielding performance of carbon nanostructure reinforced, 3D printed polymer composites // J. Mater. Sci. Springer US, 2021. Vol. 56, № 20. P. 11769–11788.

106. Bayat M. et al. Electromagnetic interference shielding effectiveness of hybrid multifunctional Fe3O4/carbon nanofiber composite // Polymer (Guildf). 2014. Vol. 55, № 3. P. 936–943.

107. Hong Y.K. et al. Method and apparatus to measure electromagnetic interference shielding efficiency and its shielding characteristics in broadband frequency ranges // Rev. Sci. Instrum. 2003. Vol. 74, № 2. P. 1098–1102.

108. El Nahrawy A.M. et al. Crystallographic and magnetic properties of Al3+co-doped NiZnFe2O4 nano-particles prepared by sol-gel process // Egypt. J. Chem. 2019. Vol. 62, № 3. P. 925–932.

109. Hu E. et al. The role of soot particles in the tribological behavior of engine lubricating oils // Wear. Elsevier, 2013. Vol. 304, № 1–2. P. 152–161.

110. Bahri-Laleh N. et al. Microwave Absorption Properties of Polyaniline/Carbonyl Iron Composites // Silicon. Silicon, 2018. Vol. 10, № 4. P. 1337–1343.

111. Ezzati S.N. et al. Conducting, magnetic polyaniline/Ba0.25Sr0.75 Fe11(Ni0.5Mn0.5)O19 nanocomposite: Fabrication, characterization and application // J. Alloys Compd. Elsevier Ltd, 2015. Vol. 646. P. 1157–1164.

112. Meng X. et al. Facile synthesis of shell-core polyaniline/SrFe12O19 composites and magnetic properties // RSC Adv. Royal Society of Chemistry, 2016. Vol. 6, № 6. P. 4946–4949.

113. Ali N.N. et al. Comparative study of microwave absorption characteristics of (Polyaniline/NiZn ferrite) nanocomposites with different ferrite percentages // Mater. Chem. Phys. Elsevier B.V., 2018. Vol. 211. P. 79–87.

114. Elsayed A.H. et al. Synthesis and Properties of Polyaniline / ferrites Nanocomposites. 2011. Vol. 6. P. 206–221.

115. Kondawar S.B., Nandapure A.I. Magnetic and electrical properties of zinc-substituted nickel ferrite reinforced conducting polyaniline nanocomposites // J. Chinese Adv. Mater. Soc. 2014. Vol. 2, № 3. P. 186–198.

116. Figueroa Ramírez S.J., Miranda-Hernánde M. Carbon film electrodes as support of metallic particles // Int. J. Electrochem. Sci. 2012. Vol. 7, № 1. P. 150–166.

117. Kim S.Y. et al. Core-shell-structured cross-linked poly(glycidyl methacrylate)-coated carbonyl iron microspheres and their magnetorheology // J. Mater. Sci. 2014. Vol. 49, № 3. P. 1345–1352.

118. Gairola S.P. et al. Enhanced microwave absorption properties in polyaniline and nano-ferrite composite in X-band // Synth. Met. Elsevier B.V., 2010. Vol. 160, № 21–22. P. 2315–2318.

119. Li G. et al. Preparation of magnetic and conductive NiZn ferrite-polyaniline nanocomposites with core-shell structure // Colloids Surfaces A Physicochem. Eng. Asp. 2006. Vol. 276, № 1–3. P. 40–44.

120. Peng C.H. et al. Microwave-absorbing characteristics for the composites of thermal-plastic polyurethane (TPU)-bonded NiZn-ferrites prepared by combustion synthesis method // Mater. Sci. Eng. B Solid-State Mater. Adv. Technol. 2005. Vol. 117, № 1. P. 27–36.

121. Hwang Y. Microwave absorbing properties of NiZn-ferrite synthesized from waste iron oxide catalyst // Mater. Lett. 2006. Vol. 60, № 27. P. 3277–3280.

122. Kim D.Y. et al. Dependence of microwave absorbing property on ferrite volume fraction in MnZn ferrite-rubber composites // IEEE Trans. Magn. 1996. Vol. 32, № 2. P. 555–558.

123. Diniz V.C.S. et al. Effects of Mn1-xZnxFe2O4 Nanoparticles Concentration in a Silicone Matrix on Complex Permeability and Permittivity in the 1-10 GHz Range // Mater. Res. 2022. Vol. 25. P. 1–9.

124. Lee J. et al. Absorber for 1 GHz Application // October. 2009. Vol. 45, № 10. P. 4230–4233.

125. Lima U.R. et al. Synthesis of NiCuZn ferrite nanoparticles and microwave absorption characterization // Mater. Sci. Eng. B Solid-State Mater. Adv. Technol. 2008. Vol. 151, № 3. P. 238–242.

126. Shu R. et al. Synthesis and high-performance microwave absorption of reduced graphene oxide/zinc ferrite hybrid nanocomposite // Mater. Lett. Elsevier B.V., 2018. Vol. 215. P. 229–232.

127. Zong M. et al. One-step hydrothermal synthesis and microwave electromagnetic properties of RGO/NiFe2O4 composite // Ceram. Int. Elsevier, 2014. Vol. 40, № 5. P. 6821–6828.

128. Zong M., Huang Y., Zhang N. Reduced graphene oxide-CoFe 2 O 4 composite: Synthesis and electromagnetic absorption properties // Appl. Surf. Sci. Elsevier B.V., 2015. Vol. 345. P. 272–278.

129. Mustaffa M.S. et al. An investigation of microstructural, magnetic and microwave absorption properties of multi-walled carbon nanotubes/Ni0.5Zn0.5Fe2O4 // Sci. Rep. 2019. Vol. 9, № 1. P. 3–9.

130. Ye W. et al. Preparation and properties of CF-Fe3O4-BN composite electromagnetic wave-absorbing materials // RSC Adv. Royal Society of Chemistry, 2020. Vol. 10, № 19. P. 11121–11131.

131. Zou T. et al. Electromagnetic and microwave absorbing properties of multi-walled carbon nanotubes filled with Ni nanowire // J. Alloys Compd. 2010. Vol. 496, № 1–2. P. 22–24.

132. Zhang L., Zhu H. Dielectric, magnetic, and microwave absorbing properties of multi-walled carbon nanotubes filled with Sm2O3 nanoparticles // Mater. Lett. Elsevier B.V., 2009. Vol. 63, № 2. P. 272–274.

133. Xu P. et al. A study of the magnetic and electromagnetic properties of γ-Fe2O3-multiwalled carbon nanotubes (MWCNT) and Fe/Fe3C-MWCNT composites // Mater. Chem. Phys. 2009. Vol. 114, № 2–3. P. 556–560.

134. Zhao D.L., Li X., Shen Z.M. Preparation and electromagnetic and microwave absorbing properties of Fe-filled carbon nanotubes // J. Alloys Compd. 2009. Vol. 471, № 1–2. P. 457–460.

135. Xu X. et al. Cactus-Inspired Bimetallic Metal-Organic Framework-Derived 1D-2D Hierarchical Co/N-Decorated Carbon Architecture toward Enhanced Electromagnetic Wave Absorbing Performance // ACS Appl. Mater. Interfaces. 2019. Vol. 11, № 14. P. 13564–13573.

136. Xiang J. et al. Synthesis and characterization of FeCo/C hybrid nanofibers with high performance of microwave absorption // Mater. Res. Bull. Elsevier Ltd, 2014. Vol. 60. P. 589–595.

137. Didehban K. et al. Radar Absorption Properties of Ni0.5Zn0.5Fe2O4/PANI/epoxy Nanocomposites // J. Chinese Chem. Soc. 2015. Vol. 62, № 9. P. 826–831.